



# City Research Online

## City, University of London Institutional Repository

---

**Citation:** Tuling, A. (2010). The effect of precipitation and microstructure on hot ductility in high Al, Nb containing TRIP steels. (Unpublished Doctoral thesis, City, University of London)

This is the accepted version of the paper.

This version of the publication may differ from the final published version.

---

**Permanent repository link:** <https://openaccess.city.ac.uk/id/eprint/19660/>

**Link to published version:**

**Copyright:** City Research Online aims to make research outputs of City, University of London available to a wider audience. Copyright and Moral Rights remain with the author(s) and/or copyright holders. URLs from City Research Online may be freely distributed and linked to.

**Reuse:** Copies of full items can be used for personal research or study, educational, or not-for-profit purposes without prior permission or charge. Provided that the authors, title and full bibliographic details are credited, a hyperlink and/or URL is given for the original metadata page and the content is not changed in any way.

# The effect of precipitation and microstructure on hot ductility in high Al, Nb containing TRIP steels

**Alison Susan Tuling**

A thesis submitted to the School of Engineering and Mathematical Sciences, City University, London, United Kingdom, in fulfilment of the requirements for the degree of Doctor of Philosophy. This research was performed in the Industrial Metals and Minerals Research Institute and at the University of Pretoria, South Africa, except where otherwise acknowledged.

October 2010

# Contents

<b>Contents</b>	<b>2</b>
<b>List of Tables</b>	<b>8</b>
<b>List of Figures</b>	<b>11</b>
<b>Acknowledgements</b>	<b>25</b>
<b>Declaration</b>	<b>26</b>
<b>Abstract</b>	<b>27</b>
<b>List of Symbols</b>	<b>28</b>
<b>1 Introduction</b>	<b>32</b>
1.1 Transformation induced plasticity steels, their application and relevance . . .	32
1.1.1 A brief explanation of the transformation induced plasticity mechanism	32
1.1.2 Applications of transformation induced plasticity steels . . . . .	33
1.1.3 Complexities of transformation induced plasticity steels . . . . .	33
1.1.4 Rationale for the study of transformation induced plasticity steels . .	34
<b>2 Literature survey</b>	<b>35</b>
2.1 Summary of applications of transformation induced plasticity steels . . . . .	35

2.2	Industrial practice and hot tensile testing . . . . .	36
2.2.1	Industrial casting practice . . . . .	36
2.2.2	Transverse cracking in industry . . . . .	39
2.2.3	Test characteristics . . . . .	44
2.2.4	The applicability of hot ductility testing . . . . .	52
2.2.5	Definitions in/of hot ductility and other aspects of the hot ductility curve . . . . .	56
2.3	Mechanism/types of ductility loss at temperatures between 1000°C-700°C . .	57
2.3.1	Grain boundary sliding in austenite . . . . .	58
2.3.2	Ferrite . . . . .	59
2.3.3	Precipitation . . . . .	65
2.3.4	Dynamic recrystallisation . . . . .	67
2.4	Factors influencing the hot ductility mechanisms and properties . . . . .	69
2.4.1	The effect of chemistry on reduction of area . . . . .	69
2.4.2	Aluminium nitride, niobium carbo-nitride and manganese sulphide solubility equations . . . . .	87
2.4.3	Phase stabilities: liquidus and solidus, the peritectic reaction and the Ae <sub>3</sub> . . . . .	89
2.4.4	The effect of grain size on hot ductility . . . . .	94
2.4.5	The effect of strain rate on hot ductility . . . . .	96
2.4.6	The effect of cooling path and cooling rate on hot ductility . . . . .	100
2.5	Combining parameters: modelling . . . . .	102
<b>3</b>	<b>Hot Ductility (Reduction of Area) Analysis</b>	<b>105</b>
3.1	Experimental procedure at City University, London . . . . .	105

3.2	Evaluation of reduction of area . . . . .	108
3.2.1	Evaluation procedure at City University, London . . . . .	108
3.2.2	Evaluation procedure at University of Pretoria . . . . .	108
3.3	Results and remarks . . . . .	110
3.4	Conclusions of hot ductility analysis . . . . .	115
<b>4</b>	<b>Optical Microscopy Analysis</b>	<b>116</b>
4.1	Macro optical microscopy and optical microscopy of the fracture surface . . .	117
4.1.1	Aim and experimental procedure for macro optical microscopy . . . .	117
4.1.2	Results and remarks on the macro optical microscopy analysis . . . .	117
4.2	Cross sectional optical microscopy . . . . .	121
4.2.1	Aim and experimental procedure for cross sectional optical microscopy	121
4.2.2	Results and remarks on the cross sectional optical microscopy analysis	121
4.3	General remarks on the optical microscopy . . . . .	134
4.4	Conclusions of the optical microscopy analysis . . . . .	134
<b>5</b>	<b>Scanning Electron Microscopy Analysis</b>	<b>135</b>
5.1	Introduction . . . . .	135
5.2	Experimental procedure . . . . .	136
5.3	Results . . . . .	136
5.3.1	0.05% Aluminium Steel . . . . .	142
5.3.2	1.05% Aluminium steel . . . . .	143
5.3.3	1.53% Aluminium steel . . . . .	147
5.4	Conclusions of scanning electron microscopy analysis . . . . .	150

<b>6</b>	<b>Transmission Electron Microscopy Analysis</b>	<b>151</b>
6.1	Introduction . . . . .	151
6.2	Experimental procedure for transmission electron microscopy . . . . .	152
6.3	Results . . . . .	153
6.3.1	0.05% Aluminium steel . . . . .	155
6.3.2	1.05% Aluminium steel . . . . .	159
6.3.3	1.53% Aluminium steel . . . . .	170
6.4	General remarks on the transmission electron microscopy results . . . . .	172
6.5	Conclusions of transmission electron microscopy analysis . . . . .	173
<b>7</b>	<b>Thermodynamic Modelling Simulations</b>	<b>174</b>
7.1	Introduction . . . . .	174
7.2	Peritectic calculator for aluminium containing steels of varying carbon and manganese levels . . . . .	175
7.3	FactSage and Thermo-Calc programmes for phase diagram and precipitation volume fractions . . . . .	178
7.3.1	Use of calculations for predicting ductility behaviour . . . . .	182
7.4	Constitutive phase diagrams for the current steels . . . . .	187
7.5	Other solubility equations . . . . .	187
7.6	Ar <sub>3</sub> . . . . .	193
7.7	Conclusions of thermodynamic modelling simulations . . . . .	193
<b>8</b>	<b>Discussion</b>	<b>194</b>
8.1	Introduction . . . . .	195
8.2	Ductility . . . . .	196

8.3	Microscopy . . . . .	201
8.3.1	0.05% Aluminium steel . . . . .	201
8.3.2	1.05% Aluminium steel . . . . .	201
8.3.3	1.53% Aluminium steel . . . . .	202
8.3.4	General discussion on the microscopy . . . . .	203
8.3.5	Regression equations for grain size and precipitate size on the ductility of 0.05 and 1.53% aluminium steels . . . . .	204
8.4	Thermodynamic simulations . . . . .	206
8.4.1	Simulation validation . . . . .	207
8.4.2	Anomalies for Su steel 3, Su steel 5 . . . . .	212
8.4.3	Ae <sub>3</sub> for Mintz steel 4 . . . . .	212
8.5	Integration of results chapters . . . . .	214
8.5.1	Grain size and the peritectic reaction . . . . .	214
8.5.2	Effective aluminium nitride precipitation in austenite . . . . .	214
8.5.3	Niobium carbo-nitride precipitation . . . . .	220
8.5.4	Recrystallisation . . . . .	223
8.5.5	The effect of Ae <sub>3</sub> , Ar <sub>3</sub> and deformation induced ferrite on ductility. . .	224
8.6	Experimental issues . . . . .	225
8.6.1	Porosity . . . . .	226
8.6.2	Melting/reheat . . . . .	226
8.7	Failure mechanisms . . . . .	226
<b>9</b>	<b>Conclusions</b>	<b>229</b>
<b>10</b>	<b>Contributions to Original Knowledge</b>	<b>231</b>

<b>11 Recommendations for the Industrial Applications</b>	<b>233</b>
11.1 Introduction . . . . .	233
11.2 Alloy design considerations . . . . .	234
<b>12 Recommendations for Further Experimental Work</b>	<b>237</b>
<b>Appendices</b>	
<b>A Ductility Appendix</b>	<b>239</b>
<b>B Optical Microscopy Appendix</b>	<b>244</b>
B.1 Macro optical microscopy . . . . .	244
B.2 Cross sectional microscopy . . . . .	244
<b>C Scanning Electron Microscopy Appendix</b>	<b>250</b>
<b>D Transmission Electron Microscopy Appendix</b>	<b>251</b>
D.1 Diffraction analysis using an electron diffraction simulation program . . . . .	251
D.2 Slow cool rate transmission electron microscopy appendix . . . . .	254
<b>E Thermodynamic Modelling Appendix</b>	<b>255</b>
E.1 The effective peritectic point and relative carbon level from peritectic point for all steels . . . . .	255
E.2 Data base details for FactSage and Thermo-Calc . . . . .	256
E.3 Typical FactSage and Thermo-Calc results . . . . .	258
<b>References</b>	<b>260</b>

# List of Tables

2.1	Lattice parameter for various forms of AlN. . . . .	79
2.2	Composition (wt%) of Al TRIP steels from Mintz <i>et al.</i> [10]. . . . .	84
2.3	Composition (wt%) of steels from Su <i>et al.</i> [11]. . . . .	86
2.4	Solubilities, $K_s$ , of MnS, AlN and Nb(C,N). $K_s$ is the solubility product( $[M][X]$ ) in various phases of solid steel, and $T$ is the temperature in Kelvin. . . . .	88
2.5	Ranges (wt%) for alloying elements in Equations 2.7 and 2.8 from [140]. . . . .	92
2.6	Composition range for the Ae <sub>3</sub> from Andrews [167]. . . . .	93
3.1	Composition of TRIP steels, wt% [178]. . . . .	106
4.1	List of average grain sizes for the unmelted and melted 0.05%Al steel samples. Grain size average excludes samples with DRX. (P) indicates samples with porosity, $\phi$ is the original diameter of the specimen. . . . .	122
4.2	List of grain sizes for the unmelted and melted grain sizes in the 1%Al steel. Grain size average excludes samples with DRX. (P) indicates samples with porosity, $\phi$ is the original diameter of the specimen. . . . .	124
4.3	List of grain sizes for the unmelted and melted grain sizes in the 1.53%Al steel. Grain size average excludes samples with DRX. (P) indicates samples with porosity, $\phi$ is the original diameter of the specimen. . . . .	129
5.1	SEM observations for 0.05%Al steel, ‘unmelted’ tests. . . . .	142
5.2	SEM observations for 0.05%Al steel, melted tests. . . . .	142

5.3	Grain sizes by SEM fracture surface and optical $c/s$ for 0.05%Al steel, indicating that grain size tends to be over estimated with SEM. . . . .	143
5.4	SEM observations for 1.05%Al steel, ‘unmelted’ samples. . . . .	144
5.5	SEM observations for 1.05%Al steel, melted samples. . . . .	145
5.6	SEM observations for 1.53%Al steel, ‘unmelted’ samples. . . . .	148
5.7	SEM observations for 1.44%Al steel, melted samples. . . . .	148
6.1	General precipitation summary for 0.05%Al steel. . . . .	153
6.2	General precipitation summary for 1%Al steel. . . . .	153
6.3	General precipitation summary for 1.5%Al steel. . . . .	154
6.4	Summary of TEM results. . . . .	173
7.1	Compositions (wt%) used in the phase simulations. . . . .	178
7.2	Additional compositions (wt%) used in the phase simulations. . . . .	181
7.3	Maximum variation, average variation and standard deviation between the Thermo-Calc and FactSage simulations for all phase field boundaries for all steels in Table 7.1. The maximum variation is Thermo-Calc value minus FactSage value. . . . .	182
7.4	Theoretical AlN precipitation in delta ferrite and austenite. . . . .	183
7.5	Maximum precipitation temperature and volume fraction ( $V_f$ ) Nb(C,N) precipitated (FactSage model). . . . .	184
7.6	Ar <sub>3</sub> temperatures as determined using a theta dilatometer [182]. . . . .	193
8.1	Regression statistics and coefficients for the regression of grain size and precipitate size on ductility. . . . .	206
8.2	Reported liquidus and solidus temperatures (°C). . . . .	208
8.3	Reported Ae <sub>3</sub> and Ar <sub>3</sub> temperatures (°C). . . . .	210
8.4	Ae <sub>3</sub> problems with Su. Temperatures in °C. . . . .	212

8.5	Observed, theoretical AlN precipitation and [Al][N] product giving effective AlN precipitation. . . . .	217
A.1	R of A data for 0.05%Al steel. . . . .	240
A.2	R of A data for 1.05%Al steel. . . . .	242
A.3	R of A data for 1.53%Al steel. . . . .	243
B.1	Hot ductility (%) for 0.05%Al steels, indicating the type of failure from macro OM. Intergranular failure predominates at low Al content. “P” indicates that the sample has greater than 10% porosity. . . . .	245
B.2	Hot ductility (%) for 1.05%Al steels, indicating the type of failure from macro OM. A combination of intergranular and transgranular failure occurs at intermediate Al contents. “P” indicates that the sample has greater than 10% porosity. . . . .	246
B.3	Hot ductility (%) for 1.53%Al steels, indicating the type of failure from macro OM. A combination of intergranular and transgranular failure occurs at high Al contents. “P” indicates that the sample has greater than 10% porosity. . . . .	247
C.1	SEM grain size for 0.05%Al steel. . . . .	250
C.2	SEM grain size for unmelted 1.05%Al steel. . . . .	250
C.3	SEM grain size for unmelted 1.53%Al steel. . . . .	250
D.1	Precipitation summary for samples cooled at the slower cooling rate. . . . .	254
E.1	$C_{actual} - C_{peritectic}$ values for all steels. . . . .	255
E.2	Thermo-Calc4 for windows data base. . . . .	256
E.3	Data base (FACT53, Fsstel) for FactSage: Duplicates were suppressed, Pure liquid and solid species considered. . . . .	257
E.4	Comparison of the FactSage (FS) and Thermo-Calc (TC) simulations for all phase field boundaries for all Trip steels in Table 7.1. All temperatures in °C. Relative difference (%) is with respect to the Thermo-Calc value. . . . .	259

# List of Figures

2.1	Schematic diagram of a typical continuous casting machine, not to scale [17].	37
2.2	The predicted thermal history of billet casting is displayed according to a software simulation developed by the University of British Columbia [20]. . .	38
2.3	Broad and narrow faces in continuous cast slabs. . . . .	39
2.4	Formation mechanism of segregation at the meniscus [18]. . . . .	40
2.5	Scanning electron micrograph of grain boundary surface. Surface shows fine dendritic appearance superimposed on which are larger, crystallographically orientated plate like features. [31]. Presumably the AlN is in the areas indicated with the arrows. . . . .	42
2.6	Correlation between the points along the length of the slab where deep oscillation marks are observed in comparison to where the transverse cracking is observed [16]. This shows that transverse cracks predominantly occur in the deep oscillation marks. . . . .	42
2.7	Schematic of standard testing procedure. . . . .	44
2.8	Effect of holding time on the hot ductility of 0.15%C-0.054%Nb steel for two different cooling cycles. The holding temperature (T) is shown in the thermal cycle [49]. . . . .	49
2.9	Temperature differences between interior and outer surfaces of a 10mm diameter specimen (0.1%C steel) [42]. . . . .	49
2.10	Hot ductility curves for C-Mn-Al-Nb steel (0.1C, 1.43Mn, 0.029Al, 0.030Nb for reheated, hot rolled, as cast conditions -austenite grain sizes are given in parenthesis) [59]. . . . .	50

2.11	Ultimate reduction in area versus temperature for C-Mn-Nb-V/Ca steel [69]. The grain coarsening tests (“M+H/1450°C”) show an increase in depth but no displacement along the temperature axis when compared to melt tests (“M”). . . . .	55
2.12	Principle sketch of a ductility curve. . . . .	57
2.13	Intergranular microvoid coalescence of low alloy steels by deformation in a-c) low temperature austenite region [80]. $\sigma$ is the applied stress and PFZ is the precipitate free zone. . . . .	59
2.14	Schematic representation of grain boundary embrittlement in the temperature range 1000 to 600°C. [79]. Note that the ferrite cannot be present above $Ae_3$ . . . . .	60
2.15	Minimum ductility controlled by phase transformation in coarse grained steels (grain size $\geq 200\mu\text{m}$ ): steels solution treated and cooled to test temperature [17]. . . . .	61
2.16	Effect of ferrite thickness on hot ductility of a 0.032%Nb steel [49]. . . . .	61
2.17	Influence of strain rate on hot ductility of a 0.4%C steel [86]. . . . .	64
2.18	Ductility trough controlled by dynamic precipitation of microalloying addi- tions: steel solution treated and cooled to test temperature [17]. . . . .	65
2.19	Influence of a) particle size and b) interparticle distance on hot ductility of Nb-containing steels, solution treated at 1330°C, cooled to test temperature of 850°C, and fractured at strain rate of $3 \times 10^{-1}\text{s}^{-1}$ [17]. . . . .	66
2.20	Influence of particle size on reduction of area values [94]. . . . .	67
2.21	Schematic diagrams showing a) how the width of the ductility trough could be controlled by dynamic recrystallisation and b) how increasing the strain rate reduces the depth and width of the trough. $\varepsilon_{c1}$ , $\varepsilon_{f1}$ refer to the lower strain rates. $\varepsilon_{c2}$ , $\varepsilon_{f2}$ refer to the higher strain rates [76]. Temperature increases towards the right hand side in each diagram. . . . .	68
2.22	Hot ductility curves for a series of plain C-Mn steels having the same grain size ( $\sim 300\mu\text{m}$ ); values given in wt%C [57]. . . . .	69
2.23	Effect of A) C and B) P on hot ductility in steel with 0.03%Nb and 0.35%Nb- 0.075%V [49]. . . . .	70

2.24	Effect of C content on a) grain size and b) calculated R of A. R of A measured at 800°C at strain rate of $0.83 \times 10^{-3} \text{s}^{-1}$ [92]. . . . .	71
2.25	Effect of Mn/S ration on the ductility of as-cast hot tensile 0.14%C steel at 1100°C [110]. . . . .	72
2.26	Variation of reduction in area at fracture with temperature. Fe-500: 190ppmC, 514ppmAl, 120ppmN, <5ppmS; Fe+30S: 220ppmC, <25ppmAl, <10ppm N, 35ppmS; Fe-150+30S: 180ppmC, 156ppmAl, 80ppmAl, 32ppmS [78]. . . . .	74
2.27	Effect of P on hot ductility in low carbon steels without Nb/V [79]. . . . .	75
2.28	Effect of Nb content and deformation temperature on hot ductility and strength [49]. . . . .	76
2.29	Hot ductility curves at various Al and N contents [91] (samples reheated). . .	78
2.30	Dendritic AlN in a)TEM replica and b)cross sectional optical microscopy (OM) [136]. . . . .	80
2.31	Grain boundary precipitation in a) 0.37Al-165ppmN steel and plate AlN in b)0.865Al-220ppmN steel [46], presumed to be the features indicated by arrows. 82	82
2.32	Percentage of distressed casts (casts with one or more rejected plates) as a function of sol. Al content: numbers in brackets refer to total number of casts (distressed and problem free) in each composition interval [54]. . . . .	83
2.33	Influence of aluminium on hot ductility of C-Mn-Al steels [10]. Samples were melted. . . . .	85
2.34	Hot ductility curves for a) Su 1[11] and Su 6[11]; b) Su 3[11]; c) Su 4[11]; d) Su 5[11] and Su 7[11] (Su7=Mintz 4[10]) and steel Su 8[11] (Su8=Mintz 3[10]). 86	86
2.35	Phase transformations at high temperatures in the peritectic region of the Fe-C equilibrium diagram [164]. . . . .	90
2.36	Phase transformations during continuous cooling ( $0.5^\circ\text{Cs}^{-1}$ ) of a base steel containing 0.02%P and 0.002%S. Broken lines are Fe-C equilibrium diagram [166]. . . . .	90
2.37	The relationship between $T_\gamma$ (temperature at which the steel becomes fully austenitic) and austenite grain size for various steels [166], at a single cooling rate of $0.5^\circ\text{Cs}^{-1}$ . . . . .	91

2.38	Peritectic region phase diagram (schematic), showing the three-phase region (L+ $\delta$ + $\gamma$ ) as shadowed region [140]. . . . .	91
2.39	Influence of grain size on reduction in area values for C-Mn steels tested at 750°C. 0.15%C, 1.44%Mn, 0.17%Al [41]. . . . .	94
2.40	Relationship between tensile properties and reciprocal of the austenite grain size ( $D_\gamma$ ). Specimens (0.12C-0.33Si-1.51Mn-0.047Al-56ppmN-0.055Nb) were solution treated at 1100-1350°C and deformed at 800 or 900°C at strain rate of $0.83 \times 10^{-3} \text{s}^{-1}$ [92]. . . . .	95
2.41	Influence of $D_o^{\frac{1}{2}}$ (initial undeformed grain size after heat treatment) on minimum R of A value. ref15=[169], ref35=[41], ref45=[92] from [17]. . . . .	95
2.42	Hot ductility curves of 0.18C steel at grain sizes between 0.4-3.8mm. (0.18%C 0.01%Mn, 0.034%Al, 0,0016%N) [25]. . . . .	97
2.43	Effect of test temperature and strain rate on hot ductility (1200-600°C) for low carbon steel (0.05%C, 1.46%Mn, <0.01%Al) [42]. . . . .	98
2.44	Influence of strain rate on the hot ductility of a plain carbon steel[42]. . . . .	98
2.45	Dependence of hot ductility on the strain rate and test temperature for a niobium steel (0.06C, 1.6Mn, 0.03Al, 0.006N, 0.04Nb) [79]. . . . .	100
2.46	Key process variables in continuous casting simulation [20]. . . . .	101
2.47	Effect of $T_{min}$ on hot ductility [20]. . . . .	102
2.48	Hot ductility appears to be sensitive to secondary cooling, within limits [20].	103
3.1	Tensile test sample manufacturing drawing [179]. . . . .	107
3.2	Typical temperature profiles for reheat and melted specimens [178]. . . . .	107
3.3	Schematic diagram of testing arrangement for in-situ melted hot ductility tests in the as cast condition [179]. . . . .	108

3.4	Diagram giving various images at various focussing heights for taking calibrated through focus series images of R of A sample fracture surfaces. A series of images at different focus heights was taken (a). Software was used to automatically assemble them and the final image was calibrated, to give the final image (b). . . . .	109
3.5	Measurement of R of A from sample fracture surfaces. . . . .	110
3.6	Hot ductility curves for TRIP steels a) melted and b) ‘unmelted’ during reheat, reproduced from Kang <i>et al.</i> [178]. . . . .	111
3.7	Hot ductility curves for 0.05%Al TRIP steels Kang’s complete curve and curve with <10%porosity. Ductility rises above 50% at >850°C. This curve can be directly compared with Mintz and Mohamed’s work [62], but this will be dealt with in the discussion (Section 8.2, page 196). . . . .	112
3.8	Hot ductility curves for 1.05%Al TRIP steels Kang’s complete curve and curve with <10%porosity. Ductility rises above 50% at >1050°C. . . . .	113
3.9	Hot ductility curves for 1.53%Al TRIP steels Kang’s complete curve and curve with <10%porosity. Ductility rises above 50% at >850°C. . . . .	113
3.10	Hot ductility sample for 1.53%Al TRIP steels tested at 950°C. The ductility measured at area A will be lower than the true ductility if the sample had fractures at area A instead of at area B. Therefore the ductility for this sample is a lower estimate than the real ductility. . . . .	114
3.11	Cumulative probability plot for 1.05%Al TRIP steels at 1000°C with <10% porosity, R of A is $41 \pm 9.7\%$ . . . . .	115
4.1	Illustration of the types fracture surfaces seen by macro OM a) intergranular failure (ig), b) transgranular failure (tg), c) a mix of intergranular and transgranular failure (ig/tg) with porosity in area ‘P’ and d) high temperature ductile rupture (HTDR). . . . .	118
4.2	Type of failure as a function of ductility and temperature for a) 0.05%Al b) 1.05%Al and c) 1.53%Al steel respectively, samples with <10% porosity. . . .	120

4.3	Relationship between inverse grain size and reduction in area in unmelted 0.05%Al steel where no DRX occurred. The error bars show the standard deviation for each sample, whereas the $R^2$ indicates the goodness of fit of the data to the line. The addition of the DRX samples and the melted samples may be found in Figure B.3. . . . .	123
4.4	0.05%Al steel, a) recrystallisation at the fracture tip of sample ‘unmelted’ and tested at 1000°C (92% R of A) with b) tip and c) bulk grain size enlarged, compared with d) non-recrystallised fracture tip of sample melted and tested at 650°C(68% R of A) with e) tip and f) bulk grain size enlarged. Light nital etch. In the case of a,b,c and d some grain boundaries have been outlined to aid interpretation. . . . .	125
4.5	MnS inclusion in as cast 0.05%Al steel. Unetched c/s. . . . .	126
4.6	Relationship between grain size in the unmelted samples and R of A in the 1.05%Al steel. No clear correlation between these two variables for the unmelted samples. The error bars show the standard deviation for each sample, whereas the $R^2$ indicates the goodness of fit of the data to the line. . . . .	126
4.7	Dendritic AlN precipitation in 1.05%Al steel tested at a) 1100°C, b) 1050°C, c) 650°C. As polished section except (a) lightly etched with Nital. These observations were confirmed by SEM - Figure 5.8. Note how at 1100°C (a) the austenite grain boundary has managed to migrate from the AlN as indicated by the arrows. . . . .	127
4.8	Steel 2 tested at 950°C. Higher magnification photograph of the particles at the austenite grain boundaries 1.05%Al steel (Unmelted test with R of A 59%). Nital etch. Reproduced from [179]. Presumed by Kang[179] to be AlN. 128	
4.9	Relationship between grain size and R of A in the 1.53%Al steel (regression only for unmelted tests without DRX). A good relationship exists between R of A and austenite grain size for the unmelted samples. Grain size is remarkably finer than the other steels. The error bars show the standard deviation for each sample, whereas the $R^2$ indicates the goodness of fit of the data to the line. Regression inclusive of the DRX samples may be found in Figure B.4. . . . .	130
4.10	AlN precipitation in as cast 1.53%Al steel, unetched. . . . .	130

4.11	AlN precipitation in 1.53%Al steel ‘unmelted’ and tested at 800 and 1100°C. a) unetched and b) nital etched and carbon coated. . . . .	131
4.12	OM image (using Normarski interference microscopy) showing (A) dendritic AlN precipitation (B) plate AlN in unmelted 1.53%Al steel, tested at 850°C, light etch. . . . .	131
4.13	Steel 3 tested at 1100°C. Steel is now fully austenitic still showing a few particles at the boundaries. Nital etch. R of A 97% (Ae <sub>3</sub> 1069°C) from [179] 1.53%Al steel. . . . .	132
4.14	1.53%Al steel, a) recrystallisation at the fracture tip of sample ‘unmelted’ and tested at 1000°C (97% R of A) with b) tip and c) bulk grain size enlarged, compared with d) non-recrystallised fracture tip of sample melted and tested at 700°C(75% R of A) with e) tip and f) bulk grain size enlarged. Light nital etch. DRX occurred in (a) only. . . . .	133
5.1	Illustration of the types of meso-fracture surfaces in ductility testing: a) intergranular (ig), b) transgranular (tg), c) HTDR d) porosity (P). . . . .	137
5.2	Illustration of types of micro-fracture surface in ductility testing: a) grain boundary sliding (gbs) where the ridges are the successive positions on grain surfaces as they slide past each other, b) micro-void coalescence (mvc), c) rock candy fracture (rc). The samples used in this categorisation were from the following conditions: a), b) steel 9 tested at 700°C, c) steel 2-2 tested at 1000°C. . . . .	138
5.3	Illustration of hexagonal AlN precipitates observed with SEM a) a region showing porosity b) on fracture surface. Steels used in the categorisation were a) Steel 3 at 1000°C, b) steel 3 at 700°C. Both samples were heated to 1460°C so are ‘unmelted’ tests. . . . .	139
5.4	Illustration of types of precipitates and analysis observed with SEM a) needle AlN, with analysis, b) dendritic AlN, with analysis, c) MnS and oxides with analysis. Steels used in the categorisation were a) steel 2-1 ‘unmelted’ and tested at 1000°C, b) steel 2-2 melted and tested at 1000°C and c) steel 9 melted and tested at 700°C. . . . .	140

5.5	FEG SEM observation of pro-eutectoid ferrite in a) 0.05%Al steel at 800°C, b)1.05%Al steel at 800°C and c) 1.53%Al steel at 950°C. Arrows indicate wedges of deformation induced ferrite formed prior to fracture. Steels used in the categorisation were a) steel 1 ‘unmelted’ and tested at 800°C, b) steel 2-1 ‘unmelted’ and tested at 800°C and steel 10 melted and tested at 950°C.	141
5.6	1.05%Al steel, showing the thickness of the AlN dendrites. Steel 2-3 melted and tested at 900°C. . . . .	145
5.7	Hexagonal plate AlN in regions of porosity in a) ‘unmelted’ and b) melted 1.05%Al steel. There are oxide filaments around AlN in (a). Steels samples were a) steel 2-1 ‘unmelted’ tested at 800°C, b) steel 2-2 melted, tested at 1000°C. . . . .	146
5.8	Cross section of a) dendritic AlN in ‘unmelted’ 1.05%Al steel tested at 1100°C with b) analysis (sample 10521at1100uM). This confirms the presence of AlN in Figure 4.7, page 127. Steel 2-1 ‘unmelted’ and tested at 1100°C. . . . .	147
5.9	Hexagonal AlN in porosity in 1.53%Al steel. Steel 10 melted and tested at 650°C. . . . .	149
5.10	Fracture surface of 1.53%Al steel sample tested at 800°C, showing that the poorest ductility (R of A of 38%) is due to intergranular mvc. Steel 3 ‘unmelted’ and tested at 800°C. . . . .	149
6.1	Sectioning procedure for the preparation of TEM samples. Sample section length wise and mounted in perspex. . . . .	152
6.2	Plot of all matrix Nb(C,N) precipitate size in all steels vs temperature. . . . .	154
6.3	0.05%Al steel, reheated to 1460°C and tested at 700°C (TEM sample 005-9-700-uM) a) Pro-eutectoid ferrite, with precipitation. Inset (b) is an enlargement, with (c) analysis, of fine Nb(C,N). The CuK $\alpha$ peak originates from the copper support grid. . . . .	156
6.4	0.05%Al steel, heated to 1520°C and tested at 700°C (TEM sample 005-9-750-2smN) showing a) large Nb(C,N) needles with b) analysis. The CuK $\alpha$ peak originates from the copper support grid. . . . .	157

6.5	0.05%Al steel, a) average Nb(C,N) size as a function of test temperature and b) ductility as a function of average Nb(C,N) size. Trend line for b) is a regression of the form $y = m \log(x) + c$ . . . . .	158
6.6	1.05%Al steel, reheated to 1460°C and tested at 1050°C (TEM sample 2-1-1050-uD) showing dendritic AlN precipitation. . . . .	159
6.7	1.05%Al steel, showing AlN dendrite plate having width of approximately 70nm. . . . .	160
6.8	Selected area diffraction patterns of dendritic AlN precipitate in 1.05%Al steel, identified by a) fcc (zincblende) $\bar{1}11$ zone axis pattern and b) $\bar{1}12$ zone axis pattern. Lattice spacing was calculated to be 0.460nm. Sample was steel 2-1 tested at 700°C. . . . .	160
6.9	1.05%Al steel, reheated to 1460°C and tested at 800°C (TEM sample 1052-1800-uD) showing dendritic AlN precipitation on which CuS has precipitated. The CuK $\alpha$ peak originates from the copper support grid. . . . .	161
6.10	1.05%Al steel, reheated to 1460°C and tested at 900°C (TEM sample 1052-3900-1uD) showing fine Nb(C,N) precipitation with finest precipitate size of 9nm, and average precipitate size of $11 \pm 1.7$ nm. The CuK $\alpha$ peak originates from the copper support grid. . . . .	162
6.11	1.05%Al steel, reheated to 1460°C and tested at 900°C (TEM sample 1052-3900-1uD) showing grain boundary Nb(C,N) precipitation associated with plate AlN precipitation. . . . .	163
6.12	1.05%Al steel, reheated to 1460°C and tested at 900°C (TEM sample 1052-3900-1uD) a) plate AlN with Nb(C,N) at centre, b) EDS analysis for the central region showing high Nb content and c) EDS of plate edge showing high Al content. The CuK $\alpha$ peak originates from the copper support grid. . . . .	164
6.13	1.05%Al steel, reheated to 1460°C and tested at 900°C (TEM sample 1052-3900-1uD) showing a) needle AlN, b) EDS analysis of the same. The CuK $\alpha$ peak originates from the copper support grid. . . . .	165
6.14	1.05%Al steel, reheated to 1460°C and tested at 1100°C (TEM sample 105 2-1 at 1100uM, 2 replicas, 3 observations): Fine ( $>7$ nm) Nb(C,N) precipitation, $15 \pm 7.6$ nm. The CuK $\alpha$ peak originates from the copper support grid. . . . .	166

6.15	1.05%Al steel, reheated to 1460°C and tested at 1100°C (TEM sample 105 2-1 at 1100uM, 2 replicas, 3 observations)a) and b) Large (577nm) eutectic Nb(C,N)precipitation. c) Zone axis pattern [011] fcc, d) Zone axis pattern $[\bar{1}12]$ fcc crystal structure). Lattice spacing is calculated to be 0.456nm. The CuK $\alpha$ peak originates from the copper support grid. . . . .	167
6.16	1.05%Al steel, reheated to 1460°C and tested at 1100°C (TEM sample 105 2-1 at 1100uM, 2 replicas, 3 observations) Showing a) AlN needle, b) analysis of particle. The CuK $\alpha$ peak originates from the copper support grid. . . . .	168
6.17	1.05%Al steel, a) average Nb(C,N) size as a function of test temperature and b) ductility as a function of average Nb(C,N) size. . . . .	169
6.18	1.53%Al steel, a) Nb(C,N) with b) analysis at 950°C test temperature. The CuK $\alpha$ peak originates from the copper support grid. . . . .	170
6.19	1.53%Al steel, a) average Nb(C,N) size as a function of test temperature and b) ductility as a function of average Nb(C,N) size. Trend line in b) is of the form $y = m \log(x) + c$ . . . . .	171
6.20	Diffraction patterns for AlN precipitate in the 1.5%Al steel, reheated to 1460°C and tested at 1100°C, a) Zone axis pattern [01 $\bar{1}$ 0] hcp crystal structure b) Zone axis pattern [01 $\bar{1}$ 1] hcp crystal structure). Lattice spacing is calculated to be as a=0.323nm and c=0.499nm. . . . .	172
7.1	Ductility vs $C_{actual} - C_{peritectic}$ . The ductility in the trough is poorest close to the peritectic point, ie $C_{actual} - C_{peritectic} = 0$ . %Al contents in brackets. . . . .	176
7.2	Phase transformations at high temperatures in the peritectic region of the a) Fe-C constitutional diagram, b) Fe-C constitutional diagram with additional elements 0.02%P and 0.002%S, adapted from [164] and [166], showing how, at the peritectic point ( $C_{actual} - C_{peritectic} = 0$ ), the pure austenite phase forms at the highest temperature. In practice the worst peritectic contraction occurs at slightly lower carbon contents than the peritectic point [140]. . . . .	177
7.3	FactSage phase and solubility fields a) entire field b) enlargement of higher temperature range. Identification of each steel is given at one data point and applies to all other curves in vertical alignment with that data point. . . . .	179

7.4	Thermo-Calc phase and solubility fields a) entire field b) enlargement of higher temperature range. Identification of each steel is given at one data point and applies to all other curves in vertical alignment with that data point. . . . .	180
7.5	Relationship between AlN precipitation in delta ferrite and minimum ductility for the steels which have AlN precipitation in the delta ferrite (Trip2-1 and Trip 3 with 1.05 and 1.53%Al respectively, as well as Mintz 3, 4 with 1.93 and 0.98%Al from [10]). The volume fraction is taken from the Factsage program and the minimum ductility taken from the ductility curves. . . . .	185
7.6	Mintz steel 3[10] $Ae_3$ determination. . . . .	185
7.7	Plot of phase proportion vs temperature for a) Mintz 3[10] and b) Trip 3 steels with modified Al and Mn contents (original content in brackets). Decreasing the Al in the Mintz 3 steel on the $Ae_3$ has the same effect as increasing Mn in the Trip 3 steel. It is reasonable to use the peak austenite level as the $Ae_3$ . Increasing Mn leads to a higher carbon equivalent, while increasing Al leads to a lower carbon equivalent. . . . .	186
7.8	Plot of phase diagram along the 0.05%Al iso-plane. Dotted line indicates Mn = 2.4%. . . . .	188
7.9	Plot of phase diagram along the 1%Al iso-plane. Dotted line indicates Mn = 2.4%. . . . .	189
7.10	Plot of phase diagram along the 1.5%Al iso-plane. Dotted line indicates Mn = 2.4%. . . . .	190
7.11	MnS solubility temperatures for steels in Table 7.1 and 7.2. . . . .	191
7.12	AlN solubility temperatures for steels in Table 7.1 and 7.2. . . . .	191
7.13	Nb(C,N) solubility temperatures for TRIP steels in Table 7.1 and 7.2. . . . .	192
8.1	Hot ductility curves for present 0.05%Al steel and previous ductility curves from the work of Mintz and Mohamed [62]. Mohamed steel B contains 0.1C; 1.39Mn; 0.007P; 0.01S; 0.42Si; 0.026Nb; 0.038Al; 0.0038N. . . . .	197

8.2	Hot ductility curves for a) present study ductility. Ductility curves from the work of b) Mintz <i>et al.</i> [10]. Mintz steel 1 contains 0.017Al, Mintz 3 - 1.93%Al and Mintz 4 - 0.98%Al. The present results (a) showed wider trough behaviour while the previous work (b) showed deeper trough behaviour. . . .	199
8.3	Plot of aluminium content versus minimum ductility for the present study (Trip). Also included are the results for Mintz <i>et al.</i> [10] (Mintz2003) and Su <i>et al.</i> [11] (Su 2007) investigations. . . . .	200
8.4	Effect of grain size and precipitation density on the grain boundaries. For the same amount of precipitation, the finer grain material (a) has a higher grain boundary area and a lower precipitate density than the coarse grain material (b). . . . .	205
8.5	Relationship between grain size at 750°C and the effective carbon content, $C_{actual} - C_{peritectic}$ . . . . .	205
8.6	Multiple regression for precipitate size and grain size for 0.05 and 1.5%Al steels. $R^2=0.88$ . Measurements taken over the temperature range 750-1000°C.	207
8.7	Liquidus and solidus vs $C_{actual} - C_{peritectic}$ for steels in Table 7.1. Data from Table 8.2. . . . .	209
8.8	Comparison of $Ae_3$ vs $C_{actual} - C_{peritectic}$ for steels from Tables 7.1, 7.2. Data may be found in Table 8.3. . . . .	211
8.9	$Ae_3$ anomalies for Su <i>et al.</i> 's steels. . . . .	213
8.10	Grain size at 750°C vs the temperature at which the TRIP samples are single phase austenite. There is a good correlation between these parameters. Numbers in brackets denote Al content. . . . .	216
8.11	Schematic to illustrate the effect of phases transformation on the position of AlN precipitation along grain boundaries. If the AlN precipitates at the delta ferrite grain boundaries a) then it is less likely to exist on the austenite phase boundaries at test temperature, while b) when precipitation predominates in the austenite it is more likely to remain at the grain boundaries and affect ductility. . . . .	216

8.12	Effective precipitation and minimum ductility showing the good correlation between precipitation of AlN in austenite and loss of ductility. A: R of A (on secondary y-axis), B: AlN precipitation in delta ferrite, C: AlN precipitation in austenite, D: AlN precipitation in alpha ferrite. . . . .	218
8.13	[Al][N] product vs minimum ductility for the steels in the hyper-peritectic carbon range. There is a marked drop in ductility when the [Al][N] product exceeds $1.5 \times 10^{-4}\text{wt}\%^2$ . . . . .	219
8.14	Effective precipitation and minimum ductility showing how the Nb decreases ductility in the hyper-peritectic region. A: R of A, B: Nb(C,N) precipitation. . . . .	221
8.15	Effect of Nb and Nb additions on R of A at different $C_{actual} - C_{peritectic}$ . . . . .	222
8.16	$Ae_3$ and $Ar_3$ values for the 0.05%Al steels superimposed on the ductility curve for 0.05%Al steel steel. . . . .	224
8.17	$Ae_3$ and $Ar_3$ values for the 1.0%Al steel superimposed on the ductility curve for the same steel. . . . .	225
8.18	$Ae_3$ and $Ar_3$ values for the 1.5%Al steel superimposed on the ductility curve for the same steel. . . . .	227
8.19	Predicted solidii and liquidii temperatures compared with the melting and reheating temperatures in for this study, FactSage model. . . . .	227
11.1	Effect of Al content on the peritectic point and peritectic region. As the Al content increases, the peritectic point is moved to lower carbon levels (indicated by arrow A) and the peritectic region becomes wider (indicated by arrow B). . . . .	235
11.2	Effect of Mn content on the peritectic point and peritectic region. As the Mn content increases, the peritectic point moves to slightly higher carbon levels (indicated by arrow C). . . . .	236
A.1	Hot ductility curves for 0.05%Al TRIP steels. . . . .	239
A.2	Hot ductility curves for 1.05%Al TRIP steels. . . . .	241
A.3	Hot ductility curves for 1.53%Al TRIP steels. . . . .	241

B.1	Relationship between inverse maximum grain size (from the macro OM fracture surface) and hot ductility. . . . .	244
B.2	Relationship between ductility and grain size a)-e) 0.05%Al steel for $d$ , $\log(d)$ , $d^{-1}$ , $d^{0.5}$ , $d^{-0.5}$ respectively; f)-g) 1.53%Al steels for $d$ , $\log(d)$ , $d^{-1}$ , $d^{0.5}$ , $d^{-0.5}$ respectively. The population excludes samples with >10% porosity and DRX.	248
B.3	Relationship between inverse grain size and reduction in area in all 0.05%Al steel. The addition of the DRX samples and the melted samples reduces the correlation slightly. . . . .	249
B.4	Relationship between grain size and R of A in the 1.53%Al steel (regression only for unmelted tests). A very good relationship between R of A and austenite grain size. . . . .	249
D.1	Selected area diffraction patterns of dendritic AlN precipitate in 1.05%Al steel, (the same SAD's from Figure 6.8) identified with JEMS electron diffraction simulation program as a) fcc [111] zone axis pattern and b) [112] zone axis pattern. Used [185] from the International Crystal Structure Database [186]. . . . .	252
D.2	Diffraction patterns for AlN precipitate in the 1.5%Al steel, reheated to 1460°C and tested at 1100°C, (the same SAD's from Figure 6.20) a) Zone axis pattern [210] or $[10\bar{1}0]$ hcp crystal structure b) Zone axis pattern [211] or $[10\bar{1}1]$ hcp crystal structure. Used [187] from the International Crystal Structure Database [186]. . . . .	253
E.1	Typical a) FactSage (wt% vs temperature) and b) Thermo-Calc (volume fraction vs temperature) curves, (Trip 9, 0.05%Al). The Fe phases are plotted on the second Y axis. . . . .	258

# Acknowledgements

- Barrie Mintz not only knowledge but wisdom.
- Johan DeVilliers for good advice over good coffee.
- Kevin Banks for references, arguments and wit-sharpening.
- Tom von Moltke for financial, managerial and statistical support.
- Phalalani Gule for sample preparation.
- Lorraine DeBeer and especially Jackson Mathabatha at Exxaro library for the out of print, hard to find, gratefully accepted papers.
- Microscopy at UP: Alan Hall, Chris van der Merwe and Andre Botha for being so accommodating.
- Markus Erwee for FactSage modelling (and then some...).
- Dave Smith of Columbus Stainless Steel for Thermo-Calc modelling.
- Mike Witcomb for initiating me in the art of electron microscopy.
- To my parents for their continued support.
- To dear friends and sisters for sharing.
- Sean – the other side of me.
- Our Creator and Sustainer for many joys including making iron so we can study steel.

# Declaration

I grant powers of discretion to the University Librarian, to allow this thesis to be copied in whole or part without further reference to me. This permission covers only single copies made for study purposes, subject to normal conditions of acknowledgement.

I declare that this thesis is my own, unaided work, except where otherwise acknowledged. It is being submitted for the degree of Doctor of Philosophy in City University, London. It has not been submitted before for any degree or examination in any other university.

Signed this \_\_\_ day of \_\_\_\_\_ 20\_\_\_

---

Alison Susan Tuling

# Abstract

Transformation induced plasticity assisted steels (TRIP steels) are alloyed with Al, Mn and Nb, among other elements, to provide a combination of high strength and ductility. While these additions are necessary for the TRIP effect, their influence on the steel's castability must be addressed. Al and Nb are known to be detrimental for hot ductility and casting. Yet the combination of very high Al contents with Nb is unique. Therefore, the ductility loss mechanisms during casting high Al-Nb TRIP steels were investigated. Using a simple hot ductility simulation, 0.15C-2.5Mn-0.025Nb TRIP steels had similar ductility trough shapes at low ( $<0.05\%$ ) and high (1.53%) Al levels, but at the 1.05%Al steel there was an extended trough. The ductility loss in the 0.05%Al and 1.5%Al steel was shown to be dependant on the Nb(C,N) precipitation size and the austenite grain size. The 0.05%Al steel had a poorer ductility than the 1.5%Al steel at the same volume fraction and size Nb precipitation, since it had a larger grain size resulting in a lower inter-particle distance. Intergranular failure occurred as the Nb(C,N) precipitates pinned the grain boundaries and facilitated cavity/crack link up. The Al additions radically altered the phase stabilities of these steels, leading to steels that vary from hypo-peritectic to hyper-peritectic compositions. At 1%Al level, not only was the steel peritectic, leading to a large austenite grain size, but dendritic AlN precipitated at the austenite grain boundaries. This resulted in intergranular rock candy fracture along the AlN dendrites at the immobile grain boundaries. Therefore, the 1%Al steel the ductility trough was wider than the  $A_{e3} - A_{r3}$ , due to the high density of AlN precipitation along the grain boundaries at all temperatures. While this precipitation has been observed before as a hexagonal close packed crystal, in the current analysis it was identified as a face centered cubic structure. With further confirmatory investigation it is recommended that 1.5%Al levels be used over the 1%Al levels in these steels.

(Keywords: High Al TRIP steels, Nb additions, hot ductility, peritectic, dendritic AlN precipitation)

# List of Symbols

$a, c$	Lattice parameters for cubic and hexagonal close packed crystals
$Ae_1$	The equilibrium temperature at which the austenite to ferrite and pearlite transformation is complete on cooling or the start of the ferrite and pearlite to austenite transformation on heating
$Ae_3$	The equilibrium temperature at which austenite starts forming ferrite on cooling or the ferrite transforms to austenite on heating
$Ae_4$	The equilibrium temperature at which austenite transforms to delta ferrite on heating or the delta ferrite transforms to austenite on cooling in pure iron
$Ar_1$	The temperature at which the austenite to ferrite and pearlite transformation is complete on non-equilibrium cooling
$Ar_3$	Temperature at which austenite starts forming ferrite during non-equilibrium cooling
$A_0$	Original area of hot ductility specimen
$A_{\text{fracture area}}$	Gross fracture area on a fractured hot ductility specimen as measured by optical microscopy
$A_{\text{machine or melting}}$	Initial area from machining or melting of a fractured hot ductility specimen as measured with a vernier
$A_{\text{pipe or internal neck}}$	Pipe or internal necking area on a fractured hot ductility specimen as measured by optical microscopy
$A_{\text{porosity}}$	Porosity area on a fractured hot ductility specimen as measured by optical microscopy or scanning electron microscopy

$\Delta A$	The change in area on a hot ductility specimen that occurs on fracture, measured after fracture
$\varnothing$	Diameter
CC	Continuous casting(er)
c/s	Cross section
$c_{actual} - c_{peritectic}$	The difference between the actual carbon content of a steel and the carbon content of the effective peritectic point, considering all other alloying elements
$C_{peritectic}$	The effective peritectic point: the carbon content at which a steel would experience the greatest contraction associated with the peritectic reaction, considering all other alloying elements
$d$	d-spacing, or distance in reciprocal space, usually measured between spots on a diffraction pattern
D	Grain size
$D_o$	Original/starting grain size
$D_\gamma$	Austenite grain size
DIF	Deformation induced ferrite
DRX	Dynamic recrystallisation
FEG-SEM	Field emission gun scanning electron microscope
fcc	Face centred cubic
gbs	Grain boundary sliding.
hcp	Hexagonal close packed
$h, k, l$	Indices of a crystal in reciprocal space, usually used to label spots in a diffraction pattern
HDTR	High temperature ductile rupture
ig	Intergranular description of fracture surface
$K_s$	Equilibrium solubility product

mvc	Microvoid coalescence appearance of fracture surface
OM	Optical microscopy
P	Porosity description of fracture surface
p	Precipitate size
PFZ	Precipitate free zone
ppm	Parts per million
ppt(s)	Precipitate(s)
$P_s$	Precipitate start
$P_f$	Precipitate finish
$Q_{\text{def}}$	Activation energy for deformation in the steel
$R$	Gas constant
RA	Reduction of area
rc	Rock candy description of fracture surface
R of A	Reduction of area
SEM	Scanning electron microscopy
$T_{\text{AV}}$	The temperature at the lower temperature end of the range of poor ductility
$T_{\text{BEV}}$	The temperature of renewed rise in ductility
$T_D$	Temperature above which dynamic recrystallisation starts
$T_{\text{EV}}$	The temperature of incipient decline in ductility
TEM	Transmission electron microscopy
tg	Transgranular description of fracture surface
TRIP	Transformation induced plasticity

$T_\gamma$	Highest temperature where the steel structure is single phase austenite
$V_f$	Volume fraction
$Z$	Zener–Hollomon parameter
$\alpha$	Ferrite
pe- $\alpha$	Pro-eutectoid ferrite
$\delta$	Delta ferrite
$\varepsilon_c$	Critical strain for DRX
$\varepsilon_f$	Strain to fracture in the absence of DRX
$\dot{\varepsilon}$	Strain rate
$\gamma$	Austenite
$\sigma$	Applied stress

# Chapter 1

## Introduction

### *Summary of introduction*

Strong formable structural steels such as TRIP (Transformation induced plasticity) steels, while costly, are becoming increasingly popular in the automotive industry in the quest to decrease weight and so reduce fuel consumption and emissions. Thus, steel manufacturers are seeking to add these steels to their repertoire. The manufacturing route of these steels includes continuous casting. Investigation into the hot ductility of the steels is therefore essential. Since these steels have significant amounts of microalloying agents (Al,Nb), combined with high Mn contents, there are uncertainties in the mechanisms involved in the hot ductility properties of these steels.

## **1.1 Transformation induced plasticity steels, their application and relevance**

### **1.1.1 A brief explanation of the transformation induced plasticity mechanism**

The high ductility of Transformation Induced Plasticity (TRIP) steel results from the transformation of metastable retained austenite to martensite under straining [1]. This transformation is accompanied by a local increase in strain hardening rate, strengthening the material and shifting the point of plastic instability (necking) elsewhere and to higher strains [2]. The cumulative effect is a higher uniform and total elongation [1] as well as an increase in strength [2].

### 1.1.2 Applications of transformation induced plasticity steels

The combination of high strength levels with high ductility is attractive for applications in the automotive industry, in particular, for stretch forming applications [3, 4, 5]. This results in improved safety with increased dent resistance and reduced weight combined with the potential for more rationalised and cost effective manufacturing [4, 6]. TRIP steels have also been used commercially for fasteners, surgical needles and high strength wire [7]. Additionally, they have potential for cold forging, where the steel could be directly cold formed into finished bolts. In this way, mechanical properties could meet the appropriate strength standard through thermomechanical processing without the normal expense of annealing and final heat treatment. Costs can be drastically reduced by this simplified manufacturing process [8].

### 1.1.3 Complexities of transformation induced plasticity steels

The use of new steels does require some adaptation to existing processing. For instance, the use of thinner gauge strip means that corrosion resistance is of prime importance [9]. Additionally, the chemistry needs to be modified to produce austenite that is stable at room temperature so that it can transform during cold forming applications to martensite. The cheapest approach to austenite stabilization is carbon enrichment [7]. Whereas the original TRIP steels depended on a high C content to achieve austenite stability; modern TRIP steels have much lower C levels ( $\leq 0.2\%C$ ) with the high C austenite being obtained with an intercritical anneal so that the C levels in the austenite fraction are around 1%.

The steel originally had high levels of Si which prevented carbides from precipitating on transformation to ensure that the high C austenite was retained at room temperature [10]. However, high Si levels can lower ductility after casting, so that P and Al additions are also considered for replacing Si [3, 9]. More importantly, Si also results in poor hot band surfaces due to rolled oxide (red oxide), and leads to pickling difficulties [1]. Thus, the selection of an optimum composition for galvanising is an issue [9] and alloying alternatives such as Al become attractive, especially for processing routes that include galvanizing [1]. Al acts in the same way as Si, slowing down the precipitation of carbides in bainite, allowing a high carbon retained austenite to be formed at room temperature [3, 11].

In fact, Al replacement of Si leads to improved mechanical properties (ultimate tensile strength and elongations among others) [3]. However, and most importantly for this study, casting of the high Al type of TRIP steel in the peritectic range poses difficulties in continuous casting [9] which need to be overcome. TRIP steels can also be microalloyed for

higher strength with Nb, Ti and V [12]. Alloying with Nb to increase the amount of retained austenite [12] and acicular ferrite [13] can also be considered. However, the effect of these on TRIP steel castability has not been investigated in detail.

#### **1.1.4 Rationale for the study of transformation induced plasticity steels**

While the effect of Al on castability has been studied at low Al levels of up to 0.1% [14], only a few higher Al levels have been considered [10, 11] and never before in combination with Nb, the latter being generally well known for its detrimental effect on ductility. This is the main aim of this current study: to determine the mechanisms of ductility loss than can be expected when casting the high Al-Nb TRIP steels.

The thesis will start with a survey of how the continuous casting operation is simulated by the laboratory hot ductility test and subsequently discuss the many variables that affect ductility. Other TRIP steel investigations will be discussed and the different models of ductility behaviour examined. The next part of the thesis will deal with the results, with a small amount of discussion in each of the analysis chapters, however, the main discussion will follow the result chapters as the explanation of the failure mechanisms requires an integrated approach using microscopy and thermodynamic simulation. This is because the ductility of the 1.05%Al steel was so remarkably different to that at higher and lower Al contents. While the ductility loss in the 0.05%Al and 1.5%Al steel was related to Nb(C,N) precipitation and the grain size, at the 1%Al level the ductility loss was mainly attributed to the significant amount of AlN precipitated at coarse grained austenite boundaries which resulted in rock candy fracture along the AlN dendrites at all temperatures.

## Chapter 2

# Literature survey

### *Summary of literature survey*

TRIP steel properties are attractive, giving high strength levels with high ductility. However, there are known detrimental implications for continuous casting in steels with Al and Nb additions. The first part of this review aims to survey the accuracy and reliability of hot tensile testing in simulating industrial transverse cracking. Following this, in the greater part of the survey, the mechanisms of ductility loss between 1000-700°C was reviewed. This was correlated to the factors that influence transverse cracking. Thus mechanisms such as grain boundary sliding in austenite, recrystallisation, the formation of grain boundary ferrite and precipitation were linked with chemistry, grain size, strain rate, cooling path, cooling rate, thermodynamic solubility and interaction of Nb-Al. The mechanism is related to the formation of ferrite along the austenite grain boundaries and the precipitation of AlN, MnS and/or Nb(C,N) precipitates which pin the grain boundaries and hasten intergranular failure. This is the most commonly held explanation of how ductility is reduced and appears to go some way to explaining how extremely high Al (> 0.5%Al) influences the ductility. However, the interaction of high Al with Nb has never been investigated before.

## 2.1 Summary of applications of transformation induced plasticity steels

TRIP steels obtain their high strength and ductility from the transformation of metastable retained austenite to martensite under straining. While this makes them attractive for the automotive industry, fasteners, surgical needles, high strength wire and cold forging with improved safety, reduced weight and cost effective manufacturing, the use of new steels does require some adaptations to processing. The modified chemistry with higher C, P, Si or Al

additions can lead to processing problems. In particular for this study, casting of the high Al type of TRIP steel in the peritectic range poses difficulties in continuous casting. Since these steels have significant amounts of microalloying agents (Al,Nb), combined with high alloying, there are some uncertainties as to the mechanisms involved in the hot ductility properties of the steels. It is thus the aim of this study to determine the mechanisms at work when casting the high Al TRIP steels.

## **2.2 Industrial practice and hot tensile testing**

Before the enormous amount of laboratory hot ductility investigations were carried out, steelmakers had to be satisfied with simplified recommendations such as Mori's [15] 'Either to maintain the ingot temperature below 700°C during straightening or above 900°C.' The mere fact that so many MSc's and PhD's have been achieved in this field does indicate that, while there is some matching of laboratory and industrial experience, there are many subtleties to be explored. For simple plain C-Mn steels with low Al levels few problems are encountered. However at higher Al levels, and particularly with the presence of Nb, transverse cracking of slabs is common and considerable work has been instituted to help solve the problem. The simple laboratory hot ductility test is used to simulate the continuous casting condition. Whilst this simple test is very useful for assessing the likelihood to transverse cracking during continuous casting it is important to evaluate the relevance of such testing to industrial practice. This section will thus; a) review industrial practice and problems and will then move to b) description of the test techniques and c) compare the industrial practice and test technique.

### **2.2.1 Industrial casting practice**

Since the early semi-industrial pilot plants that were developed after World War Two [16], continuous casting has become the route of large scale steel production: over 90% of western world steel is now produced by this route. The basic principle of continuous casting (CC) process can be described as follows, Figure 2.1: Molten steel is poured into a curved, tapered, water cooled copper mould [17]. An even shell of solidified steel is formed by uniform, efficient heat transfer [16]. The mould oscillates to prevent sticking [17] as well as 'stroking' which allows the steel to be removed from the bottom of the mould [18]. This 'Junghans mould oscillation system' allows for 'negative strip' where the mould moves downward faster than the steel skin for a part of the cycle, preventing sticking of the steel to the mould. Additionally a lubricant is provided between the mould and the skin to reduce sticking [16].

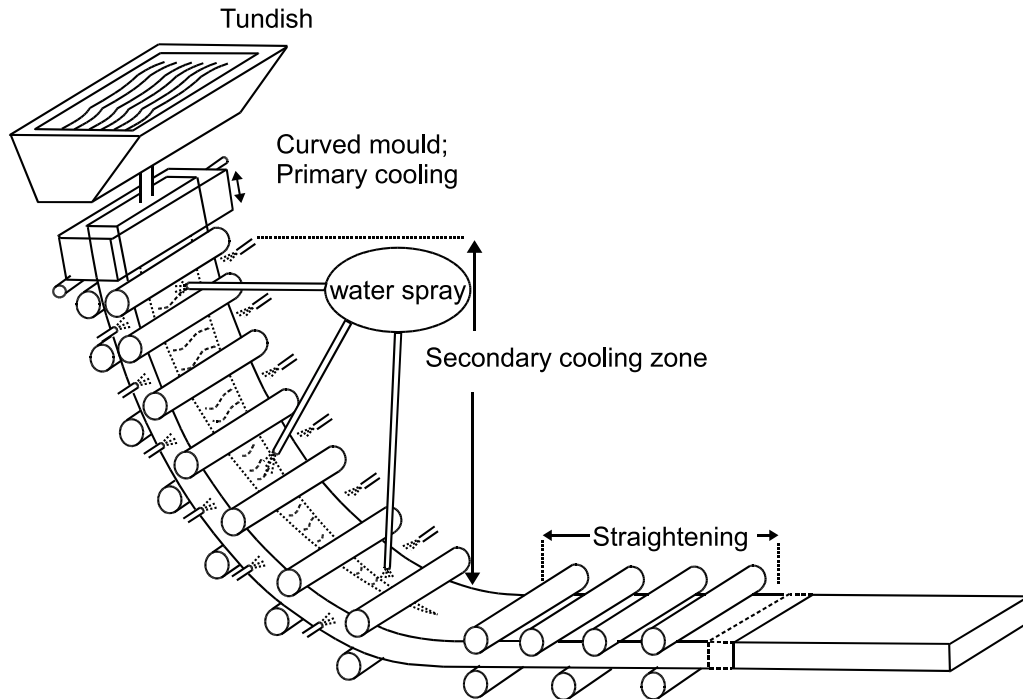


Figure 2.1: Schematic diagram of a typical continuous casting machine, not to scale [17].

The reciprocation motion results in oscillation marks on the strand surface whose frequency is a function of ‘heal time’; a combination of the stroke and oscillation frequency [18].

When the steel exits the mould it enters the secondary cooling zone. The secondary cooling spray pattern can be altered to select the unbending temperature, generally chosen within the temperature range 700-1000°C [17]. The surface temperatures of steel slabs have been measured in the secondary cooling system of an operational continuous caster, and transition boiling is probably operative in the upper zones [19]. This is undesirable as it gives rise to high heat extraction rates and overcooling that is strongly dependant on the slab temperature, so that surface temperature is poorly controlled [19]. Reducing the spray cooling in the higher zones helps, but even if transition boiling is avoided, the cooling rates still remains high and may lead to transverse surface cracks in susceptible steels. This is why cooling techniques such as air-water sprays or mist cooling may also be used to provide more uniform cooling over a larger area between the rolls than the conventional sprays, reducing the magnitude of the drop in surface temperature which occurs under the sprays [19, 17]. Air sprays break up the water droplets and provide a fine spray at higher speeds and wider angles which increases the heat transfer coefficient. The rolls which support the solidifying strand are also crucial. They are designed to minimise the bulging of the strand between the rolls as well as remaining geometrically stable themselves as their mis-alignment will dramatically increase the strain on the strand [16].

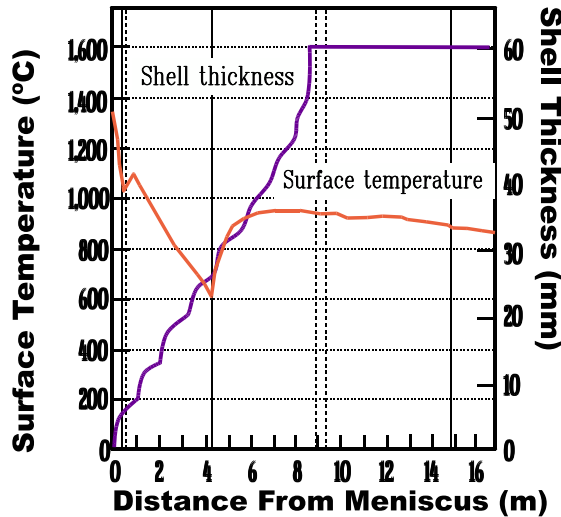


Figure 2.2: The predicted thermal history of billet casting is displayed according to a software simulation developed by the University of British Columbia [20].

El-wazri *et al.*[20] used a casting simulation package (Crack/Expert System from University of British Columbia, B.C. Canada) to show that the steel surface experiences a large temperature drop (to temperatures as low as 600-700°C) just below the mould, after which the temperature increases to a maximum and then cools to the unbending temperature, Figure 2.2. Different casting speeds and secondary cooling conditions have a marked effect on the surface temperature [20]. Also during unbending, depending on the cooling path, the centre may still be molten, this alters the strand's response to stress, and depending on the geometry there may be more or less strain on the strand surface [16]. At a certain stage the strand has to be straightened so that it can be transferred to a horizontal plane making it convenient for cutting into slabs. It is this straightening operation that puts the top surface and edges into tension and results in transverse cracking. For conventional casting, slabs are 220-240mm thick and straightening always takes place after full solidification has taken place [21].

A thin slab caster is narrower than a conventional continuous casting mould (thickness < 70mm), and in some thin slab casters there is a reduction of the strand thickness (before straightening) while there is still a liquid core [22]. The liquid core reduction reduces the thickness of the strand by the bulging of the narrow sides, so that the edges of the broad faces, Figure 2.3 do not experience longitudinal tensile strains which would result in transverse tearing of susceptible steel grades [22]. Thin slab casting also generates ~5 times higher strain rates during straightening than continuous casting, which slightly refines the grain size [17].

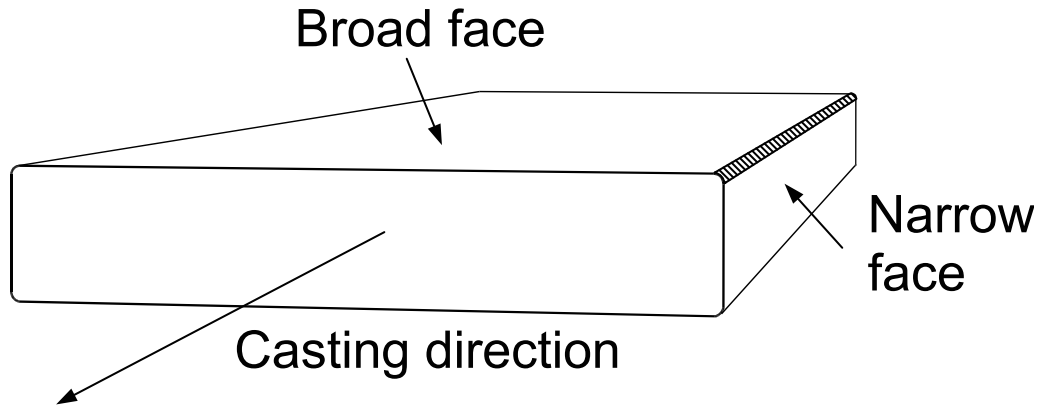


Figure 2.3: Broad and narrow faces in continuous cast slabs.

## 2.2.2 Transverse cracking in industry

### Description of the transverse cracking defect

As early as 1978 Nozaki *et al.*[23], report that the formation of AlN precipitates results in transverse corner cracks. These cracks form on the corner of the slab, usually on the upper surface (broad face), along an oscillation mark [17]. Corner cracks are difficult to detect except with a control pass scarf [24]. They can be associated with micro-cracking, which is invisible on a scaled surface [25].

### The transverse cracking mechanism

Transverse surface cracks and local segregation was studied by Harada *et al.*[18], who showed how segregation occurs at the oscillation mark, Figure 2.4. When the tip of the partially solidified shell at the meniscus is bent down during mould oscillation or when the bulk liquid overflows on the tip of the shell, it leads, in both cases, to interdendritic ‘dirty’ liquid being squeezed out and accumulating in the valley of an oscillation mark [18]. Cicutti *et al.*[26] (using Oberhofer’s etch technique to investigate segregation), named these ‘hook’ type oscillation marks that matched the shape of the meniscus at the time of solidification. This positive segregation area contains P and Mn [18]. Cracks tend to initiate in this weak part of the shell under any external stresses [18]. The stresses can be from mechanical, transformation and thermal strains, and the oscillation marks also act as stress raisers [27]. The cracks are first internal and propagate along austenite grain boundaries [17, 18]. This is confirmed by Cicutti *et al.*[26] who note that the absence of mould powder in the cracks and low decarburisation suggests that they do not open in the mould region. Finally, during unbending a large transverse crack can propagate from the internal crack [18]. This is most

likely along prior austenite grain boundaries when the strand is subject to tension on the top surface (the inner radius) and edges during straightening [17, 27]. In microalloyed steels straightening tends to coincide with fine precipitation of carbonitrides which weakens the austenite grain boundaries by the relative strengthening of the matrix [17]. Additionally, the formation of fine films of ferrite on the grain boundaries has also been implicated in causing transverse cracking [28].

The problem of segregation of elements can persist to lower temperatures, for instance Subramanian *et al.*[29], show that in industrial casting, although the segregation of C and N is negligible in the delta ferrite phase, substitutional solutes are less homogenized in the delta phase and substitutional solutes are even more segregated in the austenite phase. This segregation persists to lower temperatures, often leading to dendritic precipitation of Nb and Ti in the austenite. If the delta phase is extensive (as in the case of lower carbon steels), there is a greater degree of homogenization of substitutional solute due to better diffusion in the delta ferrite than in the austenite because the structure is more open [29].

Other related industrial phenomena include AlN embrittlement in castings (shaped steel castings) where the fracture surface consists of intergranular facets, and is described as intergranular fracture [30]. This AlN embrittlement is a combination of dendritic and plate precipitates in the  $\alpha + \gamma$  region, so that the fracture gives a fine dendritic appearance superimposed on the larger crystallographically orientated plate-like features, Figure 2.5 [31].

### Susceptible steels

It is generally agreed that the most susceptible steels to transverse cracking are the high strength low alloy (HSLA) peritectic steels with  $>1\%Mn$ ,  $0.02\%Al$  containing Nb or V [17, 27]. This tendency to crack can be exacerbated by poor secondary cooling spray practice

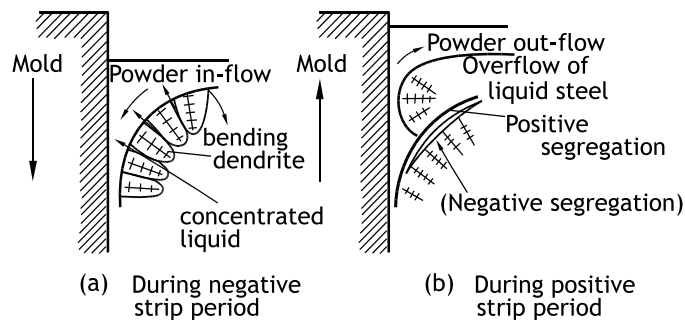


Figure 2.4: Formation mechanism of segregation at the meniscus [18].

[24]. Avoiding compositions between 0.1-0.15%C, a reduction of P and a Mn/S ratio over 80 is desirable [18] since peritectic steels are susceptible to cracking [26].

### **Process accommodations**

Alterations in mould powder, mould characteristics, mechanical stresses, and unbending temperature can go some way to accommodate these susceptible steels during the continuous casting process.

Mould powder has been noted to have some influence on corner cracking. When a glassy powder is used the corner cracks are reduced. This is because the glassy powder improves the heat extraction in the mould, thereby refining grain size at the slab surface [32]. In contrast to this, the use of less glassy, moderately basic powder to reduce thermal transfer has also been suggested [26]. This is in line with those [18] who recommend slower cooling in the mould to reduce segregation.

Increasing superheat causes oscillation marks at the mid face to become shallower, but has less effect on the off corner cracks [33]. The mould oscillation parameters which have an influence on the oscillation mark depth are the mould reciprocating characteristics and the mould level control [27, 26]. Both parameters have an effect on meniscus fluctuations, high meniscus fluctuations promote the formation of oscillation marks [26]. While the presence of deep oscillation marks is not an *a priori* cause of transverse cracks, since transverse cracks can still form even if the oscillation marks are shallow [34], they can act as stress raisers [16], Figure 2.6. Figure 2.6 shows that, in 27 out of 28 cases of transverse cracking on a slab, the transverse cracks occur in the oscillation mark. Reducing the depth of the oscillation marks by increasing their frequency and stroke leads to lower heat times and more uniform mould cooling which is desirable to reduce oscillation depth [18]. The mould level control can be improved by avoidance of clogging as well as reducing the number of changes in casting speed [26].

While Suzuki *et al.*[35] calculate that the accumulated strain for cracking during casting including unbending is around 5%, Triolet *et al.*[32] show that the highest accumulated strains are on the corners of the inward face where they are between 1-17% depending on width and misalignment. In contrast with the inward face, far from the corner, the strains are typically 0.1%. The strain rate can be as high as  $10^{-1}\text{s}^{-1}$  in the corner although generally it is  $10^{-4}\text{s}^{-1}$ . Thermal stresses can be reduced with improved mould design and slow uniform secondary cooling. Mechanical stresses are reduced by accurate roll gap adjustment to prevent bulging [18] or misalignment [26, 32]. This is more critical at the top of the caster where the shell is thinner and the rolls are smaller [32]. Bending/unbending stresses should

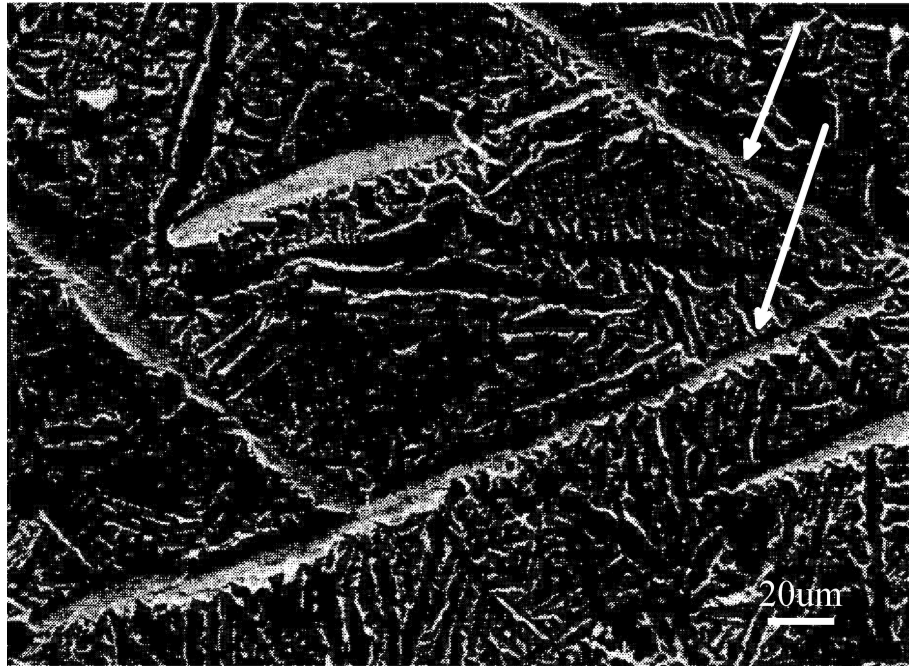


Figure 2.5: Scanning electron micrograph of grain boundary surface. Surface shows fine dendritic appearance superimposed on which are larger, crystallographically orientated plate like features. [31]. Presumably the AlN is in the areas indicated with the arrows.

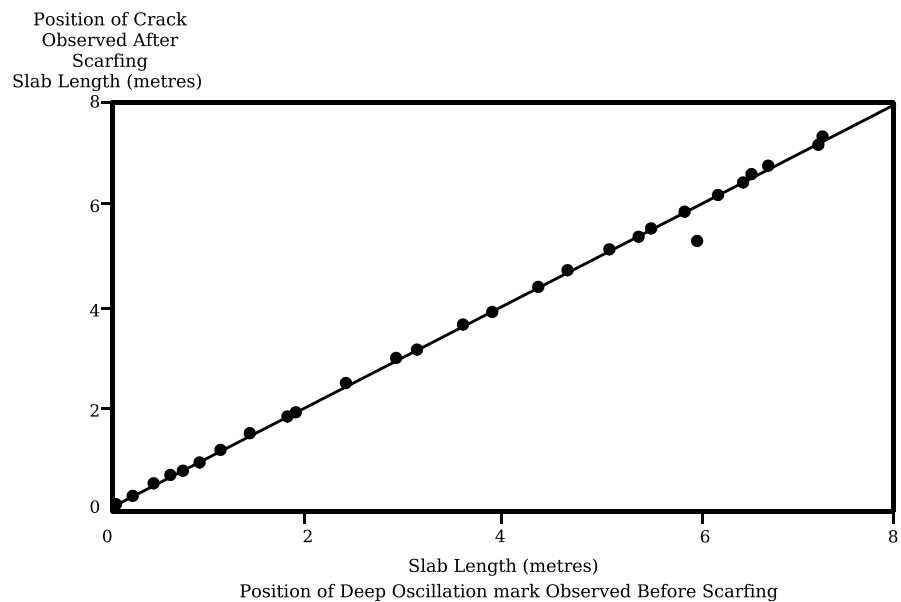


Figure 2.6: Correlation between the points along the length of the slab where deep oscillation marks are observed in comparison to where the transverse cracking is observed [16]. This shows that transverse cracks predominantly occur in the deep oscillation marks.

be avoided at the hot ductility trough to minimise cracking [18].

Control of secondary cooling water dictates the unbending temperature [27]. Because of ductility troughs, casters operate according to one of two strand unbending temperature scenarios. With a high temperature approach, the surface temperature at the straightener is kept above the trough. Whilst for the lower temperature route the surface temperature at the straightener is below 700-650°C [16, 25, 24, 36]. In using less water, so as to achieve a surface temperature above 900°C at the straightener [24], the fine precipitation of carbonitrides during unbending can be avoided [17]. With lower unbending temperatures, spray practice must include applying high volume in the lower zones to cool the surface to below 700°C at the straightener [24]. Kato *et al.*[37] recommend intensive cooling directly below the mould, as they claim it restrains the growth of film like ferrite along the austenite grain boundaries but instead produces large amounts of ferrite and so improves crack resistance more than mild cooling in the secondary cooling system. However, lowering the temperature of unbending leads to higher roll stresses due to higher strength at lower temperature and greater machine wear. Local overcooling can also cause transition boiling which leads to poorly controlled temperatures [19] and aggravates the formation of transverse surface cracks in steels containing > 0.02%Al, 1%Mn or Nb [17].

A spray practice ('plateau' cooling) to avoid the problem includes a restriction of cooling rate in the upper zones to  $<1.7^{\circ}\text{C}\text{s}^{-1}$  and in the lower zones to  $0.17\text{-}0.33^{\circ}\text{C}\text{s}^{-1}$ , keeping the surface temperature in the spray zone above 700°C throughout the secondary cooling zone, which discourages AlN precipitation and minimizes the severity of longitudinal, mid-face cracks [24]. This is because the cycling of the surface temperature through 700°C was shown to accelerate AlN precipitation [23]. Further techniques such as air-water sprays or mist cooling are used to provide more uniform cooling over a larger area between the rolls by reducing the magnitude of the surface temperature drop under the sprays [17, 19].

A relatively new strategy for reducing transverse cracking, 'surface structure control' has been developed by Sumitomo Metal Industries [38]. The slab surface is cooled below the  $\text{Ae}_3$  just below the mould, which causes allotromorphic ferrite to nucleate and carbonitride precipitation. The surface is then allowed to re-warm, redissolving the ferrite and coarsening the precipitates. When the  $\text{Ae}_3$  again is reached the precipitation causes the allotromorphic ferrite to form, the end result being a uniform fine precipitation of carbonitrides and the prevention of a film like ferrite morphology [38]. While successes have been reported for the two unbending routes (high and low cooling rate), usually the low surface temperatures are difficult to achieve where a liquid core still exists at the straightener. Newer continuous casters tend to follow the former route by casting faster and minimising spray water cooling [25]. This route is also more beneficial for internal quality, as long as the distribution

of cooling water remains uniform [16]. No other reports of the ‘surface structure control’ strategy have been reported.

### 2.2.3 Test characteristics

#### Description of standard test

The most popular test for investigations on transverse cracking has been the hot tensile test. A schematic thermal profile can be found in Figure 2.7. Samples are heated to above the solution temperature or melted *in-situ* to produce a coarse grain size that approximates to the cast grain size [17]. If the sample is melted, experimentalists make use of a quartz sleeve to support the central molten section, protecting the sample from oxidation by flushing the specimen with argon [20]. The sample is then cooled to unbending temperature according to the average thermal cooling rate of the strand surface  $\sim 1-3 \text{ K}\cdot\text{s}^{-1}$  depending on if the simulation is for conventional continuous casting or thin slab casting [39]. However, usually the dip and recovery in temperature that the surface experiences (Figure 2.2) is not simulated. The sample is strained at rates of  $10^{-3} - 10^{-4} \text{ s}^{-1}$  to simulate straightening [17, 39]. After fracture the reduction in area at the fracture surface is calculated [17].

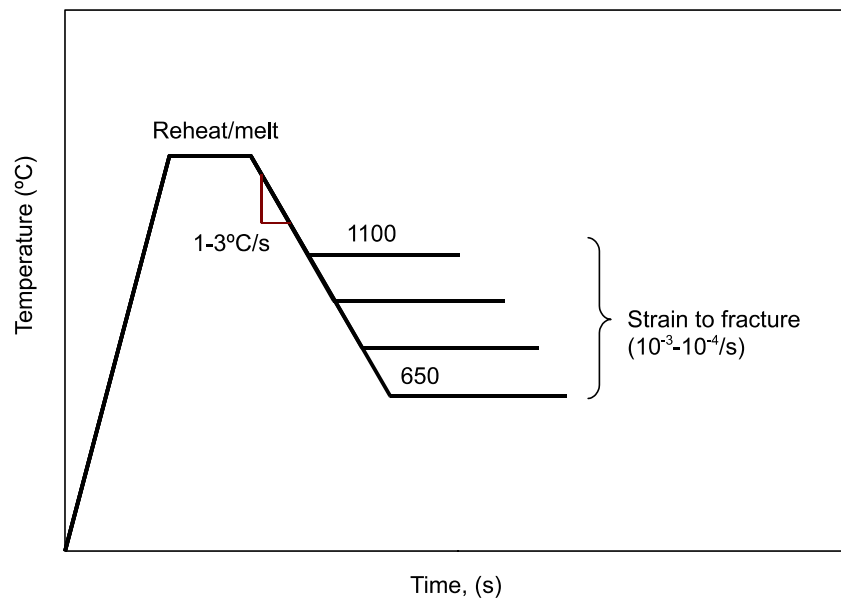


Figure 2.7: Schematic of standard testing procedure.

## Analysis of fracture surfaces

Originally the study of the fracture surfaces for precipitate morphology and grain boundary area needed to be performed with an extraction replica technique[40] and transmission electron microscopy (TEM), since scanning electron microscopy (SEM) resolution was inferior. This is no longer the case as <10nm resolution is achieved with field emission gun scanning electron microscopy, (FEG-SEM), with a best resolution of 0.67nm.

Fracture surface characteristics that have been observed have been described as follows:

**High temperature ductile rupture, (HTDR)** is associated with R of  $A \geq 80\%$ . In this fracture type large voids which do not seem to be associated with second phase particles are present. These voids probably originate from intergranular cracks that form early in deformation, and as deformation proceed they are elongated until all voids link up [41]. Other associated terms are transgranular dimple fracture [42] and fibrous fracture [43]. This occurs at the upper end of the ductility trough where dynamic recrystallisation occurs, and where the grain boundaries migrate away from the cracks so that the cracks only link up at very high strains [39].

**Intergranular decohesion** shows flat austenitic grain facets, which lack microvoids, although some second phase inclusions are present (eg. MnS). The facets may also show wavy ridges [41] which form from the intersection of slip bands with the grain boundary during deformation [41], leaving ridges on the fracture surface as the sliding proceeds. Suzuki *et al.*[42] identified this fracture type as austenite grain boundary fracture. It is also associated with grain boundary sliding (gbs).

**Intergranular microvoid coalescence, (mvc)** shows the same deformation along facets, but the fracture surface has microvoids with second phase particles in them [41]. This type of fracture is observed at test temperatures both where the material is fully austenitic and where it contains pro-eutectoid ferrite [41, 43].

**Interdendritic** fracture which is attributed to micro-shrinkage [43] or porosity. It is similar in appearance to the ‘interdendritic’ reported by Zhang *et al.*[44]. Mintz *et al.*[43] do not speculate on its affect on the R of A values, but the presence of interdendritic failure is a result of testing practice and is not representative of casting (porosity is not expected on the surfaces of a slab). However, it can be useful for revealing the segregation patterns that occur during solidification.

**‘Rock-candy’** fracture is defined as ‘a discontinuity in a metal formed by separation along boundaries of primary crystallization’ [45]. Wilson and Gladman [14], also report fracture in slow cooled ingots with high aluminium and nitrogen as ‘rock candy’ fracture.

It is characterised by large smooth facets [46], (similar to Figure 2.5 [31]) which is due to the presence of coarse dendritic and plate-like AlN at the interdendritic and prior austenite grain boundaries which provide preferential sites for fracture propagation [14].

Microstructures are usually taken from a cross section perpendicular to the fracture surface, and often grain size and amount of ferrite is measured from this. Microsegregation, characterized by concentration of elements in interdendritic regions that range from few to several hundred microns indicates the degree of homogenisation [47]. This phenomenon can be revealed in the microstructure as either a variation in etching by energy dispersive spectroscopy, or by studying the variability in precipitation.

Precipitation is generally studied using higher resolution techniques such as TEM; samples generally being prepared by extraction replica. The replica technique is, frequently, difficult to implement. In an unusual technique, Wilcox and Honeycombe [40] used carbon extraction replicas taken from fracture surfaces induced by hydrogen embrittlement. These replicas showed up the much larger AlN and Nb(C,N) precipitates having similar dendritic and plate like morphologies. Unfortunately, the extraction efficiency of carbon replicas may vary from one replica to another, and volume fraction cannot be determined satisfactorily by this technique [48].

### **Other tests - variation on a theme**

Ouchi *et al.*[49] investigated the effect of holding time and thermal cycle on the hot ductility in a 0.15%C-0.054%Nb steel, Figure 2.8. Their thermal cycles separate the effects of precipitation and ferrite formation. Mintz *et al.*[50], performed modified tests in a commercial continuous cast slab of austenitic stainless steel to ascertain the effect of columnar grain structure on ductility. They machined samples so that the tensile direction is at various orientations to the long dimension of the columnar grains. The grain dimensions were 1, 2, 8mm respectively, and they showed that if the long direction of the grain is parallel to the tensile direction, ductility is better than in any other direction. The implication is that in normal casting when the columnar grains are perpendicular to the slab length, crack propagation is encouraged [50]. This shows that the stress direction is important, which is why Hertel *et al.*[51] suggest that simulations should mimic the thermal shocks and strain compression cycles as they occur in the caster. This was achieved by Hiebler and Bernhard [52] in a test that more realistically simulates the thermal gradients and stress state in the mould. They demonstrated that the shell in the mould (<10mm) cannot tolerate strains above 0.15-0.4%, but as it thickens can tolerate strains of up to 1.6%. Thus the

strength near the solidus temperature is lower than that of comparable hot tensile tests [52]. Suzuki *et al.*[35] also used modified tests along these lines by using a hot tensile test with a notch to determine the critical strain for the formation of transverse cracks, subjecting their samples to the thermal gradients that exist in the shell in the mould. They showed that, at strain rates of  $5 \times 10^{-4} \text{s}^{-1}$ , the critical strain to fracture with V and semicircular notches (1-1.5mm depth) was around 10% and concluded that oscillation depth mark is an extremely significant factor in the reduction of transverse cracking [35]. However even with their own calculations of accumulated strain during casting (5%), it seems that the strain in the caster will never reach this critical strain. While they are critical of reduction in area measurements (particularly the minimum R of A to prevent transverse cracking), they do not convincingly show that critical strain can be related to the industrial practice or to the R of A value. They did not consider grain size as a influence on critical strain, and while they used as-cast material, they reheated rather than melted their samples (no doubt because of difficulties with getting a complex shape such as a V-notch in an *in-situ* cast piece). El-wazri *et al.*[20] have performed experiments aimed at investigating the thermal history of the slab surface during continuous casting. Rather than just performing conventional tests of heating to melting point, cooling to test temperature and pulling to fracture, they also performed a closer physical simulation of the thermal history experienced during continuous casting. They showed that there were dramatic changes in ductility with thermal history (refer to Section 2.4.6 page 101). In a comparison of physical simulation of continuous casting with conventional hot ductility testing (named 'isothermal' testing in the paper) of a low carbon steel (0.04C, 1.4Mn, 0.2Si, 0.05Al, 0.046Nb, 0.016Ti, 78ppmN). El-wazri *et al.*[53] showed that almost all physical simulation variants lead to hot ductility values lower than predicted by conventional hot ductility tests at the corresponding tensile test temperature. If a critical minimum temperature is attained during the during thermal history ( $T_{\text{min}}$ , Figure 2.46), the hot ductility at the test temperature is poor, most likely due to the formation of grain boundary ferrite and the acceleration of Nb(C,N) precipitation in this ferrite [53].

### **Hot ductility test qualities/disadvantages**

In early research at the British Steel Corporation, Mintz and Arrowsmith [54] determined the reliability of hot ductility testing. The statistical deviation of the R of A measurement for a population of 6 was found to be  $\pm 3\%$ . These samples were reheated, rather than melted, but no hold time was given prior to testing [54]. Considerable work has been done on rigs with very accurate thermal control ( $\pm 5^\circ\text{C}$ ), but only for solution treatments between 1300- 1350°C, and wide troughs are still present [55, 56]. It is only for melted *in-situ* tensile specimen testing that it is virtually impossible to avoid these high gradients and techniques using Gleeble or induction have to be used [21]. The repeatability of *in-situ* melting results

with different testing rigs has been reported on by two research groups. Suzuki [42] showed that there is a thermal profile in a sample heated by resistance in a Gleeble thermomechanical simulation machine. From Figure 2.9 the variation in temperature in the specimen increases as the heating temperature increases, the smallest variation being 50°C and 100°C is the highest variability which occurs at melting temperatures. This is part of the explanation why the trough can be wider than expected, as high temperature tests are actually at lower temperatures, where the ductility is poorer. However, when other researchers were forced to use various testing rigs for the same work, they were able to show that resistance heated Gleeble testing and the Hounsfield induction heated setup were comparable in terms of R of A at strain rates of  $3 \times 10^{-3} \text{s}^{-1}$  [57]. Undoubtedly there have been differences in testing, but given the cautionary warnings issued by Mintz [39] in the effectiveness of the test to simulate reality in the best of circumstances, an engineering approach of ‘good indication’ rather than ‘irrefutable proof’ is the wisest route to take. Induction heating also leads to variability in temperature between surface and centre, with the surface being at a higher temperature than the centre, the variation being around 50°C below 1000°C [58]. Where melting is not required the Gleeble and induction testing should not be used if accurate results are desired.

One of the important changes in hot ductility testing over the years has been the change in testing reheated samples to melted samples *in-situ*. There are some factors less influenced by reheating than others.

For instance, Crowther and Mintz, [41], showed that precipitation was not influenced by reheat temperature, as long as complete dissolution of the precipitates was achieved. However, differences between reheat and remelt tests were found at grain sizes above  $200 \mu\text{m}$  (Figure 2.10 from Mintz and Abushosha[59]). Mintz [43] also found that the hot ductility of directly tested cast material was superior to reheated material. Coarse precipitation of NbCN and sulphides occurred in as cast material as opposed to dissolution and re-precipitation along the austenite grain boundaries in a finer and thus more detrimental form in the reheated material [43]. The aim of testing is to apply results to industry. For example, the absence of remelting in Ouchi’s *et al.* [49] work on Ti containing steels will be difficult to apply in industry. Thus in many instances it may be desirable to perform the test with re-melting.

So while melting may give closer simulation, the casting of these little samples can result in unexpected segregation. Some of the sulphides formed are (Mn,Fe)S [60], indicating that there is too little Mn available locally to produce a pure MnS. This ability to redissolve is enhanced by the segregation, which was in this case made worse in the laboratory than in industrial conditions. Casting during testing of microalloy steels (0.1%C, 1.4%Mn, 0.3%Si 40-60ppm N) can even appear to reduce the effect of composition on ductility, because the

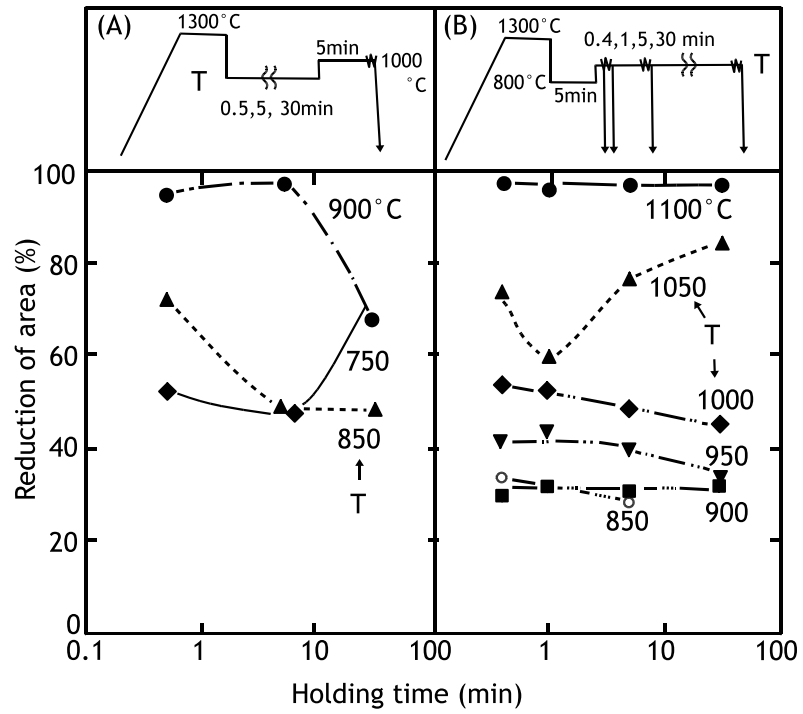


Figure 2.8: Effect of holding time on the hot ductility of 0.15%C-0.054%Nb steel for two different cooling cycles. The holding temperature (T) is shown in the thermal cycle [49].

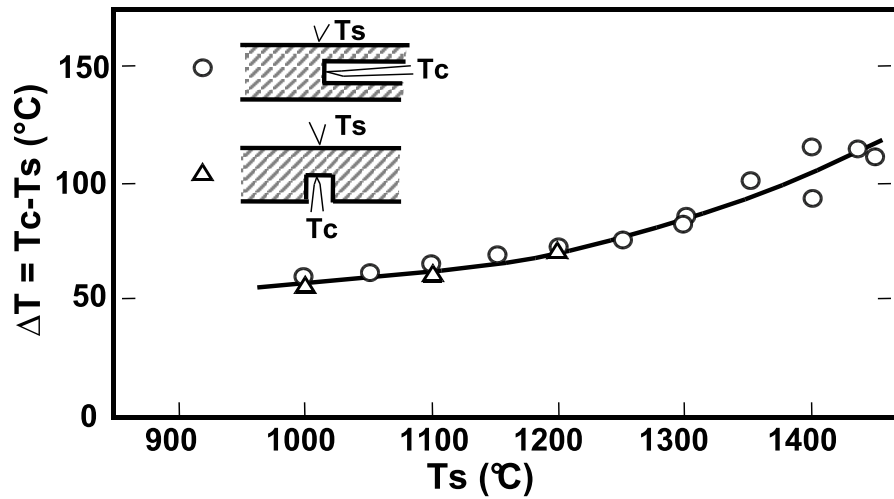


Figure 2.9: Temperature differences between interior and outer surfaces of a 10mm diameter specimen (0.1%C steel) [42].

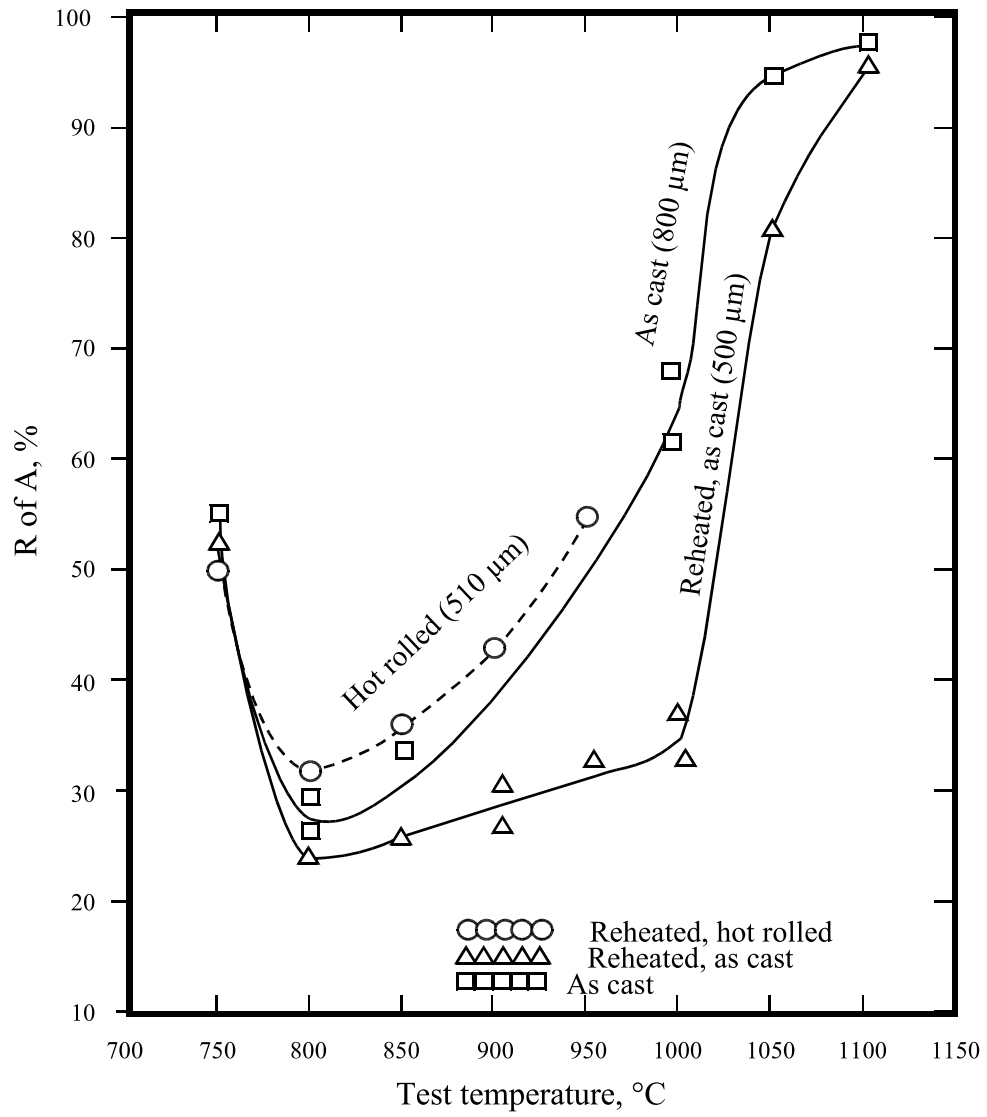


Figure 2.10: Hot ductility curves for C-Mn-Al-Nb steel (0.1C, 1.43Mn, 0.029Al, 0.030Nb for reheated, hot rolled, as cast conditions -austenite grain sizes are given in parenthesis) [59].

microalloys precipitate out as coarse eutectic precipitates, reducing the amount of solute microalloy available to contribute to fine precipitate during straining [61]. While these eutectics may be present in casting, they are expected to be more frequent in the simulations. Later work [62], also shows that segregation is more intense in the test sample than in a commercial slab. Thus melting is not without disadvantages.

Another disadvantage is the formation of porosity during melting [38]. Zhang *et al.*[44] found that fracture in melted samples occurred along the interdendritic regions of the primary solidification structure, and these samples had poorer ductility than the re-heated samples. They explain the interdendritic fracture as being the result of decohesion of dendritic interface, which is weakened by primary segregation. While they claim to be able to differentiate between microshrinkage and interdendritic fracture, they do not give any details of the difference. It is more likely that the difference in ductility is as a result of porosity generated by the contraction of the steel during solidification not being taken into account during the testing. It has also been pointed out that friction between the tube and the specimen may lead to problems in testing [38]. However, an interdendritic area is useful, since Cowley and Mintz [56], are able to show the sulphide distribution from these areas, and Zhang *et al.*[44] observe that interdendritic AlN and coarse Nb precipitate occurred. The danger is that it implies that the AlN is not fully dissolved in the steel even at melting temperatures, leading to less fine AlN precipitating during testing and better than expected results.

Additionally, the question of the occurrence of transverse cracks in the oscillation marks rather than randomly on the strand surface has not been dealt with, neither do all oscillations show cracks. It is possible that conditions other than ductility loss alone are contributing to transverse cracking [25].

While it should be accepted that no physical simulation can fulfil all the characteristics of the commercial process [59], a number of correlations may be made, based on accepting of some differences:

- Reheating as cast material refines the grain size and reduces segregation as compared to the highly segregated as cast grain structure.
- As cast tensiles are more insensitive to composition, since some of the microalloy elements are taken into eutectic precipitates that are unavailable for subsequent precipitation during testing.

## 2.2.4 The applicability of hot ductility testing

While early workers like Hannerz [63], boldly declared the predictive performance of simple thermomechanical simulation to predict crack susceptibility, the later workers [20, 39] draw strong provisors around that claim.

### Segregation

As discussed in the previous section (page 48), reheat type tests are further removed from the industrial reality than the melted tests. For example S is not taken into solution in higher Mn steels if the samples are not melted *in-situ*, and then the adverse effect of S on ductility is not revealed [39, 43]. It seems that segregation can be more intense in the melted test samples than in commercial slab possibly due to the slower cooling rate ( $1\text{Ks}^{-1}$ ), allowing the production of coarser MnS [43]. However, an increase from 1 to  $1.7^\circ\text{C}/\text{min}$  in the cooling rate at solidification did not prevent segregation [62]. Even so, neither dendritic structure nor segregation patterns found in continuous casting can be simulated in simple hot ductility tests [64]. There have been *in-situ* melted tests which predicted ‘good’ strand surface temperatures at the straightener which should have lead to crack free casting, where industrially the steel has yielded cracks and vice versa [25]. To make laboratory hot-ductility tests more commercially relevant, the tests should include a melt and solidification *in-situ* [25]. Nevertheless some of the early work [54, 65] on C-Mn-Nb-Al steels did indicate very good agreement between the simple hot ductility tests in which the tensile specimens were only solution treated, and the industrial cracking experience.

### Grain size

One criticism of the ductility testing is that many researchers continue to test specimens with prior austenite grain sizes (D) far smaller than the sizes known to be associated with the surface cracking problem. Thus there will be difficulties in applying this data to industry, especially since many papers do not make mention of sample grain size. However in Dippenaar *et al.*'s [25] own laboratory work they show that for a peritectic steel (0.18%C) there is little difference between the reheat and remelt grain sizes (the differences were much greater for low carbon steels). There is therefore some hope for relevance. The microstructure in a solution treated laboratory test is likely to differ from the strand microstructure, especially with respect to grain sizes (2-5 times larger in industry) and while as-cast simulations the grain size is similar to industrial conditions, the formation of columnar grains that occurs in industry cannot be reproduced in *in-situ* cast the tensile test [17].

## Thermal path

The simplified cooling path in the test, as well as the lower segregation alters the precipitate size, morphology and kinetics as well as the phase transformation temperatures [17, 39]. The effectiveness of various simulation routes was studied by Mintz *et al.*[43]. They point out that while reheat cycles have had some success in predicting the likelihood of transverse cracking occurring during straightening of the strand on the continuous casting, the complexity of the thermal path in the industrial operation, such as the local cooling created by the water spray and the cyclical rise and fall of the strand temperature as it passes through the support rolls, introduces a thermal profile and thermal stresses that are not reproduced by the simple test. Increase in cooling rate and introduction of cyclical rise and fall in temperature to simulate strand conditions is recommended for improved simulation [43]. When El-wazri *et al.*[20] used more accurate cooling simulations (the fast cooling in the mould and the temperature rise in secondary cooling but excluding the cyclical rise and fall as the water sprays impinge on the strand) there were dramatic changes in ductility with thermal history (refer to Section 2.4.6 page 101). They point out that hot ductility may be controlled by one or two key process variables in the thermal history. It may therefore not be necessary to have a completely accurate cooling path, but rather one that simulates some key features of the industrial process. However, research is needed to substantiate this.

## Dynamic recrystallisation

In the ductility test the fracture strains are in the order of 5-100% while in the straightening operation it is around 2-17% [17, 32], so that while much testing has highlighted the influence of dynamic recrystallisation (DRX), it is unlikely to occur at the low strains and coarse grain sizes present in the unbending operation during industrial continuous casting [25, 66]. In commenting on the relevance of the hot ductility curve to cracking, Mintz *et al.*[67] point out that, in plain carbon steels, the upper edge of the trough is controlled by DRX and therefore not directly applicable to industrial operation. The depth of the trough is more relevant to the problem of transverse cracking [67]. Thus attention should be paid to factors such as deformation induced ferrite and precipitation [66] and caution should especially be given to the prediction of the onset of poor ductility at the high end of the trough [39], as this is less significant (phenomena discussed in section 2.3.4, page 68).

## Deformation induced ferrite

Deformation induced ferrite (DIF), which forms as thin films on the grain boundary at temperatures between the  $A_{e3}$  and the  $A_{r3}$  (temperature at which austenite starts forming ferrite during non-equilibrium cooling), can also be detrimental to ductility. It will be shown later (Section 2.3.2, page 62) that when DIF does not form in sufficient amounts to improve ductility, and remains as a thin film, it is critical in controlling ductility.

## Precipitation

In a C-Mn steel with Al and Nb additions, Mintz and Arrowsmith [54] showed with a fair degree of confidence that hot ductility testing using a gleeble thermo-mechanical simulator could indicate the crack propagation sensitivity during straightening in continuous casting. This was shown by the similar (but not exactly the same) mode of precipitation of Nb(C,N) in the simulation and continuous casting, so that hot ductility testing has a fair degree of confidence for predicting continuous casting behaviour. While this indicates that no ‘one to one’ relationship between hot ductility value and continuous casting cracking exists, there is nevertheless a strong correlation between the two. Mintz and Abushosha [59], while conceding that in-situ casting reduces the relative changes in ductility with composition, point out that it is the only method to assess the influence of elements such as Ti and S in high Mn steel, where complete dissolution of the elements only occurs in the melt. This may also be true of high Al (>1%) steels when the AlN dissolution temperature is high enough (at high Al and N contents [30]).

## Peritectic steels

Peritectic steels (C levels approximately 0.07-0.14wt%) are also known to be particularly susceptible to cracking, due to the shrinkage of the shell during the  $\delta \rightarrow \gamma$  transformation. This leads to poor contact between the shell and the mould and poor heat transfer. Clearly this shrinkage cannot be simulated with a simple reheat hot tensile test [39]. This is confirmed in an investigation of the influence of heat treatment and C (the peritectic range) on ductility by Guillels *et al.*[68]. They found that the full embrittlement (trough widening) due to the peritectic reaction is not shown unless the material is taken close to melting point. This implies that even super-solidus but sub-liquidus heating may be representative of the industrial castability, so that samples reheated into the mushy zone can still be used as valid tests.

## A last word on relevance

An interesting perspective on the applicability of hot tensile testing to industrial conditions was given by Revaux *et al.*[69]. In an experimental development of the tensile test technique aimed at producing a tensile testing specimen with the columnar solidification structure of the continuously casting slab surface they made use of a notched, slightly cone shaped crucible, leading to a notched, cone shaped tensile test piece. Their thermal path included melting *in-situ*, as well as a grain coarsening step (1min at 1450°C), in which they managed to obtain extremely low R of A values in the trough, Figure 2.11. Most importantly the trough shape is remarkably similar to the simpler *in-situ* melting tests, leading to the conclusion that the simpler melting tests is in fact a satisfactory technique with the proviso that the trough depth is, in reality, 10-20% deeper.

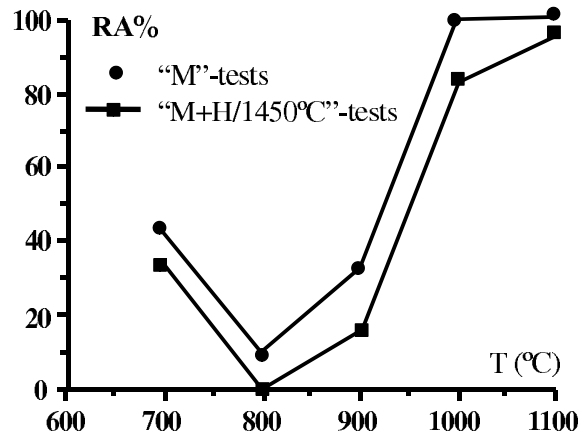


Figure 2.11: Ultimate reduction in area versus temperature for C-Mn-Nb-V/Ca steel [69]. The grain coarsening tests ("M+H/1450°C") show an increase in depth but no displacement along the temperature axis when compared to melt tests ("M").

On a fundamental level the hot tensile test therefore does not precisely simulate the straightening operation in casting. Nevertheless, it appears that hot ductility gives a reasonable estimate of the likelihood for transverse cracking because at the very least the depth of the trough is influenced by the same variables as transverse cracking. Thus simple tests have been of immense help to industry, but could be refined more by *in-situ* melting which includes more accurate thermal paths to testing [17]. Some allowance should also be made for the fact that that ductilities are higher in test than in industrial conditions.

## 2.2.5 Definitions in/of hot ductility and other aspects of the hot ductility curve

This section is a ‘definitions and limits’ section and deals with what is considered good ductility as well as what defines a wide/narrow trough.

**Good ductility** is the composition or temperature where unbending is not expected to result in transverse corner cracks. Work in the 1980’s set the limit of good ductility at a conservative 60% [70, 71]. However Hannerz [63] and reviewers such as Mintz [39], state that researchers now generally agree that for a defect free casting, a lower value of 40%R of A will suffice. This is true even for reheat testing of microalloyed steels where transverse cracking is said to not occur when the minimum R of A is  $\geq 40\%$  [67]. With the improvement of commercial casters (by better alignment and more sophisticated cooling regimes) this value will probably drop further.

A **wide trough** is one that stretches from below the  $A_{r3}$  (undeformed) to at least the  $A_{e3}$  and the amount of ferrite that forms between these temperatures is always less than 45% [55].

A **narrow trough** has the  $A_{e3}$  centred at the bottom of the trough [55] (no temperature values for the limit of narrow to wide are given), large amounts of deformation induced ferrite can form just below the  $A_{e3}$ , so that ductility recovers quickly, (within 50-100°C) [39, 72, 73].

The **minimum ductility** is the ductility (%R of A) in the lowest part of the trough. It is known to correlate with the problem of transverse cracking (discussed further on in Section 2.2.4 page 53).

$T_D$  (shown in Figure 2.21) is the temperature where the critical strain for recrystallisation ( $\epsilon_c$ ) is greater than the strain required for fracture ( $\epsilon_f$ ), discussed further in Section 2.3.4, page 67.

Bannenberg *et al.*[74] use three points to describe the ductility curve  $T_{EV}$ ,  $T_{BEV}$  and  $T_{AV}$ , as indicated in Figure 2.12. Where  $T_{EV}$ , is the temperature of incipient decline in ductility,  $T_{BEV}$  is the temperature of renewed rise in ductility and  $T_{AV}$  is the temperature at the lower temperature end of the range of poor ductility [74]. This model contributes to the understanding of the recovery mechanisms at high ferrite volumes, page 61.

## 2.3 Mechanism/types of ductility loss at temperatures between 1000°C-700°C

Historically, transverse surface cracks were described by Mori[15] in 1974, ‘to occur along the oscillation marks only on the upper side of the strands... in steels containing copper and columbium’. Yamanaka *et al.*[28], attributed ductility loss to intergranular fracture: ‘micro-void coalescence nucleated at the grain boundary precipitates, such as AlN or MnS, as a result of strain concentration at the film like primary ferrite formed along the austenite grain boundaries’.

It is by now well accepted that the mechanisms of hot ductility loss in microalloyed steels is grain boundary sliding in the low temperature region of austenite phase as well as the presence of (deformation induced) ferrite films below the  $A_{e3}$  which leads to mvc in the ferrite. Both of these mechanisms are especially promoted by fine matrix precipitation which causes strain concentration at the grain boundaries. More detail on each part of the mechanism will follow:

- grain boundary sliding (gbs) in the austenite - Section 2.3.1
- ferrite formation - Sections 2.3.2
- the effect of precipitation - Section 2.3.3,
- the influence of DRX/recovery in austenite and ferrite - Section 2.3.4.

After which, the main parameters that influence hot ductility will be discussed.

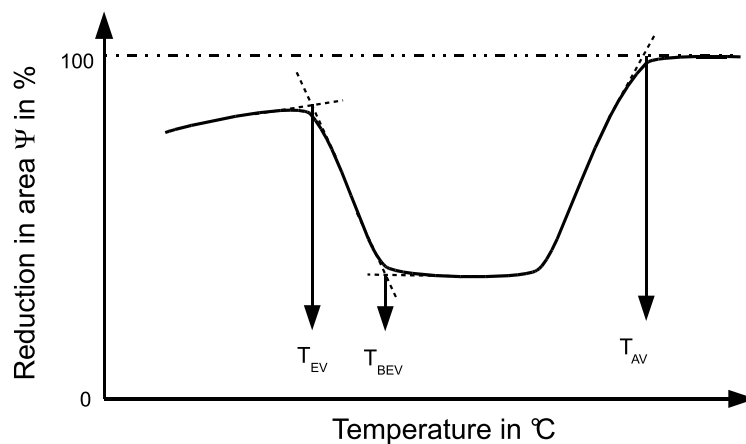


Figure 2.12: Principle sketch of a ductility curve.

### 2.3.1 Grain boundary sliding in austenite

The change in fracture mode from transgranular (high temperature ductile rupture) in the upper austenite to faceted surface (granular or intergranular decohesion) in the lower austenite occurs with decreasing deformation temperature as well as decreasing strain rate [75]. Grain boundary sliding occurs at the upper end of the trough close to the  $Ae_3$ . It is there that the austenite has its highest strength and resists deformation [44] since the strain to fracture,  $\varepsilon_f$ , decreases as temperature decreases [76]. This is why in carbon steels (no microalloy precipitation), Mintz *et al.*[76] observed that the trough always starts just above the  $Ae_1$  temperature (equilibrium temperature at which the austenite to ferrite and pearlite transformation is complete) and that the minimum ductility corresponds to the  $Ae_3$  (equilibrium temperature at which austenite starts forming ferrite), suggesting at that time, that grain boundary sliding in the austenite is controlling the R of A. Later the trough width would be linked to the formation of ferrite below the  $Ae_3$  as when the ferrite forms around the boundaries grain boundary sliding is reduced [39]. A lot of early work was carried out before it was realized that ferrite could form by deformation. Increasing the temperature favours grain boundary sliding in austenite but recovery/recrystallisation is enhanced and the two opposing factors approximately balance each other out [76]. While ferrite is often expected, due to undercooling, it may actually not be present. Nicolaou *et al.*[77], modeled cavity formation in metals, and showed that when failure occurs by mvc the cavities are slow growing, and the strain rate sensitivity is low. High ductility occurs when the cavity growth is small but the the strain rate sensitivity is high, so that the ligaments between the cavities are stabilised. The strengthening in the matrix leads to heightened stresses at the boundaries so that intergranular fracture results. S segregation is also required for this failure mode to happen at low stress [78] although it is not clear whether the S effect is on grain boundary sliding in austenite or austenite-ferrite (0.019%C steel).

While Ouchi *et al.*[49] are of the same opinion as Mintz *et al.*[17] that austenitic grain boundary sliding may be necessary for initiation of a grain boundary crack, they do not concede that it is the controlling factor of hot ductility. However, it seems reasonable that ductility is related to the void formation process and interlinkage of cavities, which will be encouraged by grain boundary sliding or shear (which is related to the size and volume fraction of inclusions, and the strain rate) [17].

The intergranular, faceted fracture surface can be either covered with microvoids, suggesting preferential deformation in the area close to the grain boundary with voids initiating at inclusions or precipitates. Alternatively it is smooth, with a possible mechanism being that grain boundary sliding occurred, followed by wedge cracking at the triple points [17, 79]. With precipitation of microalloys in the austenite region the strain will concentrate in the

soft precipitate free zone along the austenite grain boundaries, resulting in the initiation of fracture at precipitates on the prior austenite grain boundaries, Figure 2.13a-c.

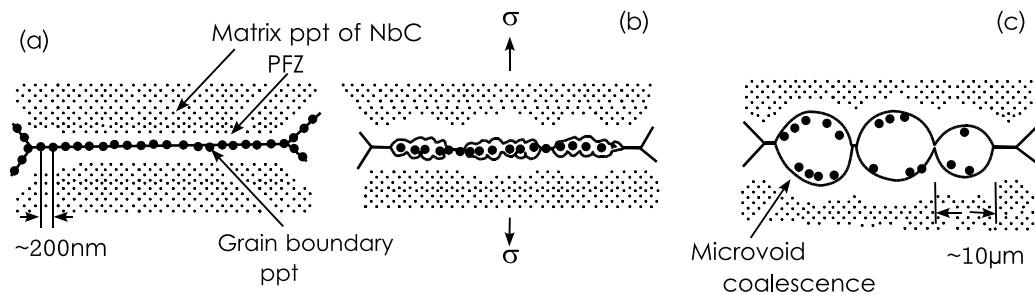


Figure 2.13: Intergranular microvoid coalescence of low alloy steels by deformation in a-c) low temperature austenite region [80].  $\sigma$  is the applied stress and PFZ is the precipitate free zone.

*To summarise:* Grain boundary sliding is an intrinsic effect at large grain sizes, but for it to occur, grain boundary migration needs to stop. Grain boundary migration is slowed by;

1. ferrite formation,
2. precipitation and inclusions,
3. elements such as Nb in solution and
4. the retardation of DRX by low temperatures.

These factors will be now be discussed.

### 2.3.2 Ferrite

Ferrite networks have been identified as a cause of embrittlement for over 50 years [81]. The failure occurs transgranularly in the ferrite [44], which may appear intergranular if the ferrite is in the form of a film on the austenite grain boundaries.

#### Ferrite embrittlement mechanism

In coarse ( $\geq 200 \mu\text{m}$ ) grained steels where precipitation is not controlling ductility (eg. C-Mn and C-Mn-Al steels), ductility is controlled more by phase transformations [57]. Embrittlement is due to localisation of the strain in the thin film proeutectoid ferrite produced by the  $\gamma \rightarrow \alpha$  transformation, Figure 2.14 [79, 82]. The ductility trough starts at the  $Ae_3$

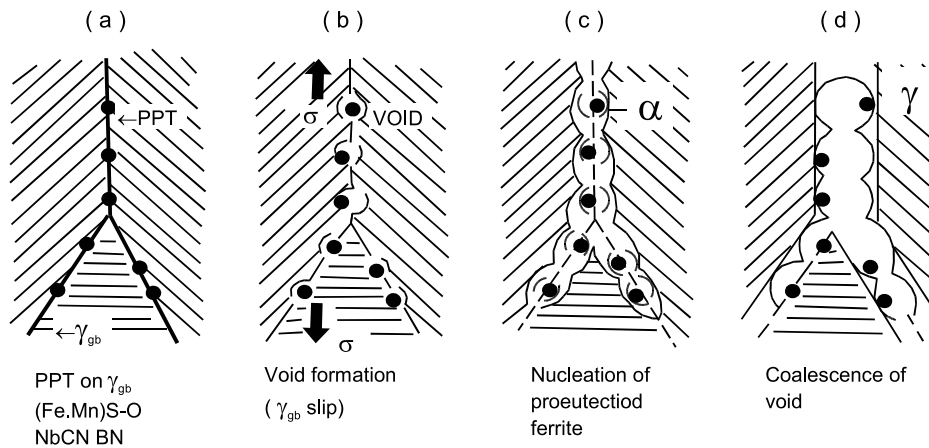


Figure 2.14: Schematic representation of grain boundary embrittlement in the temperature range 1000 to 600°C. [79]. Note that the ferrite cannot be present above  $Ae_3$ .

and recovers 20°C below the  $Ar_3$  where there is sufficient ferrite to sustain the strain [57], Figure 2.15 [17]. In finer grained steels the trough can be narrower as the ferrite starts forming in large amounts closer to the  $Ae_3$  [17]. However, in coarse grained C-Mn steel it was found that the ductility started to drop close to the equilibrium  $Ae_3$  temperature and the minimum ductility occurred above the  $Ar_3$ , so it is clear that deformation can raise the transformation temperature producing thin films of deformation induced ferrite (DIF) at the boundaries and extending the trough [57]. When the ferrite films remain thin, wide trough behaviour occurs and the depth of the trough can be very much influenced by inclusions and precipitation [55]. In plain carbon steels the ductility trough follows the  $Ae_3$ , which is chemistry (carbon equivalent) related [83]. Higher  $Ar_3$  temperatures occur at lower C and Mn levels, refined grain size or slower cooling rates, and the higher the  $Ar_3$  the better the ductility and the narrower the trough [73].

The strain rate has an important influence on the extent of recovery in the deformation induced ferrite, the lowest strain rate enables full recovery to occur, thus keeping the film soft [84], ensuring that the strain concentrates in the ferrite [85]. Raising strain rates leads to improved ductility due to the ferrite hardening, preventing strain concentration in the ferrite [84]. Mintz *et al.*[86] show that the 2% strain that occurs during the straightening operation in continuous casting is sufficient to produce deformation induced ferrite in steel containing 0.08%C, because the actual strain is concentrated in the soft ferrite region rather than uniformly in both the austenite and ferrite phases [39].

Precipitation of Nb(CN) or AlN can take place in the ferrite formed on the  $\gamma$  grain boundary in microalloyed steels [49, 53]. The ductility falls at the start of precipitation and only recovers when the temperature falls just below the  $Ar_3$  when substantial amounts of ferrite

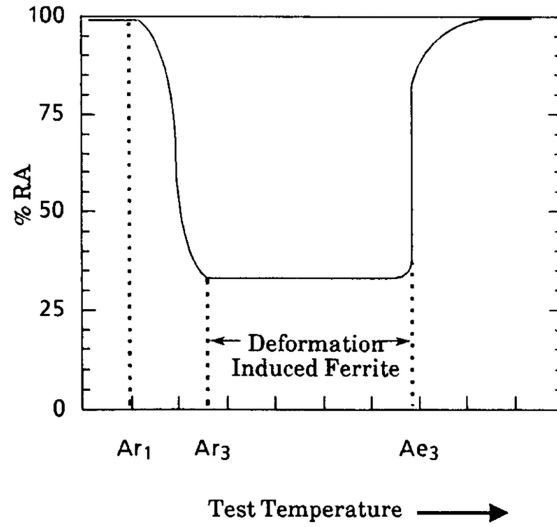


Figure 2.15: Minimum ductility controlled by phase transformation in coarse grained steels (grain size  $\geq 200\mu\text{m}$ ): steels solution treated and cooled to test temperature [17].

are formed [17]. Coarse precipitation of elongated MnS allows the recovery of ductility just below the  $Ae_3$  due to the ability of large MnS to nucleate both normal and deformation induced ferrite [67].

Thus in the ferrite, where transgranular fracture occurs and there is no ferrite film forming, the ductility is controlled by the second phase population (precipitates and inclusions) and the amount of recovery [85].

### Recovery of ductility at high ferrite volumes

At the lower end of the trough, increasing the ferrite film thickness is observed to improve ductility, Figure 2.16 [49]. Thus recovery is due to an increase in the volume fraction of

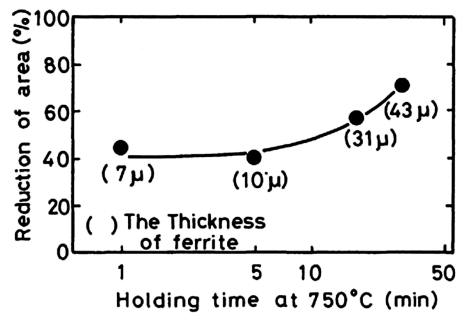


Figure 2.16: Effect of ferrite thickness on hot ductility of a 0.032%Nb steel [49].

ferrite, so that the strain is no longer concentrated at the thin ferrite film. Additionally, as the temperature decreases, the strength differential between the austenite and ferrite

decreases, and grain boundary sliding or shear and voids growth is slower, improving the stress distribution, and thus the ductility [17]. In narrow troughs, the ductility at the lower temperature is almost entirely dependant on the amount of deformation induced ferrite that forms [55, 74]. There is a very clear relationship between the  $A_{r3}$  and the temperature at which the ductility starts to rise ( $T_{BEV}$  in Figure 2.12) as well as the temperature where there is complete recovery of ductility ( $T_{EV}$  in Figure 2.12) being correlated to 50% transformation to ferrite in a wide range of steels [74]. Mintz and Cowley [55] also use 50% ferrite as the amount that gives R of A >40% in plain C-Mn steels. The formation of large volumes of ferrite can even swamp the detrimental influence of inclusions and precipitation on hot ductility. Decreasing the cooling rate causes the ductility to improve, since the ferrite thickness increases [87], (but also the MnS inclusions in the thin film are coarser and further apart). Fine grained material has better ductility, and there are two potential mechanisms to explain the lowering of the effect of ferrite on ductility; a) volume fraction ferrite increases quickly, resulting in the reduction of stress concentration, and b) the connectedness of the thin film may be important in reducing ductility [17]. The ferrite network is more continuous when the grain size is large [88]. When grain size is finer the film becomes continuous at lower temperatures [17]. While both mechanisms account for the narrowing of the trough at finer grain sizes, they both do not explain the reduction in trough depth that occurs [17]. It is likely that the a higher amount of strain can be tolerated at small grain sizes since recovery/DRX occurs at lower critical strains in fine grained material.

The ferrite morphology is also important: when fracture is by wedge-type cracking at the grain boundary triple points, the formation of blocky proeutectoid ferrite in fine grained austenite retards cracking at these points [88].

### **Deformation induced ferrite**

Deformation induced ferrite, (DIF) forms readily in Nb and C-Mn steels close to the  $A_{e3}$  [55]. It has been observed to form in both fine ( $25\mu\text{m}$ ) and coarse ( $200\mu\text{m}$ ) grained samples at rates several magnitudes higher than in the absence of deformation [89]. If the deformation induced ferrite grows readily as it does in low C, low Mn steels, large amounts of ferrite form just below the  $A_{e3}$ , resulting in the improvement of ductility, and narrow trough behaviour [55, 90]. When the ferrite remains a film then wide trough behaviour occurs [55]. The possible reasons for deformation increasing ferrite formation are two fold:

1. Nucleation sites are created by
  - (a) elongation of austenite grains and
  - (b) local grain boundary migration (bulging)

2. and stored energy increases by
  - (a) subgrain formation near the grain boundary
  - (b) the increased dislocation density [17, 55].

However, the precise mechanism is yet to be agreed on [55]. Although deformation induced ferrite can be formed readily during straining in hot tensile testing, there is not yet positive confirmation of its presence in coarse grained steels at the low strains ( $\sim 2\%$ ) applied during straightening [17].

### **Austenite or ferrite, which is worse?**

There seems to be some confusion as to whether, in the absence of microalloy precipitation, the thin film or un-recrystallised austenite present at lower temperatures is the primary cause of the ductility drop. For instance in C-Mn-Al steels with high Al and N levels, the ductility trough is as a result of both grain boundary sliding and mvc, the change from one mechanism to the other does not necessarily give a discontinuity in the curve, suggesting that both mechanisms involve the same stress intensification at the boundaries. Altering the strain rate can facilitate differentiation between the two mechanisms. Temperature also plays a role, as at high temperatures the voids grow quicker while at lower temperatures the flow stress in the ferrite and austenite becomes comparable [17]. An illustration of the influence of each may be seen in Figure 2.17, where the high strain rate on a high carbon steel shows there to be two (normally overlapping) mechanisms, the appearance of ferrite at the  $Ae_3$  and the cessation of DRX leading to grain boundary sliding [86]. This type of behaviour has also been seen in Al containing steels [91], discussed in Section 2.4.1<sup>1</sup>.

However, a small amount of second phase such as ferrite can even be beneficial as the growth of the austenite grain at medium carbon levels can be retarded [92].

A model of recovery at the lower end of the trough in plain C-Mn steel can be described as follows: recovery occurs when a large amount of ferrite is formed either before or during deformation. Depending on whether the ferrite forms at the onset of the  $Ae_3$  or  $Ar_3$ , the ductility recovers  $\sim 30\text{-}40^\circ\text{C}$  below this when the ferrite fraction has reached 45% [67].

---

<sup>1</sup>page 77

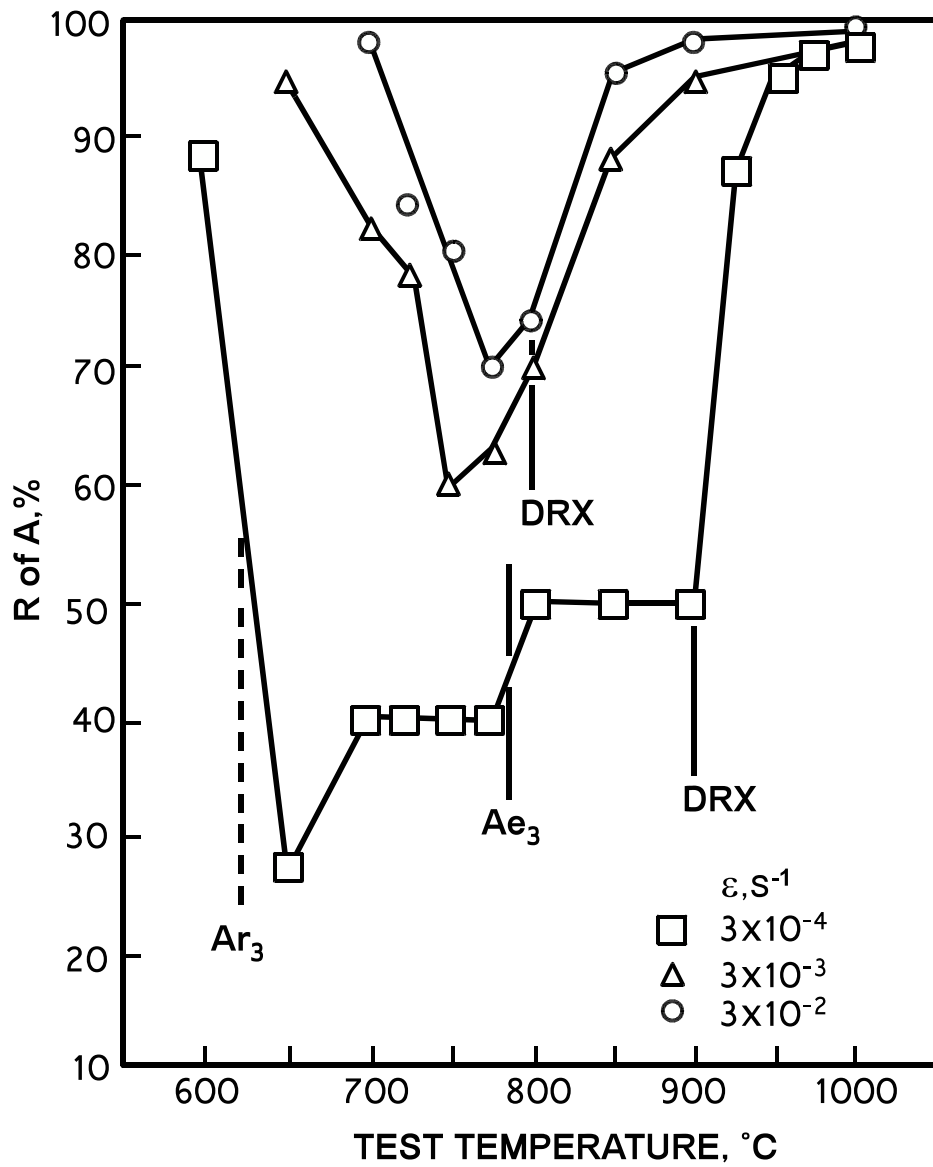


Figure 2.17: Influence of strain rate on hot ductility of a 0.4%C steel [86].

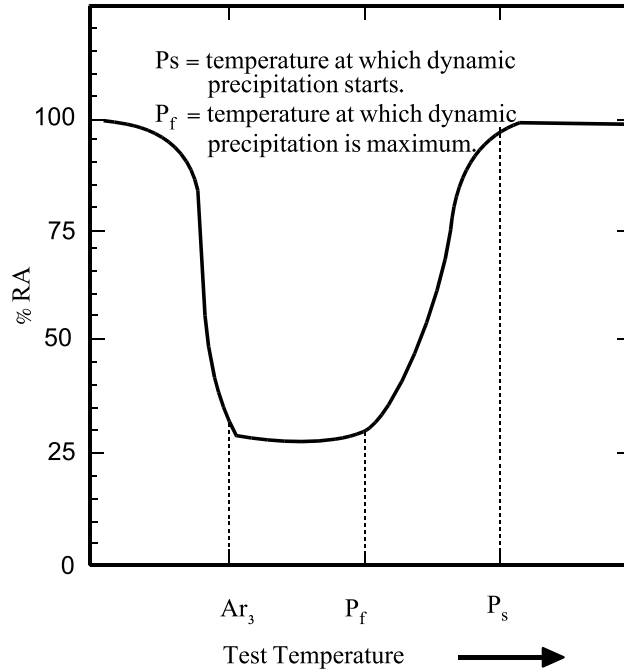


Figure 2.18: Ductility trough controlled by dynamic precipitation of microalloying additions: steel solution treated and cooled to test temperature [17].

### 2.3.3 Precipitation

Nucleation of fine precipitation can occur homogeneously in ferrite or heterogeneously on dislocations in the austenite [93]. Early observers [17, 49] noted that in the lower  $\gamma$  range, while austenitic grain boundary sliding may be necessary for initiation of a grain boundary crack, precipitation (when it occurs) becomes the controlling phenomenon and grain boundary sliding is ‘enhanced’ by precipitation. This is presumably due to the effectiveness of fine precipitates reducing the mobility of the austenite grain boundaries [34]. Decohesion of matrix - precipitation interfaces at the grain boundaries develop into voids and fracture occurs [80]. Precipitation also accelerates ductile failure in the thin films of deformation induced ferrite when failure is induced by phase transformation [59]. Many researchers, [41, 79, 94, 95, 96] have shown that the drop in ductility is shown to be related to the degree of precipitation which increases with microalloying content [96]. Figure 2.18 shows this: the ductility starts to fall at the high temperature end of the trough when precipitation starts ( $P_s$ ) and is a minimum when the maximum volume fraction is present  $P_f$  [17] combined with a film of ferrite. This leads to troughs that extend beyond the  $Ae_3$  in wide trough behaviour.

The most important factors influencing ductility, other things being equal, is the volume fraction and size of the precipitates and inclusions present [67, 94, 97]. The influence of Nb(C,N) precipitates at the austenite grain boundaries can be seen in Figure 2.19, taken from

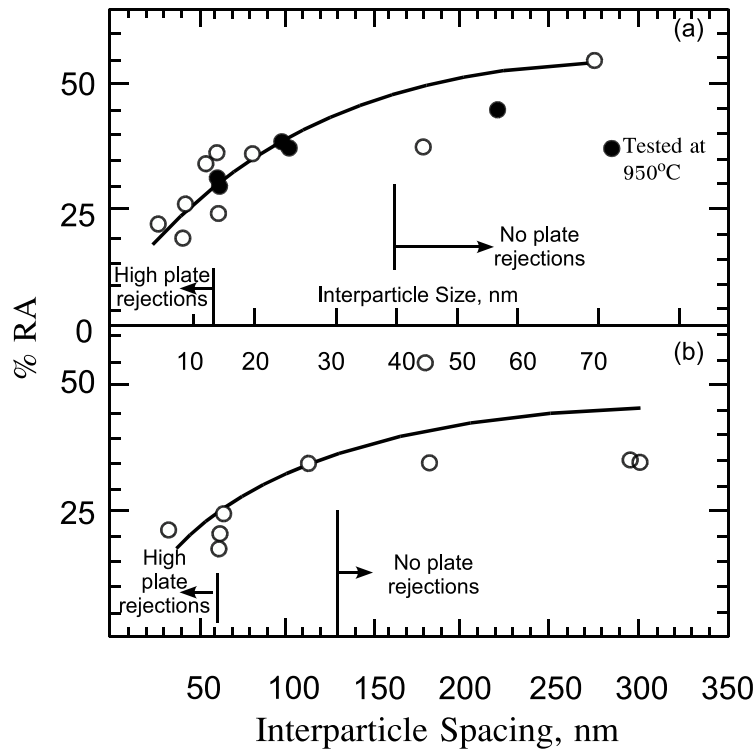


Figure 2.19: Influence of a) particle size and b) interparticle distance on hot ductility of Nb-containing steels, solution treated at 1330°C, cooled to test temperature of 850°C, and fractured at strain rate of  $3 \times 10^{-1} \text{s}^{-1}$  [17].

a commercial examination of precipitates distributions from the austenite grain boundaries close to the surface of the slab. Casts without cracks had mean particle sizes  $\geq 40 \text{nm}$  and interparticle spacing of  $\geq 140 \text{nm}$ , while rejected slabs contained precipitates  $\leq 14 \text{nm}$  and spacing of  $\leq 60 \text{nm}$  respectively, this corresponds to a R of A  $\geq 40\%$  [17]. For specimens with similar grain size and tested at the same strain rate a matrix precipitate size larger than  $\sim 15 \text{nm}$  leads to acceptable ductility [94], Figure 2.20. A regression (not directly applicable to the current research due to the presence of Ti) shows that ductility is proportional to the cube root of particle size (this regression is discussed in more detail in Section 2.5<sup>2</sup>).

Sometimes the high temperature precipitation of one carbonitride can act to reduce the effect of a second carbonitride (by altering the precipitate size/morphology). For example Ti can cause Nb to precipitate on the coarse Ti precipitates improving ductility [98]. High cooling rates can cause fine TiN precipitation that would also be detrimental to ductility. Precipitation location is also of great importance [17], since even the volume fraction of sulphides at the inter-dendritic boundaries affects ductility [59]. High cooling rates (250K/min) cause fine (10-100nm) precipitation of (Cu,Mn)S [99]. The effect of alloying elements may be quite complex, especially at high alloying amounts, for instance Comineli *et al.*[100] show

<sup>2</sup>page 102

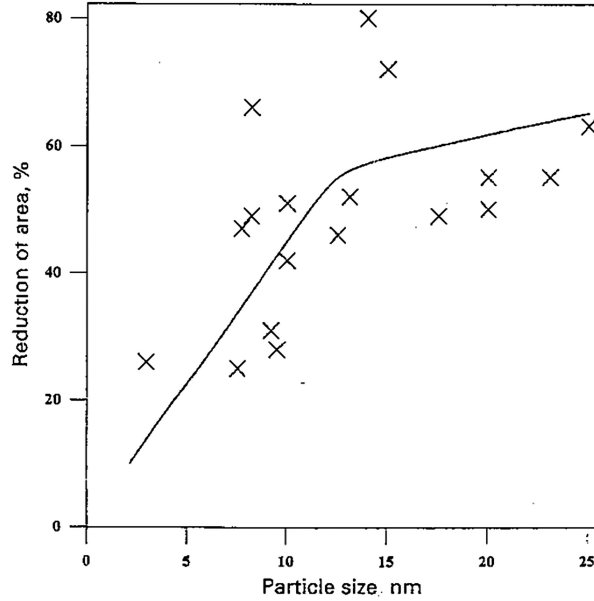


Figure 2.20: Influence of particle size on reduction of area values [94].

that alloying a microalloy steel (in their case Ti-Nb) with Ni lead to a coarsening of precipitation and an improvement in ductility. They suggested that this was due to the Ni encouraging the retention of vacancies in the steel, improving diffusion of the microalloys.

In C-Mn-Al and C-Mn-Nb steels before and after hot deformation when precipitation occurred before deformation (at high and low temperatures) the precipitation was less detrimental than when precipitation occurred during deformation. This strain induced precipitation is thought to concentrate the stress on to the grain boundary regions [101]. Strain decreases the incubation time of induced precipitation, but as the microalloy content increases this influence decreases [102]. In fact Jonas and Weiss [103], show that precipitation in deformed austenite is at least one order of magnitude faster than precipitation in undeformed austenite and at low strain rates the precipitation is complete at very small strains and dynamic coarsening occurs [103, 104].

### 2.3.4 Dynamic recrystallisation

When cooling in the austenite occurs during ductility testing (as opposed to the industrial conditions), the loss of ductility at the high temperature end of the trough often corresponds to the cessation of dynamic recrystallisation [49, 96]. A simple model based on DRX being responsible for the recovery in hot ductility at higher temperatures is as follows: If  $\varepsilon_c$  is the critical strain for DRX, and  $\varepsilon_f$  is the total strain to failure in the absence of DRX then when the temperature,  $T_D$ , is high enough for DRX to occur before fracture, ( $\varepsilon_c < \varepsilon_f$ ) ductility improves, Figure 2.21. The relative movement of  $\varepsilon_c$  and  $\varepsilon_f$  will then dictate the limit of

ductility on the higher temperatures of the trough as well as its depth, since raising strain rate increases both  $\epsilon_c$  and  $\epsilon_f$  and as long as  $\epsilon_f$  is more dependant on strain rate, both a narrower and shallower trough would result.

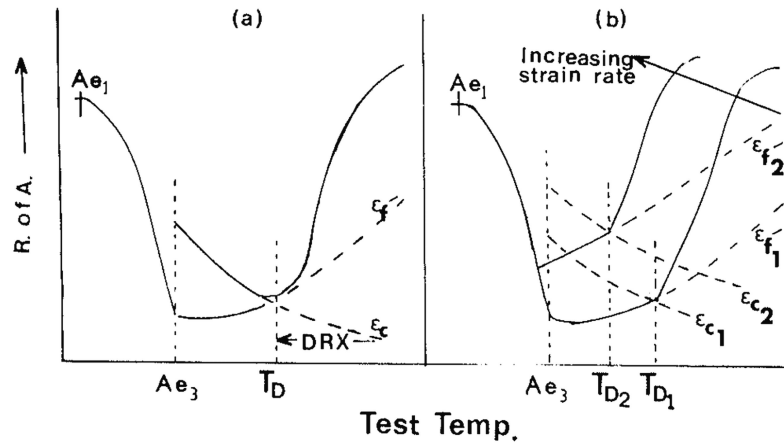


Figure 2.21: Schematic diagrams showing a) how the width of the ductility trough could be controlled by dynamic recrystallisation and b) how increasing the strain rate reduces the depth and width of the trough.  $\epsilon_{c1}$ ,  $\epsilon_{f1}$  refer to the lower strain rates.  $\epsilon_{c2}$ ,  $\epsilon_{f2}$  refer to the higher strain rates [76]. Temperature increases towards the right hand side in each diagram.

Precipitation can have an influence on DRX, coarser precipitation allows DRX, while fine AlN on the austenite grain boundaries delays DRX [41]. Thin films of ferrite at the austenite grain boundaries between the  $Ae_3$  and the undeformed  $Ar_3$  prevent DRX. However, as the initial grain size is refined, DRX is accelerated. Unfortunately, DRX is unlikely at the low strains and coarse grain sizes present in the unbending operation during industrial continuous casting [66]. Thus focus should be paid to factors which decrease the trough when unrecrystallised austenite is present, such as the avoidance of deformation induced ferrite and the resolution and coarsening of precipitates, especially those at the austenite grain boundaries [66]. In the high ductility, high temperature region, another cause of the improved ductility is that grain boundary migration can occur even after voids have been initiated, which isolates the cracks rendering them less harmful [17]. Mintz *et al.*[17], conclude that rather than recrystallisation being the cause of improved ductility, it is this grain boundary motion that is effective in ductility recovery at the high end of the trough, however, the two are certainly linked.

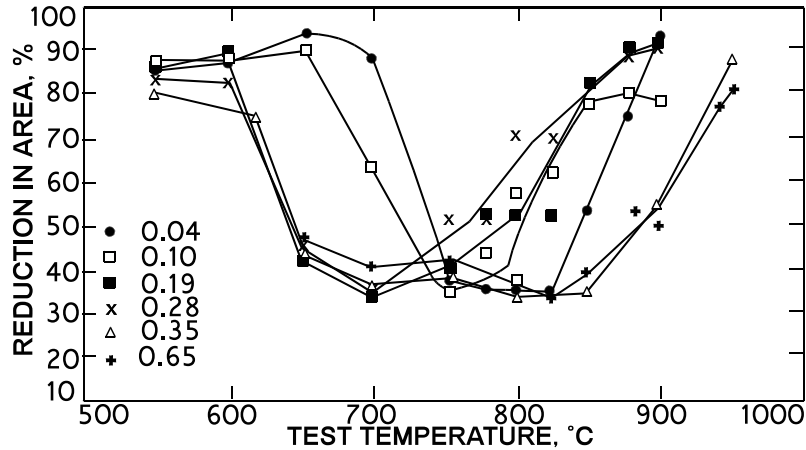


Figure 2.22: Hot ductility curves for a series of plain C-Mn steels having the same grain size ( $\sim 300\mu\text{m}$ ); values given in wt%C [57].

## 2.4 Factors influencing the hot ductility mechanisms and properties

### 2.4.1 The effect of chemistry on reduction of area

This section describes the effect of C, Mn, Si, P, S, Nb, Al and N on hot ductility. Some elements are interactive so there is overlap in places.

#### Carbon

The effect of C on reduction in area was first recorded in 1974 [15]. Suzuki *et al.*[79] showed that in the case of carbon steels (0.05-0.4%C) raising the carbon level is detrimental to ductility in the range 1000-600°C. On the other hand Hannerz [63] performed a comparison between transverse cracking of continuous casting and thermomechanical simulation (Gleeble) for various carbon levels and showed that, unusually, decreasing carbon (0.06-0.28%) increased the propensity for transverse cracking. These anomalies highlight some of the difficulties in comparing results. Hannerz [63] reheated the samples, causing uniform grain size over a wide carbon range which does not reflect the reality of the peritectic reaction - discussed further below.

Carbon does not appear to have a direct influence on the depth of the trough for 1.4%Mn steels. As shown in Figure 2.22, for a given grain size, the trough remains at a similar depth but the temperature of the trough varies with carbon content (as related to the start of ferrite formation)[57]. Increasing the C level in plain carbon steel moves the minimum

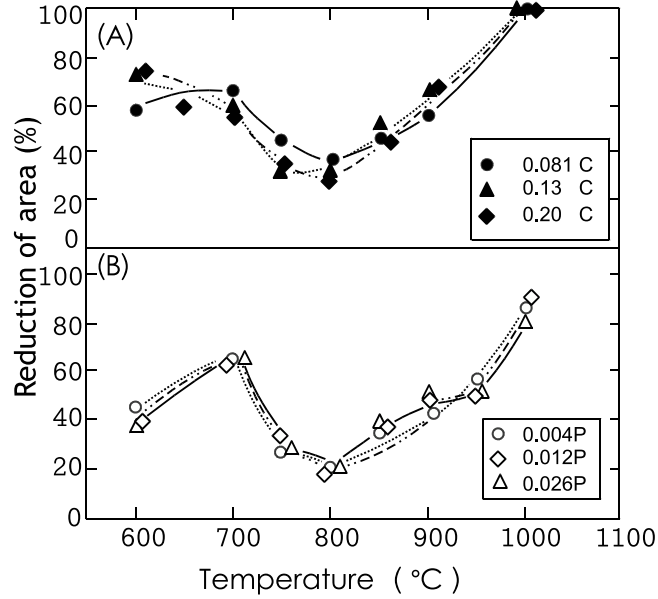


Figure 2.23: Effect of A) C and B) P on hot ductility in steel with 0.03%Nb and 0.35%Nb-0.075%V [49].

ductility to lower temperatures, due to the expected lowering of the  $A_{e3}$  [83, 105]. Further increases in C beyond 0.1%C in a high Mn Nb steel only have a small effect [83]. This is also partially due to the presence of deformation induced ferrite and partially because transformation occurs at lower temperatures with increasing carbon content, and less ferrite is formed at higher carbon contents and remains as a thin film over a wider temperature range [64]. Raising the carbon content above 0.28% also causes a change in the fracture mode, due to the increase in activation energy and hence the critical strain for DRX [105], although the influence of C on the the start of dynamic recrystallisation is reportedly very small [102] between 0.14-0.36%C. In Nb steels, raising the carbon leads to drop in ductility due to an increase in volume fraction of NbC precipitates [83], while other researchers show, Figure 2.23, that there is little influence of C on ductility in Nb steels [49]. However, the mere presence of the Nb(C,N) may have a greater influence on the hot ductility than the C thus masking the effect of C on  $A_{r3}$ . This shows that care is required in interpreting and comparing results where the C or carbon equivalent changes as well.

This is especially critical in the peritectic range. The carbon content of this range traditionally varies from 0.06-0.14%C and is associated with casting difficulties. The acute shrinkage with  $L + \delta \rightarrow \gamma$  leads to uneven shell thicknesses [16] as well as differences in the segregation behaviour of P and S [70]. At around 0.1%C the microsegregation is at a minimum, (as there is rapid solidification), and a finite gap between the mould and the steel is produced early in casting [106], leading to uneven and poor thermal extraction [16]. Poor thermal extraction and ease of large columnar grain formation in medium carbon steel significantly

accelerates surface cracking of the slabs. The C dependency of R of A (see Figure 2.24) can be much enhanced by this effect, because the effective grain size for intergranular fracture is taken as the columnar length. The higher austenite formation temperature in this C region rapidly coarsens the austenite as there is no second phase ( $\delta$  (delta) ferrite or liquid phase) to impede growth. This grain size - carbon dependency is more marked as the cooling rate approaches that of continuous casting [92]. It is thus a primary cause of hot cracking susceptibility in continuous casting [80]. When this coarsening occurs intergranular fracture is enhanced, resulting in the ductility loss inversely proportional to the austenite grain size, discussed further on page 95, and in Figure 2.40. This finding was independent of the Nb content of the steel. Thus, the large C dependency on ductility even at lower temperature region arises from the grain growth behaviour during cooling [92].

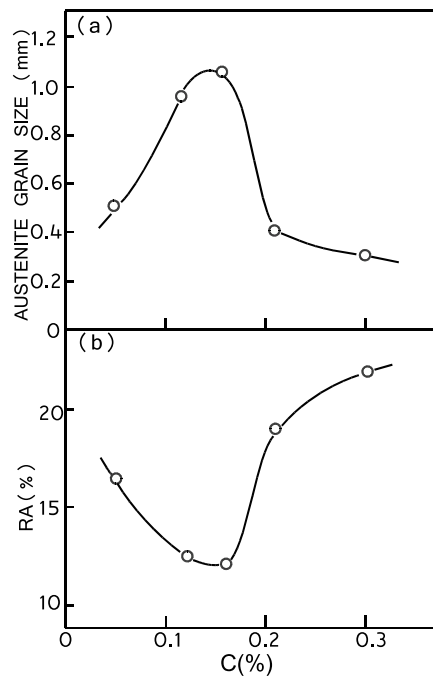


Figure 2.24: Effect of C content on a) grain size and b) calculated R of A. R of A measured at 800°C at strain rate of  $0.83 \times 10^{-3} \text{s}^{-1}$  [92].

## Manganese

With high Mn contents, for a given temperature at which DIF forms, there will be a stronger (less ductile) austenite phase as well as a greater proportion of austenite and this causes the trough to be wide at high Mn levels [55]. Also Mintz *et al.*[67] note that higher Mn contents tend to be associated with thinner ferrite films, and by implication, poorer ductility. The influence of Mn on the the start of dynamic recrystallisation of austenite is very small, [102]. The influence of Mn on the nucleation and growth of ferrite is that the Mn exerts a drag like

effect on the interface[107] so that the growth kinetics are controlled by carbon diffusion in the austenite, which is modified by interfacial segregation of Mn [107]. Mn has a retarding effect on the precipitation kinetics of both AlN and Nb(C,N) [108]. The influence of MnS is discussed below.

## Sulphur

As early as 1964, poor forgeability has been attributed to type II sulphides that are produced when a steel is ‘fine-grained with aluminium’ [109]. A number of detrimental sulphides have been described, and, until it is economically feasible to remove S completely, its effect on ductility will need to be investigated. Mintz and Abushosha [59] also warn that S has a strong effect on ductility so it is important to make compositional comparisons for cast steels at the same S content. The control of the Mn/S ratio is most important.

Increasing the Mn/S ratio improves ductility, as seen in Figure 2.25. This is partially due to the change in precipitation behaviour: at low Mn:S ratios spherical precipitation at the prior austenite grain boundaries occurs, while at higher Mn:S ratios (>60), the MnS precipitated as plates in the matrix adjacent to the austenite grain boundaries [110]. Mori [15] recom-

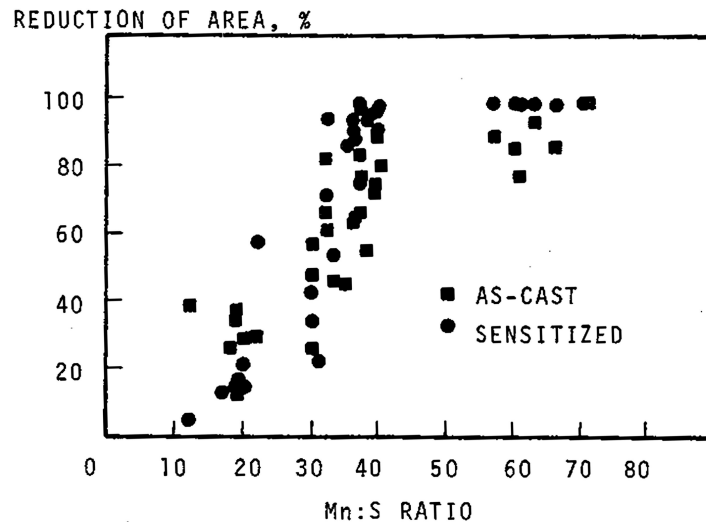


Figure 2.25: Effect of Mn/S ration on the ductility of as-cast hot tensile 0.14%C steel at 1100°C [110].

mends a Mn/S ratio of above 25 in a silicon killed steel, while industrially some authors recommend a composition limit of  $S < 30\text{ppm}$ , [32]. De Toledo *et al.*[111], demonstrated that there is a Mn/S critical ratio,  $(\text{Mn}/\text{S})_c$ , below which a high susceptibility to cracking exists:

$$(\text{Mn}/\text{S})_c = 1.345 \cdot \text{S}^{-0.7934} \quad (2.1)$$

Ductility reducing type III sulphides ( $1\mu\text{m}$ , dendritic precipitation) and type II sulphides ( $2\text{-}5\mu\text{m}$  angular MnS interdendritic precipitation) were seen on the dendrites in melted samples [43]. The shape of sulphides has also been considered critical, an appropriate calcium treatment with sulphur levels below 0.01% converts existing sulphides into a spherical shape with an improvement in the castability [16]. In fact, in C-Mn-Al steels, at the higher end of the trough where embrittlement is by grain boundary sliding, the sulphides may be encouraging void formation or preventing grain boundary movement [17]. High temperature MnS precipitation will be coarser than low temperature MnS and therefore may be more desirable from a hot ductility point of view. Higher sulphur levels can also be as detrimental to ductility as Nb. This is as a result of the precipitation of sufficiently high volume fraction of sulphides [56] so that finely spaced matrix and grain boundary precipitation of fine sulphides prevents dynamic recrystallisation and thereby reduces hot ductility in the 800-1050°C temperature range [62]. Both coarse and fine precipitation is a source of void formation during final fracture [85].

Fine precipitation of hexagonal  $\sim 100\text{nm}$  MnS in reheated samples leads to a greater proportion of intergranular fracture than in as cast material [43]. At low C and Mn contents the transformation temperatures are high, resulting in narrow troughs and the speedy transformation of austenite to deformation induced ferrite. This dominates over the influence of the detrimental sulphides. In the presence of oxygen, oxysulphides form, lowering the solidus temperature of Mn(O)S below 1150°C and thus it can precipitate as a liquid [110]. This embrittling mechanism may be quite difficult to determine in laboratory tests as the fracture surface experiences oxidation at fracture. S is more detrimental to ductility at higher strain rates ( $0.01\text{-}2.3\text{s}^{-1}$ ) when the Mn/S ratio is too low, precipitation of Fe rich (Fe,Mn)S within the grains and at the grain boundaries, causes strain localisation in the precipitate free zone adjacent to the boundaries occurs [60].

Generally the aim of alloying with Mn to form MnS has conventionally been the avoidance of grain boundary FeS which has a low melting point, but S is also detrimental as a segregant on its own, as discussed in the following section.

Heritier *et al.*[78] shows that in low carbon (0.02%) steels containing no S, no loss in ductility occurs between 1000-800°C, Figure 2.26. In both Nb [112] and Al [113] steels the ductility loss is greatly reduced at low S levels. Sulphur encourages decohesion at the precipitates by segregating to the austenite grain boundaries and precipitate - austenite interfaces[112]. At high cooling rates segregation at the boundaries is higher than the equilibrium amount. This occurs when a material is cooled from a higher temperature so that there are excess vacancies. This results in the combination of vacancies and the impurity atoms, which, at the grain boundary dissociate; the vacancies being annihilated at the boundary and

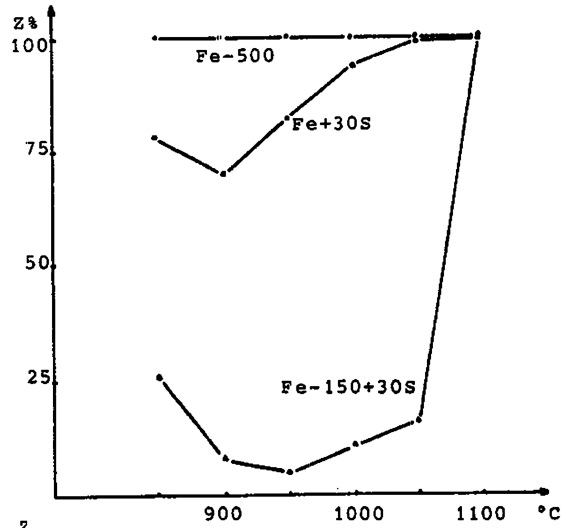
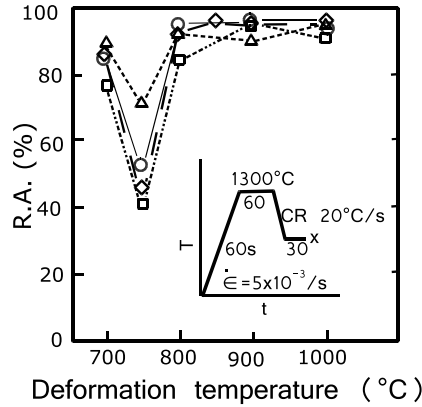


Figure 2.26: Variation of reduction in area at fracture with temperature. Fe-500: 190ppmC, 514ppmAl, 120ppmN, <5ppmS; Fe+30S: 220ppmC, <25ppmAl, <10ppm N, 35ppmS; Fe-150+30S: 180ppmC, 156ppmAl, 80ppmAl, 32ppmS [78].

the impurity is segregated there [114]. The influence of S at lower Mn (0.15%) becomes more complex as S itself can be responsible for embrittling the austenite grain boundaries, however this only occurs at high cooling rates ( $30^{\circ}\text{C}\text{s}^{-1}$ ) and the ductility recovers when MnS precipitation takes place [115]. While this cooling rate is extremely unlikely in casting, it may be interesting to study the effect of sulphur during grain boundary motion, although this may not be practically possible.

## Phosphorous

Phosphorous, in the presence of Si is an attractive addition for producing the retained austenite in the TRIP steels[116]. The majority of researchers report on the beneficial addition of phosphorous [63, 65, 79], although a few researchers report that it has no effect, Figure 2.23 [49]. Mintz and Arrowsmith [65] suggest that raising the P levels improves hot ductility by preventing Nb(C,N) precipitation at grain boundaries, and this has been confirmed in later work[72]. Suzuki [79] showed that phosphorous promoted polygonal ferrite and subsequently improved ductility, as seen in Figure 2.27. All of these researchers used reheat practice and therefore the segregation may be different from industrial practice especially at the low carbon contents. Industrially, it has been shown that reducing the P levels causes the number of plate rejections to increase [54] and Hannerz [63] confirms that high P contents do reduce the incidence of transverse cracking. Yet in later work Mintz *et al.*[117] showed that high levels of P (0.04-0.05%) gave the worst ductility. This is because of the phosphides at the grain boundaries being more pronounced at the higher P level. An



	C	Si	Mn	P	S	N
◇	0.05	0.02	1.46	0.003	0.005	0.0014
□	0.059	”	1.51	0.039	0.004	—
○	0.049	0.021	1.48	0.11	0.005	—
△	”	”	”	0.32	”	—

Figure 2.27: Effect of P on hot ductility in low carbon steels without Nb/V [79].

improved study of the influence of P may be necessary to unequivocally reveal its character.

## Niobium

Nb is exceptionally detrimental to hot ductility [59, 62, 63, 65, 79, 83, 93, 112, 118, 119, 120], as well as encouraging industrial transverse cracking [63]. The reasons are multiple; Nb reduces dislocation mobility (both as solute and precipitate) which in turn affects grain boundary migration (and thus DRX, GBS), as well as giving rise to mvc and matrix strengthening.

Prior to precipitation, solute Nb slows the mobility of dislocations by ‘solute drag’, and then as fine semi/coherent precipitation pins dislocations in the matrix and at a migrating boundary [121]. Dislocations also encourage the precipitation of Nb(C,N) [119], which results in precipitation at earlier times and at higher temperatures than would be expected for the kinetics of Nb precipitation in unstrained material. Dynamic precipitation of Nb(C,N) is observed to occur at strain rates of  $10^{-3} - 10^{-4} \text{s}^{-1}$  [65, 112, 119]. The result is the reduction of grain boundary mobility, leading to grain boundary sliding with mvc and fracture [65, 112]. On the other hand, the addition of Mn is seen to retard dynamic precipitation of Nb(C,N), due to a decrease in solubility temperature of Nb(C,N) from the reduction in the carbon and nitrogen activities [120]. The result is a narrower deeper trough as precipitation occurs at lower temperatures. Nb is known to have a strong delaying action on DRX [102]. It acts in two ways, the first is as a solute, and the second is during precipitation of fine carbonitrides (below 6nm) [62, 104]. By implication, coarsening of Nb(C,N) reduces its effect on DRX.

Of all the microalloying additions, Nb gives finest precipitation at unbending temperatures [118]. The onset of Nb(C,N) precipitation can supersede the  $Ar_3$  temperature at the upper limit of the trough [83], leading to a deepening and widening of the ductility trough [88, 61, 122]. At the lower temperature end of the trough, in the  $\alpha + \gamma$  region the Nb content has less influence on the depth of the trough, since increasing the ferrite film thickness on the  $\gamma$  grain boundaries improves ductility, Figure 2.16 [49] but Nb has a major effect in decreasing the  $Ar_3$  thus widening the trough [56]. Elsewhere in the ductility curve the ductility decreases with increasing Nb content. Note that the tests in these references were done from reheating and not from melting. Reheating is generally regarded as acceptable for non-Ti containing steels. Nb is reported to precipitate as  $NbC_{0.85}$  when the N content is

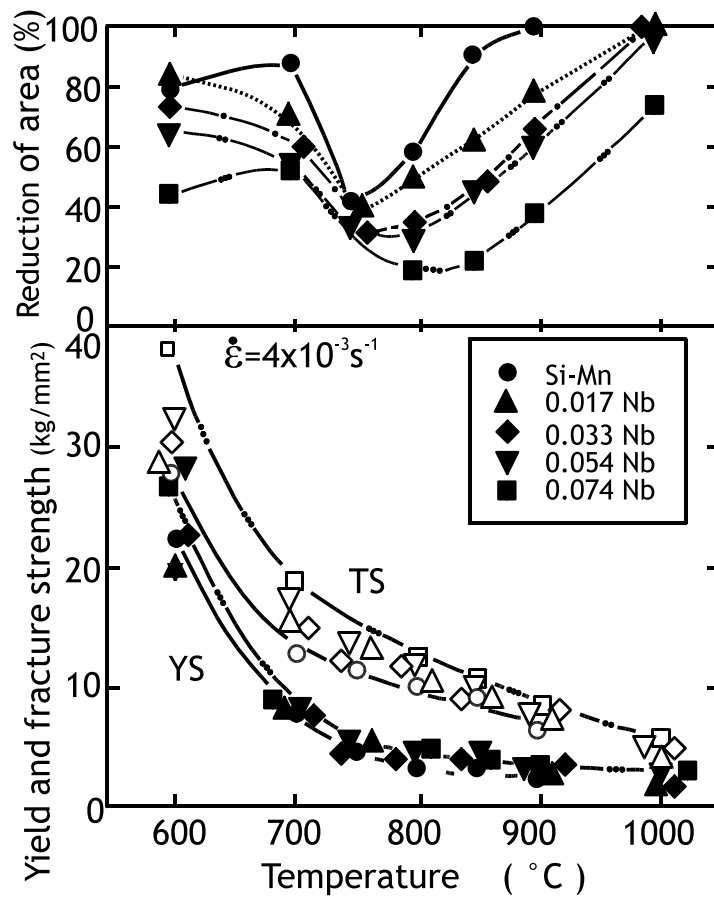


Figure 2.28: Effect of Nb content and deformation temperature on hot ductility and strength [49].

around 0.0020%, while  $NbC_{0.60}N_{0.25}$  is formed in steels where the N content is higher than 0.0050% [49]. These compositions of the Nb precipitates may cause different precipitation kinetics in the  $\gamma$ , that is,  $NbC_{0.60}N_{0.25}$  may precipitate more easily than the  $NbC_{0.85}$  in the lower temperature region of the  $\gamma$ . Unfortunately they do not detail how they determined the difference between the two precipitates, and considering that they are expected [123] to

be a continuous solid solution<sup>3</sup> it is surprising that such an issue is made of differentiating the two. In fact, sometimes the Nb(C,N) precipitation acts synergistically. For example with increasing C levels the trough deepens due to and increase in NbC volume fraction [83]. Alternatively, V additions can improve the behaviour of a Nb containing (0.03Nb) steel, by slowing the precipitation of carbonitrides during testing [61].

The Nb(C,N)<sub>x</sub> is a face centred cubic precipitate with NaCl structure, and is considered to be two interpenetrating crystals, one of Nb (or Nb atom vacancies) and one of C, N (with C/N atom vacancies). The lattice parameter is strongly a function of the vacancy concentration (*x*), and varies between 0.4470nm and 0.443nm as *x* varies from 1 to 0.7. The solubility product of Nb(C,N) is substantially lowered as the compound becomes enriched in N or the vacancy content reduces [123].

There is a second type of niobium precipitate that is reported to occur in steels when there is a high Nb/C ratio (Nb levels greater than 0.04%). It is an Nb<sub>2</sub>C with a hexagonal close packed crystal structure with lattice parameters a=0.312nm and c=0.495nm [123].

Eutectic NbC is reported to appear a characteristic yellow. 20-70μm eutectic NbC decorates primary grain boundaries along with AlN. NbC eutectic is formed irrespective of the initial Nb content or the cooling rate. The amount of eutectic increases with increasing carbon content. This eutectic precipitate does not dissolve at reheating temperatures or even in the heat affected zone (HAZ) of welds [124].

Nb is not always detrimental, as Nb in the presence of Mn is reported to reduce the formation of columnar grains in the mould, and to encourage equiaxed grains [124]. This would presumably be beneficial to casting as it would reduce grain size and improve the strength of the shell.

In general, niobium – so desirable for its contributions to room temperature strength – has a detrimental influence on the hot ductility.

## **Aluminium**

Both MnS and AlN have a marked influence in deteriorating ductility as they can precipitate preferentially at the austenite grain boundaries during cooling. They are the most detrimental grain boundary precipitation in C-Mn-Nb-Al steels at the time of fracture as cavities nucleate primarily at these particles [125]. Increasing soluble Al levels to 0.07% in Nb steels,

---

<sup>3</sup>see Table 2.4 page 88

leads to an extension of the hot ductility trough to higher temperatures[54], effectively because the  $[Al][N]$  product increases [118] as seen in Figure 2.29 [91]. It is the combination

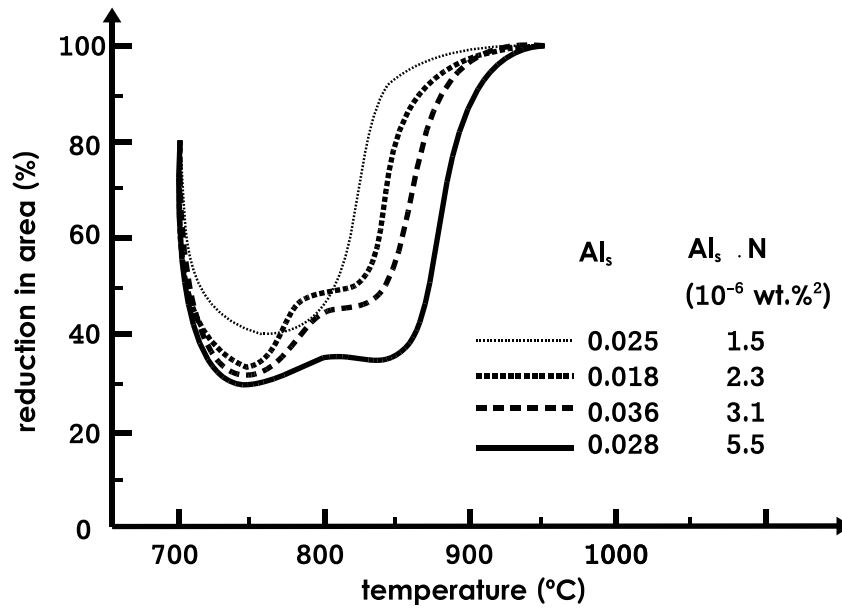


Figure 2.29: Hot ductility curves at various Al and N contents [91] (samples reheated).

of Al and N (ie the AlN precipitation) that is detrimental to transverse cracking and hot ductility, by precipitating on the austenite grain boundaries or reducing grain boundary mobility and nucleating grain boundary voids resulting in intergranular failure [63]. This set of ductility curves, Figure 2.29, also shows the step in ductility when the AlN precipitation alone is reducing ductility (800-900°C), and when the ferrite films are influencing the ductility. The more AlN precipitation present, the wider the trough becomes.

Generally AlN precipitates out with difficulty in the simple hot tensile test, giving good ductility [17], unless the product of  $[Al] \times [N]$  is high, but when it does precipitate, it is very detrimental to ductility [126]. For instance in C-Mn-Al steels sufficient intergranular precipitation (presumably of AlN), to cause poor hot ductility, is only formed after a 15min delay before testing [101]. Others [91] show that, without deformation, temperatures must remain in the lower austenite region for long times (900°C for 2hrs) for detrimental AlN precipitation to occur. Prior thermal history is thus more important in the hot ductility behaviour of C-Mn-Al steels in comparison to C-Mn-Nb steel.

AlN precipitation can also be induced by straining [127]. Grain boundary precipitation of AlN (1 $\mu$ m plate) was observed after straining in addition to the matrix precipitation by Chamont *et al.*[91] in steels with 0.02-0.03%Al. AlN precipitation can be deformation induced and when this occurs, it may not be observed anywhere else than the fracture surface, which can be very difficult to detect [21]. Importantly, Chamont *et al.*[91] show

Table 2.1: Lattice parameter for various forms of AlN.

lattice	a(nm)	c(nm)	c/a	Space group	description	reference
cubic	0.405- 0.417	-	-	not reported	cubic	Wever in [14]
cubic	0.4051	-	-	not reported		Kretschner in [14]
fcc	not reported	- -	- -	not reported	fcc	Engl in [14]
fcc	0.408	-	-	not reported	fcc/ NaCl cubic	Hanai in [133]
fcc	0.405	-	-	not reported	fcc	Choi1978
NaCl cubic	0.407	-	-	not reported	Cubic NaCl (fcc)	Hanai in [14]
hcp	0.31- 0.312	0.498- 0.499	1.5	P6 <sub>3</sub> mc P6 <sub>3</sub> mc	wurtzite, B4	Various in [14]

that at  $[Al][N]$  products of  $> 1.5 - 2.3 \times 10^{-4} \text{wt}\%^2$ , the AlN precipitated at the fracture surface effectively deepens (by  $\sim 10\%$  R of A) and widens the ductility trough. While Crowther *et al.*[119] have shown that static precipitation of AlN occurs after two minutes at temperature (this was a reheated test procedure with strain rates of  $3 \times 10^{-3} \text{s}^{-1}$ ), they report that dynamic precipitation of AlN has been seen before at higher solubility products. AlN precipitation occurs preferentially on dislocation loops formed from deformation rather than grain boundary sites in  $\alpha$  ferrite [128]. This may also be valid for precipitation in the  $\delta$  ferrite if the AlN is stable at those temperatures.

In the extreme case, if the Al and N content is high enough, it precipitates in the interdendritic liquid [34]. In fact in liquid steel with very low oxygen activity, AlN inclusions can exist in the liquid steel (1.2%Al,33ppm N) [129]. In a study of the role of AlN in restraining grain growth during reheating, Hall and Bennett [130] observed that grain growth is retarded somewhat below the AlN solubility temperature in high aluminium - high nitrogen steels, since the precipitates coarsen at high temperatures. The Al will be the rate determining element in the growth of AlN precipitates. Thus very high Al contents may be more beneficial than intermediate or low levels as precipitate coarsening will be faster at the higher solubility temperature. The addition of Al to TRIP steel has been observed to shift the austenite area of the constitutive phase diagram to the right [131].

AlN precipitation occurs in more than one crystallographic form: cubic, face centered cubic (fcc), NaCl cubic and hexagonal close packed (hcp) as well as more than one size range in steel as shown in Table 2.1 [14, 132]. Their morphology can vary from dendritic, large

plate, rod, needle, rectangular/cuboidal or prismatic. This is a function of alloy content, strain and thermal path [14]. AlN has also been found to provide sites for growth of other carbonitrides [34, 134]. This is partially a function of its morphology, as will now be discussed.

**Cubic** In compact strip production of low C steel AlN precipitates below 950°C in <8nm cubic form [132]. Hasebe [135] observed fine (globular or cubic) AlN precipitates at 700°C along austenite grain boundaries.

**Dendritic** During solidification in medium carbon (0.3wt%C) steels, the dendritic type precipitates first in the interdendritic residual liquid steel at a late stage in solidification. Since the last solidifying steel is between grains these precipitates end up being intergranular [31]. They also act as nucleating sites for subsequent solid state precipitation of AlN on the grain boundary. Wright and Quarrell [136] have also observed these precipitates, Figure 2.30a in high N (140ppm) steel castings. Each dendrite arm is thin enough to be electron transparent [136], thus a maximum of ~200nm thick, although others [14] say <10nm thick. The lattice spacing of these hexagonal close packed precipitates was slightly larger (a=0.328nm, c=0.504nm) [136] than that reported in previous literature for AlN (a=0.311nm, c=0.498nm) [14]. In cross section these precipitates occur on the grain boundary but their orientation is often perpendicular to the boundary, Figure 2.30b [136].

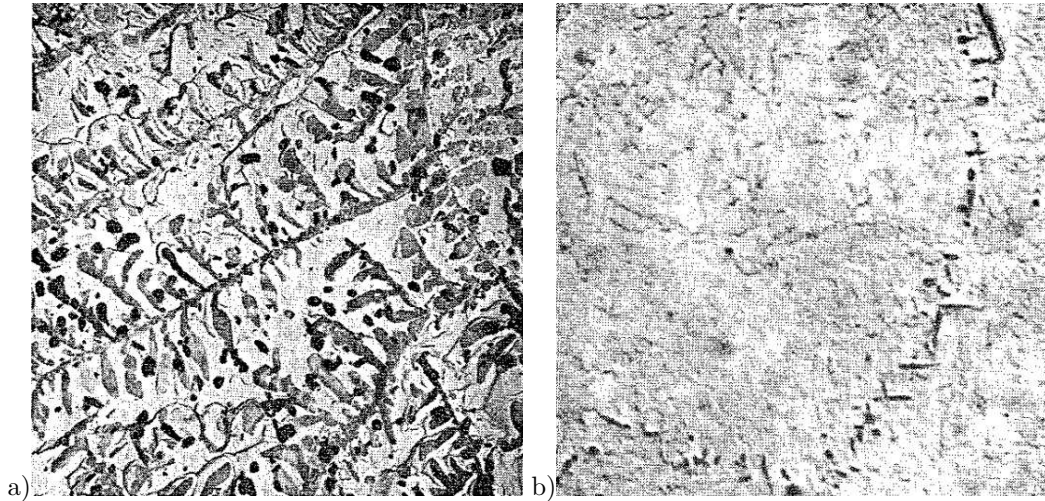


Figure 2.30: Dendritic AlN in a) TEM replica and b) cross sectional optical microscopy (OM) [136].

**Plate** After solidification, in the solid state, plate like precipitates grow into the austenite with a specific relationship [31]:

$$\{0001\}_{\text{AlN}} \parallel \{111\}_{\gamma}. \quad (2.2)$$

This precipitate has a closer lattice spacing ( $a=0.316\text{nm}$   $c=0.474\text{nm}$ ) to the standard AlN values than the dendritic AlN [136]. Others also find plate like precipitation after slow cooling with high AlN products [14, 31, 91, 137]. This type of hexagonal plate precipitate has also been called prismatic AlN according by Wilson and Gladman [14]. It is uncertain whether plate and the dendritic type are differentiated from each other in all studies, but they are most often associated with ‘rock candy’ fracture. Plate type AlN is reported in Al TRIP steels, (0.22%C, 1.51%Mn, 0.41%Si, 0.87%Al, 0.0022%N, steel 5 [11]).

**Rod/needle.** Hasebe [135] found that coarser needle precipitation occurs at 1000°C. Su *et al.*[11], observed needle type AlN in TRIP steels plate (0.22%C, 1.51%Mn, 0.41%Si, 0.87%Al, 0.0022%N steel 5).

In the case of solidification of castings, in medium carbon (0.3wt%C) steels, AlN precipitates into different forms depending on when it precipitates during solidification. When a combination of dendritic and plate precipitates cause intergranular fracture in the  $\alpha + \gamma$  region, the surface shows a fine dendritic appearance with larger crystallographically orientated plate-like features superimposed on it [31]. Whilst AlN precipitation after slow cooling below 1150°C is associated with intergranular fracture (rock-candy), if the [Al][N] product is high (0.865%Al - 220ppmN vs 0.37%Al - 165ppmN), the precipitation is no longer along the grain boundary, Figure 2.31a, but presents as large dark grey angular particles in the matrix, Figure 2.31b [46]. Woodfine and Quarrell[46] described these as needles, but further investigation by Wright and Quarrell [136], showed these to be dendritic or plate like. It is presumed that sectioning precipitation eliminates one dimension, leaving Woodfine and Quarrell to erroneously describe the AlN precipitation as needle-like. Leger and Guillaume [138] also found needle like more or less directionally orientated AlN which, at higher magnifications, are pseudocleavage facets. It is possible that they also dendritic AlN precipitation.

Choi *et al.*[133] have extensively characterised AlN precipitation in an ultra low C steel (0.005C, 0.082-0.01Al, 0.011-0.016N). Cubic AlN forms at the initial stages of precipitation, as spherical particles, which is also seen by Kanget *al.*[132], this is later transformed to rod-like hexagonal close packed AlN (occasionally polygonal) [133]. While Hasebe [135] showed that in a 0.2%C, 0.29%Si, 1.36%Mn, 0.05%Al and 0.05%N steel that coarser needle precipitation occurs at 1000°C, while fine (globular or cubic) AlN precipitates at 700°C. Both types precipitate preferentially along austenite grain boundaries.

AlN precipitation can thus be rather complex and this is a function of the thermal path, strain and carbon levels.

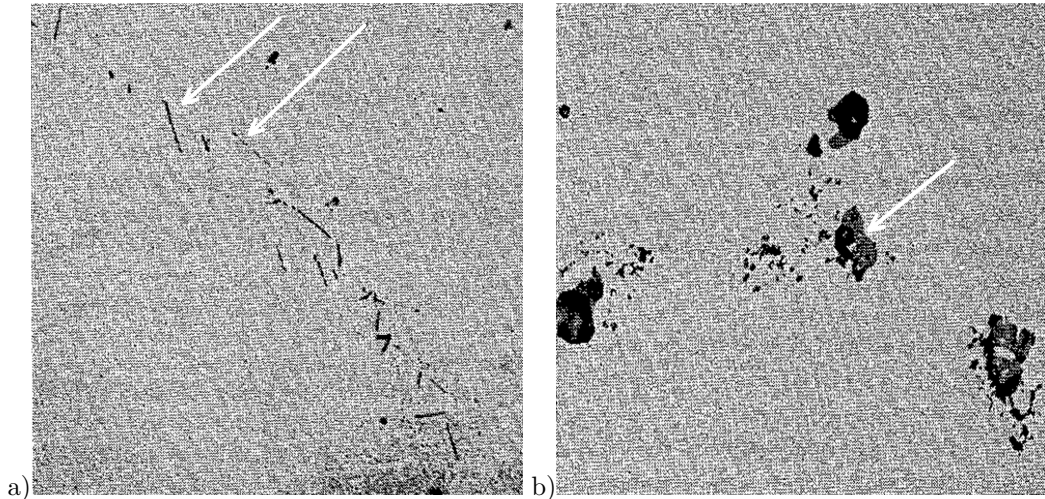


Figure 2.31: Grain boundary precipitation in a) 0.37Al-165ppmN steel and plate AlN in b) 0.865Al-220ppmN steel [46], presumed to be the features indicated by arrows.

There can also be an inter-relationship between Al and other elements. For instance Michel and Jonas [108] show that Mn has a retarding effect on the precipitation kinetics of AlN. Mintz and Arrowsmith [54], show that at the temperature range 825-875°C in a 0.16%C, 1.3%Mn, 0.2-0.5%Si, Nb steel, increasing the P level improves hot ductility at the lower soluble Al levels, but appears to have little influence when the soluble Al exceeds 0.04%. This is attributed to distribution and size of the Nb(C,N) precipitation which forms coarse, widely dispersed precipitates when the soluble Al is low (less than 0.04%) and the P high [54].

Interestingly, Heritier *et al.*[78] isolated the role of AlN in decreasing hot ductility. AlN has no influence on ductility in ultra high purity low carbon (0.02%C) steels, but in normal steel it pins the grain boundaries so that S can segregate and embrittlement can take place. This only happens at the lowest S level, as Coleman and Wilcox [125] found that reducing the sulphur is not effective as S still segregates strongly and MnS and AlN still act as primary cavities nucleation point. Mintz and Arrowsmith [65], showed that raising Al levels (from 0.01 to 0.07%sol.Al) also reduces the R of A values in the Nb containing steels. By adding soluble Al, more closely spaced Nb(C,N) results, which pins the boundaries more effectively, resulting in cavitation/mvc [54]. This has also been observed in industrial casting by Irving *et al.*[27]. However, Bannenberg *et al.*[74], observe that Nb(C,N) precipitation is ineffective in causing embrittlement at high [Al][N] products ( $[Al][N] > 1 \times 10^{-4} \text{wt}\%^2$ ) where the AlN precipitates before Nb(C,N) and is the cause of the trough widening (ie. increases  $T_{AV}$  in Figure 2.12). AlN and Nb(C,N) have been found to co-precipitate, with the Nb(C,N) forming a cap on the AlN needles. The crystallographic relationship between the Nb(C,N)

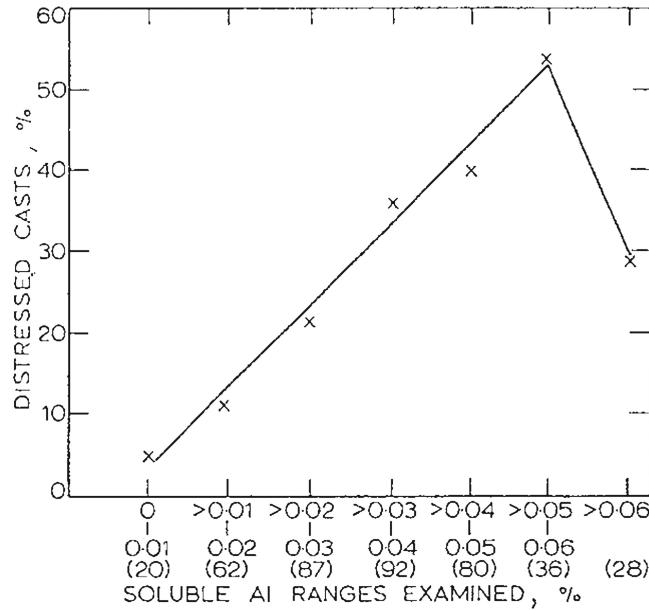


Figure 2.32: Percentage of distressed casts (casts with one or more rejected plates) as a function of sol. Al content: numbers in brackets refer to total number of casts (distressed and problem free) in each composition interval [54].

and AlN is:

$$\frac{(\bar{3}11)_{\text{Nb(C,N)}}}{(\bar{2}21)_{\text{AlN}}}$$

$$\frac{[112]_{\text{Nb(C,N)}}}{[112]_{\text{AlN}}}$$

The surface trace analysis shows a  $\{100\}$  habit plane for the Nb(C,N) and a nominally  $\{124\}$  habit plane for AlN at the Nb(C,N)-AlN interface, indicating that heterogenous nucleation of Nb(C,N) on AlN occurred. The coarsening of the AlN was observed to be inhibited by the Nb(C,N) at precipitate sizes above 50nm at temperatures between 930-1010°C. Above 1010°C the Nb(C,N) dissolved and ripening occurred [139]. This coarse duplex type of precipitate is not expected to reduce grain boundary motion in the hot ductility trough.

*Al industrial.* Industrially it has been shown that regarding the soluble Al, rejection levels reach a maximum with 0.05-0.06%Al with 50-70ppmN, Figure 2.32 [54]. In Al treated steels, increasing nitrogen increases the transverse cracking incidence [63]. While the amount of AlN available for precipitation is a function of the product of the Al and N contents of the steel, in normal de-oxidation practice in an Al killed steel, Al is added in stoichiometric excess to nitrogen. This is so as to have AlN particles available to refine grain size on normalising. However, reduction of N is the parameter of choice in reducing the susceptibility of a steel to intergranular fracture [30]. Thus some authors limit N to <40ppm and the [Al][N] product to below 10000ppm<sup>2</sup> or  $[\text{Al}][\text{N}] < 1 \times 10^{-4} \text{wt}\% ^2$ , although this was in the presence of Ti [32]. The precipitation of fine AlN on the grain boundaries is exacerbated by segregation during

the solidification and thermal cycling that occurs during strand cooling in continuous casting [118]. Temperature cycling has been shown to encourage precipitation, and it is possible that the temperature oscillations which occur when the strand enters and leaves the guide rolls during continuous casting favours AlN precipitation [126]. When Al shows ductility impoverishment in testing, industrial expectations must be lowered.

### The effect of other elements on hot ductility

Si has little influence on the start of dynamic recrystallisation [102], but its effect on the peritectic point is significant [140, 106] where it moves the peritectic point to lower carbon contents [140]. It suppresses Fe<sub>3</sub>C carbide formation[9], and promotes Nb(C,N) precipitation[141].

Lui *et al.*[142] characterized copper sulphide precipitation (both thermodynamics and kinetics) and showed that while MnS precipitates in the high austenite, Cu<sub>2</sub>S is favored in the lower austenite and in the ferrite. Also when samples were tested in air to simulate continuous casting conditions more precisely, a deterioration of ductility was found, which is caused by formation of fine copper sulphides rather than a film of Cu-rich phase at the boundary [143].

### Transformation induced plasticity steels

The TRIP steels have such high Al that it puts them ‘in another league’ of precipitation behaviour, thus they are worth discussing on their own with respect to alloying elements. The influence of very high Al levels on ductility has been observed before in samples melted in situ. The ductility in the 2%Al steel is good throughout the temperature region, but at the 1%Al level the ductility is poor especially at 750-850°C. Table 2.2 shows the compositions and the ductility curves are in Figure 2.33. The good ductility in the 2%Al steel is attributed

Table 2.2: Composition (wt%) of Al TRIP steels from Mintz *et al.*[10].

Steel	C	Si	Mn	P	S	Al	N	Ae <sub>3</sub>
Mintz 1 ref[10]	0.15	0.29	1.45	0.003	0.008	0.017	0.006	820°C
Mintz 2 ref[10]	0.16	1.22	1.41	0.009	0.005	0.02	0.0032	none
Mintz 3 ref[10]	0.22	0.02	1.45	0.009	0.005	1.93	0.0034	none
Mintz 4 ref[10]	0.21	0.61	1.41	0.01	0.004	0.98	0.0042	978

to a large volume fraction of coarse 1-2µm AlN precipitates and the formation of large amounts of ferrite at all temperatures. The 1%Al steel is also expected to have coarse AlN,

but the ferrite is present as thin films at 800°C. In both cases this ferrite is expected to be deformation induced as it occurs above the  $Ar_3$ . A particular difficulty of casting a 2%Al

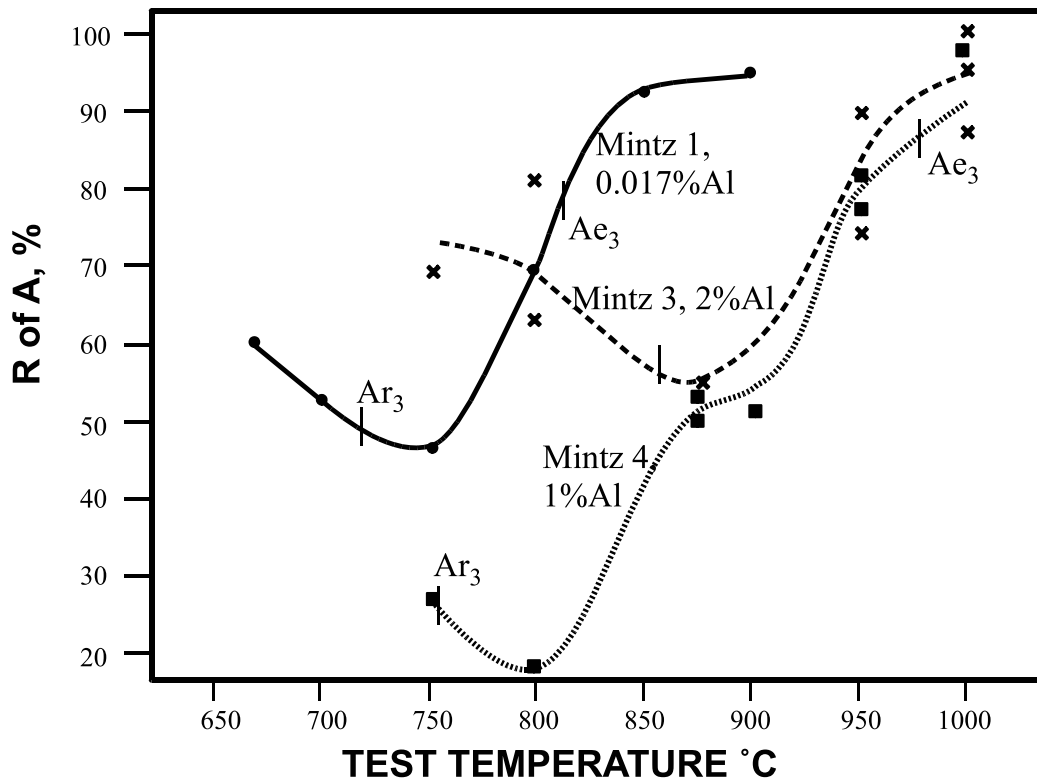


Figure 2.33: Influence of aluminium on hot ductility of C-Mn-Al steels [10]. Samples were melted.

steel is the potential for submerged entry nozzle blocking at such high Al contents. The influence of Si was examined but the largest influence Si had is in raising of the  $Ae_3$  which extended the ductility trough to higher temperatures ( $>850^\circ\text{C}$ ). Al also increases the  $Ae_3$  and in the case of 1%Al the ferrite remains thin for an extended range, leading to very poor ductility [10].

In another TRIP study, Su *et al.*[11] also showed that Al additions widen the trough, and has a disproportional effect on the depth of the ductility curve: At low 0.03%Al levels (Su 1[11] and Su 6[11], Figure 2.34) a narrow trough is seen, but at Al levels of 0.41%, the trough is both wide and deep (Su 4[11], Figure 2.34), but at higher levels (0.87%Al) the ductility is improved, but the trough is at its widest (Steel 5[11] compared with steels Mintz 3[10], Mintz 4[10] of Mintz *et al.*[10], Figure 2.34). *In-situ* melting was used in their experimental work.

In all the steels containing  $<0.87\%$ Al fine films of ferrite are seen at poor ductility. While the Su *et al.* study shows that 1%Al levels are less detrimental for ductility, the previous study (Mintz *et al.*) seems to indicate the opposite, (Compare 'Mintz 4/steel 7' with 'Su

Table 2.3: Composition (wt%) of steels from Su *et al.*[11].

Steel	C	Mn	Si	P	S	Al	N	Ae <sub>3</sub> (°C)	Ar <sub>3</sub> (°C)
Su 1 ref[11]	0.20	1.50	0.39	0.077	0.001	0.03	0.0012	842	
Su 2 ref[11]	0.21	1.49	0.39	0.078	0.001	0.21	0.0018	884	
Su 3 ref[11]	0.22	1.53	0.40	0.081	0.001	0.43	0.0024	990	1025
Su 4 ref[11]	0.20	1.49	0.25	0.110	0.001	0.41	0.0034	979	
Su 5 ref[11]	0.22	1.51	0.41	0.077	0.001	0.87	0.0022	1190	750

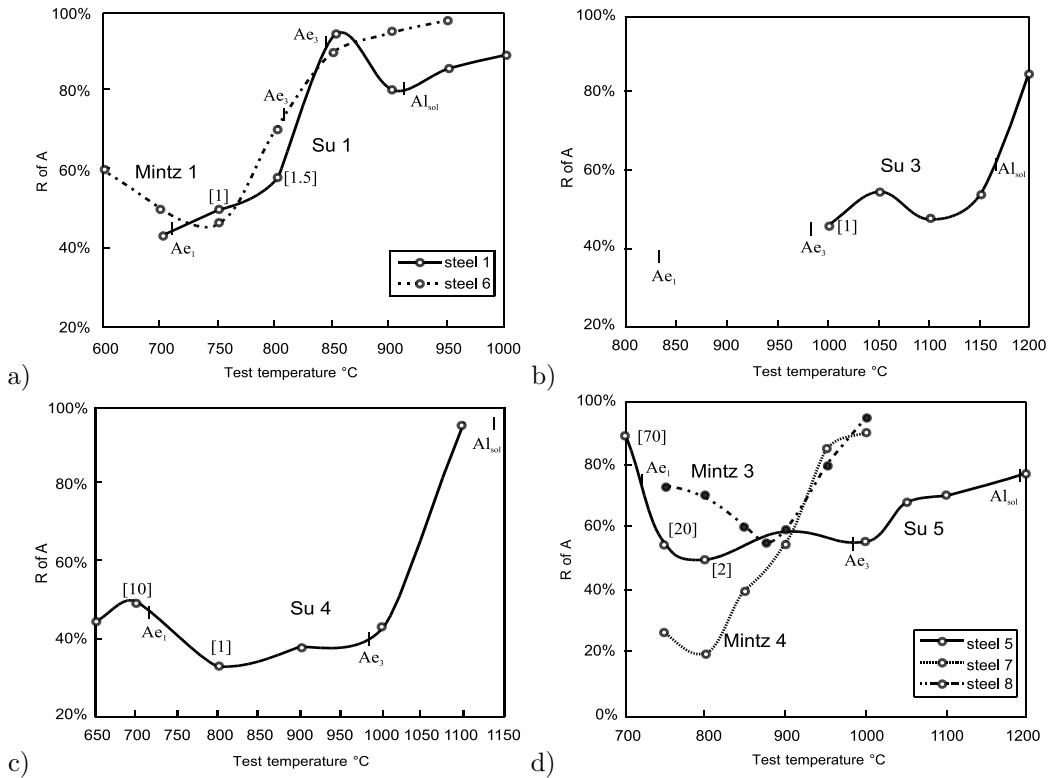


Figure 2.34: Hot ductility curves for a) Su 1[11] and Su 6[11]; b) Su 3[11]; c) Su 4[11]; d) Su 5[11] and Su 7[11] (Su7=Mintz 4[10]) and steel Su 8[11] (Su8=Mintz 3[10]).

5/steel 5' of Figure 2.34d, which have 0.98 and 0.87 %Al respectively). While it may appear that the low P steels at this Al level have poorer ductilities [11] the S and N levels are higher (Tables 2.2, 2.3) which may increase the volume fraction of second phase particles. While this study does show the importance of reducing residuals in these steels, this may not be commercially feasible [11].

In the 0.87%Al steel the AlN precipitation is not found in sizes smaller than 50nm and is thus unlikely to contribute to poor ductility. While it would seem to be a fair assumption that AlN precipitation is controlling the ductility at the higher end of the trough, the TEM examination seems to refute this cause. In fact the Al addition raises the  $Ae_3$  and the ferrite encourages AlN precipitation in amounts close to equilibrium. Remarkably, the researchers show the presence of ferrite above the  $Ae_3$ , possibly due to segregation of Al to the boundaries, although its volume fraction is high [11]. Nevertheless this indicates that the normal equations (in this case Thermo-Calc [11]) may have difficulties in predicting the extent of AlN precipitation at such high Al levels.

When deformation induced ferrite forms rapidly below the  $Ae_3$ , it leads to narrow trough behaviour. If this does not occur then the trough becomes wide, spreading to the  $Ae_3$ [11]. The conditions that lead to the ferrite formation is an important industrial question [11]. In the TRIP steels with high Al, it is possible to have wide troughs as the  $Ae_3$  is very high, but ferrite is discouraged from forming and retained austenite is encouraged by a combination of high C and Si or Al.

#### **2.4.2 Aluminium nitride, niobium carbo-nitride and manganese sulphide solubility equations**

This section tabulates (Table 2.4) the thermodynamic behaviour of AlN, Nb(C,N), MnS.

On the whole most authors [34, 149, 154, 159, 160] use Leslie's equation [144] for AlN. Cheng *et al.*[161] modeled the precipitation of AlN in Al killed low carbon steels but since they considered low Al levels, the Al-N interaction is ignored. Sharma *et al.*[141] established a set of interaction parameters for predicting austenite and carbonitride equilibria as a function of alloy composition (Mn, Si, Cr and Ni) for temperatures between 900-1300°C. Since they do not include Al, the predictions are less relevant for the present work.

Table 2.4: Solubilities,  $K_s$ , of MnS, AlN and Nb(C,N).  $K_s$  is the solubility product( $[M][X]$ ) in various phases of solid steel, and  $T$  is the temperature in Kelvin.

Compound	$K_s$	Ref	Comments
[Mn][S]	$-\frac{9020}{T} + 2.929$	[146]	For Fe-Mn solutions with Mn>0.3%. Data used by Lui <i>et al.</i> [147] for precipitation model.
[Al][N]	$-\frac{7400}{T} + 1.95$	[148]	Data obtained using extended periods of time at solution temperature (equilibrium and homogenization was complete).
[Al][N]	$-\frac{6770}{T} + 1.033$	[144]	Data with limited solution used time to give an ‘apparent solubility’. It is more applicable to Al in the range of 0.023-0.15%Al [149] and to commercial grade steel at temperatures between 900-1350°C and can be used to represent AlN in austenite [34]
[Al][N]	$-\frac{11900}{T} + 3.56$	[150]	AlN in ferrite in 3%Si steel
[Al][N]	$-\frac{9800}{T} + 2.71$	[34]	From [150] for low alloy steel
[Al][N]	$-\frac{8790}{T} + 2.05$	[34]	
[Al][N]	$-\frac{12950}{T} + 5.58$	[151]	
[Al][N]	$-\frac{18420}{T} + 6.40$	[152]	
[Al][N]	$-\frac{6180}{T} + 0.725$	[153]	
[Al][N]	$-\frac{7400}{T} + 1.95$	[153]	
[Al][N]	$-\frac{7750}{T} + 1.8$	[153]	
[Al][N]	$-\frac{7500}{T} + 1.48$	[153]	
[Al][N]	$-\frac{890}{T} + 4.45$	[152]	
[Nb][C + $\frac{12}{14}$ N]	$-\frac{6770}{T} + 2.26$	[149]	at 900-1200°C, also used by [154]
[Nb][C] <sup>0.7</sup> [N] <sup>0.2</sup>	$-\frac{9454}{T} + 4.12$	[34]	for austenite from [155].
[Nb][C] <sup>0.7</sup> [N] <sup>0.2</sup>	$-\frac{12120}{T} + 5.57$	[34]	for ferrite from [155].
[Nb][C + $\frac{12}{14}$ N]	$-\frac{7520}{T} + 3.11 \pm 0.1$	[156]	for austenite
[Nb][N] <sup>0.65</sup> [C] <sup>0.24</sup>	$-\frac{10400}{T} + 4.09$	[157]	in a steel with 0.02%N, 0.2%Nb and 0.008%C
[Nb][C + 12/14N]	$-\frac{8800}{T} + 3.97$	[158]	

### 2.4.3 Phase stabilities: liquidus and solidus, the peritectic reaction and the $Ae_3$

#### Liquidus and solidus

The equation from Thomas *et al.*[162] for the liquidus is:

$$T_{liq} = 1537 - 88[C] - 8[Si] - 5[Mn] - 30[P] - 25[S] - 5[Cu] - 2[Mo] - 4[Ni] - 1.5[Cr] - 2[V] - 18[Ti] \quad (2.3)$$

and for solidus is:

$$T_{sol} = 1535 - 200[C] - 12[Si] - 7[Mn] - 125[P] - 184[S] - 4[Al] - 4[Ni] - 1.4[Cr] \quad (2.4)$$

These equations were developed [162] empirically from other literature, however, the chemistry ranges for the regression were not given.

#### Peritectic reactions

The peritectic reaction is a result of the change in phase at the peritectic point and can be predicted as a function of temperature and carbon content [163]. The conventional constitutional diagram is shown in Figure 2.35 from [164]. The three phase peritectic reaction is  $\mathbf{L} + \delta \rightarrow \gamma$ . Because of the rapid diffusion of C, the cooling rate has little influence on the peritectic reaction and equilibrium conditions exist [165].

Alloying additions to steels strongly affect the equilibrium phase lines in the Fe-C diagram as displayed in Figure 2.36 so that the reaction becomes  $\mathbf{L} + \delta \rightarrow \mathbf{L} + \delta + \gamma \rightarrow \gamma$ . Austenite grain size is directly controlled by the temperature ( $T_\gamma$ ) at which the steel becomes fully austenitic, Figure 2.37 [166].

Yasumoto *et al.*[166] first derived an equation for the influence of Mn, Ni, Si, Cr and S on the carbon equivalent and thus the temperature,  $T_\gamma$ , is as follows (Equation 2.5) for a continuous cooling rate of  $0.5^\circ\text{C s}^{-1}$ :

$$C_{eq} = C + 0.02\text{Mn} + 0.04\text{Ni} - 0.01\text{Si} + 0.02\text{Cr} + 0.67\text{S} \quad (2.5)$$

where C, Mn, Ni, Si, Cr, S represent the respective elements in wt%. This equation is then used to determine the  $T_\gamma$ . Wolf [165] altered this equation and derives the carbon peritectic equivalent,  $C_p$ , to be

$$C_p = C + 0.04\text{Mn} + 0.1\text{Ni} + 0.7\text{N} - 0.14\text{Si} - 0.04\text{Cr} - 0.1\text{Mo} - 0.24\text{Ti}. \quad (2.6)$$

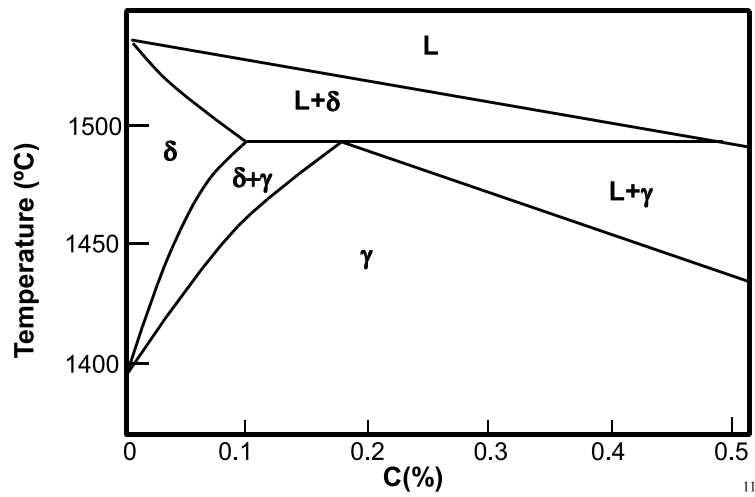


Figure 2.35: Phase transformations at high temperatures in the peritectic region of the Fe-C equilibrium diagram [164].

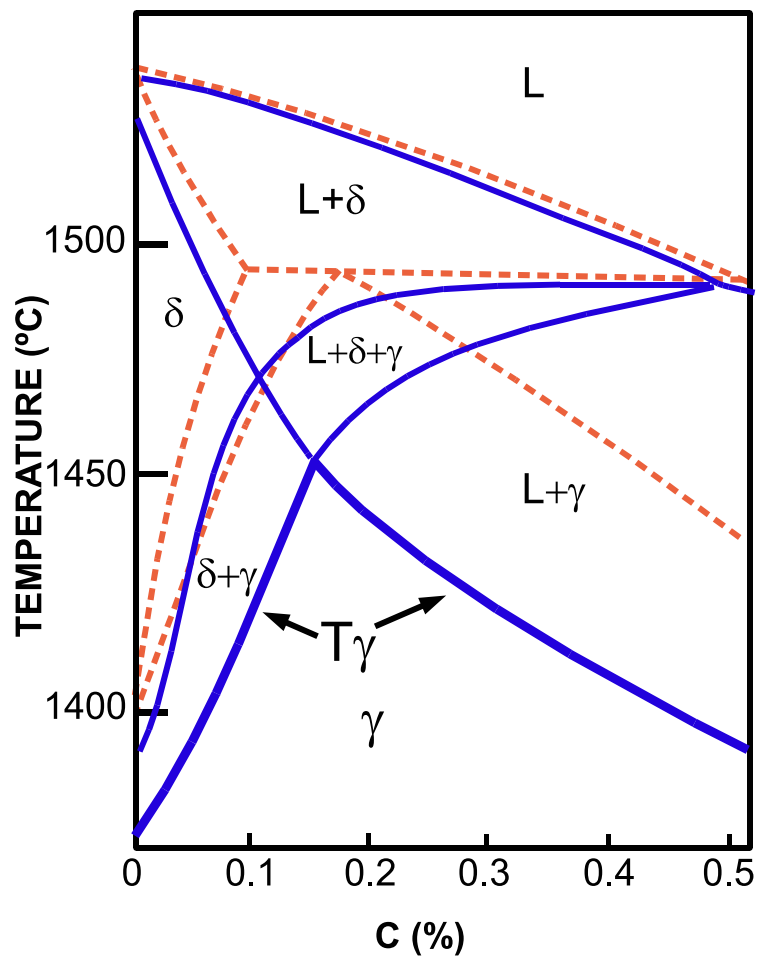


Figure 2.36: Phase transformations during continuous cooling ( $0.5^{\circ}\text{C}\text{s}^{-1}$ ) of a base steel containing 0.02%P and 0.002%S. Broken lines are Fe-C equilibrium diagram) [166].

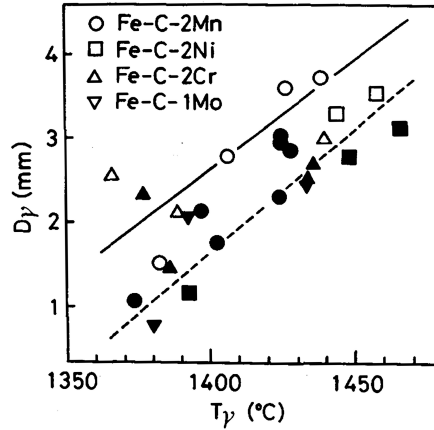


Figure 2.37: The relationship between  $T_\gamma$  (temperature at which the steel becomes fully austenitic) and austenite grain size for various steels [166], at a single cooling rate of  $0.5^\circ\text{Cs}^{-1}$ .

Wolf [165] gives the limits  $0.08 < C_p < 0.16$  as the carbon equivalent where the contraction associated with the peritectic reaction is greatest. The steels in this range are characterized by maximum contraction immediately after solidification, minimum microsegregation and thus maximum solid fraction and maximum strength in hot tensile tests. These characteristics enhance the unevenness of the shell formation and result in deep oscillation marks [165].

More recently, in high Al TRIP steels, casting defects associated with the peritectic reaction have been noted 0.22% C, 1.5% Al steels (by previous predictions a hyper-peritectic steel), thus an equation specifically for high Al compositions was developed [140]. In order to develop regressions that fit both low and high Al contents more rigorous non-linear fits were used for the predictor equations. Two equations were developed using Thermo-Calc version M to describe the points  $C_A$  and  $C_B$  as defined in Figure 2.38 [140]. This range of carbon

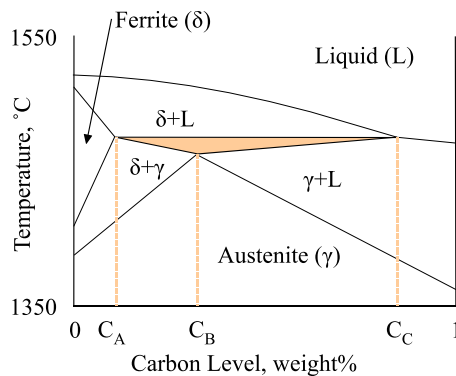


Figure 2.38: Peritectic region phase diagram (schematic), showing the three-phase region ( $L + \delta + \gamma$ ) as shadowed region [140].

Table 2.5: Ranges (wt%) for alloying elements in Equations 2.7 and 2.8 from [140].

Element	Range (%)	Element	Range (%)
Al	0-2.0	Cu	0-1.35
Cr	0-18.3	Ni	0-10.3
Mn	0-2.1	V	0-1.03
Mo	0-2.2	Ti	0-0.33
Si	0-2.05	Sn	0-0.03
P	0-0.1	Nb	0-0.075
S	0-0.15	W	0-0.5

contents relates to the surface wrinkling and loss of contact with the mould.  $C_A$  is defined as

$$C_A = 0.0896 + 0.0458Al - 0.0205Mn - 0.0077Si + 0.0223Al^2 - 0.0239Ni \\ + 0.0106Mo + 0.0134V - 0.0032Cr + 0.00059Cr^2 + 0.0197W \quad (2.7)$$

with RMS error of 0.0053 and  $r^2 > 0.99$ .  $C_B$  is defined as

$$C_B = 0.1967 + 0.0036Al - 0.0316Mn - 0.0103Si + 0.1411Al^2 + 0.05Al \times Si \\ - 0.0401Ni + 0.03255Mo + 0.0603V + 0.0024Cr + 0.00142Cr^2 \\ - 0.00059Cr \times Ni + 0.0266W \quad (2.8)$$

with RMS error of 0.0126 and  $r^2 > 0.98$  [140]. These equations apply for the ranges of alloying in Table 2.5. The equations show the range in which the peritectic reaction will be the most severe in high strength products, and ideally should be avoided, and if this is impossible, then what casting practice should be applied to minimise the effect of the peritectic reaction on surface quality [140]. They also determine a point at which the heat transfer rate is a minimum and the peritectic reaction is worst. It is at  $\sim \frac{1}{3}$  carbon content from  $C_A$  and will be defined as  $C_{peritectic}$ , where

$$C_{peritectic} = C_A + 0.3(C_B - C_A) \quad (2.9)$$

This is lower than than the peritectic carbon level but in practice this was found to be where the peritectic contraction was worst and mould heat transfer is a minimum [140]. It is not clear whether the last model (Equations 2.7 and 2.8[140]), accounts for the change in composition that occurs when Al is removed from the solution by precipitation of AlN in the melt/solidification range, since there is no N term.

Table 2.6: Composition range for the  $Ae_3$  from Andrews [167].

Element	Range (wt%)
C	0.08-0.59
Mn	0.04-1.98
Ni	0.00-5.00
Si	0.09-1.78
Cr	0.00-4.48
V	0.00-0.70
Mo	0.00-1.00
W	0.00-4.10
As	0.00-0.072

### $Ae_3$

Andrews [167] proposed a regression approach based on the experimentally determined  $Ae_3$  temperatures. By considering the empirical data of binary alloy diagrams he calculated the  $Ae_3$  temperature to an accuracy of  $\pm 10^\circ\text{C}$ . The estimate becomes less accurate for steels with  $\text{Mn} > 1\%$ , also the terms within the brackets have “considerable doubt attached” [167]. This is particularly so for the Al and Ti terms which would be expected to be positive terms. While the equation is based on steels with alloy ranges in Table 2.6, Andrews [167] does allow for extrapolation to lower carbon contents, and presumably this is also so for other elements. In the original method, C, and Ni must be interpolated from a table, which with statistical analysis has been incorporated into the equation using cubic regression with  $R^2=0.9995$  as the term  $f(C, Ni)$  [168]. The greatest error in the second regression is  $2.25^\circ\text{C}$  at  $0\%C$ .

$$\begin{aligned}
 Ae_3 = & 910 + f(C, Ni) - 25\text{Mn} - 11\text{Cr} - 20\text{Cu} + 60\text{Si} + 60\text{Mo} + 40\text{W} \\
 & + 100\text{V} + 700\text{P} + 3 - (250\text{Al} + 120\text{As} + 400\text{Ti})
 \end{aligned} \tag{2.10}$$

where

$$f(C, Ni) = -259.96 \left( C + \frac{Ni}{10} \right)^3 + 513.8 \left( C + \frac{Ni}{10} \right)^2 - 475.47 \left( C + \frac{Ni}{10} \right) - 3.08 \tag{2.11}$$

This equation has been found to be still extremely useful because of its simplicity of use even though there are now thermodynamic calculations available in software packages which can be used to calculate the  $Ae_3$ .

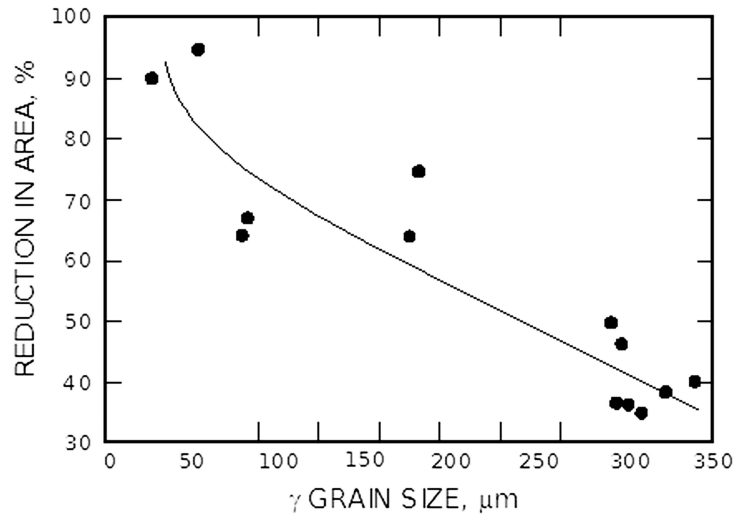


Figure 2.39: Influence of grain size on reduction in area values for C-Mn steels tested at 750°C. 0.15%C, 1.44%Mn, 0.17%Al [41].

#### 2.4.4 The effect of grain size on hot ductility

Decreasing the grain size from 300 to 150 $\mu\text{m}$ , improves the reduction in area values by 15-20% at 750°C in a C-Mn-Al and C-Mn-Nb-Al steels, Figure 2.39.[41]. Maehara *et al.*[92] describe an inversely proportional relationship between ductility and grain size for grain sizes in the range of 190-1300 $\mu\text{m}$ , Figure 2.40. This is why Mintz and Mohamed [62] can report that  $> 300\mu\text{m}$  there is no apparent effect on grain size at the largest grain sizes as the effect on ductility is reduced (tends to horizontal line). Other reviews show that R of A is inversely proportional to the initial undeformed grain size,  $D_0^{\frac{1}{2}}$ , Figure 2.41. Numerous authors concur that as grain size increases ductility decreases [41, 85, 126, 169, 170]. The mechanisms that have been used to explain the effect of grain size need to explain the the effect of precipitation and as well grain boundary ferrite and the ability of these phenomena to prevent grain boundary migration.

As grain size decreases, grain boundary area increases and precipitation density decreases leading to an improvement in ductility [49, 88]. However, ductility appears independent of grain sizes above 300-1000 $\mu\text{m}$ , in C-Mn-Al and C-Mn-Nb-Al steels, presumably where the AlN and NbCN precipitation reaches a critical density on the grain boundaries above a certain grain size [57]. Mintz and Arrowsmith [65], showed that grain boundary mobility controls R of A values. When grain boundaries are effectively pinned by precipitation, the grain size remains the same and ductility is poor, if the grain boundaries are mobile and recrystallization occurs finer grain sizes result and lead to a higher R of A. Unfortunately this type of recovery is absent in casting as recrystallization is not expected industrially because the strains and strain rates are too low and the grain size is so large.

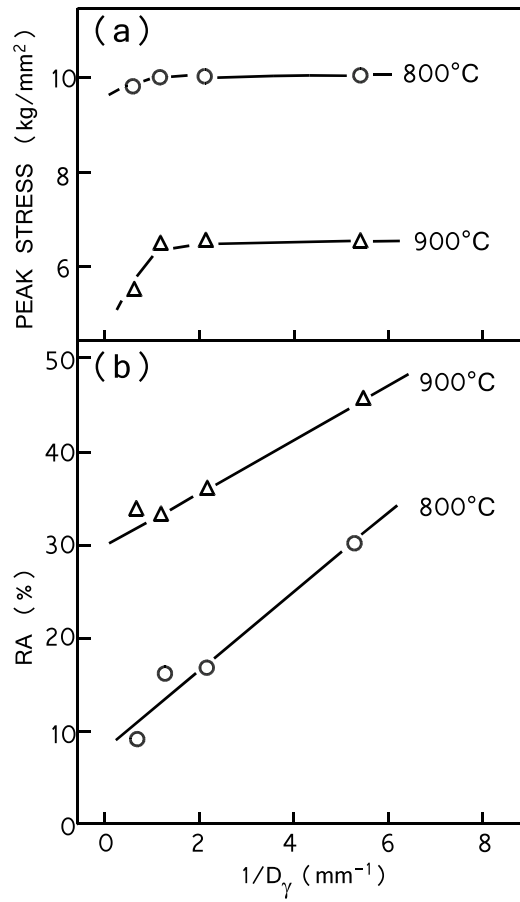


Figure 2.40: Relationship between tensile properties and reciprocal of the austenite grain size ( $D_\gamma$ ). Specimens (0.12C-0.33Si-1.51Mn-0.047Al-56ppmN-0.055Nb) were solution treated at 1100-1350°C and deformed at 800 or 900°C at strain rate of  $0.83 \times 10^{-3} \text{s}^{-1}$  [92].

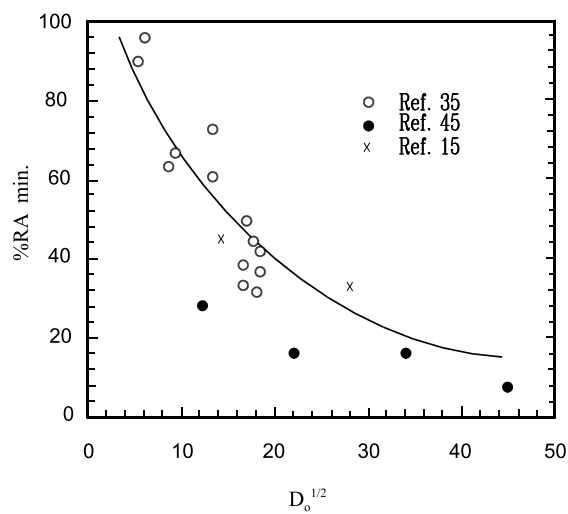


Figure 2.41: Influence of  $D_0^{1/2}$  (initial undeformed grain size after heat treatment) on minimum R of A value. ref15=[169], ref35=[41], ref45=[92] from [17].

Grain boundaries also affect the ferrite nucleation, in fine grained austenite, at slow to moderate cooling rates ( $1-80^{\circ}\text{Cs}^{-1}$ ), Militzer *et al.*[107] noted that ferrite nucleates from the corners of the austenite grains only [107]. For higher cooling rates or large austenite grain sizes, nucleation is also encouraged at the remaining sites along the austenite grain boundary.

Similarly, in an early study Maki *et al.*[171], showed that with a coarse grained austenite ( $350\mu\text{m}$ ) a film like ferrite is formed along austenite grain boundaries, whereas globular ferrite forms when the grain size is small ( $100\mu\text{m}$ ). The ductility is at a minimum when the film like ferrite formed, which occurs commonly during dynamic precipitation of ferrite [171]. In fine grained steels, deformation induced ferrite forms and grows rapidly (due to the high surface area/volume ratio of the grains, which lowers the amount of strain to below critical strain for DIF). The film may also be discontinuous, or the nucleation sites so numerous that the ferrite grows quickly [57]. Fu *et al.*[88] also found in plain C-Mn that the hot ductility trough is much deeper for larger austenite grain sizes (16 vs  $169\mu\text{m}$ ). Where the proeutectoid ferrite film is starting to form, the ferrite network is more continuous when the grain size is large as opposed to a fine grain size where the ferrite film is more “blocky”. Thus large grains encourage thin film ferrite, which in turn reduces ductility.

Industrially, columnar grains are easily formed in medium carbon steel (0.11-0.13C) and these significantly accelerate surface cracking of the slabs [92]. Dippenaar *et al.*[25], caution that while there is an association between transverse cracks and large prior austenite grain size, it has not been adequately emphasized that an abnormally large grain size condition (eg at oscillation mark) is the key factor and a mandatory prerequisite for transverse cracking. ‘Blown’ grains are at a size of 1mm or greater when measured on either the as cast surface or when the steel is sectioned in the columnar region. These blown grains extend the trough to higher temperatures, Figure 2.42, in C steel (0.18%C 0.01%Mn, 0.034%Al, 0.0016%N), so that the bottom of the trough no longer corresponds with the  $\text{Ae}_3$  at the largest grain sizes [25]. This may be because recovery is slowed down at coarser grain sizes. The cause for this widening is yet unknown but it was suggested that it may be due to grain boundary sliding in large grained austenite [25]. It may be that the AlN and MnS precipitation density reaches a critical inter-precipitate distance [67, 94]<sup>4</sup>

#### 2.4.5 The effect of strain rate on hot ductility

Decreasing the strain rate leads to poorer ductility, Figure 2.43, [42], [88, 133]. This corresponds to the slow strain rates experienced in the bending/straightening operation in the

---

<sup>4</sup>Discussed on page 66.

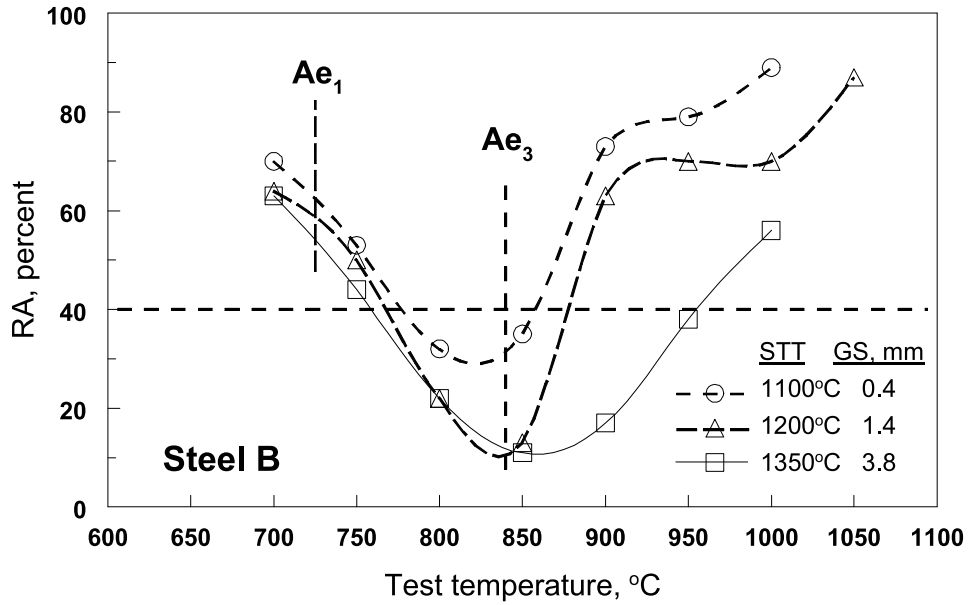


Figure 2.42: Hot ductility curves of 0.18C steel at grain sizes between 0.4-3.8mm. (0.18%C 0.01%Mn, 0.034%Al, 0.0016%N) [25].

continuous caster [75]. The manner in which strain rate influences ductility differs between austenite and ferrite and is discussed further here, as well as the effect of strain on precipitation.

In austenite, the slowest strain rates lead to strain concentration on the grain boundaries and an increase in grain boundary sliding [137]. If dynamic recrystallisation or the migration of new grain boundaries occurs, ductility improves as the growing cracks are isolated [76]. Grain boundary mobility can be reduced as a result of the precipitation of fine deformation induced Nb(C,N) since the precipitates can form on the slowly migrating grain boundary and significantly restrict its movement (even Nb in solution causes a drag effect on the grain boundaries)[49, 54, 79]. If the precipitates coarsen, the opposite result occurs, Figure 2.44, and the improvement in ductility with decreasing strain rate is attributed to the overageing of precipitation (oxy-sulphides, Nb(C,N) etc.) [42].

In the  $\gamma - \alpha$  region the improvement of hot ductility with increasing strain rate is due to the hardening of the ferrite, transferring strain to the austenite, resulting in more homogenous deformation [49, 84]. With the formation of DIF, increasing the strain rate helps work harden the ferrite, transmitting significant amounts of strain to the austenite, resulting in further transformation of ferrite leading to an improvement in ductility. However, DIF starts forming in amounts that influence the flow stress only at >16% strain in 0.14C-1.4Mn steel [55], a strain which is higher than encountered during casting.

In order to eliminate the synergistic effect of austenite and ferrite on the hot ductility

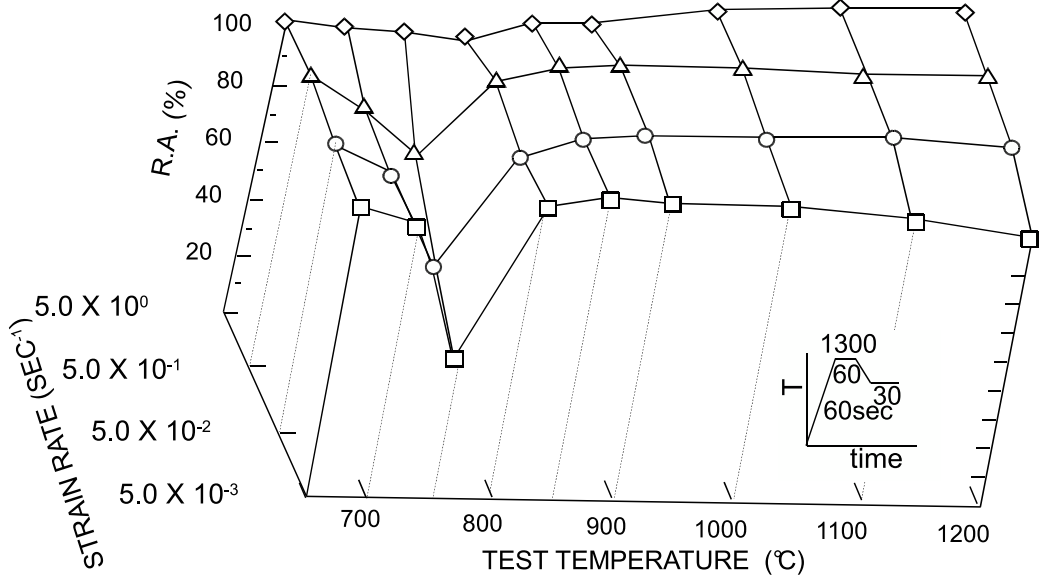


Figure 2.43: Effect of test temperature and strain rate on hot ductility (1200-600°C) for low carbon steel (0.05%C, 1.46%Mn, <0.01%Al) [42].

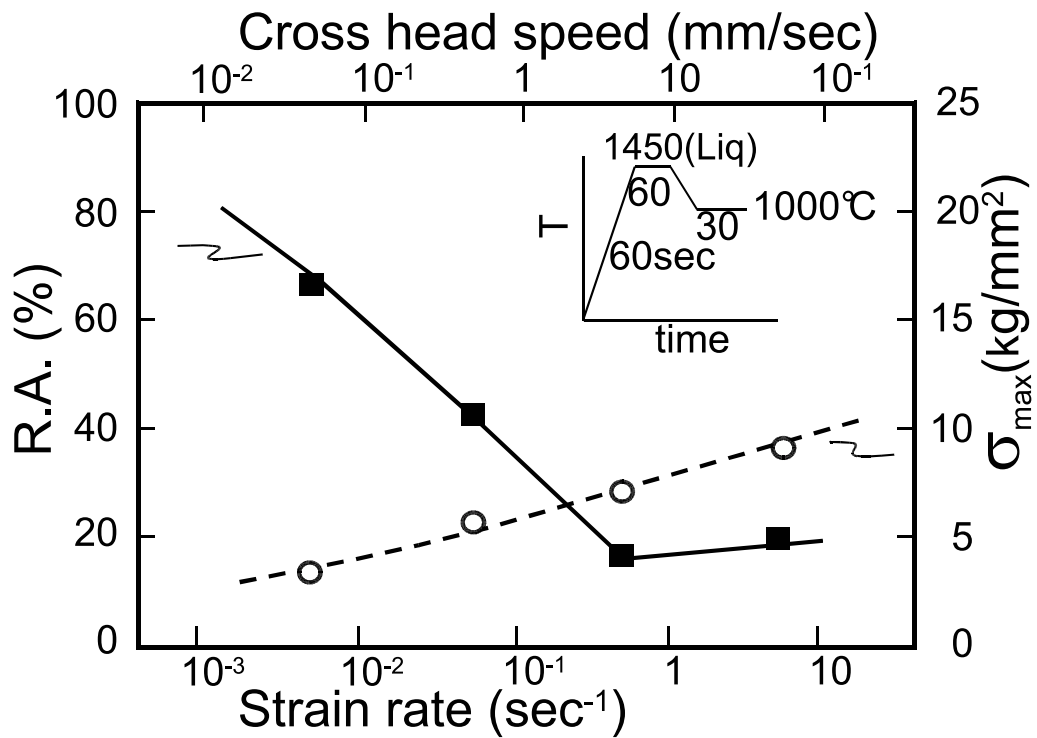


Figure 2.44: Influence of strain rate on the hot ductility of a plain carbon steel[42].

mechanisms, Mintz *et al.* [85] studied hot ductility in an austenitic and ferritic steel. At large grain sizes ( $600\mu\text{m}$ ) the effect of strain rate ( $10^{-1} - 10^{-4}\text{s}^{-1}$ ) on ductility is opposing in the two steels. In the ferritic steel the higher strain rates reduces ductility recovery while in the austenitic steels the slower strain rates are more adverse for ductility. This is a result of the different failure mechanisms in the two steels. In the austenitic steel the grain boundary sliding causes intergranular failure, while in the ferritic steel failure is by mvc. In the austenite, the ductility is therefore controlled by the ability of cracks to propagate along the boundary and the presence or absence of dynamic recrystallization [85]. An increase in strain rate (which will reduce grain boundary sliding) or grain refinement (which will reduce crack propagation) will improve ductility. This means that possibly in any steel where there is both  $\gamma + \alpha$  there may be a combination of the two different mechanisms. This is an important result when trying to differentiate the contribution of the  $\gamma$  and  $\alpha$  to the failure.

That AlN precipitation can be induced by strain has been well known [34, 127, 144]. The kinetics of dynamic precipitation of AlN is more than one order of magnitude faster than the kinetics for static precipitation [108].

At low strain rates in niobium steels, ductility is found to be largely reduced by the dynamic precipitation of Nb(C,N) and AlN within the matrix and on the grain boundaries [112, 172], which is at least one order of magnitude greater than precipitation in undeformed austenite [103]. Comparing Figure 2.43 (no Nb) and Figure 2.45 (Nb steel) shows how Nb alters the effect of strain rate and temperatures on ductility[79]. While Nb precipitation is refined if precipitation occurs during deformation, it also coarsens faster during straining [103, 104] by as much as 2-3 orders of magnitude [93]. At higher temperatures ( $1100^{\circ}\text{C}$ ) the grain boundary precipitation dominates, while at lower temperatures ( $900^{\circ}\text{C}$ ) the precipitation on dislocation predominates [173]. By decreasing the cooling rate or holding the temperature at  $1100^{\circ}\text{C}$ , precipitation can occur at high temperatures and ductility improves due to static precipitation and coarsening of the carbonitrides to approximately  $> 90\text{nm}$  [172]. This pre-deformation before testing was observed to encourage precipitation and is thought to be useful for improving the ductility (with over aging) [172, 174, 175]. Time has shown that this is not a feasible solution to the transverse cracking problem in continuous casters as there are no continuous casters with deformation rolls above the unbending zone, although thin slab casters routinely have deformation that refines the grain size.

One difficulty is that in tensile testing the amount of strain is much higher than in industry, so that increasing strain rate results in shallower troughs. This is through the interplay of dynamic recovery and critical strain to fracture [76] as detailed in section 2.3.4 on page 67, although this result cannot be applied directly in industry. Irving [16] concludes that there is no simple answer to tolerable strain levels, but that strains under the rolls are accumulative.

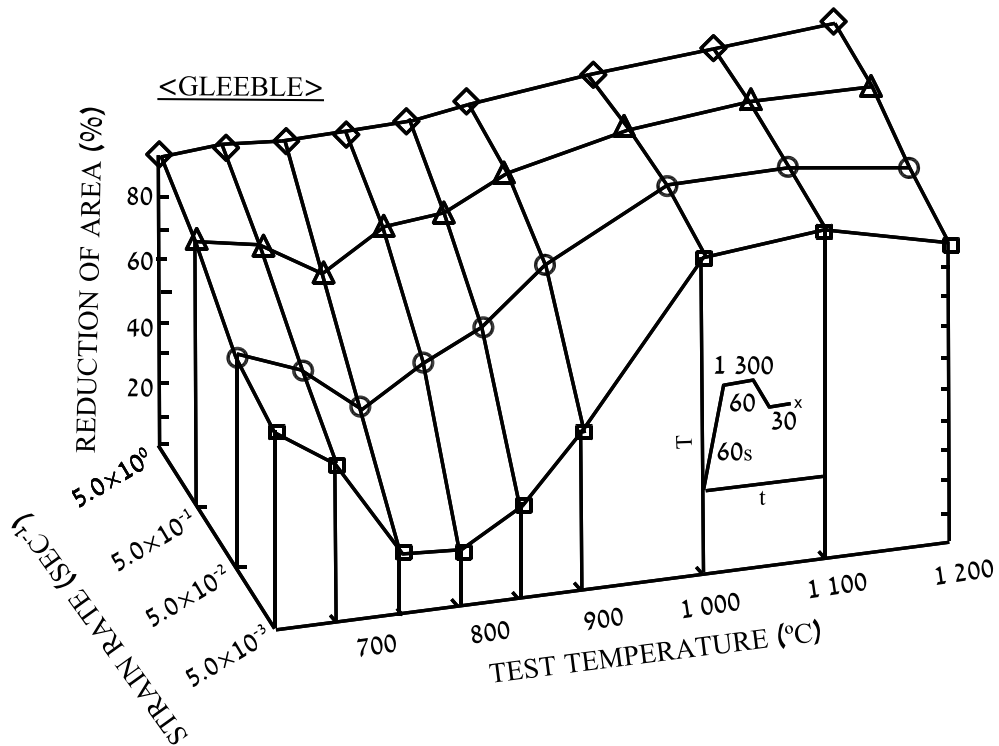


Figure 2.45: Dependence of hot ductility on the strain rate and test temperature for a niobium steel (0.06C, 1.6Mn, 0.03Al, 0.006N, 0.04Nb) [79].

#### 2.4.6 The effect of cooling path and cooling rate on hot ductility

Most testing is a compromised thermal path due to the limitations of the testing rig. The sample is often not melted, and the typical thermal path in the caster (Figure 2.2<sup>5</sup>) is simplified to a single uniform cooling rate.

With simple cooling in plain C-Mn steels, decreasing the cooling rate causes the ductility to improve since the ferrite thickness increases, and the MnS coarsens at the austenite boundaries [87]. In microalloy steels the problem is worse for example in the case of the C-Mn-Nb-Al steel there is a deterioration in the ductility on increasing the cooling rate which results in both a finer AlN precipitation and a finer dispersion of sulphides. More Nb also remains in solution so that at the test temperature a more detrimental strain induced precipitation of Nb(CN) occurs. The result is both a wider and deeper trough [176].

*Complex cooling.* An early study of the influence of a complex cooling profile on transverse corner cracks in 0.18C-0.37Si-1.33Mn-0.039Al steel by Nozaki *et al.*[23], showed that cracking is due to AlN forming on the austenite grain boundaries in the temperature region 700-950°C. When the thermal path includes a hold at 800-850°C before testing at higher temperatures (a type of single cycle), then the volume fraction of precipitation increases and a decrease

<sup>5</sup>page 38

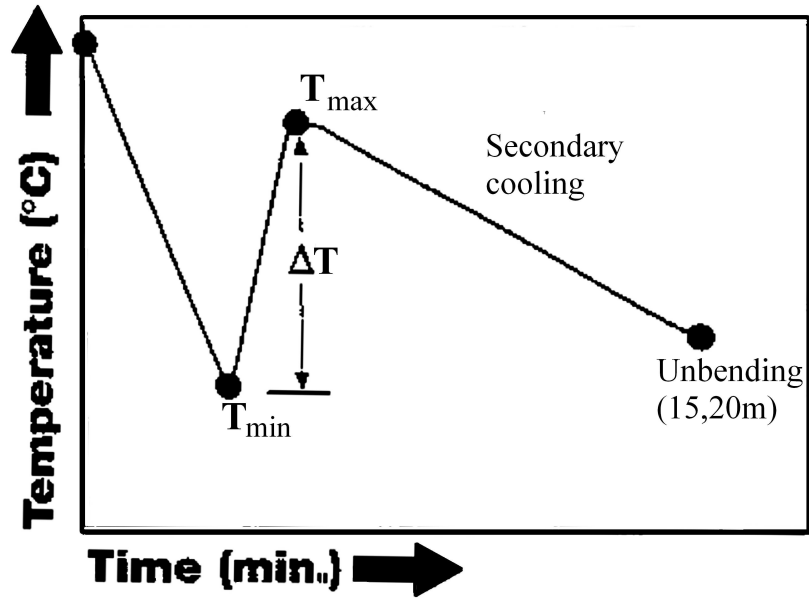


Figure 2.46: Key process variables in continuous casting simulation [20].

in ductility occurs, an effect more pronounced in Al containing steels than Nb containing steels. Cyclical reheating (as similar to the slab surface when it passes under the sprays and the rolls) causes AlN to precipitate, especially if the temperature drops below 700°C [101]. This cycling also enhances the formation of fine Nb carbonitride precipitation at the prior austenite grain boundaries, where the cracks propagate on straining. With increasing magnitude of thermal cycling (up to 250°C) there is increase in the “embrittling” effect of the carbonitrides at test temperatures in the range 750-850°C in low C cast Nb containing steels [98]. Kato *et al.*[38] also performed more complex cooling path tests and were able to suggest very innovative process adaptations as a result.

In tests aiming to investigate the key process variables during continuous casting, El-wazri *et al.*[20] performed experiments that simulated the thermal history of the steel surface as shown in Figure 2.46. This was more precise than the normal average cooling rate to test temperature. Using the steel surface cycle shown in Figure 2.2, page 38, they selected key process variables: the large temperature drop just below the mould ( $T_{min}$ ); the temperature peak,  $T_{max}$ ; and the cooling to the unbending temperature. Different casting speeds and secondary cooling conditions were found to have a marked effect on the surface temperature, and these two effects were incorporated into the experiment (see Figure 2.46). The result is that the most critical parameter is the  $T_{min}$  (see Figure 2.46), and this is plotted against reduction in area in Figure 2.47. The poor ductility is due to the onset of the austenite to ferrite transformation rather than the precipitation of microalloying elements as the kinetics for this is expected to be prohibitively slow. The effect of secondary cooling (which is a reflection of the post  $T_{min}$  thermal history, in Figure 2.46) does have some effect on

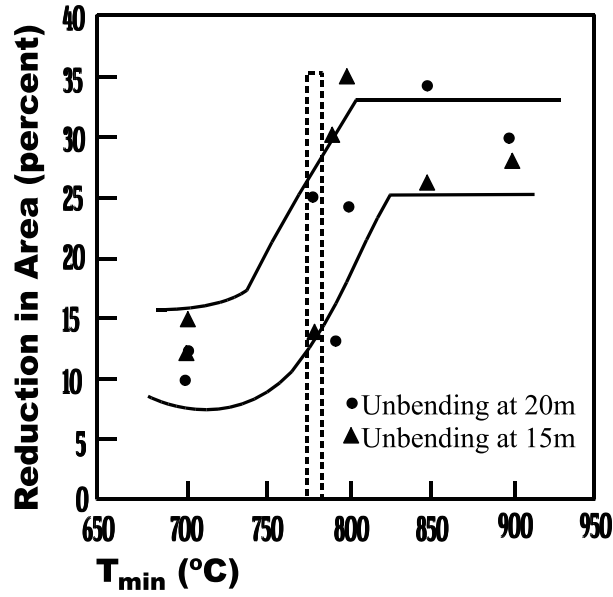


Figure 2.47: Effect of  $T_{min}$  on hot ductility [20].

ductility, Figure 2.48, via the formation of precipitates, but while it is generally true that higher secondary cooling results in poorer ductility, it is not always the case when the  $T_{min}$  is extremely high or low (the outliers in the Figure 2.2) [20]. However, the simulation used slab midface temperatures and the slab edges will be experiencing lower temperatures, thus there may be an offset from the ‘true’ critical minimum temperature.

## 2.5 Combining parameters: modelling

While the influence of grain size, cooling rate and precipitate size(etc) has been dealt with separately up to now, a number of workers [28, 94] have developed relationships for ductility as a function of the main parameters.

Yamanaka *et al.*[28], suggested that, since the fracture occurs in the ferrite, the strain to fracture,  $\varepsilon_{\alpha}^F$  is related to the volume fractions of the ferrite and austenite ( $V_{\alpha}, V_{\gamma}$ ) as well as the distribution of strain between the austenite and ferrite (as a ratio,  $R_{\varepsilon} = \varepsilon_{\gamma}/\varepsilon_{\alpha}$ ). They then include the effect of the volume fraction second phase particles,  $f$ , in the ferrite, leading to the following equation:

$$\varepsilon_{\alpha}^F = k \frac{1-f}{f} (V_{\alpha} + R_{\varepsilon} V_{\gamma}) \quad (2.12)$$

where  $k$  is a constant. In the ductility trough it can be assumed [67] that all the strain is taken in the ferrite so that equation 2.12 becomes

$$\varepsilon_f = V_{\alpha} k \frac{1-f}{f} \quad (2.13)$$

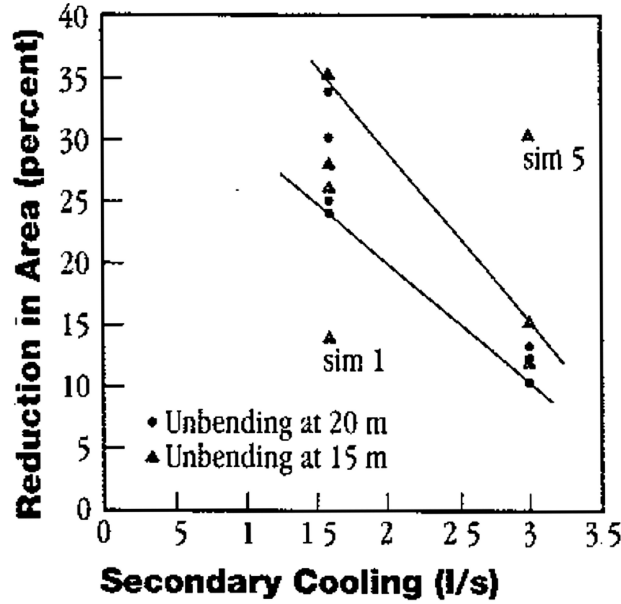


Figure 2.48: Hot ductility appears to be sensitive to secondary cooling, within limits [20].

This equation can be used in conjunction with arguments developed by [76] (page 67) to show how when the critical strain ( $\varepsilon_c$ ) for DRX is below the strain required for fracture, ductility recovers.  $\varepsilon_c$  is defined[121] as

$$\varepsilon_c = 0.8Ad_o^{\frac{1}{2}}Z^n \quad (2.14)$$

Where  $d_o$  is the initial grain size,  $A$  is a constant,  $n$  varies between 0.125-0.175 in C-Mn steels,  $Z$  is the Zener-Hollomon parameter:

$$Z = \dot{\varepsilon} \exp \frac{Q_{\text{def}}}{RT} \quad (2.15)$$

Where  $\dot{\varepsilon}$  is the strain rate,  $Q_{\text{def}}$  is the activation energy for deformation in the steel,  $R$  is the gas constant and  $T$  is the temperature (Kelvin). While equation 2.14 certainly applies to differing grain sizes [39], it is not so clear how equation 2.13 is related to grain size. The equation only applies to a film surrounding the austenite grains so that as grain size increases, the width of the film decreases.

A regression analysis has been applied to C-Mn-Al-Ti containing steels [94], characterising the ductility in terms of cooling rate (CR (K/min), particle size (nm) at the grain boundaries,  $p$ , the [Ti][N] product, and with the residual N left after TiN formation, the [Al][N<sub>residual</sub>] [94]. They show that R of A:

$$\text{RA} = 44.1 - 0.169\text{CR} + 16.3p^{\frac{1}{3}} - 0.935 \times 10^5[\text{Ti}][\text{N}] - 119.2([\text{Al}][\text{N}_{\text{residual}}])^{\frac{1}{4}} \quad (2.16)$$

In C-Mn-Nb-Al-Ti steels Comineli *et al.*[97] supplemented this with

$$\text{RA} = 26.3 - 0.118\text{CR} + 16.3p^{\frac{1}{3}} - 0.439 \times 10^5[\text{Ti}][\text{N}] \quad (2.17)$$

Another alternative relationship between minimum ductility and grain size was described by Mintz *et al.*[17], as inversely proportional to the square root of the grain size before deformation (see Figure 2.41, page 95). Mathematically this would be

$$RA \propto D^{-\frac{1}{2}} \quad (2.18)$$

Additionally, both Crowther and Mintz[41], Figure 2.39 and Maehara *et al.*[92], Figure 2.40 found a reciprocal relationship more suitable, so that

$$RA \propto D^{-1} \quad (2.19)$$

So while Sellars[121] uses  $D^{\frac{1}{2}}$ , and Mintz *et al.*[17] uses  $D^{-\frac{1}{2}}$ , both Crowther and Mintz[41] and Maehara *et al.*[92] found a reciprocal relationship more suitable.

## Chapter 3

# Hot Ductility (Reduction of Area) Analysis

### *Summary of hot ductility analysis*

This section documents the experimental procedure and ductility results from testing performed at City University, London (CUL). The presence of some porosity in the fracture surfaces required the re-evaluation of the ductility. This was done using stereo optical microscopy, as well as SEM for selected samples. More than 10% porosity was seen in samples that were melted during the ductility testing. This allowed a limited number of melted samples to be used for the calculation of R of A. Agreement with previous work by CUL was found to be good for the 0.05% and 1%Al containing steels but not for the 1.5%Al steel. The hot ductility curves were only complete for unmelted tests. It was found that the 1.5%Al steel showed the highest minimum ductility. The minimum ductility in the present analysis was similar for the low (<0.05%) Al and intermediate (1.05%) Al steels, but that in the 1.05%Al steel there was an extended trough. The statistical analysis on four samples of the 1.05%Al steel at the same temperature (1000°C) showed that the R of A had a Gaussian distribution with an average of 41% and standard deviation of 9.7%.

### 3.1 Experimental procedure at City University, London

The hot ductility testing procedure at CUL (which may be found in greater detail elsewhere [39, 177, 178]) is described below:

1. The base composition for the steels was 0.15%C, 2.5%Mn, 0.01%P, 0.005%S, 0.007%N with 0.025%Nb. All steels were produced as experimental 50kg vacuum melted ingots. Al levels varied from 0.05 to 1.5%. The detailed composition may be found in Table 3.1,

Table 3.1: Composition of TRIP steels, wt% [178].

Element	Steel 1	Steel 9	Steel 2-1	Steel 3	Steel 10
C	0.15	0.14	0.15	0.15	0.148
Si	1.05	0.21	0.49	0.00	0.02
Mn	2.42	2.41	2.47	2.49	2.50
P	0.011	0.011	0.011	0.011	0.011
S	0.0045	0.005	0.0048	0.0055	0.0040
Nb	0.025	0.025	0.024	0.026	0.028
Al	0.061	0.050	1.05	1.53	1.44
N	0.008	0.0072	0.0066	0.0057	0.0068
Predicted Liquidus	-	1511	1511	1518	1518
Predicted Solidus	-	1466	1440	1441	1441

where the compositions are considered to be similar except for the Al and Si contents. The Al is used as a Si replacement since the conventional TRIP addition of Si gives problems with galvanising. Hence, when replacing Si with Al the composition must be balanced. The three main steels were steel 9, 2-1, and 3 with Al levels of 0.05, 1.05 and 1.53%, respectively. However, these steels were supplemented where necessary by steel 1 and 10. The liquidii for the three steels was between 1511 and 1518°C. The solidii for the three steels, 9, 2-1, and 3 was 1466, 1440 and 1441°C, respectively (discussed further in Chapter 7). Since the solidus was close to the reheat temperature some melting did occur and will be discussed later, in particular, for steel 9.

- Rod samples of 1100mm length and 7.94mm diameter, with 2mm hole drilled into the centre from the one end, were machined according to the specifications in Figure 3.1.
- Ductility testing involved a thermal profile of partial melting by heating to 1460°C or complete melting by heating to 1520°C. Samples were cooled, generally at 1°Cs<sup>-1</sup>; held at test temperature and strained to failure using a strain rate of 3×10<sup>-3</sup>s<sup>-1</sup>, followed by a rapid cool as shown in Figure 3.2. The equipment is illustrated schematically in Figure 3.3.
- On fracture the argon flow was increased to cool the sample rapidly. One end of the sample remained in the jig and cooled at a lower rate than the other end which separated from the jig/furnace. The latter faster cooled sample was therefore more reliable for microstructural features such as ferrite and precipitate size which can coarsen on very slow cooling rates.

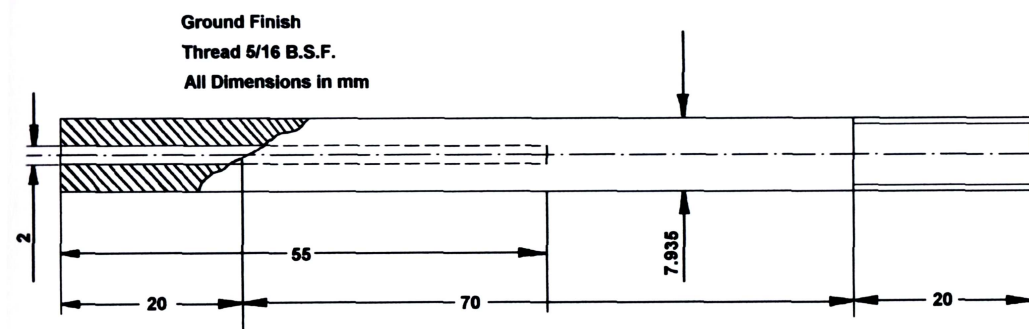


Figure 3.1: Tensile test sample manufacturing drawing [179].

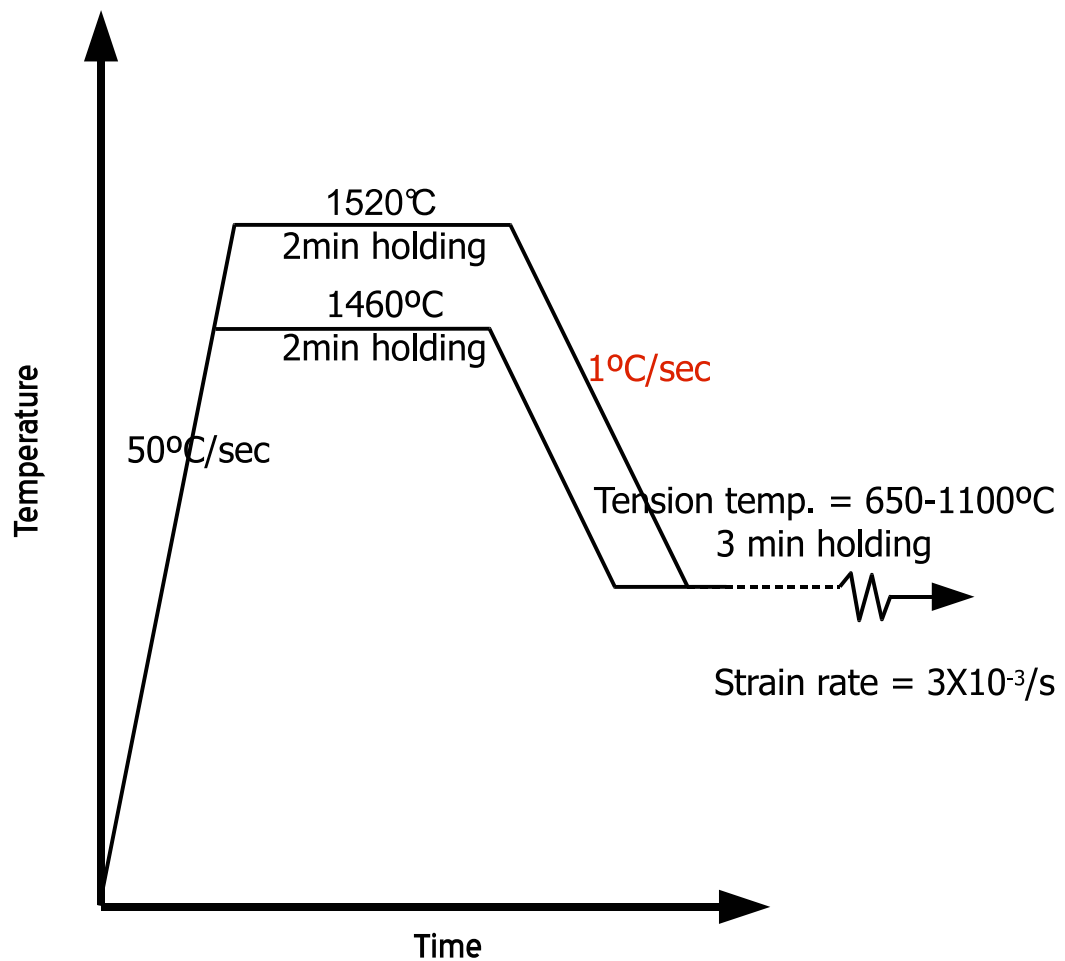


Figure 3.2: Typical temperature profiles for reheat and melted specimens [178].

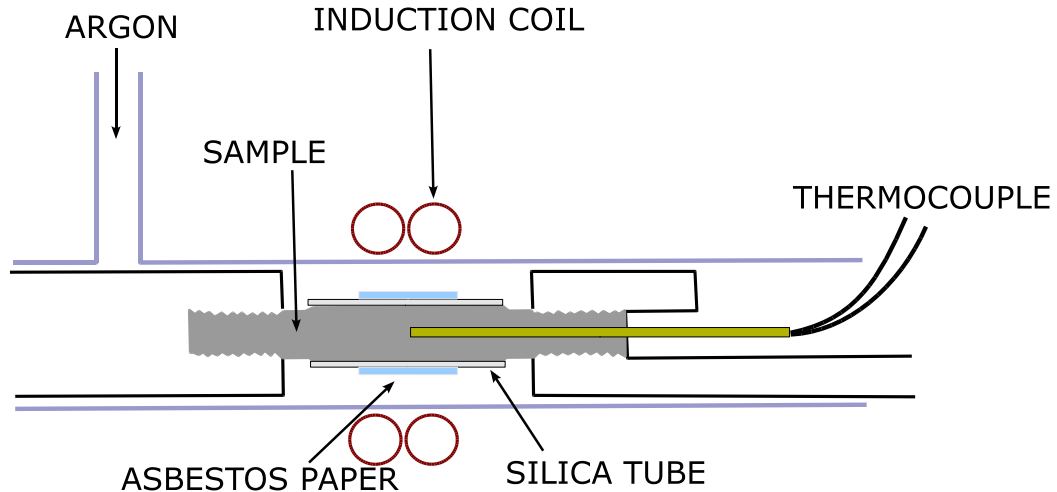


Figure 3.3: Schematic diagram of testing arrangement for in-situ melted hot ductility tests in the as cast condition [179].

## 3.2 Evaluation of reduction of area

### 3.2.1 Evaluation procedure at City University, London

The reduced diameter after fracture was measured with a Vickers Shadow Projection Microscope or Shadow-Graph. At least five readings of the final diameter were taken [178, 179]. The % R of A was measured as follows:

$$RA(\%) = \frac{D_i^2 - D_f^2}{D_i^2 - D_{pipe}^2} \times 100 \quad (3.1)$$

Where  $D_i$  is the initial diameter,  $D_f$  is the diameter at fracture and  $D_{pipe}$  is the diameter of the thermocouple hole (2mm).

### 3.2.2 Evaluation procedure at University of Pretoria

1. For accurate measurement of the fracture surface diameter, a calibrated through focus series was taken using a stereo microscope, "Analysis" CCD camera and software (the technique is shown in Figure 3.4). This involved taking a number of images at various focussing heights and assembling them, using automated software, into a final calibrated image.
2. The various areas such as the fracture surface, porosity<sup>1</sup>, necking and inner pipe were measured on the calibrated image as well as the following areas which were taken into

<sup>1</sup>The interpretation of OM images for porosity will be discussed further in the next the optical microscopy chapter, Section 4.1.2

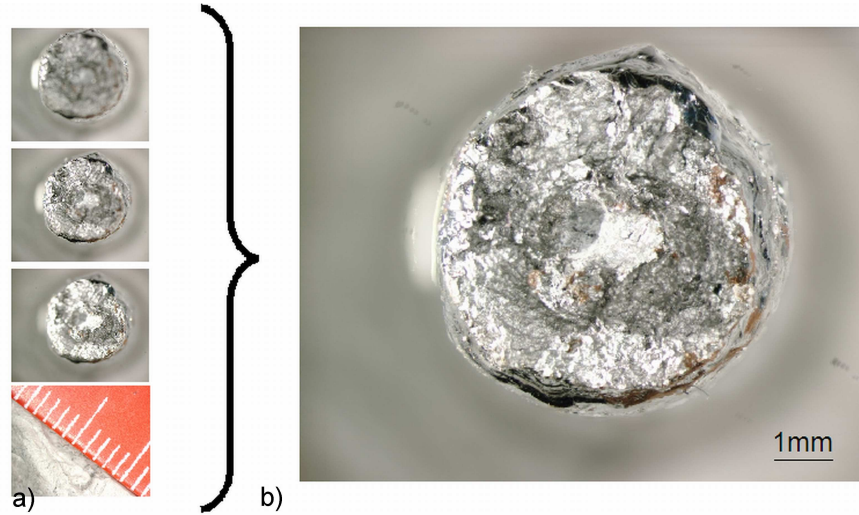


Figure 3.4: Diagram giving various images at various focussing heights for taking calibrated through focus series images of R of A sample fracture surfaces. A series of images at different focus heights was taken (a). Software was used to automatically assemble them and the final image was calibrated, to give the final image (b).

consideration in the calculation of R of A, Figure 3.5:

- (a) The initial area from machining or melting, ( $A_{\text{machine or melting}}$ ). The melt or machine diameter, the machined bore and the ceramic thermocouple tube were measured with a vernier.
- (b) The gross fracture area ( $A_{\text{fracture area}}$ ), as measured by OM.
- (c) Account was taken of the thermocouple hole (pipe) or whether internal necking had reduced the final fracture area ( $A_{\text{pipe or internal neck}}$ ), as measured by OM.
- (d) The presence of porosity ( $A_{\text{porosity}}$ ), as determined by OM and on occasion, by SEM.

The following formula was used to determine R of A:

$$RA(\%) = \frac{\Delta A}{A_0} \times 100 \quad (3.2)$$

$$= \left( 1 - \frac{A_{\text{fracture area}} - (A_{\text{pipe or internal neck}} + A_{\text{porosity}})}{A_{\text{machine or melting}}} \right) \times 100 \quad (3.3)$$

Where  $\Delta A$  is the change in area on a hot ductility specimen that occurs on fracture and  $A_0$  is the original area of hot ductility specimen. The samples where porosity  $>10\%$  were not included in the curves.

The calculation of the standard deviation could only be carried out on sets of hot ductility samples (at a single temperature) where there was more than two valid samples. There were

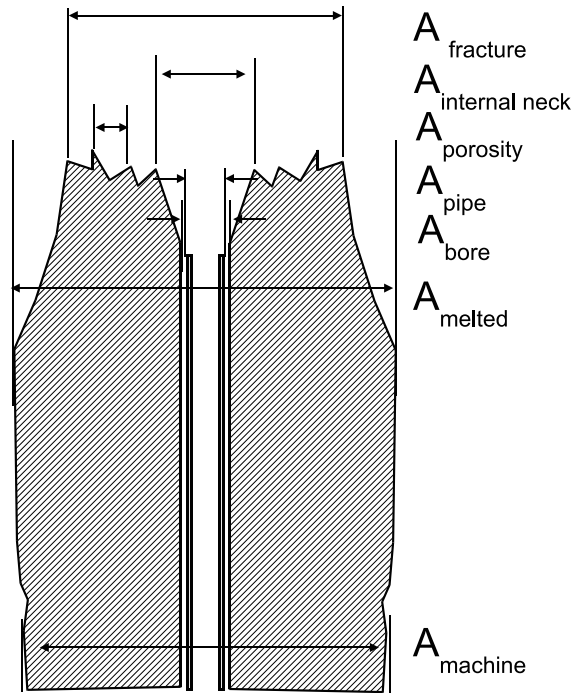


Figure 3.5: Measurement of R of A from sample fracture surfaces.

two such instances in the 1.53%Al steel at test temperatures of 850 and 1000°C where the sample populations were 3 and 4 respectively<sup>2</sup>.

### 3.3 Results and remarks

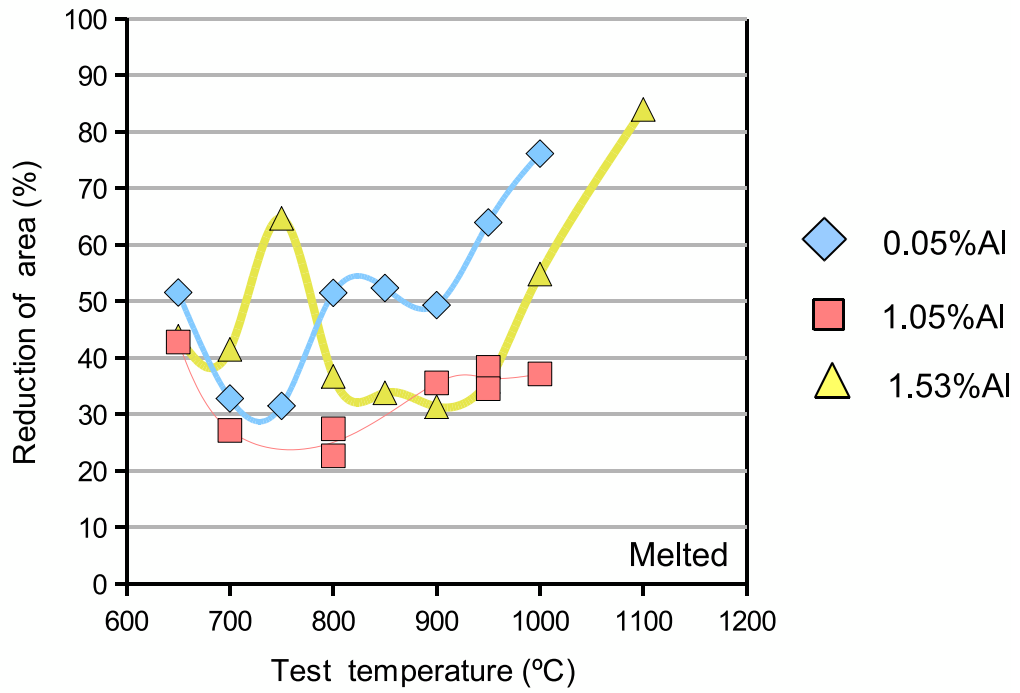
These hot ductility curves obtained at CUL will be discussed in short form here, but a fuller discussion of the TRIP steels in comparison with other steels will be set out in Chapter 8.

The scatter on the original curves, Figure 3.6 is generally low. The conclusions from the work at the City University were as follows:

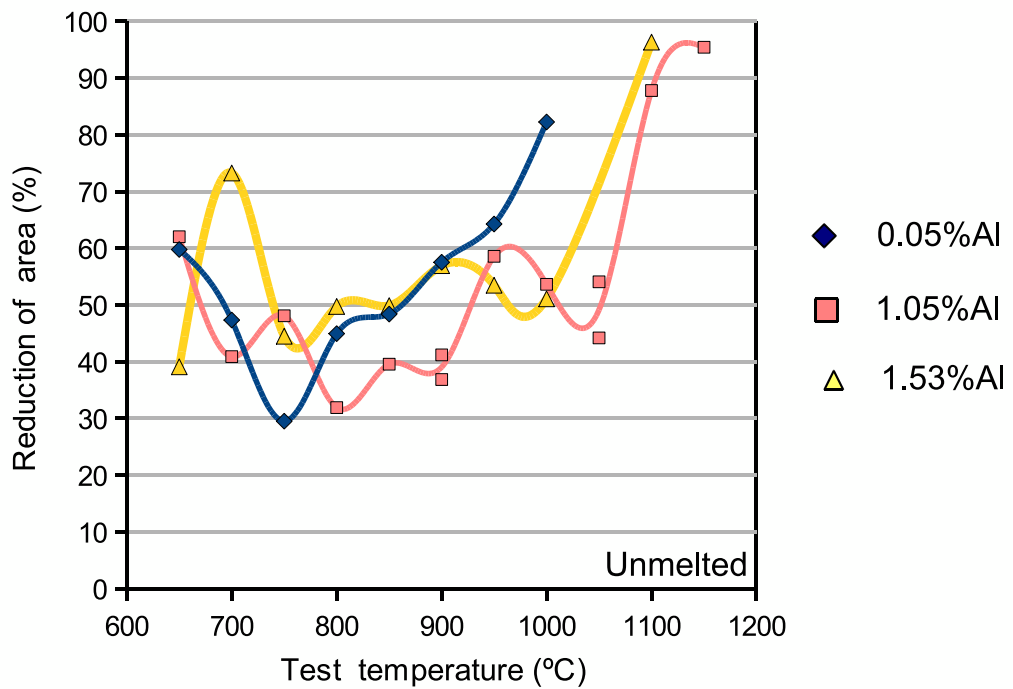
1. Increasing the Al level from 0.05, 1 to 1.5%Al level widened the trough at the high temperature end making ductility worse for the temperatures in excess of 800°C.
2. The hot ductility at the 1%Al level was the worst of the three steels both in width and depth.

It was subsequently found that many of the samples had been subject to porosity varying

<sup>2</sup>(Steel 2 – 1at850, Steel 2 – 2 850 – 1, Steel 2 – 3 850) and (2 – 1at1000, Steel 2 – 1 1000 – 3, Steel 2 – 2 1000 – 1, Steel 2 – 3 1000 – 1).



a)



b)

Figure 3.6: Hot ductility curves for TRIP steels a) melted and b) 'unmelted' during reheat, reproduced from Kang *et al.*[178].

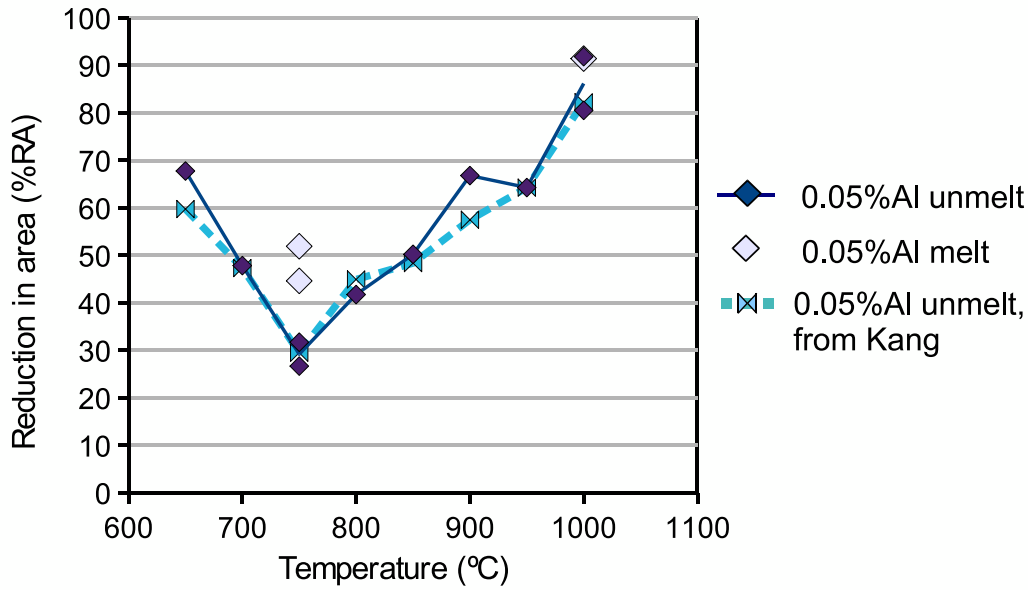


Figure 3.7: Hot ductility curves for 0.05%Al TRIP steels Kang’s complete curve and curve with <10%porosity. Ductility rises above 50% at >850°C. This curve can be directly compared with Mintz and Mohamed’s work [62], but this will be dealt with in the discussion (Section 8.2, page 196).

from 0-70% although there had been no indication of this influencing the curves. This suggests that this degree of porosity was not influencing the R of A measurement. However, at present, since there is no other evidence that a higher level of porosity is acceptable, samples having >10% porosity have not been included in the analysis.

In the original work by Kang *et al.*’s[178], no allowance had been made for porosity or internal necking and therefore the R of A values were remeasured according to equation 3.2 and the results are given in the Appendix A, Figures A.1, A.2, A.3 for all the samples. Only the data for the tensile specimens showing <10% will be considered and this limited the analysis mainly to unmelted results. The hot ductility results for the 0.05, 1.05 and 1.5%Al containing steels with <10% porosity together with the original curves determined by Kang *et al.*[178] are shown in Figures 3.7, 3.8 and 3.9. The average porosity in the melted samples was  $7.2 \pm 5.17 \text{mm}^2$  or 55%, while in the unmelted samples it was  $3.53 \pm 18.21 \text{mm}^2$  or 54%, which indicates that while there seems to be a lower porosity in the unmelted samples, there is no statistical difference between the porosity in melted and unmelted samples.

Although the melted data was limited, there tends to be an improvement in ductility in the melted samples over the non-melted samples. The unmelted results were similar to the previous results of Kang *et al.*[178], Figure 3.6, for the 0.05 and 1%Al steel. In the 1.5%Al

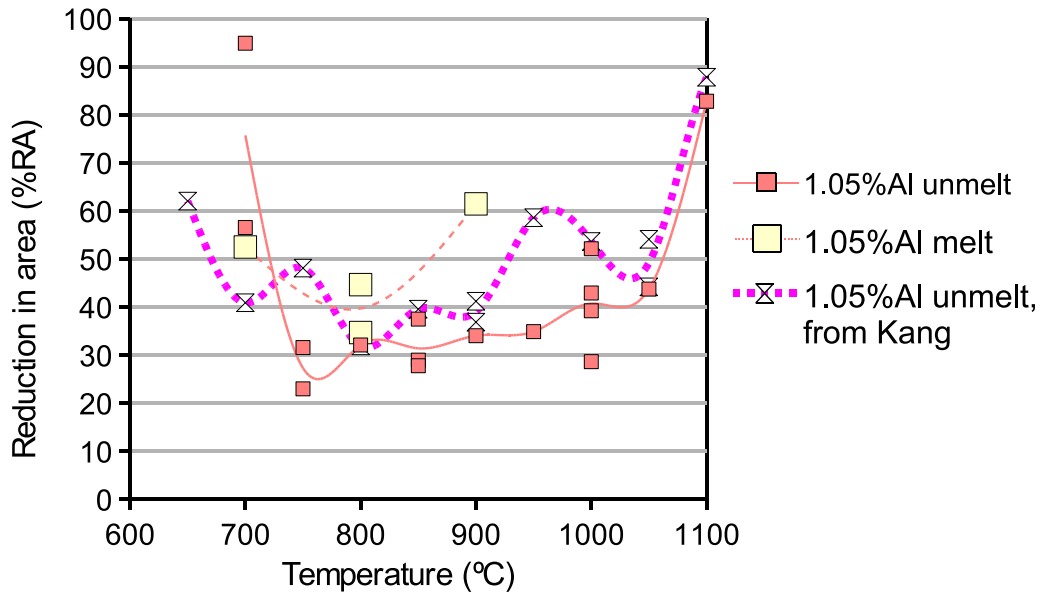


Figure 3.8: Hot ductility curves for 1.05%Al TRIP steels Kang's complete curve and curve with <10%porosity. Ductility rises above 50% at >1050°C.

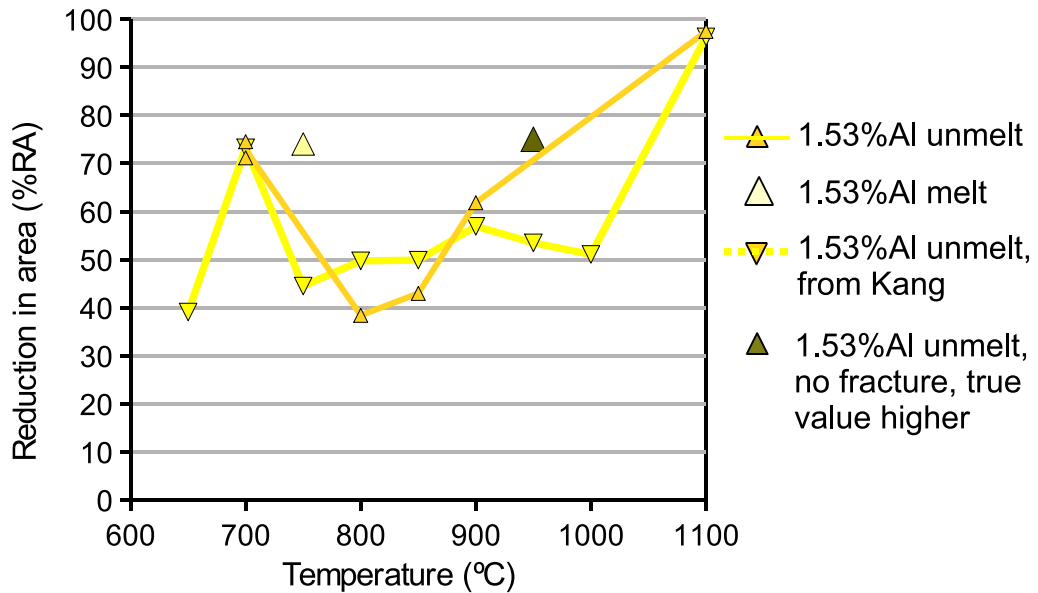


Figure 3.9: Hot ductility curves for 1.53%Al TRIP steels Kang's complete curve and curve with <10%porosity. Ductility rises above 50% at >850°C.

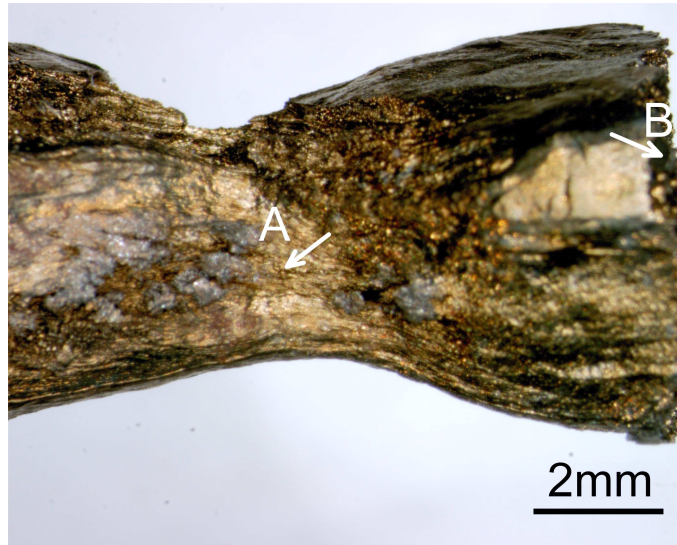


Figure 3.10: Hot ductility sample for 1.53%Al TRIP steels tested at 950°C. The ductility measured at area A will be lower than the true ductility if the sample had fractures at area A instead of at area B. Therefore the ductility for this sample is a lower estimate than the real ductility.

steel, the the difference between the CUL and current work at temperatures between 900-1050°C strictly speaking, cannot be considered as there are no valid samples. However, if the sample at 950°C which necked at the centre but fractured off centre is considered as a lower estimate of the ductility at 950°C, Figure 3.10, then ductility is higher than predicted by the CUL samples which had high levels of porosity. The current data is tabulated in full in the Appendix A, Tables A.1-A.3.

The 1%Al steel trough is marginally deeper than for the 0.05%Al steel but more importantly, it does not recover until 1100°C. This will be investigated in analytical chapters that follow. At high temperatures, in the samples where ductility was good, usually DRX or fast grain boundary motion is expected. There was more porosity in the 1.5%Al steel as it is further from the solidus in both the reheated and melted states.

To test the statistical distribution of the R of A, the statistical analysis on four samples at the same temperature was performed as follows: The cumulative probability  $((j - 0.5)/n)$  is plotted vs reduction in area [180], where j is the ordered sample value and n is number of samples, Figure 3.11. This was carried out on unmelted 1.05%Al steel tested at 1000°C as there were the greatest number (4) of low porosity tests at this temperature. The %R of A follows a normal distribution with average of 41% and standard deviation of 9.7%. The average for the 1.05%Al steel at 850°C with n=3, was  $31 \pm 5.3\%$ . This result indicates that the plateau at 950°C in the 0.05%Al steel, in Figure 3.7 and the difference in the minimum

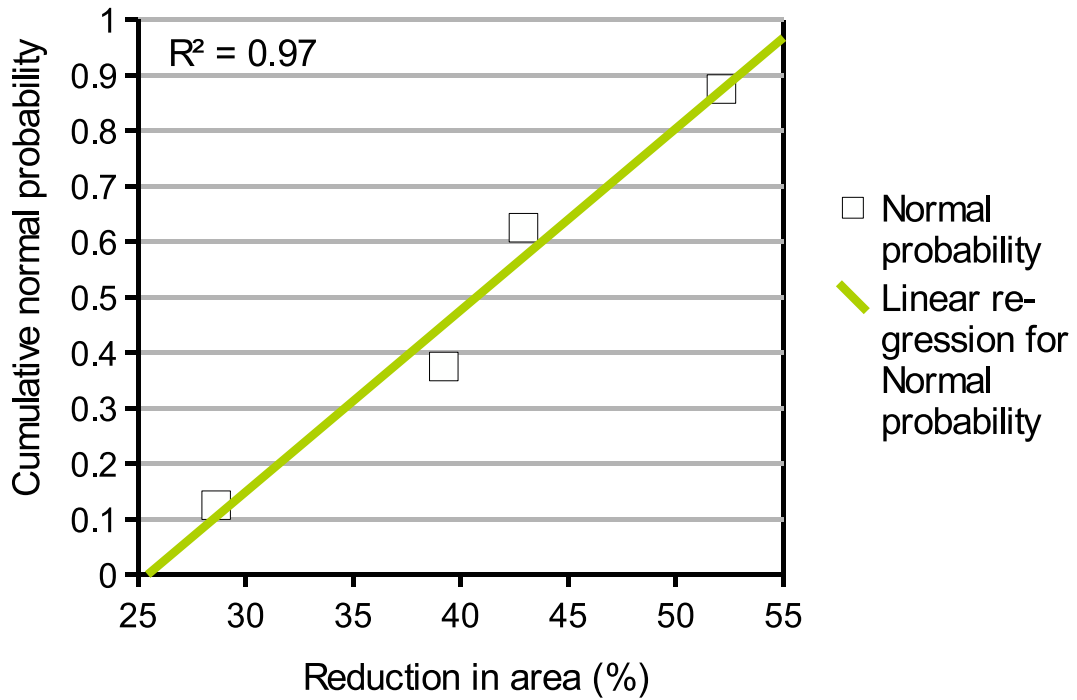


Figure 3.11: Cumulative probability plot for 1.05%Al TRIP steels at 1000°C with <10% porosity, R of A is  $41 \pm 9.7\%$ .

ductility between the 0.05 and 1.05%Al steel, Figure 3.7 and 3.8 is statistically insignificant.

### 3.4 Conclusions of hot ductility analysis

1. The numerous occurrences of porosity in the melted samples only allowed the effective study of the trends in the unmelted samples.
2. The 1.53%Al steel has the best hot ductility behaviour. The 1%Al steel trough is wider than both 0.05 and 1.53%Al which were similar in extent. These are in agreement with CUL results except for the 1.53%Al steel.
3. The statistical analysis on four samples at the same temperature of 1000°C showed that R of A has a Gaussian distribution with average of 41% and standard deviation of 9.7%.

## Chapter 4

# Optical Microscopy Analysis

### *Summary of optical microscopy analysis*

This section deals with the optical microscopy performed at both City University (CUL) and University of Pretoria (UP). This included microscopy of the fracture surface and microscopy of the cross sections prepared for TEM. Characterisation of the microstructure was performed in terms of fracture type, prior austenite grain size, precipitation/inclusions and the presence of dynamic recrystallisation (DRX). At low R of A, the fracture behaviour was intergranular in the 0.05%Al steel and a mixture of intergranular and transgranular fracture at higher Al levels. The correlation between inverse grain size and ductility in the low and high Al steel showed a good fit with  $R^2=0.76$  and  $0.82$  respectively. This indicated that the grain size and R of A are related but that grain size may not be the only variable that significantly affects the R of A. In the case of the 1.05%Al steel the grain size was a less significant contributor to R of A than in the high and low Al steels. Hexagonal plate AlN was seen in the as cast 1.05% and 1.53%Al steel. Large dendritic AlN precipitates on the grain boundaries were found in the melted and unmelted test samples in 1%Al steel. Small amounts of the dendritic AlN precipitation were detected in the 1.5%Al steel. Only MnS was identified in the low Al Steel. The dendritic grain boundary AlN precipitation in the 1.05%Al steel was present at all temperatures and its presence causes the very wide trough in this steel. DRX was observed above  $1050^{\circ}\text{C}$  in samples that had higher than 80% R of A showing high temperature ductile rupture (HTDR) fractures.

## 4.1 Macro optical microscopy and optical microscopy of the fracture surface

### 4.1.1 Aim and experimental procedure for macro optical microscopy

The importance of using OM before TEM is that “knowledge of the forest is required before studying the individual leaves”[181]. Electron microscopy has the great advantage of high resolution, but as a result only a small area of the sample may be studied. The aim of the macro OM was to correlate the macrostructure with the R of A values. Thus the macro images were analysed for the different types of failure (HTDR, intergranular failure or transgranular failure and the presence of porosity), this identification was confirmed with SEM analysis. Also, an estimation of the maximum grain size was performed when the failure mode was intergranular. These were carried out on the through focal series (ie the projected area) so that the grain size in horizontal section was recorded. The procedure for taking in focus macro images of the fracture surface is detailed in Section 3.2.2, Figure 3.4 on page 109. Although porosity may be influencing the hot ductility behaviour, it is unlikely to influence the microstructures in areas where there is no porosity.

### 4.1.2 Results and remarks on the macro optical microscopy analysis

A selection of various types of failure as shown in Figure 4.1, were classified as

1. intergranular failure (ig), Figure 4.1a,
2. transgranular failure (tg), Figure 4.1b,
3. a mix of intergranular and transgranular failure (ig/tg), Figure 4.1c,
4. high temperature ductile rupture (HTDR), Figure 4.1d, and
5. porosity (P), Figure 4.1c, in the area indicated by P.

It can be seen that intergranular fractures are present in many samples (with less than 10% porosity) which gave high ductility values (60-70% R of A). For the all microscope studies, all samples were taken into account for the analysis although again preference was given where possible to samples that had less than 10% porosity. The types of fracture present in the 0.05, 1 and 1.53%Al containing steels as a function of test temperature are given in Figure 4.2a, b and c respectively. In general intergranular failure predominated at the low Al content (Figure 4.2a details in Table B.1 in Appendix B.1) and this changed to a

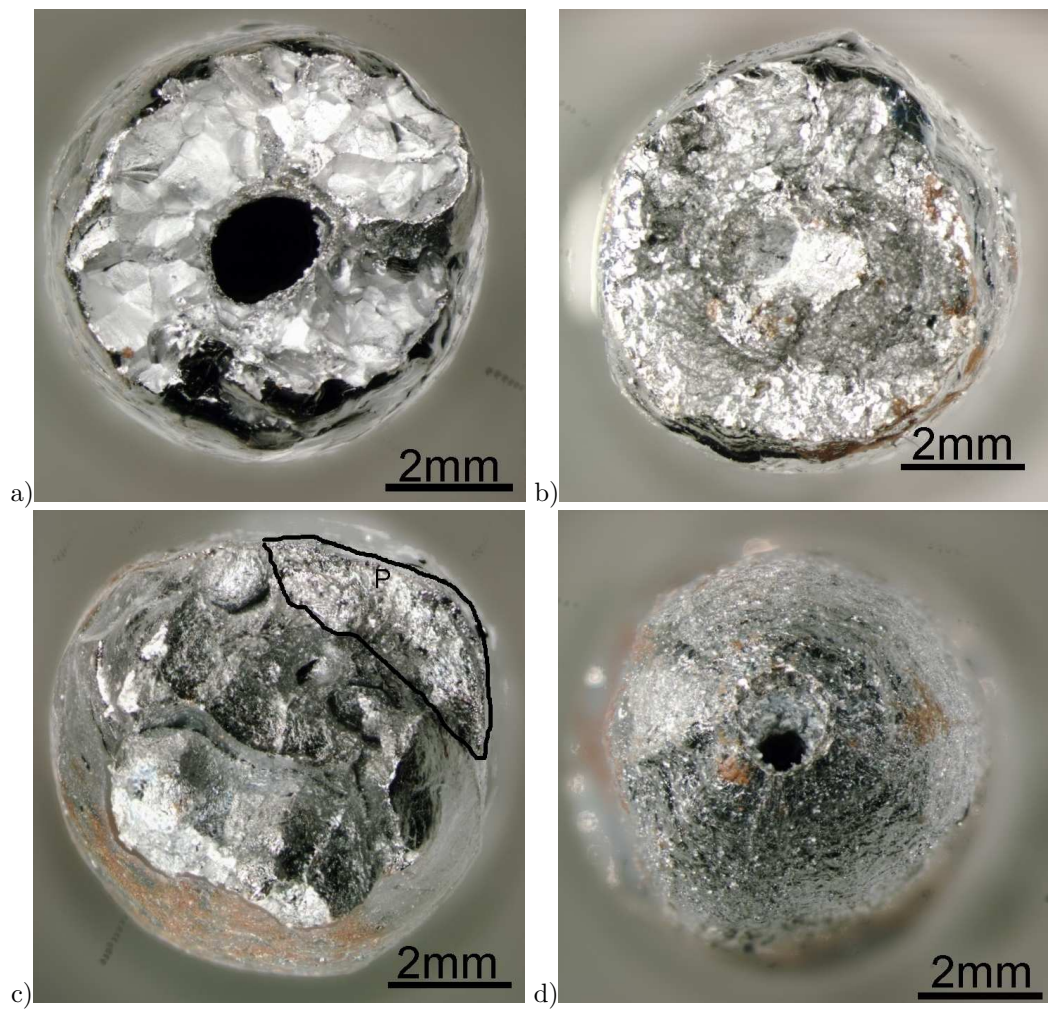


Figure 4.1: Illustration of the types fracture surfaces seen by macro OM a) intergranular failure (ig), b) transgranular failure (tg), c) a mix of intergranular and transgranular failure (ig/tg) with porosity in area 'P' and d) high temperature ductile rupture (HTDR).

combination of intergranular and transgranular failure at intermediate and high Al contents (Figure 4.2b, c, details in Table B.2 and Table B.3 in Appendix B.1). For the 1%Al steel intergranular failure and mixtures of intergranular/transgranular failure (shown in Figure 4.1c) were observed up to 1050°C when HTDR due to DRX took place (shown in Figure 4.1d). In the 1.5%Al steel, failures were a mixture of intergranular/transgranular fracture and at the highest temperature of 1100°C, HTDR and DRX was observed. Note that in the 1.53%Al steel no samples were present between 900-1100°C. There may also be some erroneous identification of intergranular versus transgranular when the grain size is small as the optical resolution is limited.

There was limited correlation between grain size and R of A using the macro OM grain size estimation on the fracture surface (Appendix B.1, Figure B.1). The grain size is more amenable to a cross sectional study, as seen in Figures 4.3, 4.6 and 4.9 where the longitudinal grain size can be studied independently of fracture mode.

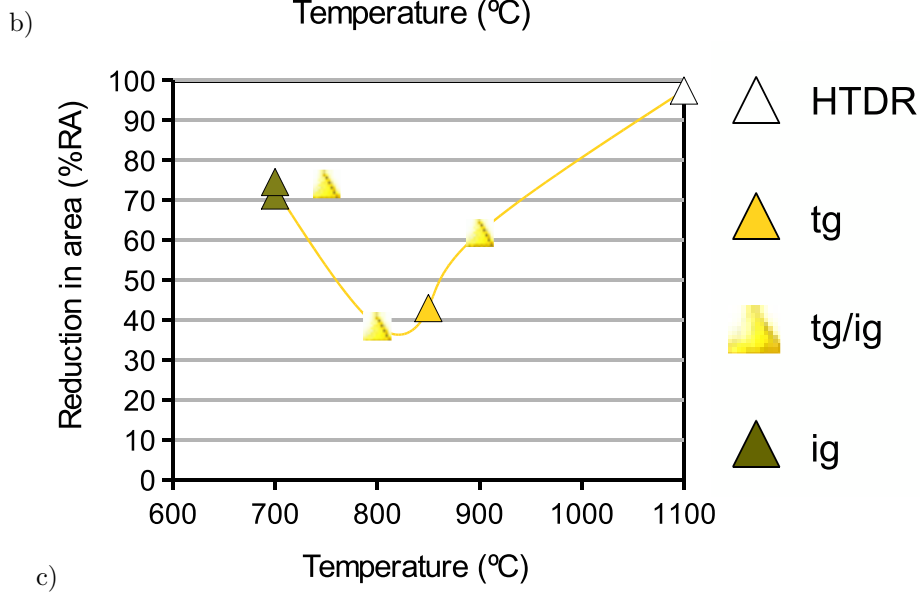
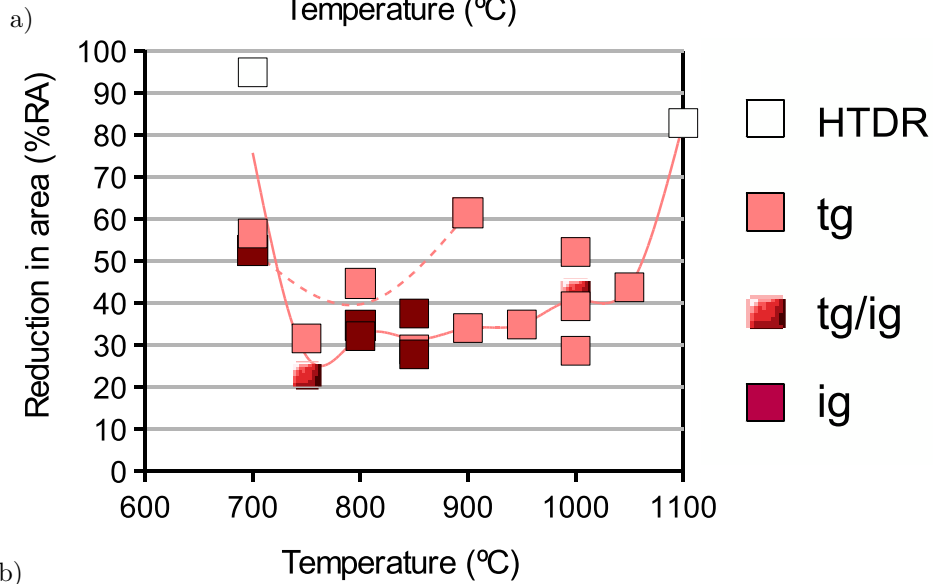
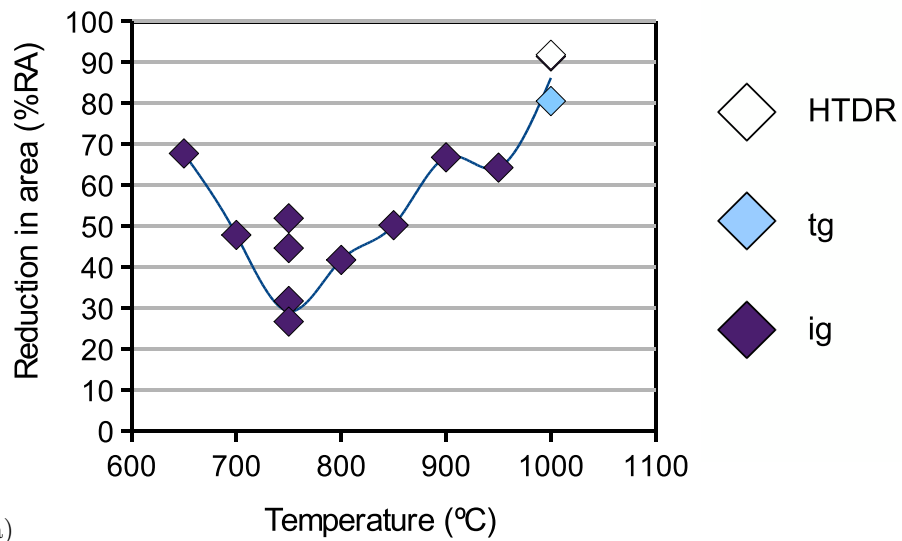


Figure 4.2: Type of failure as a function of ductility and temperature for a) 0.05%Al b) 1.05%Al and c) 1.53%Al steel respectively, samples with <10% porosity.

## 4.2 Cross sectional optical microscopy

### 4.2.1 Aim and experimental procedure for cross sectional optical microscopy

For measuring the grain size, cross sectional (*c/s*) analysis is an alternative method to the fracture surface analysis. It has advantages in the case of the samples that exhibited high temperature ductile rupture, where the fracture surface cannot be used, the *c/s* can still give a good indication of grain size prior to straining. The procedure used for preparing the cross sections is detailed in Section 6.2, Figure 6.1, page 152.

Grain size  $\bar{d}$  was calculated using the intercept method as follows,

$$\bar{d} = \frac{L}{N} \quad (4.1)$$

where  $L$  is the length of a line ( $\mu\text{m}$ ) and  $N$  is the number of grain boundaries that the line intercepts. A total of four separate lines in different orientations ( $0, 45, 90, 135^\circ$ ) on each microstructure were used so that an average and standard deviation could be calculated for each image. The area that was analysed for the grain size was close to the fracture surface, within the heated (melted) zone. However, the DRX area as well as the necked area was avoided so that, generally, the grain size was constant along each line.

Characterisation of the microstructure was made in terms of prior austenite grain size, precipitation/inclusions and the presence of DRX. The results and discussion will be presented for each steel in turn in the following sections. The presence of pro-eutectoid ferrite ( $\text{pe-}\alpha$ ) was ignored as many samples were slow cooled from the test temperature, therefore the presence of  $\text{pe-}\alpha$  was determined from SEM analysis of the fracture surface, Figure 5.5 page 141, where the cooling rate is always sufficiently fast to freeze in the microstructure immediately after fracture.

### 4.2.2 Results and remarks on the cross sectional optical microscopy analysis

#### 0.05% Aluminium steel

The list of average grain sizes for the unmelted and melted sample in the un-recrystallised state (i.e. no DRX) for the 0.05%Al steel is given in the Table 4.1. It can be seen that, on melting, there was a very wide variation in grain size. The last column is the number of grains across the sample diameter.

Table 4.1: List of average grain sizes for the unmelted and melted 0.05%Al steel samples. Grain size average excludes samples with DRX. (P) indicates samples with porosity,  $\phi$  is the original diameter of the specimen.

Test temp( $^{\circ}$ C)	Melted sample grain size ( $\mu$ m)	Unmelted sample grain size ( $\mu$ m)	$\sim$ No. grains across the $\phi$	Sample name
650	1917 (P)		2	9-650-1mF
650		1173	3	9at650uM
700	998 (P)		4	9-700
750	907		4	9-750-2smN
750		1468	3	9-750-1suO
850	1843 (P)		2	9-850-1-mF
950		1225(P)	3	1-950-1uD
1000	724 (DRX)		5	9-2at1000mJ
1000		972 (DRX)	5	9-1000-1uF
Average	1416 $\pm$ 538	1289 $\pm$ 158		

It is unlikely that there will be any growth of grains on cooling below 900 $^{\circ}$ C and all the failures were intergranular. It was not clear what causes this large variation in the as melted grain size but part of the reason is that at such large grain size the population of grains measured was very small. It is best to take the average grain size of all the austenite grains present in the un-necked areas, which when averaged for all melted and unmelted samples, is 1362 $\mu$ m. When dynamic recrystallisation occurred the grain size at the tip is refined to 420 $\mu$ m at 950 $^{\circ}$ C and 127 $\mu$ m at 1000 $^{\circ}$ C.

When reduction in area is plotted against the ‘unmelted’ inverse grain size, a fair correlation ( $R^2=0.76$ ) was found, Figure 4.3 in the cases where intergranular failure occurred. This analysis did not include samples where DRX was evident (which may be found in Figure B.3, page 249). The large standard deviation (error bars) show that the grain size is not the only variable that significantly affects the R of A. Both fast and slow cooled samples were considered as it was assumed that the cooling rate after testing would not affect the grain size significantly. However, the two factors, grain size and precipitation must be taken together if a correlation is to be made. This will be done in the discussion, Section 8.3.5, page 204. The merits of this comparison (for instance, that it is not carried out at a single temperature) is discussed further in Section 8.3.4 page 204.

In the investigation of DRX in the melted and ‘unmelted’ 0.05%Al steel grain refinement at the fracture surface indicated that DRX had occurred, Figure 4.4. Recrystallisation was

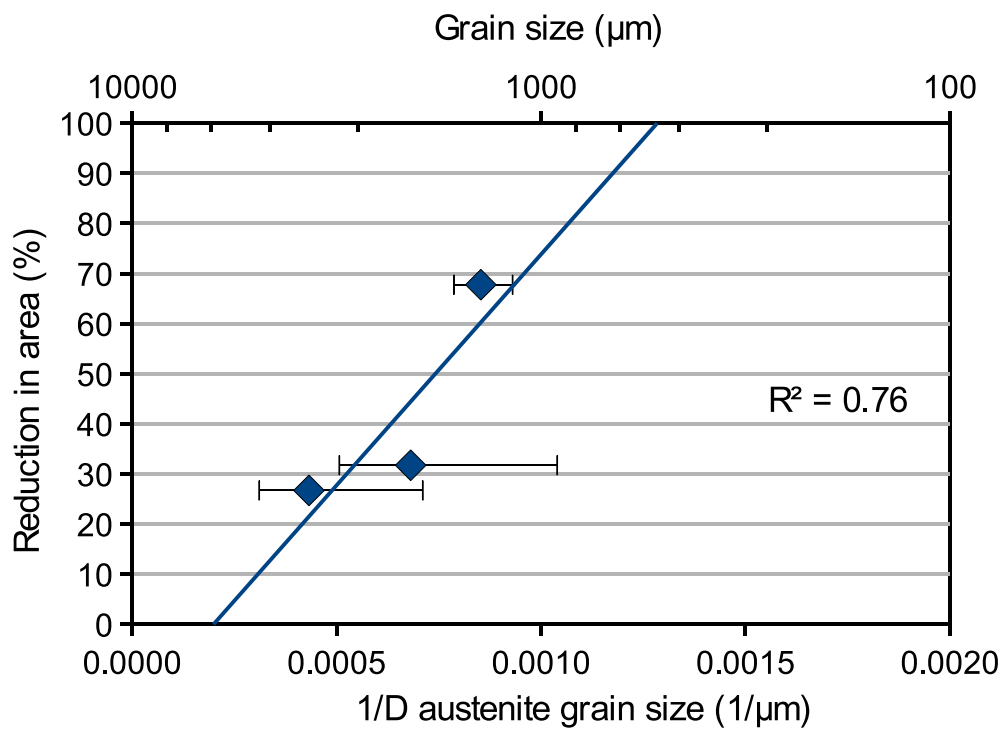


Figure 4.3: Relationship between inverse grain size and reduction in area in unmelted 0.05%Al steel where no DRX occurred. The error bars show the standard deviation for each sample, whereas the  $R^2$  indicates the goodness of fit of the data to the line. The addition of the DRX samples and the melted samples may be found in Figure B.3.

Table 4.2: List of grain sizes for the unmelted and melted grain sizes in the 1%Al steel. Grain size average excludes samples with DRX. (P) indicates samples with porosity,  $\phi$  is the original diameter of the specimen.

Test temp(°C)	Melted sample grain size ( $\mu\text{m}$ )	Unmelted sample grain size ( $\mu\text{m}$ )	$\sim$ No. grains across the $\phi$	Sample name
650	2197		2	2-3-650-1-mF
700		444	9	2-1-700-uD, 2-3-700-1-uD
750		849	5	2-2-750-1-uD
900	638		6	2-3-950-1-mD,
900		574	7	2-3-900-1-uD
950	1345 (P)		4	2-3-950-1-mD,
950		917	3	2-3-950-3-uD
1050		2302	2	2-1-1050-uD
1100		298 (DRX)	13	2-1-1100-uM, 2-1-1100-uM
Average	1393 $\pm$ 781	1017 $\pm$ 727		

in all cases only observed at test temperatures of 1000°C and ductilities above 80%<sup>1</sup>. The only inclusions observed in the as received 0.05%Al steel were MnS inclusions, Figure 4.5.

### 1.05% Aluminium steel

The list of grain sizes for the unmelted and melted samples in the un-recrystallised state (i.e. no DRX) for the 1%Al steel are given in Table 4.2 and again it can be seen on melting there is a similar wide range of grain size. The average grain size for all unmelted and melted samples is 1158 $\mu\text{m}$ .

When dynamic recrystallisation occurred, the grain size was refined. When grain size is plotted against reduction in area a poor correlation is seen, Figure 4.6. This indicates that other variables besides grain size are, in this case, having a greater influence on R of A. Dendritic AlN precipitation was found at all temperatures tested between 650 and 1050°C, Figure 4.7. This correlated with the precipitation observed on the fracture surface (Figure 5.8, page 147). It is suggested that this is the cause of the poor ductility throughout the temperature range. While in the original work by CUL, other extensive grain boundary precipitation, Figure 4.8, from [179], has been reported [179], the morphology was not the

<sup>1</sup>92 and 81% of sample 0059at1000g1uM and 00591000-1uF respectively.

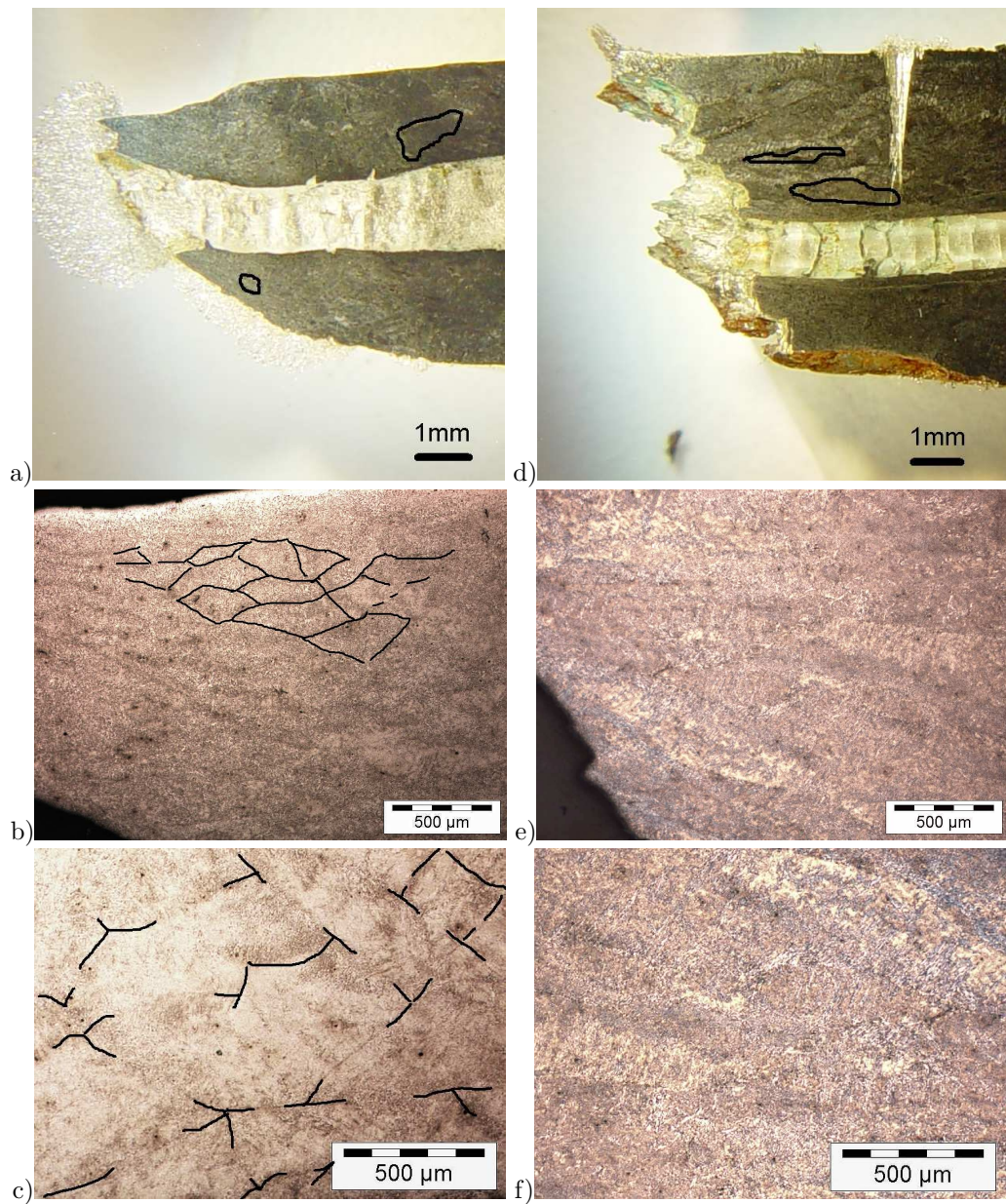


Figure 4.4: 0.05%Al steel, a) recrystallisation at the fracture tip of sample ‘unmelted’ and tested at 1000°C (92% R of A) with b) tip and c) bulk grain size enlarged, compared with d) non-recrystallised fracture tip of sample melted and tested at 650°C(68% R of A) with e) tip and f) bulk grain size enlarged. Light nital etch. In the case of a,b,c and d some grain boundaries have been outlined to aid interpretation.

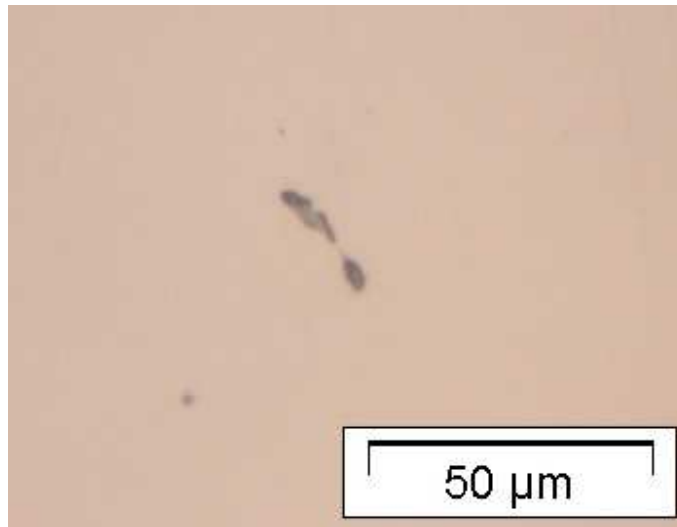


Figure 4.5: MnS inclusion in as cast 0.05%Al steel. Unetched c/s.

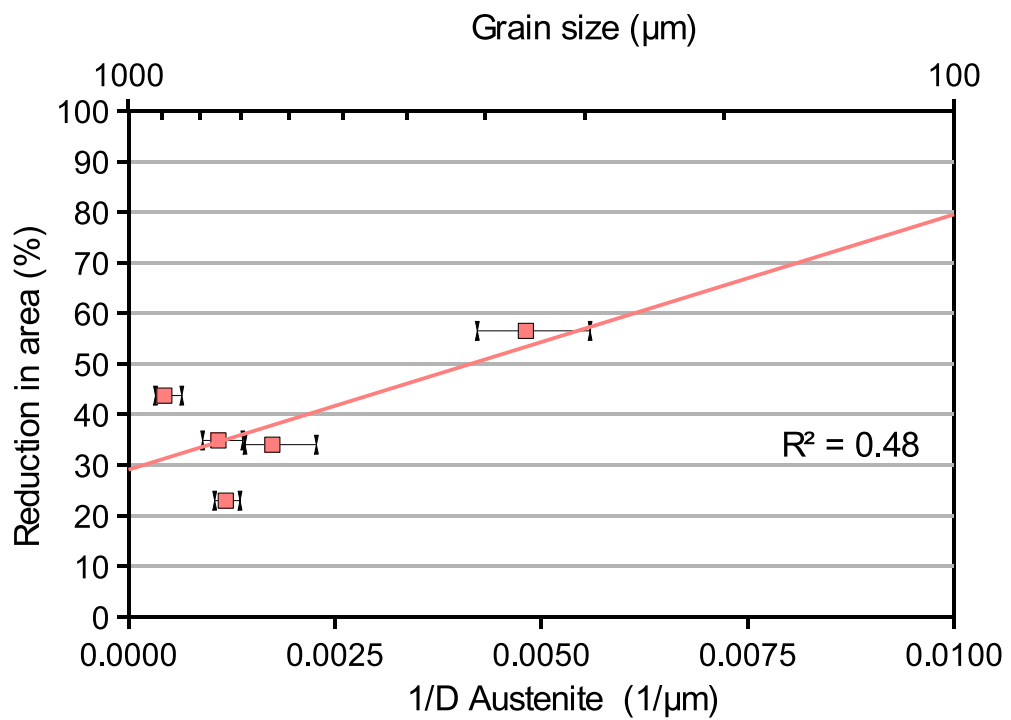


Figure 4.6: Relationship between grain size in the unmelted samples and R of A in the 1.05%Al steel. No clear correlation between these two variables for the unmelted samples. The error bars show the standard deviation for each sample, whereas the  $R^2$  indicates the goodness of fit of the data to the line.

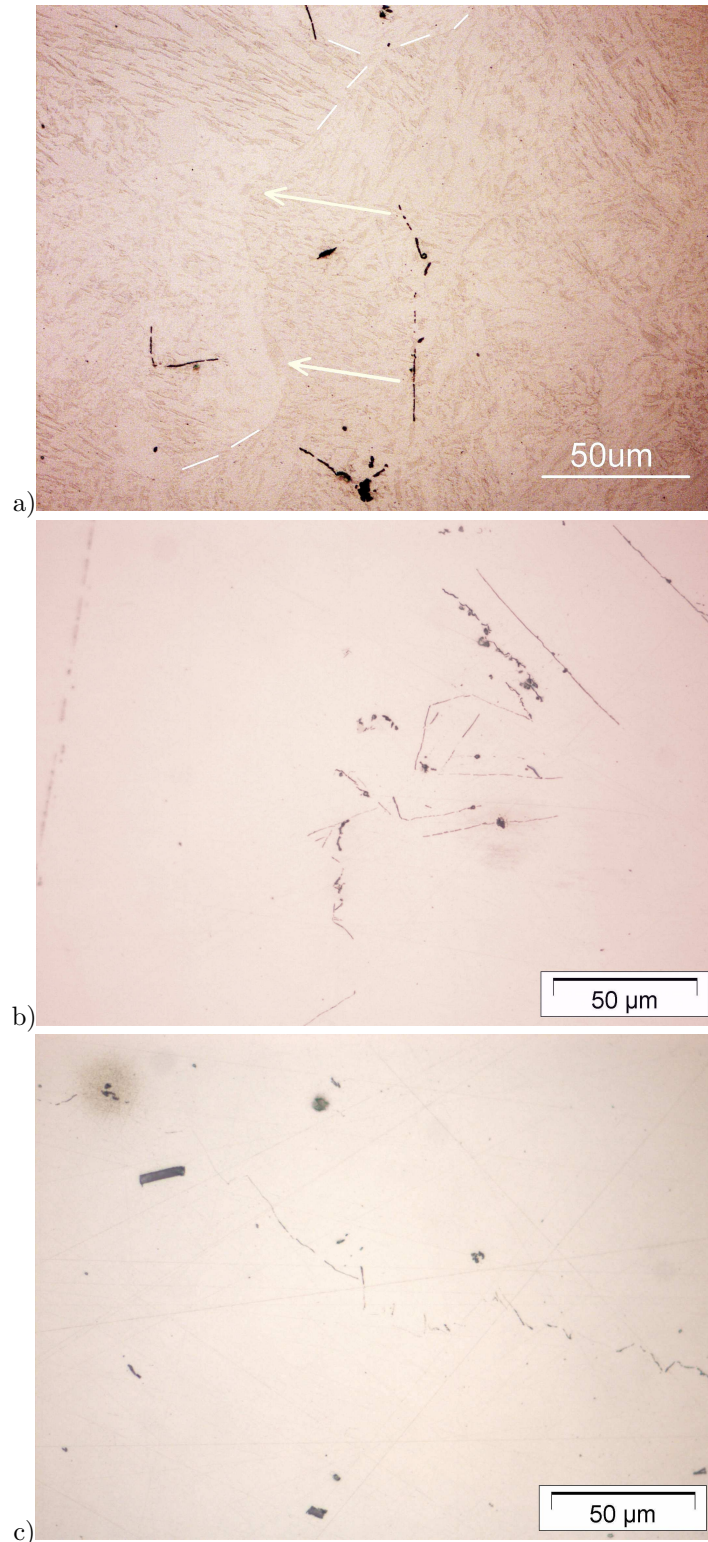


Figure 4.7: Dendritic AlN precipitation in 1.05%Al steel tested at a) 1100°C, b) 1050°C, c) 650°C. As polished section except (a) lightly etched with Nital. These observations were confirmed by SEM - Figure 5.8. Note how at 1100°C (a) the austenite grain boundary has managed to migrate from the AlN as indicated by the arrows.

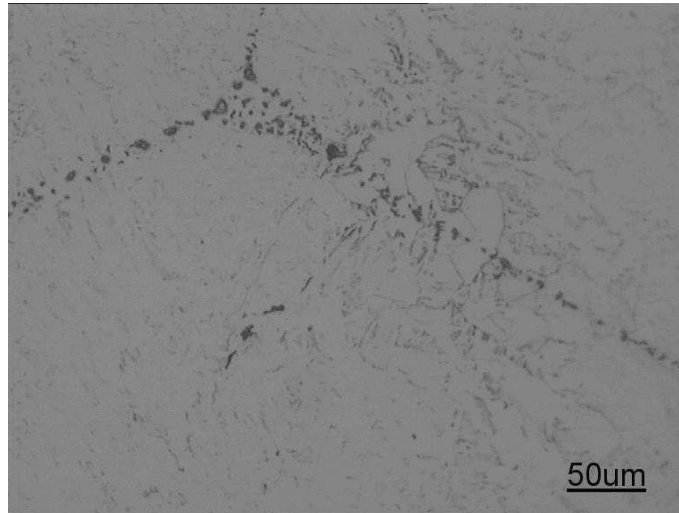


Figure 4.8: Steel 2 tested at 950°C. Higher magnification photograph of the particles at the austenite grain boundaries 1.05%Al steel (Unmelted test with R of A 59%). Nital etch. Reproduced from [179]. Presumed by Kang[179] to be AlN.

dendritic grain boundary AlN seen in this examination, Figure 4.7. Recrystallisation occurs at ductilities above 80% <sup>2</sup>.

---

<sup>2</sup>95% R of A in sample 105-2-1-700-uD and 83% in sample 105-2-1-1100-uM

Table 4.3: List of grain sizes for the unmelted and melted grain sizes in the 1.53%Al steel. Grain size average excludes samples with DRX. (P) indicates samples with porosity,  $\phi$  is the original diameter of the specimen.

Test temp( $^{\circ}$ C)	Melted sample grain size ( $\mu$ m)	Unmelted sample grain size ( $\mu$ m)	$\sim$ No. grains across the $\phi$	Sample name
650		107 (P)	37	3-650uD
700		114	35	3at700uM
750	182		22	10at750-2nmD
750		134 (P)	29	3-750-10uF
800		188	21	3-800-uD
850		242	16	3at850-uM
950		162 (P)	24	3-950-2uD
1100		79 (DRX)	50	3-1100-1uD
Average	182	158 $\pm$ 51		

### 1.53% Aluminium steel

In contrast to the 0.05 and 1%Al steel, the grain size in the unrecrystallised state for the 1.5%Al steel was much finer ( $161\mu$ m). When dynamic recrystallisation occurred the grain size refined further. A good correlation between grain size and R of A was found for this high (1.53%) Al steel in the unmelted samples in the absence of DRX, Figure 4.9. The regression with the DRX samples may be found in Figure B.4, page 249. While this indicates that grain size and R of A are strongly related, grain size may not be the only variable that significantly affects the R of A. This will be discussed further in Section 8.3.4 and 8.3.5, page 204–204.

The predominant macro-inclusions were hexagonal plate AlN (Figure 4.10) and these were present at all test temperatures, Figure 4.11. This indicated a of loss of effective Al alloying.

Additionally a limited amount of dendritic AlN was observed, Figure 4.12. Hexagonal plate grain boundary precipitation was more prominent than dendritic AlN in this steel, Figure 4.13, reproduced from [179]. Recrystallisation occurred at high (1100 $^{\circ}$ C) test temperatures and high ductility (97%R of A), and confirmed that DRX occurred with HTDR, Figure 4.14a, but it is less clear whether this occurred at lower temperatures (700 $^{\circ}$ C), Figure 4.14b. This is discussed further in Section 8.5.4, page 223.

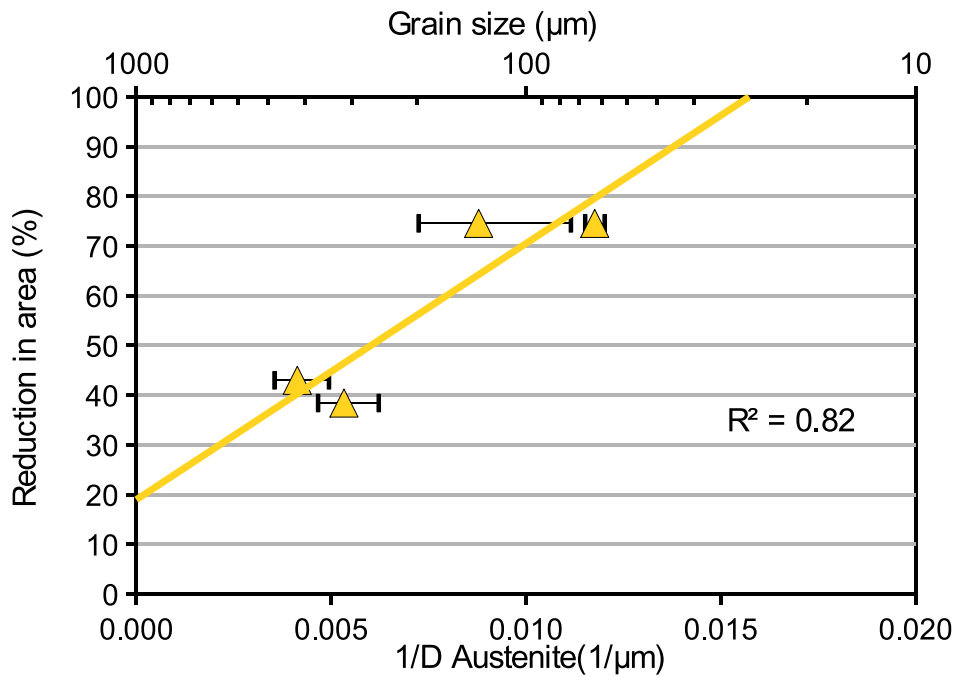


Figure 4.9: Relationship between grain size and R of A in the 1.53%Al steel (regression only for unmelted tests without DRX). A good relationship exists between R of A and austenite grain size for the unmelted samples. Grain size is remarkably finer than the other steels. The error bars show the standard deviation for each sample, whereas the  $R^2$  indicates the goodness of fit of the data to the line. Regression inclusive of the DRX samples may be found in Figure B.4.

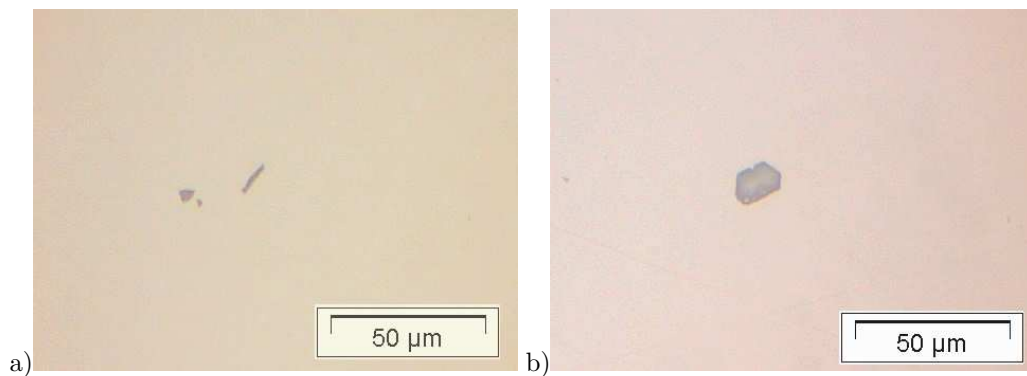


Figure 4.10: AlN precipitation in as cast 1.53%Al steel, unetched.

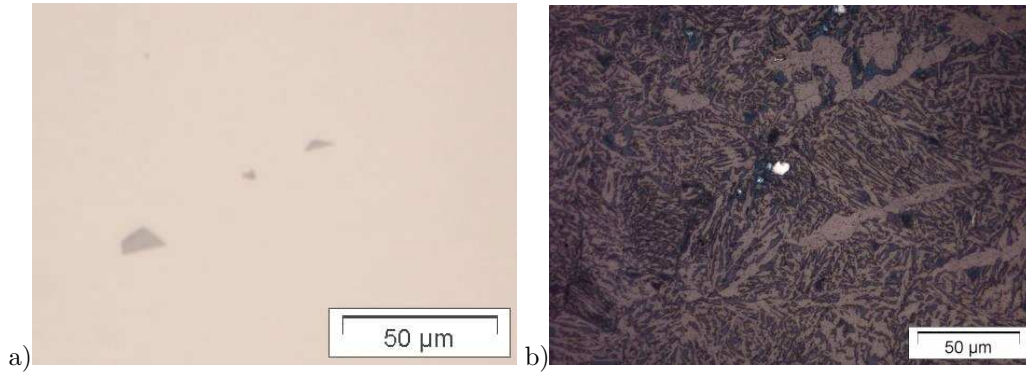


Figure 4.11: AlN precipitation in 1.53%Al steel ‘unmelted’ and tested at 800 and 1100°C. a) unetched and b) nital etched and carbon coated.

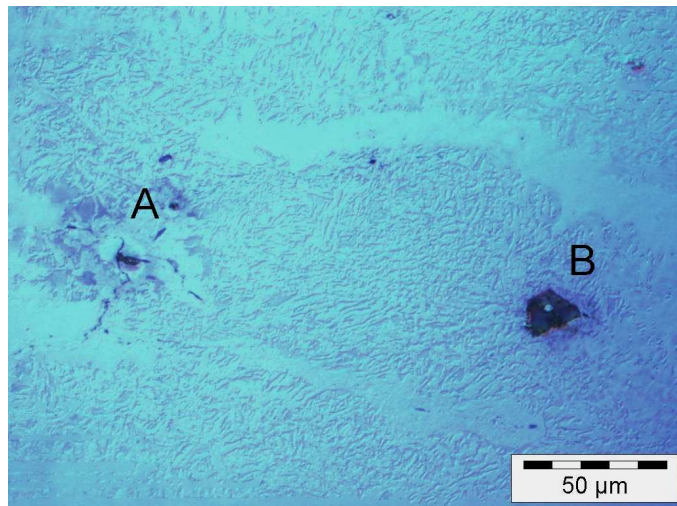


Figure 4.12: OM image (using Normarski interference microscopy) showing (A) dendritic AlN precipitation (B) plate AlN in unmelted 1.53%Al steel, tested at 850°C, light etch.

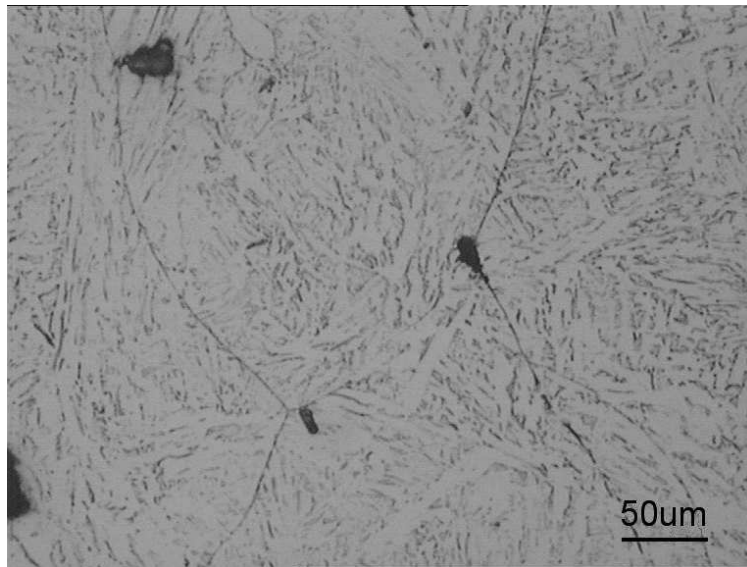


Figure 4.13: Steel 3 tested at 1100°C. Steel is now fully austenitic still showing a few particles at the boundaries. Nital etch. R of A 97% ( $A_{e3}$  1069°C) from [179] 1.53%Al steel.

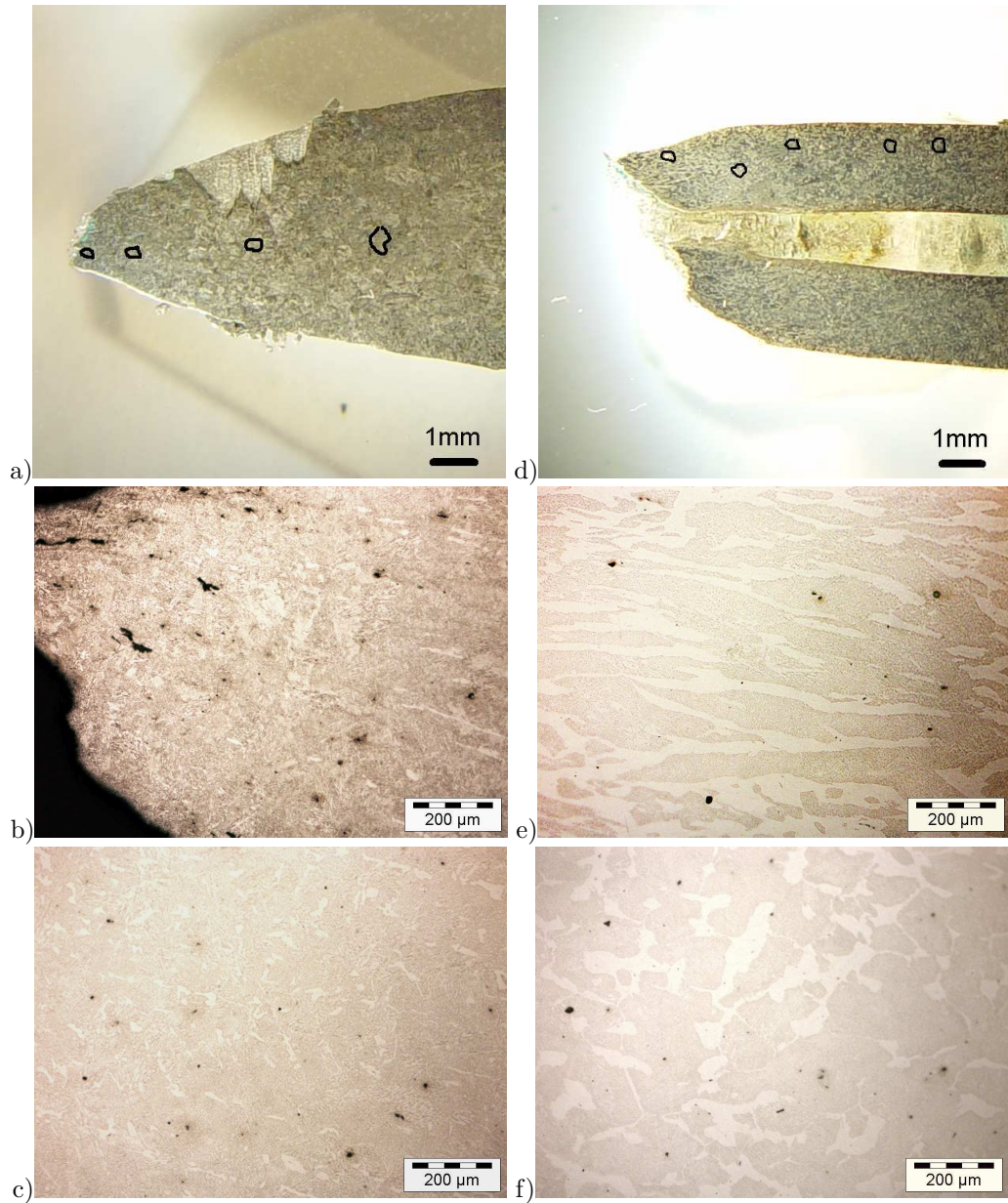


Figure 4.14: 1.53%Al steel, a) recrystallisation at the fracture tip of sample ‘unmelted’ and tested at 1000°C (97% R of A) with b) tip and c) bulk grain size enlarged, compared with d) non-recrystallised fracture tip of sample melted and tested at 700°C(75% R of A) with e) tip and f) bulk grain size enlarged. Light nital etch. DRX occurred in (a) only.

### 4.3 General remarks on the optical microscopy

HTDR occurs at high ductility and corresponds to DRX. At the low Al contents the fracture is purely intergranular, while failure is a combination of intergranular and transgranular fracture at higher Al contents. While there is a fair to good relationship between grain size and ductility in the 0.05 and 1.53%Al steels, the merits of this comparison (for instance, that it is not done at a single temperature) are discussed further in Section 8.3.4 page 204. The finer grain size in the 1.53% steel makes this a more promising steel to cast in spite of the presence of a limited amount of precipitation of dendritic AlN on grain boundaries. The poor ductility in the 1.05%Al steel is probably due to a combination of grain size and dendritic AlN precipitation at the grain boundaries. There are two mechanisms of failure at work, HTDR and the intergranular/trans granular fracture. The austenite grain size prior to tensile testing is expected to influence the ductility in the case of the ig/tg fracture but not in the case of the HTDR. The DRX samples are thus not included in the the grain size - ductility correlations (Figures 4.3, 4.6 and 4.9).

### 4.4 Conclusions of the optical microscopy analysis

1. The low R of A fracture behaviour varies from intergranular fracture in the 0.05%Al steel to a mixture of intergranular and transgranular fracture at higher Al levels.
2. The correlation between inverse grain size and ductility in the 0.05% and 1.5%Al steel has a goodness of fit of  $R^2=0.76$  and  $0.82$  respectively. This indicates that the grain size and R of A are strongly related but that grain size may not be the only variable that significantly affects the R of A. In the case of the 1.05%Al steel the grain size is a less significant contributor to R of A than in the high and low Al steels. It is suggested that, in the case of the 1.05%Al steel the dendritic AlN is the cause of the poor ductility. The grain size in the 1.53%Al steel is significantly finer than for the lower Al steels.
3. Large dendritic AlN precipitation ( $25\mu\text{m}$  in length) is seen in medium and high Al steels, most often along the austenite grain boundaries in the 1%Al steel and this is expected to widen the trough.
4. DRX is observed above  $1050^\circ\text{C}$  in samples that had higher than 80% R of A and HTDR fractures.

## Chapter 5

# Scanning Electron Microscopy Analysis

### *Summary of scanning electron microscopy analysis*

This section deals with the extensive SEM analysis that was performed between June 2007 and August 2009. Hexagonal plate AlN was observed, embedded in the dendrites of the pores in the 1.05 and 1.53%Al steel which indicated that AlN was stable or formed above the solidus. While the ductility troughs and fracture behaviour were similar for the low (<0.05%Al) and high (1.53%Al) samples, the extended trough in the 1%Al steel was attributed to the copious precipitation of dendritic AlN. This dendritic AlN was found at all temperatures (up to 1100°C), in both high and low ductility samples. The fracture type in the trough was intergranular mvc in the 0.05% and 1.5%Al samples. However, in the 1%Al material, intergranular rock candy fracture predominated.

## 5.1 Introduction

The importance of the fracture surface is that it reveals the features that resulted in final failure. The combination of moderately high resolution and depth of field that is achieved by SEM makes it ideal for studying the fracture surface of the tensile specimens. Additionally it can be coupled with elemental analysis and, while sample preparation is simple, standard resolution is limited to a precipitate size larger than  $\sim 100\text{nm}$ . Some of the work was supplemented by using a FEG-SEM with an exceptionally high resolution of 0.67nm.

The SEM study was helpful for confirming the presence of porosity which was found in samples subject to macro OM. While a high level of porosity was encountered (see Section 3.3, page 110), it was still assumed that the precipitation and fracture behaviour in the

porous samples would be similar to the non-porous for any particular test temperature and therefore both porous and non-porous samples were studied.

## 5.2 Experimental procedure

Samples were selected from the hot ductility curves from the bottom of trough and compared to the high ductility samples at the low and high temperature edges of trough. The fracture was characterised in terms of the meso- and micro- scale features as well as precipitation and the presence of ferrite. The fracture samples were trimmed to fit in the sample/holder pole piece gap, and studied with various Jeol instruments, some with energy dispersive spectroscopy (EDS) as well as a Zeiss FEG-SEM. While some EDS systems were able to analyse for N and O, other EDS systems on the Jeol microscopes lacked thin window systems so that the N and O peaks were absent from the spectra.

## 5.3 Results

The observed features are described in the following list and figures, whilst the specific types of failure, microstructure and second phase particles are shown in Table 5.1- 5.7:

1. Meso-scale fracture type failures, as illustrated in Figure 5.1:
  - (a) intergranular (ig), Figure 5.1a
  - (b) transgranular (tg), Figure 5.1b
  - (c) high temperature ductile rupture (HTDR), Figure 5.1c
  - (d) porosity (P), Figure 5.1d.
2. Micro scale observations of the fracture surface, Figure 5.2:
  - (a) grain boundary sliding (gbs), Figure 5.2a
  - (b) micro-void coalescence (mvc), Figure 5.2b
  - (c) rock candy (rc), Figure 5.2c.
3. Precipitation (Figures 5.3 and 5.4)
  - (a) plate, Figure 5.3a,b
  - (b) needle, Figure 5.4a
  - (c) dendritic AlN, Figure 5.4b

(d) MnS with oxides, Figure 5.4c

4. Thin films of ferrite at grain boundaries, Figure 5.5.

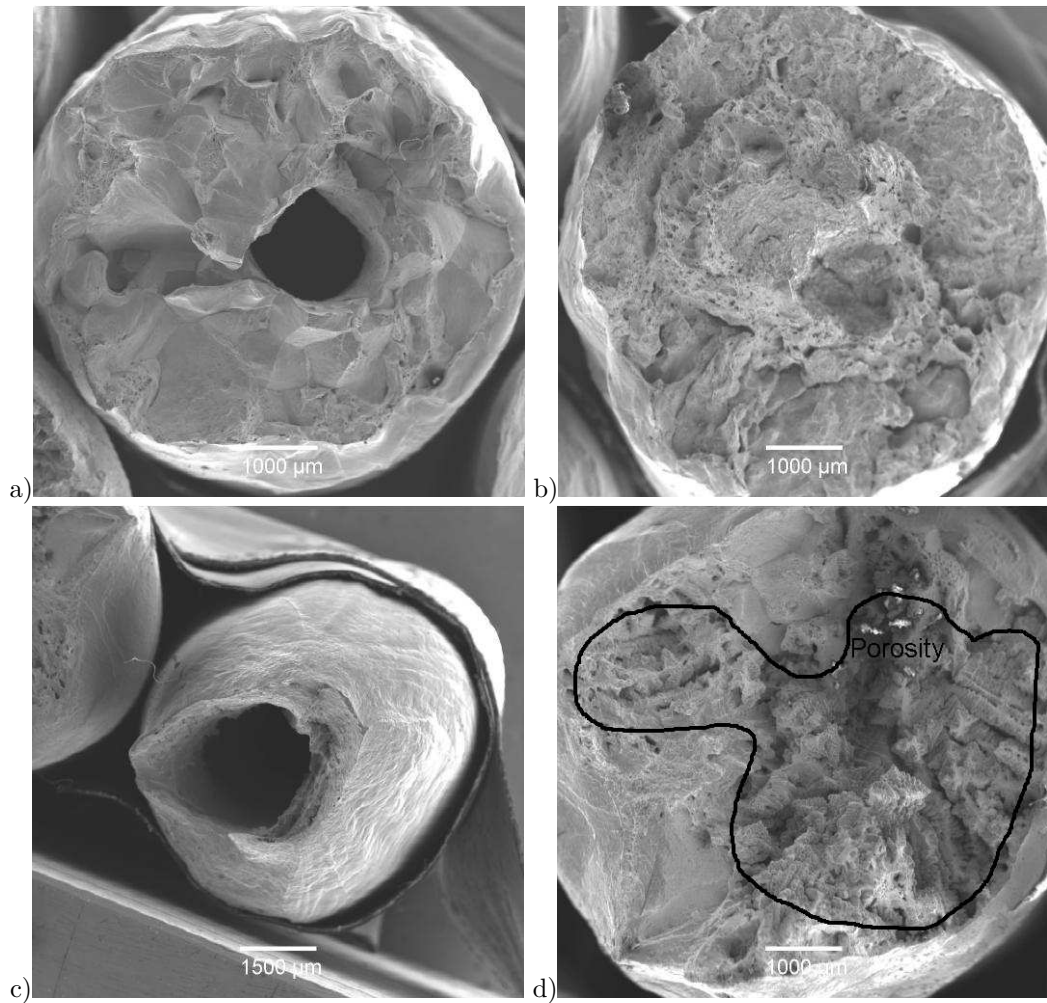


Figure 5.1: Illustration of the types of meso-fracture surfaces in ductility testing: a) intergranular (ig), b) transgranular (tg), c) HTDR d) porosity (P).

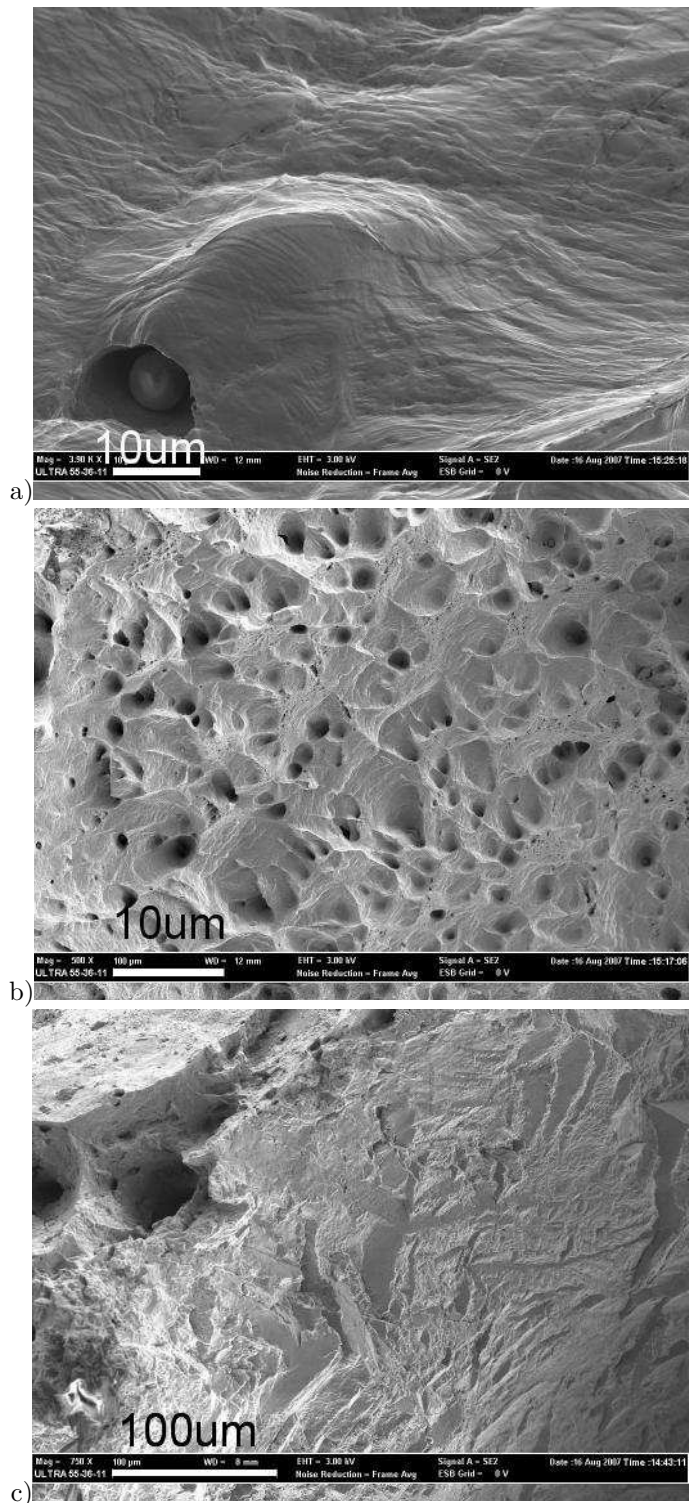


Figure 5.2: Illustration of types of micro-fracture surface in ductility testing: a) grain boundary sliding (gbs) where the ridges are the successive positions on grain surfaces as they slide past each other, b) micro-void coalescence (mvc), c) rock candy fracture (rc). The samples used in this categorisation were from the following conditions: a), b) steel 9 tested at 700°C, c) steel 2-2 tested at 1000°C.

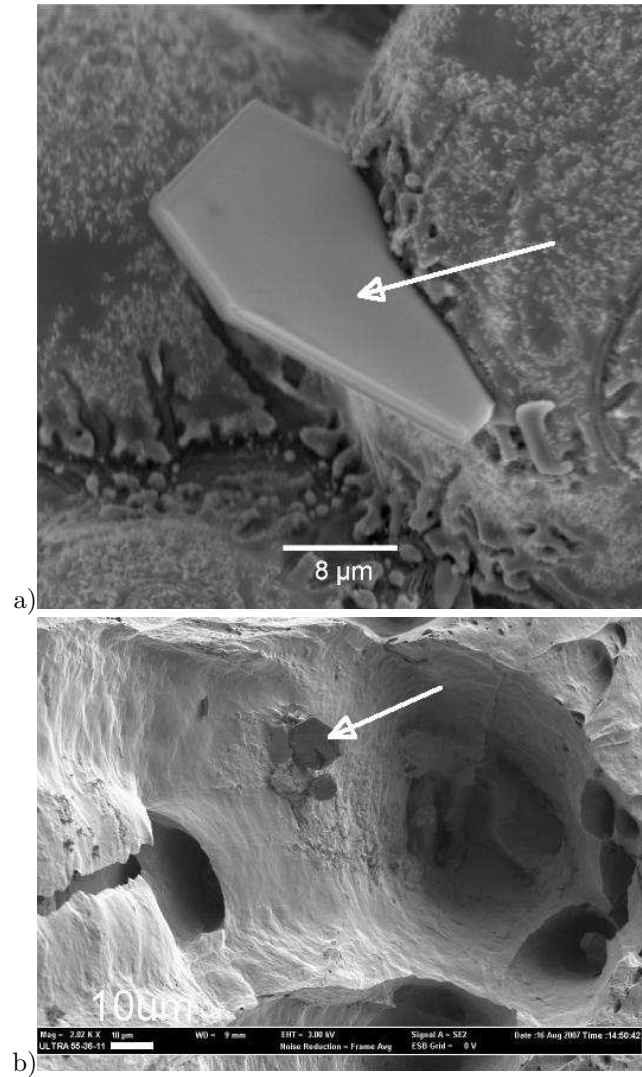


Figure 5.3: Illustration of hexagonal AlN precipitates observed with SEM a) a region showing porosity b) on fracture surface. Steels used in the categorisation were a) Steel 3 at 1000°C, b) steel 3 at 700°C. Both samples were heated to 1460°C so are ‘unmelted’ tests.

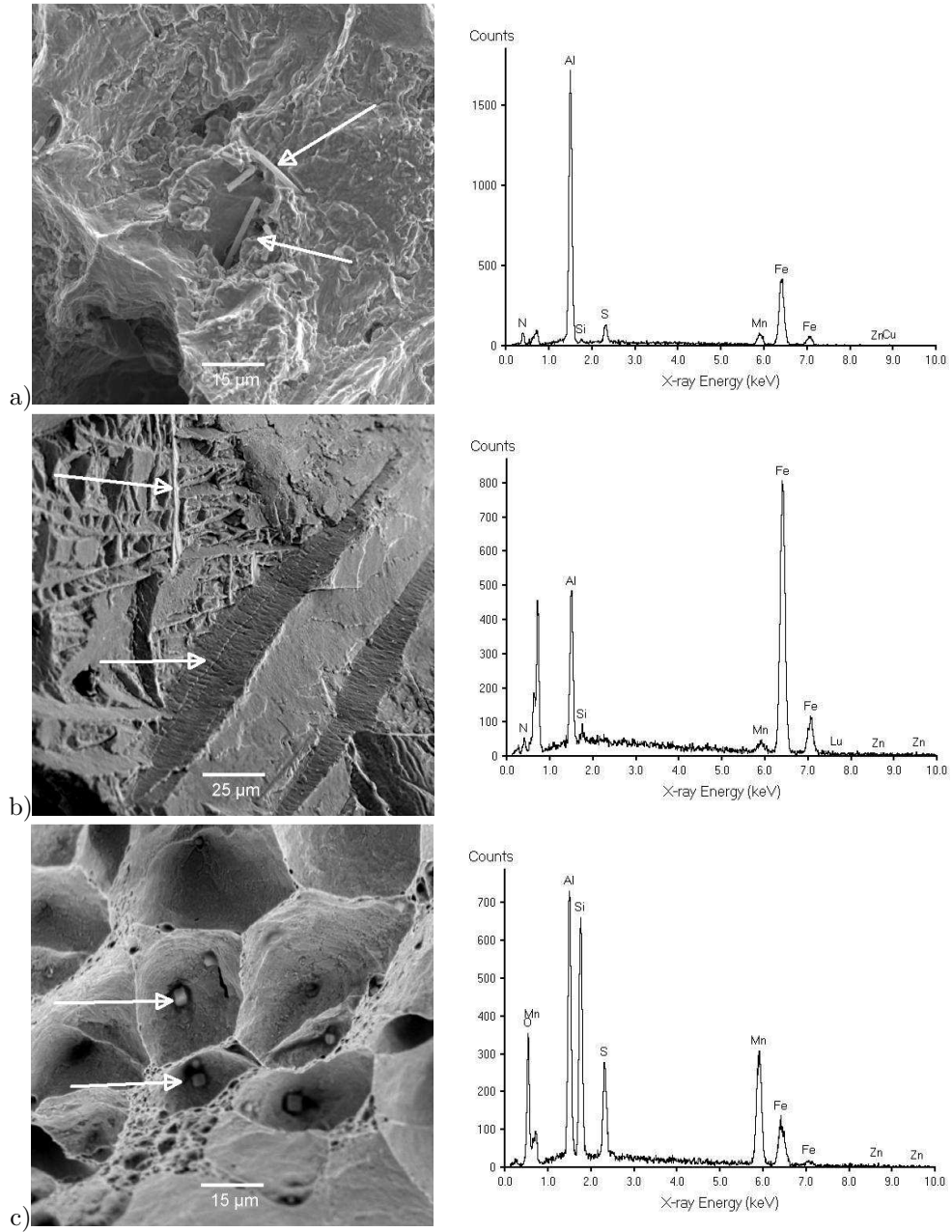


Figure 5.4: Illustration of types of precipitates and analysis observed with SEM a) needle AlN, with analysis, b) dendritic AlN, with analysis, c) MnS and oxides with analysis. Steels used in the categorisation were a) steel 2-1 ‘unmelted’ and tested at 1000°C, b) steel 2-2 melted and tested at 1000°C and c) steel 9 melted and tested at 700°C.

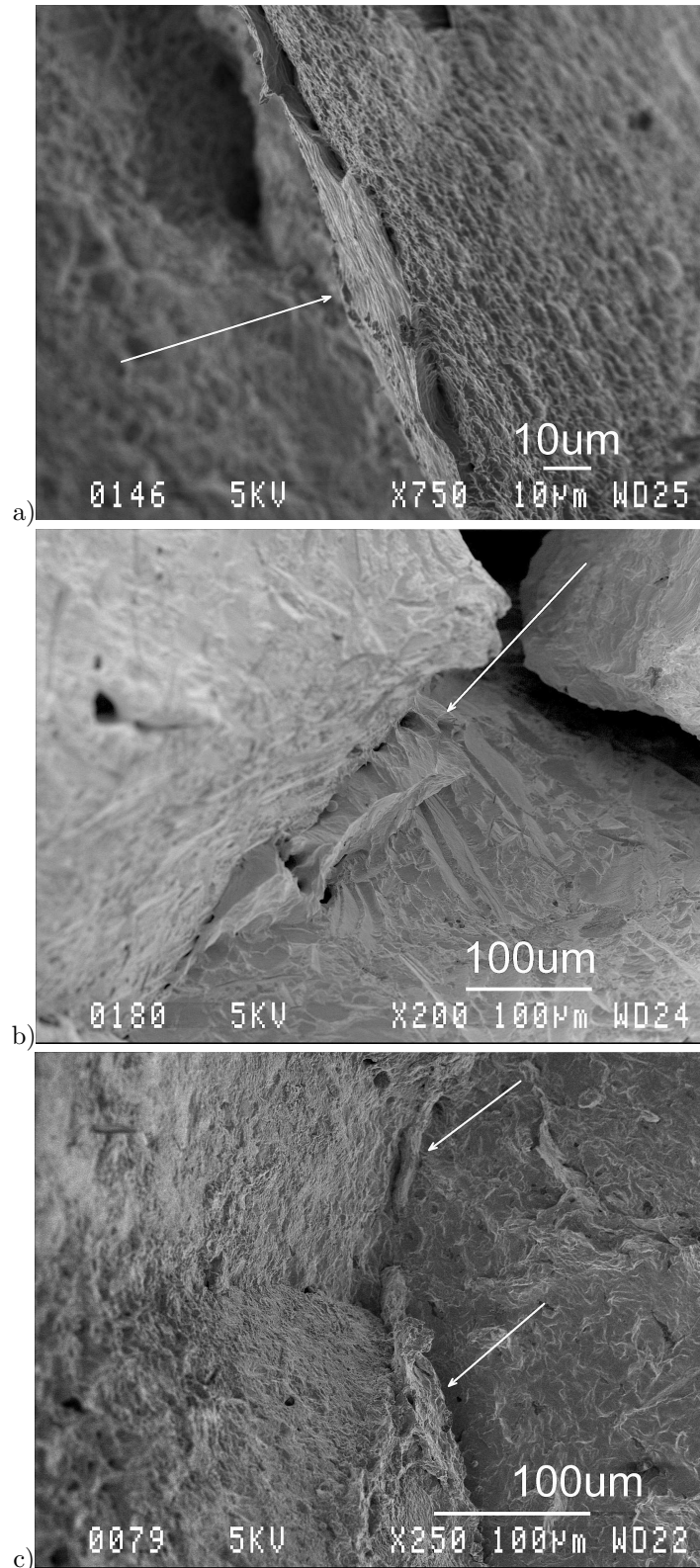


Figure 5.5: FEG SEM observation of pro-eutectoid ferrite in a) 0.05%Al steel at 800°C, b) 1.05%Al steel at 800°C and c) 1.53%Al steel at 950°C. Arrows indicate wedges of deformation induced ferrite formed prior to fracture. Steels used in the categorisation were a) steel 1 ‘unmelted’ and tested at 800°C, b) steel 2-1 ‘unmelted’ and tested at 800°C and steel 10 melted and tested at 950°C.

Table 5.1: SEM observations for 0.05%Al steel, ‘unmelted’ tests.

Test temp(°C)	%R of A	meso-structure	micro-structure	2nd phase particles and $\alpha$	sample
650	68	ig	mvc, gbs	$\alpha$ 15-20 $\mu$ m plate AlN 4 $\mu$ m	0059650uM
750	32	ig	mvc, gbs		00597501sO
750	27	ig	mvc	no $\alpha$	005975011O
800	42	ig	mvc	$\alpha$ 3.2 $\mu$ m	00518002uD
850	50	ig	mvc,gbs	$\alpha?$ 26-78 $\mu$ m	0059850uM
950	78	ig	mvs,gbs		00599501uD
1000	92	HTDR	mvc,gbs		00591000uM

Table 5.2: SEM observations for 0.05%Al steel, melted tests.

Test temp(°C)	%R of A	meso-structure	micro-structure	2nd phase ppt and $\alpha$	sample
650	75	ig, P=49	mvc,gbs		00596501mF
700	56	ig, P=78%	gbs, mvc	oxides 5-9 $\mu$ m MnS 7-8 $\mu$ m	00597002mJ
750	45	ig	mvc	$\alpha$ 10-32 $\mu$ m ppt 0.5-0.8 $\mu$ m	00597502smD
750	50	ig, P=36%	mvc,gbs	ppt 0.5-7 $\mu$ m	00597501mD
800	64	ig, P=46%	mvc,gbs		00598001mD
850	67	ig, P=38%	mvc,gbs		00598501mF
900	63	ig, P=18%	mvc		00599001mF
1000	91	HTDR		oxides 2-5 $\mu$ m	005910002mJ

### 5.3.1 0.05% Aluminium Steel

In general the fracture was mainly intergranular, (also seen with OM), with the predominant micro features on the intergranular surfaces being mvc and grain boundary sliding, Figure 5.1a, and Figure 5.2a,b. At high temperatures where the ductility recovered, there was high temperature ductile rupture, Figure 5.1c. The summaries of all the SEM observations for this steel are given in Tables 5.1 and 5.2. The porosity (36-78%) in the melted samples points to the difficulties in achieving a valid %R of A in the these samples.

The differences between the grain size on the OM sections and the fracture surfaces were comparable, but not exact, refer to Table 5.3. SEM measurements of grain size were significantly higher. It is not clear why this should be but is probably related to the coarseness

Table 5.3: Grain sizes by SEM fracture surface and optical c/s for 0.05%Al steel, indicating that grain size tends to be over estimated with SEM.

Test temp (°C)	OM c/s grain size ( $\mu\text{m}$ )	SEM fracture grain size ( $\mu\text{m}$ )	sample
650	1172 $\pm$ 97.9	1419 $\pm$ 277	0059650uM
750	1270 $\pm$ 355	2863 $\pm$ 855	00597501sN
950	1122 $\pm$ 165	1459 $\pm$ 169	00599501uD

of the grain size and the small number of grains involved in the calculation.

In summary, the worst ductility at 750°C was attributed to intergranular mvc. Ferrite was seen up to 800°C, but it did not correspond to the lowest R of A of 30% as given at 750°C compared to 50% R of A at 850°C. However, precipitation is also important in controlling ductility, so that the temperature giving lowest R of A will be dependant on both the influence of DIF and precipitation.

### 5.3.2 1.05% Aluminium steel

Tables 5.4 and 5.5 are summaries of all the observations from the fracture surfaces. The strongest contributor to poor ductility was the presence of the rock candy micro-fracture surface with dendritic AlN precipitation, both intergranularly or transgranularly, indicating that this precipitation was exceptionally pernicious for ductility. This precipitation was observed throughout the temperature range examined. The grain size for this steel was coarse and similar to the low Al containing TRIP steel.

The width of the AlN dendrites/plate was estimated from the fracture surfaces (this will not be accurate as measurements are at an angle and are expected to be larger than the true values), they were between 200-800nm wide, as in Figure 5.6. In the “unmelted” samples the plate AlN was seen in the regions showing porosity (Figure 5.7) - indicating that it formed above the solidus, and, in the case of the 1.05%Al steel the unmelted samples appear to have at least partially melted. Once again there was porosity in the samples. The poor R of A values between 750-950°C were attributed to intergranular rock candy fracture which was caused primarily by coarse dendritic AlN precipitation. Needle and plate AlN appear to be less detrimental as there was less observed on the fracture surface. The hexagonal plate AlN precipitates form when the steel is in the molten state as can be seen in Figure 5.7. Since the ferrite is present at 800°C it is likely that this ferrite contributes to the reduction in ductility, although it is not the only contributor.

Table 5.4: SEM observations for 1.05%Al steel, 'unmelted' samples.

Test temp(°C)	%R of A	meso-structure	micro-structure	2nd phase ppts and $\alpha$	sample
700	57	ig	gbs, mvc	needle AlN 7 $\mu$ m	10523700uD
750	23	ig	gbs, rc	dendritic AlN	105227501uD
800	35	ig P=38%	rc	dendritic AlN, plate AlN 8 $\mu$ m $\alpha$ 33-60um,	105218001uD
800	34	tg,ig P=74%	rc mvc, gbs	dendritic AlN	105228001uD
850	29	ig=20% tg=79%	mvc, gbs rc	possible $\alpha$ 0.3-1 $\mu$ m, dendritic AlN	10521850uM
900	47	ig P=37%	rc, mvc, gbs	dendritic AlN	10521900uD
900	34	ig tg P=2%	mvc, gbs rc	$\alpha$ 40-75 $\mu$ m, needle AlN 3-18 $\mu$ m, dendritic AlN, cuboid AlN 9-12 $\mu$ m	105239001uD
950	35	ig, tg	gbs, mvc,		105239503uD
1000	83	ig=56% tg=44%, HTDR	mvc, rc	needle AlN 8-20 $\mu$ m, dendritic AlN 34 $\mu$ m	105211000uM
1000	52	ig P=7%	mvc, gbs	hex plate AlN 5 $\mu$ m, needle AlN	1052110003uD
1100	44	ig P=5%	rc, mvc,	dendritic AlN	105211050uD
1100	83	HTDR, ig	mvc, gbs	dendritic AlN	105211100uM

Table 5.5: SEM observations for 1.05%Al steel, melted samples.

Test temp(°C)	%R of A	meso-structure	micro-structure	2nd phase ppt and $\alpha$	sample
650	53	ig	rc, gbs, mvc	dendritic AlN	10523650mF
800	45	ig,tg	rc, gbs, mvc	dendritic AlN	10522800mJ
800	35	ig P=10%	rc	dendritic AlN	105238001mD
900	17	ig P=24%	rc	dendritic AlN	105229001mD
900	61	ig	rc, mvc	plate AlN 85-190 $\mu$ m, dendritic AlN	105239003mD
950	47	ig, tg P=27%	mvc, gbs, rc	dendritic AlN	105239501mD
1000	37	ig = 82% P= 23%	mvc, rc	cuboid AlN 10 $\mu$ m, hex plate AlN 12-43um, dendritic AlN, AlN in pore	1052210002mJ

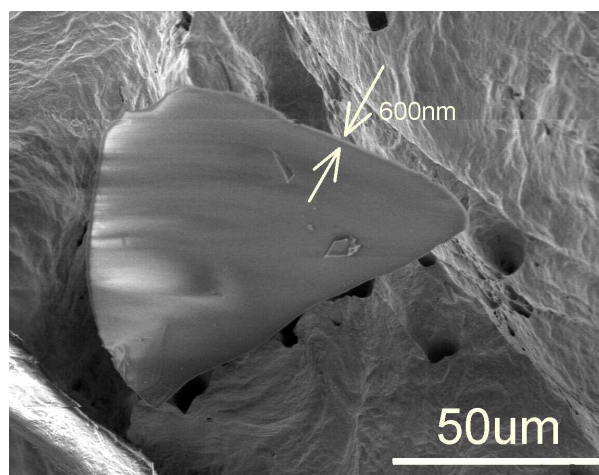


Figure 5.6: 1.05%Al steel, showing the thickness of the AlN dendrites. Steel 2-3 melted and tested at 900°C.

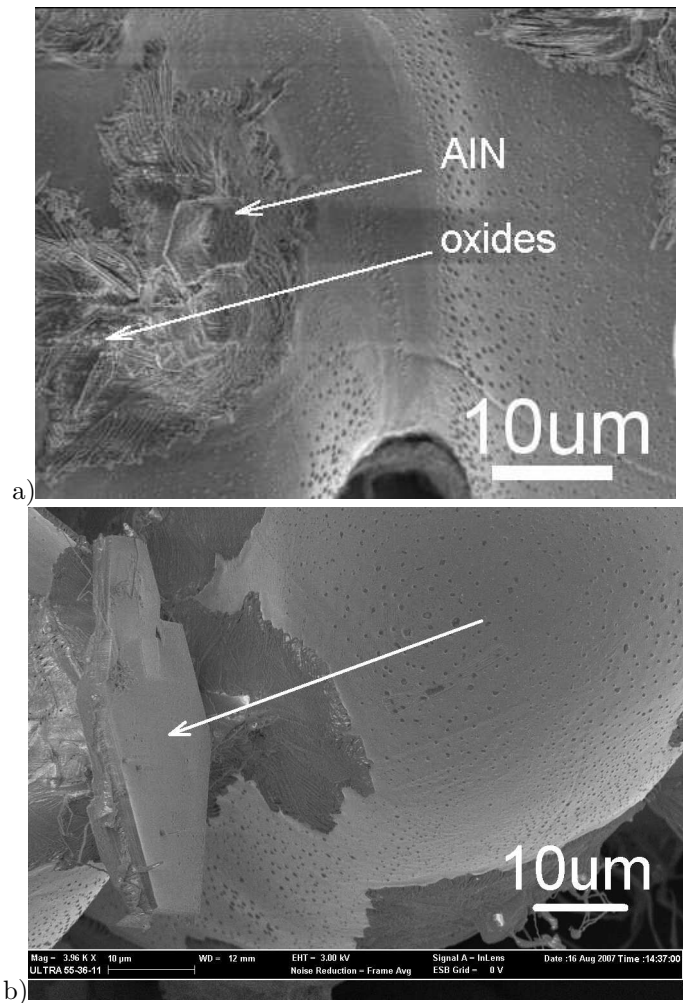


Figure 5.7: Hexagonal plate AlN in regions of porosity in a) ‘unmelted’ and b) melted 1.05%Al steel. There are oxide filaments around AlN in (a). Steels samples were a) steel 2-1 ‘unmelted’ tested at 800°C, b) steel 2-2 melted, tested at 1000°C.

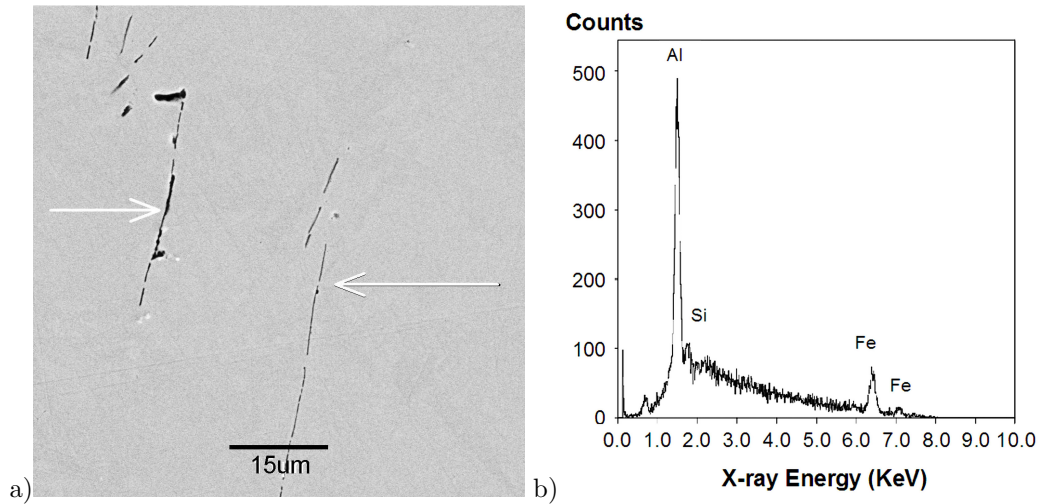


Figure 5.8: Cross section of a) dendritic AlN in ‘unmelted’ 1.05%Al steel tested at 1100°C with b) analysis (sample 10521at1100uM). This confirms the presence of AlN in Figure 4.7, page 127. Steel 2-1 ‘unmelted’ and tested at 1100°C.

To confirm the presence of dendritic AlN seen along grain boundaries in the optical cross sections (Section 4.2.2, Figure 4.7, page 127), the cross sections were also analysed with SEM to determine the composition of the precipitates, Figure 5.8. These results indicated that dendritic AlN was found at all temperatures (up to a maximum of 1100°C), in both high and low ductility samples.

### 5.3.3 1.53% Aluminium steel

All observations from the fracture surfaces of the 1.53%Al steel are summarised in Tables 5.6, 5.7 for the ‘unmelted’ and melted states respectively. Very little dendritic AlN precipitation was noted. Porosity was present in many of the samples. Ferrite was also seen at 950°C in the melted sample. Also, in the case of the 950°C test temperature<sup>1</sup> the grain size in the melted material was larger (1068µm) than in the ‘unmelted’ (690µm) sample. The grain size appears coarser in the SEM observations, Table C.3, compared with the OM results (Figure 4.9, page 130). Hexagonal plate AlN particles were observed in regions showing porosity in 1.5%Al steel, Figure 5.9. In the 1.53%Al steel the poorest ductility (minimum R of A of 38% at 800°C) was not associated with the small amount of rock candy fracture or ferrite observed, rather it is associated with intergranular mvc, Figure 5.10.

<sup>1</sup>‘Unmelted’ - 1539502uD and melted - 153109503mD have 690µm and 1068µm grain sizes respectively.

Table 5.6: SEM observations for 1.53%Al steel, 'unmelted' samples.

Test temp(°C)	%R of A	meso-structure	micro-structure	2nd phase ppt and $\alpha$	sample
700	75	tg	mvc	hex plate AlN 6,12 $\mu$ m	15337002uM
700	71	tg	mvc	needle AlN plate AlN 8,10 $\mu$ m	1533700uD
800	38	ig tg= 32%	mvc, gbs	plate AlN 20 $\mu$ m $\alpha$ 10 $\mu$ m	1533800uD
850	43	ig, tg	mvc, gbs	plate AlN 16 $\mu$ m	1533850uM
950	58	ig, P=52%	mvc, gbs	plate AlN 6-13 $\mu$ m	15339502uD
1000	53	ig, P=38%	mvc, gbs	hex plate AlN 27 $\mu$ m	15331000uM

Table 5.7: SEM observations for 1.44%Al steel, melted samples.

Test temp(°C)	%R of A	meso-structure	micro-structure	2nd phase ppt and $\alpha$	sample
650	55	P=26%, ig, tg	mvc rc	dendritic AlN cuboid AlN 8 $\mu$ m plate AlN in porosity 11 $\mu$ m needle AlN 4 $\mu$ m	153106501mD
750	74	tg, some ig	mvc	cuboid AlN 8 $\mu$ m	153107502mD
950	47	ig, P=17%	mvc, gbs, rc	$\alpha$ 4-17 $\mu$ m needle and plate AlN, in pore	153109503mD

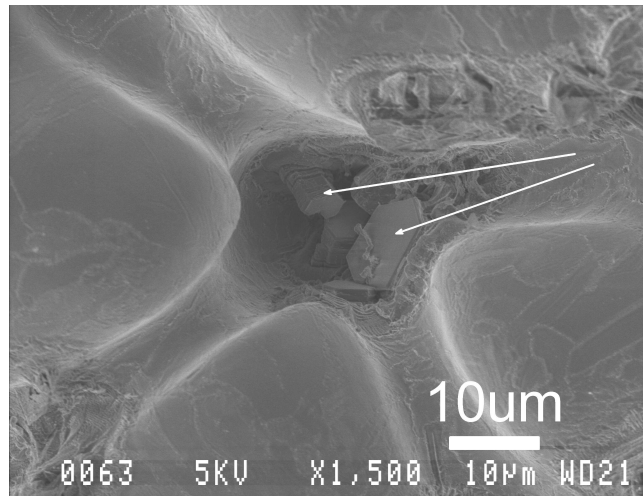


Figure 5.9: Hexagonal AlN in porosity in 1.53%Al steel. Steel 10 melted and tested at 650°C.

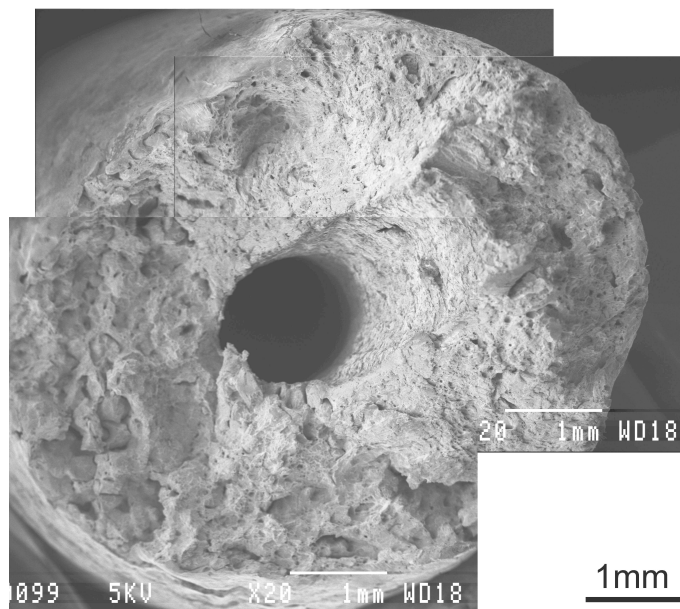


Figure 5.10: Fracture surface of 1.53%Al steel sample tested at 800°C, showing that the poorest ductility (R of A of 38%) is due to intergranular mvc. Steel 3 'unmelted' and tested at 800°C.

## 5.4 Conclusions of scanning electron microscopy analysis

1. The ductility trough and fracture behaviour was similar for both the low, 0.05%Al and high, 1.53%Al samples.
2. The extended trough in the 1.05%Al steel was attributed to the copious precipitation of dendritic AlN, resulting in an intergranular rock candy failure mode, which leads to poor ductility values over a wide range of temperatures.
3. Hexagonal AlN precipitation was observed in the porosity in the 1 and 1.5%Al steel and indicated that AlN precipitation occurs in the melt.

## Chapter 6

# Transmission Electron Microscopy Analysis

### *Summary of transmission electron microscopy analysis*

In the 0.05 and 1.5 %Al steel, ductility correlates with the Nb(C,N) precipitate size, and additionally, in the 1.5%Al steel, the Nb(CN) precipitates coarsen with increasing temperature. The Nb(C,N) precipitation in the 0.05%Al steel was only found in the vicinity of the grain boundaries. In the 1%Al steel Nb(C,N) precipitate size does not appear to be related to ductility or to test temperature. The R of A is related rather to the presence of dendritic and hexagonal plate AlN precipitation. The dendritic AlN precipitation has been identified as fcc with a lattice spacing of  $a=0.460\text{nm}$  and its thickness has been estimated to be between 70 to 130nm. Hexagonal plate AlN was identified as hcp with lattice spacing of  $a=0.323\text{nm}$  and  $c=0.499\text{nm}$ .

## 6.1 Introduction

This section details the TEM analysis that was performed in the period April 2008 to August 2009. The aim of the TEM work was to gain knowledge of Nb precipitation behaviour. Since only a few samples were made available from CUL which had been fast cooled from the test temperature, only three samples of each steel at high low and intermediate temperatures were selected from the fast cooled samples. It was assumed that the precipitation and fracture behaviour in the porous samples was still representative.

## 6.2 Experimental procedure for transmission electron microscopy

Samples were sectioned (as per schematic in Figure 6.1), mounted in perspex and prepared for OM. The final polishing step was a felt cloth impregnated with  $3\mu\text{m}$  diamond paste. Only diamond paste and no colloidal silica was used in order to avoid embedding sub 100nm artifacts of 20-100nm spherical  $\text{SiO}_2$  particles. The sections were then etched with 2%

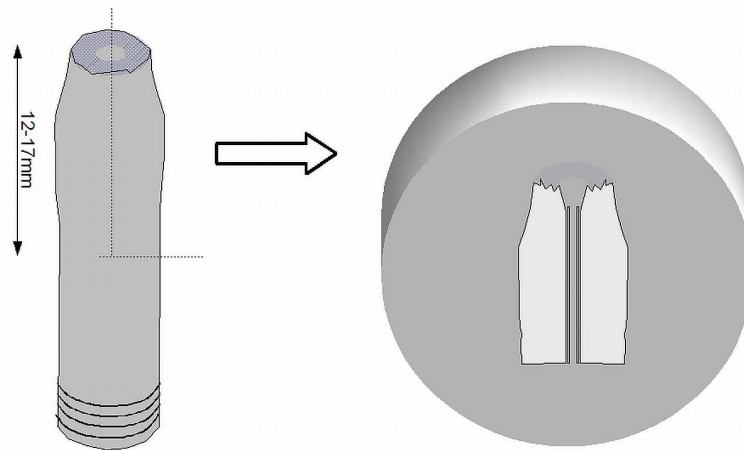


Figure 6.1: Sectioning procedure for the preparation of TEM samples. Sample section length wise and mounted in perspex.

nital and coated with a 25-50nm carbon film. Carbon coating thickness was judged by noting its colour on an aluminium foil which, at the required thickness, was red-bronze to bronze-blue. After scoring the replica into squares, the section was etched in 10% nital until the carbon replica was loose. The carbon film was collected and floated on water and caught on a copper grid (75 grids/inch). The TEM work was carried out at 160kV with a Philips CM200 equipped with EDS (super thin window, EDAX system) and CCD camera (Gatan, Erlangshen) in a low background double tilt holder. Later replicas were specifically taken in the vicinity of the austenite grain boundary, this being the region where intergranular failure occurs. Precipitation sizes were measured from the images and a statistical analysis of the precipitate distribution was performed. In order to determine if the precipitate distribution was normal, a probability plot was used (sorted precipitate size vs  $(j-0.5)/n$ ), after the manner used for the R of A values in Section 3.3, page 114. The average and standard deviations of the precipitation populations were also determined. If the difference in size between grain boundary and matrix precipitation was clear then these were treated as separate size distributions.

Table 6.1: General precipitation summary for 0.05%Al steel.

Temp. (°C)	Matrix Nb(C,N) size (nm)	Matrix Nb(C,N) distribution	Matrix Nb(C,N) sample size	AlN	sample
650	20±7.2	gaussian	34	no ppt	00592650mF
700	15±7	gaussian	90	no ppt	005 9700uM
700	no ppt in 150000μm <sup>2</sup>			no ppt	005 9700u07 r2
750	13±6	not gaussian	155	no ppt	005 97501uD
950	48±16	gaussian	137	no ppt	00519501uD
1000	18±7	gaussian	177	no ppt	005 910001uF

Table 6.2: General precipitation summary for 1%Al steel.

Temp. (°C)	Matrix Nb(C,N) size (nm)	Matrix Nb(C,N) distribution	Matrix Nb(C,N) sample size	AlN	sample
800	18±7	gaussian	36	Dendritic plate	105 21800uD
900	11±2	gaussian	42	Dendritic plate, needle	105 239001uD
1100	15±8	gaussian	29	needle	105 21at1100uM

## 6.3 Results

The observations are discussed by steel and are also summarised in Tables 6.1 - 6.3.

A plot of temperature vs precipitate sizes for all steels, Figure 6.2, shows that the sample Trip 1-950 differs from all the other steels. However, an inspection of the chemistries shows that this steel (Steel 1) contains 1.05%Si, twice the amount in any of the other steels. It is well established that Si promotes Nb(C,N) precipitation[141], which explains why this set of precipitates formed and coarsened before that of the Steel 9. Since there was only one Steel 1 sample that was analysed with TEM for precipitate size, it will be ignored for the rest of the discussion.

Table 6.3: General precipitation summary for 1.5%Al steel.

Temp. (°C)	Matrix Nb(C,N) size (nm)	Matrix Nb(C,N) distribution	Matrix Nb(C,N) sample size	AlN	sample
650	10±4	gaussian	104	needle	153 3650uDmelt
750	10±4	gaussian	150		153 375010uF melt
950	13±5	gaussian	477		153 39502uD

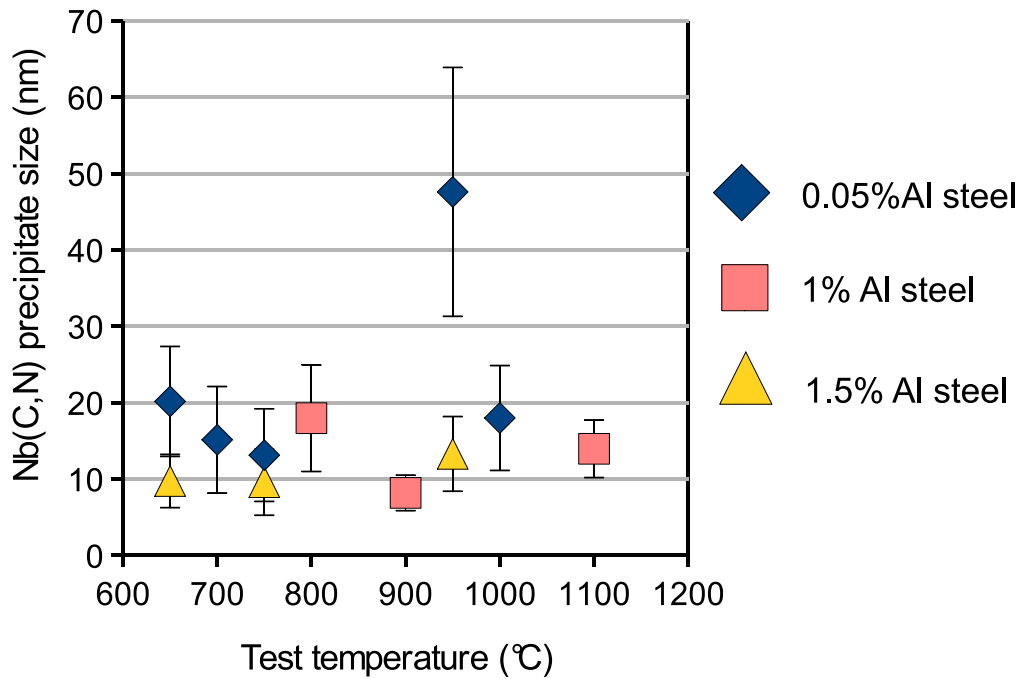


Figure 6.2: Plot of all matrix Nb(C,N) precipitate size in all steels vs temperature.

### 6.3.1 0.05% Aluminium steel

It was observed that Nb(C,N) precipitation may be absent in large areas. For instance in the sample tested at 700°C<sup>1</sup>, no Nb(C,N) was observed in a survey area of 5 grids, each 175x175µm, ~150 000µm<sup>2</sup>. With more detailed investigation it was found that the Nb(C,N) precipitation was present in the vicinity of the prior austenite grain boundary, where the ferrite forms, as shown in Figures 6.3a,b,c. On occasion extremely large (1-6µm) Nb(C,N) were also seen, Figure 6.4.

In the 750°C test<sup>2</sup> the Nb(C,N) size distribution was not normal, this is most likely due to the fact that the observations were all from areas close to grain boundaries and as a result there are two distributions (the coarser one from the grain boundary and a finer one from the grain interior/matrix) contributing to the sample population. This population was still included in further statistical analysis.

The average precipitate size showed only a small (insignificant) correlation with increasing test temperature, Figure 6.5a, but gave a very good correlation with ductility, Figure 6.5b. However, precipitation size was very fine making it difficult to monitor changes even though a large enough population of particles (n is above 90 for each test temperature) was measured. The Nb(CN) precipitates may have coarsened with increasing temperature. No AlN was observed in any of the 0.05%Al samples (n=5).

---

<sup>1</sup>TEM sample 0059700u07 repl0722

<sup>2</sup>TEM sample 00597501luD

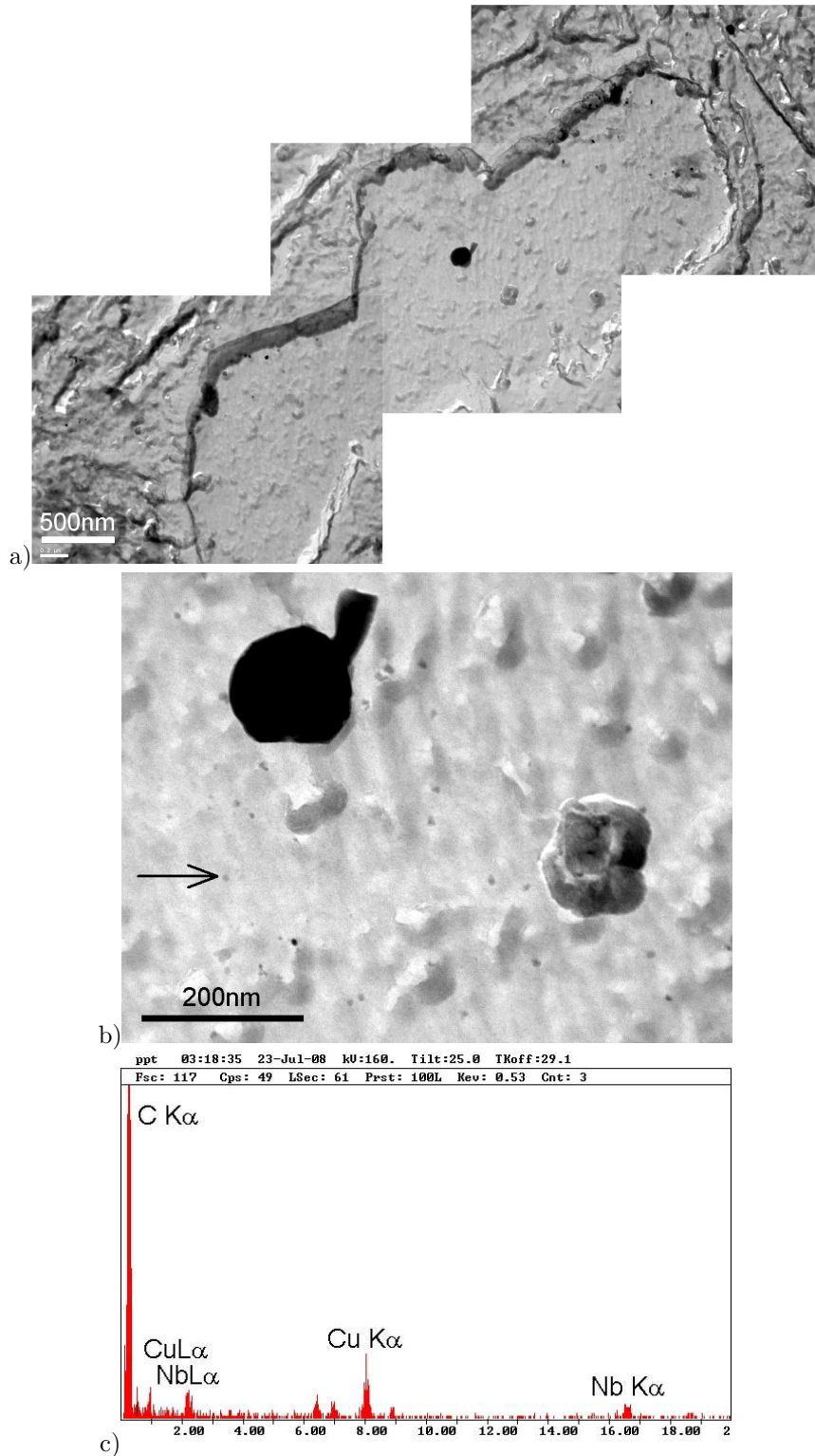


Figure 6.3: 0.05%Al steel, reheated to 1460°C and tested at 700°C (TEM sample 005-9-700-uM) a) Pro-eutectoid ferrite, with precipitation. Inset (b) is an enlargement, with (c) analysis, of fine Nb(C,N). The CuK $\alpha$  peak originates from the copper support grid.

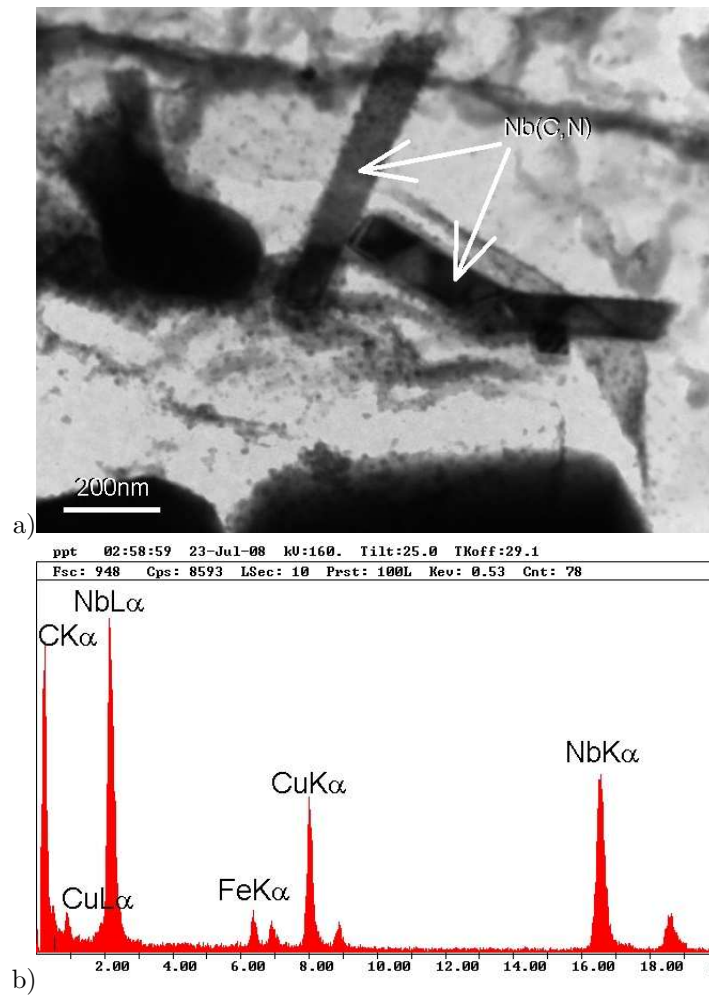
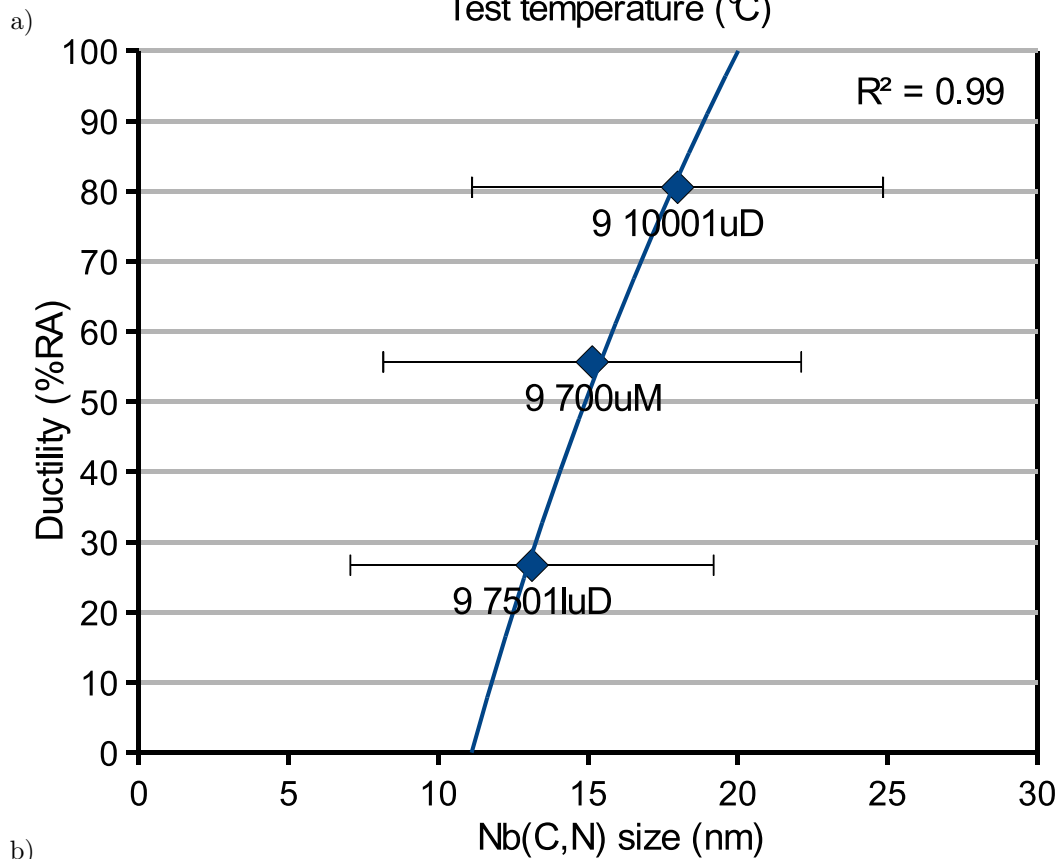
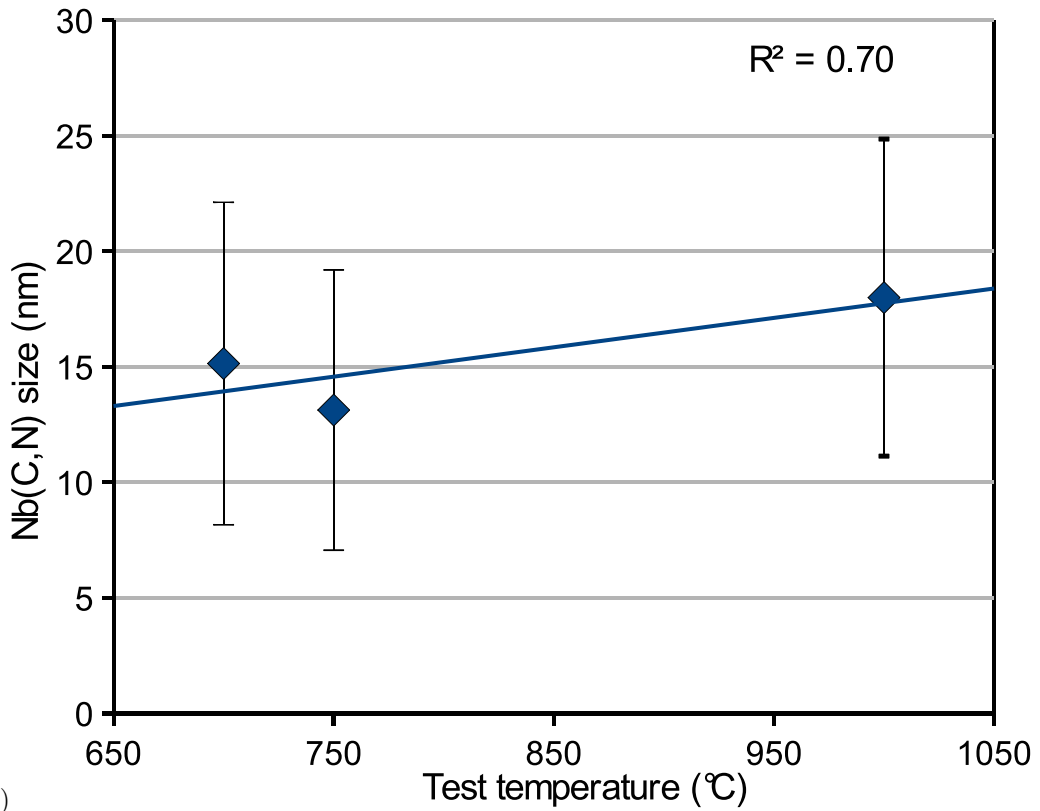


Figure 6.4: 0.05%Al steel, heated to 1520°C and tested at 700°C (TEM sample 005-9-750-2smN) showing a) large Nb(C,N) needles with b) analysis. The CuK $\alpha$  peak originates from the copper support grid.



b)

Figure 6.5: 0.05%Al steel, a) average Nb(C,N) size as a function of test temperature and b) ductility as a function of average Nb(C,N) size. Trend line for b) is a regression of the form  $y = m \log(x) + c$ .

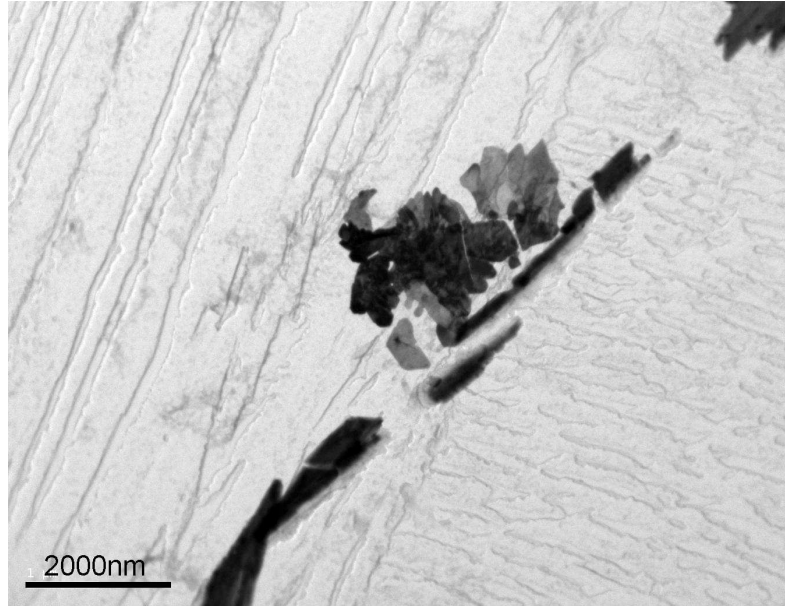


Figure 6.6: 1.05%Al steel, reheated to 1460°C and tested at 1050°C (TEM sample 2-1-1050-uD) showing dendritic AlN precipitation.

### 6.3.2 1.05% Aluminium steel

In all samples fine Nb(C,N) particles 10-20nm in size were observed and all these precipitate populations were normal. In samples tested at 950 and 1100°C, eutectic Nb(C,N) was also present. MnS and a few CuS inclusions were observed in all samples. Large dendritic AlN precipitates were successfully extracted and observed as shown in Figure 6.6.

The width of the AlN dendrites was estimated from end-on images of the dendrites/plate, as being between 70-130nm wide, Figure 6.7. Analysis of electron diffraction patterns revealed that the structure of the AlN was not the normal hexagonal close packed (hcp) structure [136], but rather a face centered cubic (fcc) type structure. The zone axis pattern seen in Figure 6.8a could be the [0001] hexagonal or the [111] fcc structure, however, the d spacing is 0.16nm rather than the expected 0.27nm for the  $\langle 10\bar{1}0 \rangle$ . Since this was  $\sim$ half the d-spacing, it was concluded that the pattern must be fcc where  $\langle 110 \rangle$  is disallowed but the  $\langle 220 \rangle$  is allowed. This was confirmed using a diffraction pattern simulation program (JEMS), Figure D.1. The lattice spacing was estimated from calibrated diffraction patterns using:

$$\frac{1}{d^2} = \frac{1}{a^2} (h^2 + k^2 + l^2). \quad (6.1)$$

where  $d$  is the d-spacing between spots and the un-diffracted spot on the diffraction pattern and  $h, k, l$  are the spot indices, the values being obtained from the diffraction patterns in Figure 6.8. It was found that  $a = 0.460\text{nm}$ .

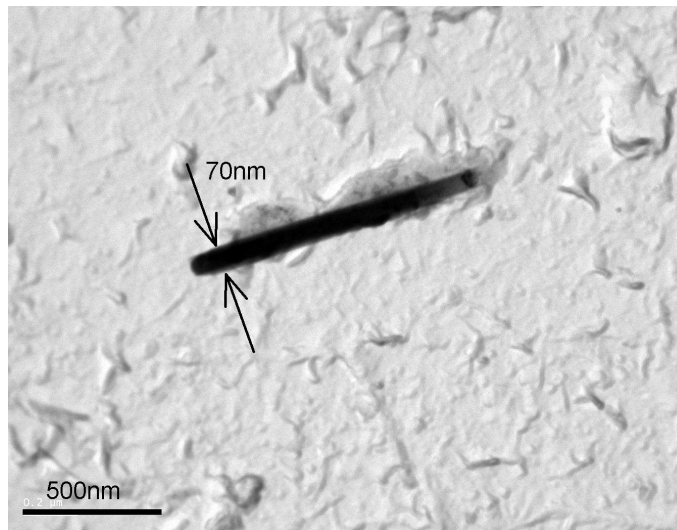


Figure 6.7: 1.05%Al steel, showing AlN dendrite plate having width of approximately 70nm.

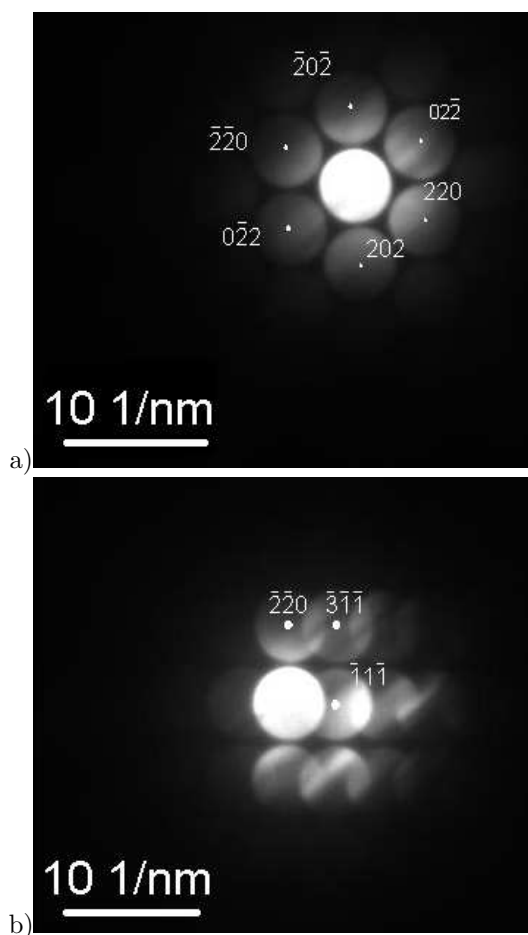


Figure 6.8: Selected area diffraction patterns of dendritic AlN precipitate in 1.05%Al steel, identified by a) fcc (zincblende)  $[111]$  zone axis pattern and b)  $[112]$  zone axis pattern. Lattice spacing was calculated to be 0.460nm. Sample was steel 2-1 tested at 700°C.

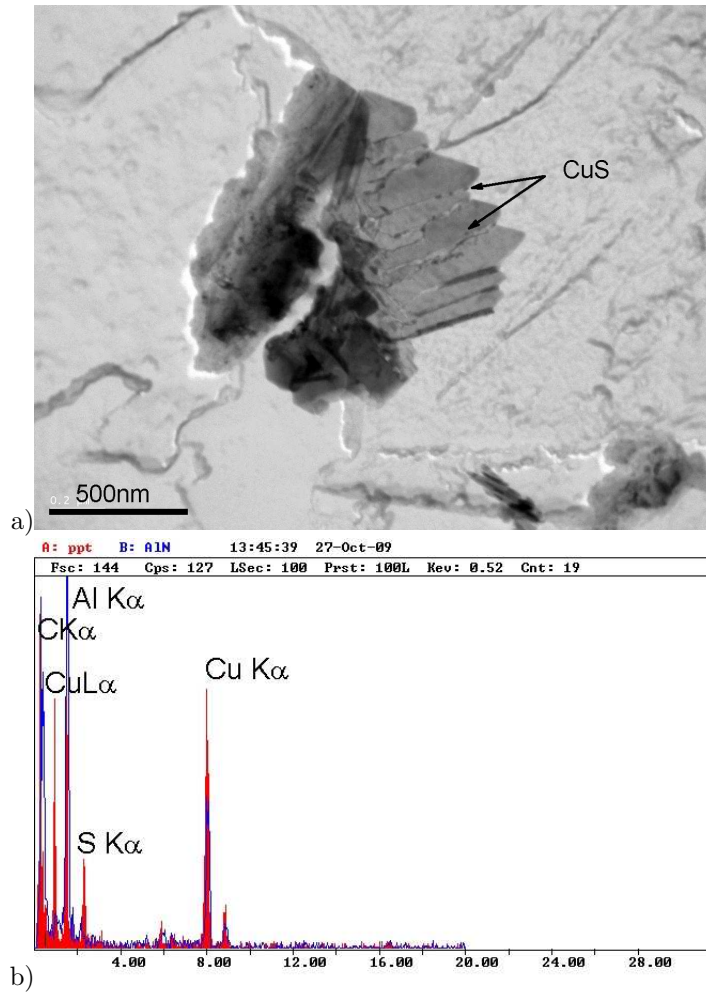


Figure 6.9: 1.05%Al steel, reheated to 1460°C and tested at 800°C (TEM sample 1052-1800-uD) showing dendritic AlN precipitation on which CuS has precipitated. The CuK $\alpha$  peak originates from the copper support grid.

In the sample tested at 800°C<sup>3</sup>, CuS appeared to precipitate on AlN dendrites, Figure 6.9. Nb(C,N) precipitates were finest at 900°C<sup>4</sup>, Figure 6.10, although there was larger grain boundary Nb(C,N) precipitation ( $16.3 \pm 8.76$ nm) associated with the plate AlN precipitation, Figure 6.11. Hexagonal plate and needle AlN were also observed (Figures 6.12, 6.13 respectively). In Figure 6.12, it can be seen that, in some cases, Nb(C,N) precipitation preceded AlN, as it is at the centre of the AlN plate and in other cases after AlN precipitation (the precipitates are also at the edge of the plate). One possibility is that the Nb(C,N) never fully dissolved - especially if it was very coarse eutectic Nb(C,N) precipitation. The needles of AlN in Figure 6.13 could also be plates orientated on edge. (It is also useful to compare with AlN on the fracture surface observed in SEM).

<sup>3</sup>TEM sample 1052-1800-uD

<sup>4</sup>TEM sample 1052-3900-1uD

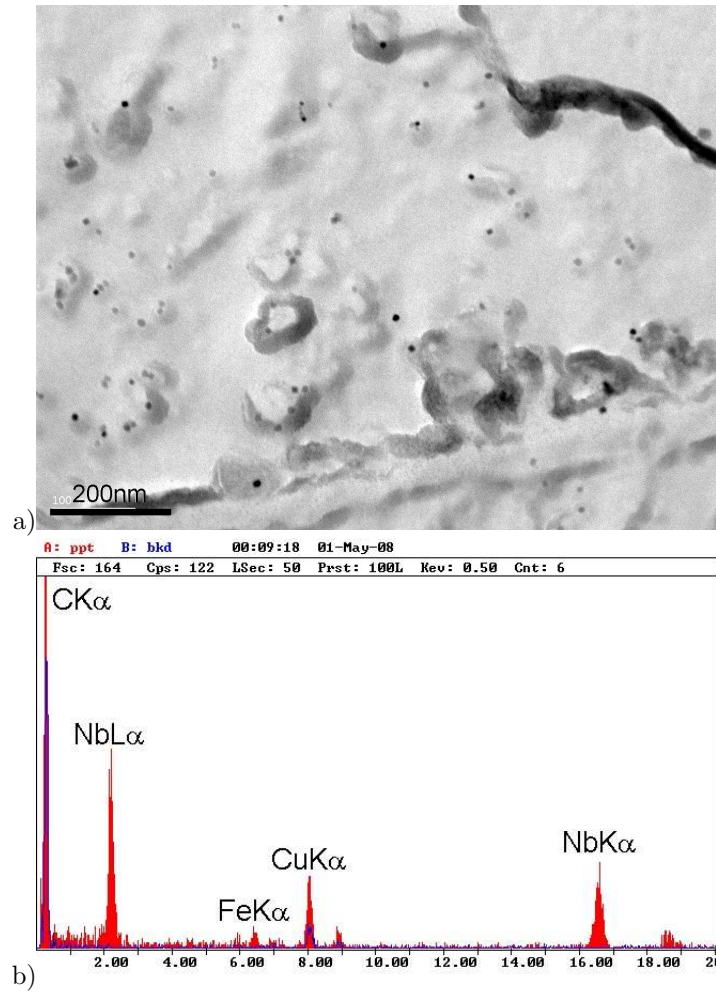


Figure 6.10: 1.05%Al steel, reheated to 1460°C and tested at 900°C (TEM sample 1052-3900-1uD) showing fine Nb(C,N) precipitation with finest precipitate size of 9nm, and average precipitate size of  $11 \pm 1.7$ nm. The CuK $\alpha$  peak originates from the copper support grid.

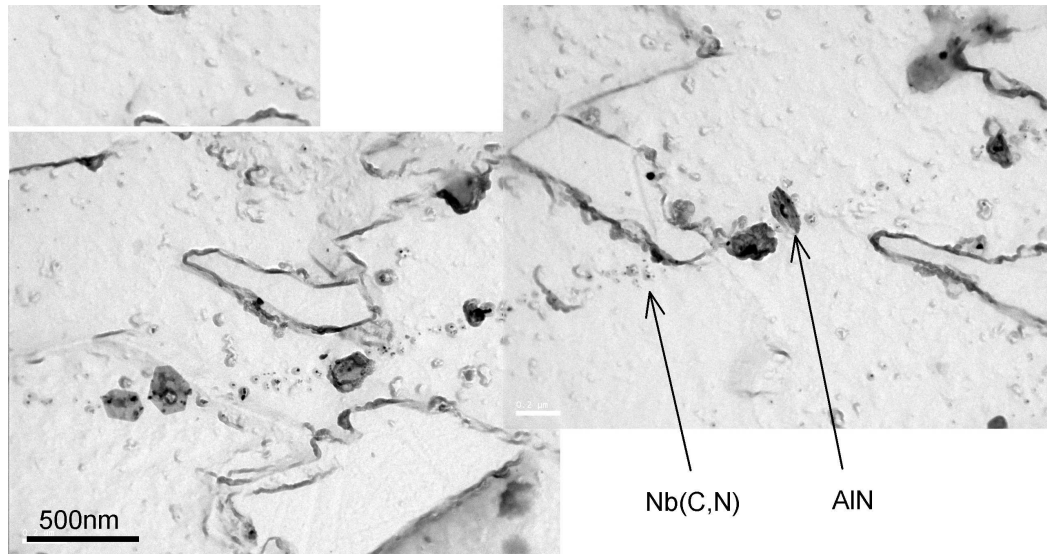


Figure 6.11: 1.05%Al steel, reheated to 1460°C and tested at 900°C (TEM sample 1052-3900-1uD) showing grain boundary Nb(C,N) precipitation associated with plate AlN precipitation.

Surprisingly fine Nb(C,N) precipitation was observed in the 1.05%Al steel, tested at 1100°C, Figure 6.14, but eutectic precipitation was also present, Figure 6.15. The diffraction patterns indicated that this precipitate has a fcc crystal structure (CBED ZAP [110] and [112]). Large (4500nm) AlN needles were also found, Figure 6.16.

The expected decrease in precipitate size with decreasing test temperature was not seen, as shown in Figure 6.17a, nor was there any correlation of Nb(C,N) precipitate size with ductility; precipitation size being fine ~10-15nm throughout the whole temperature range of 800-1100°C, Figure 6.17b.

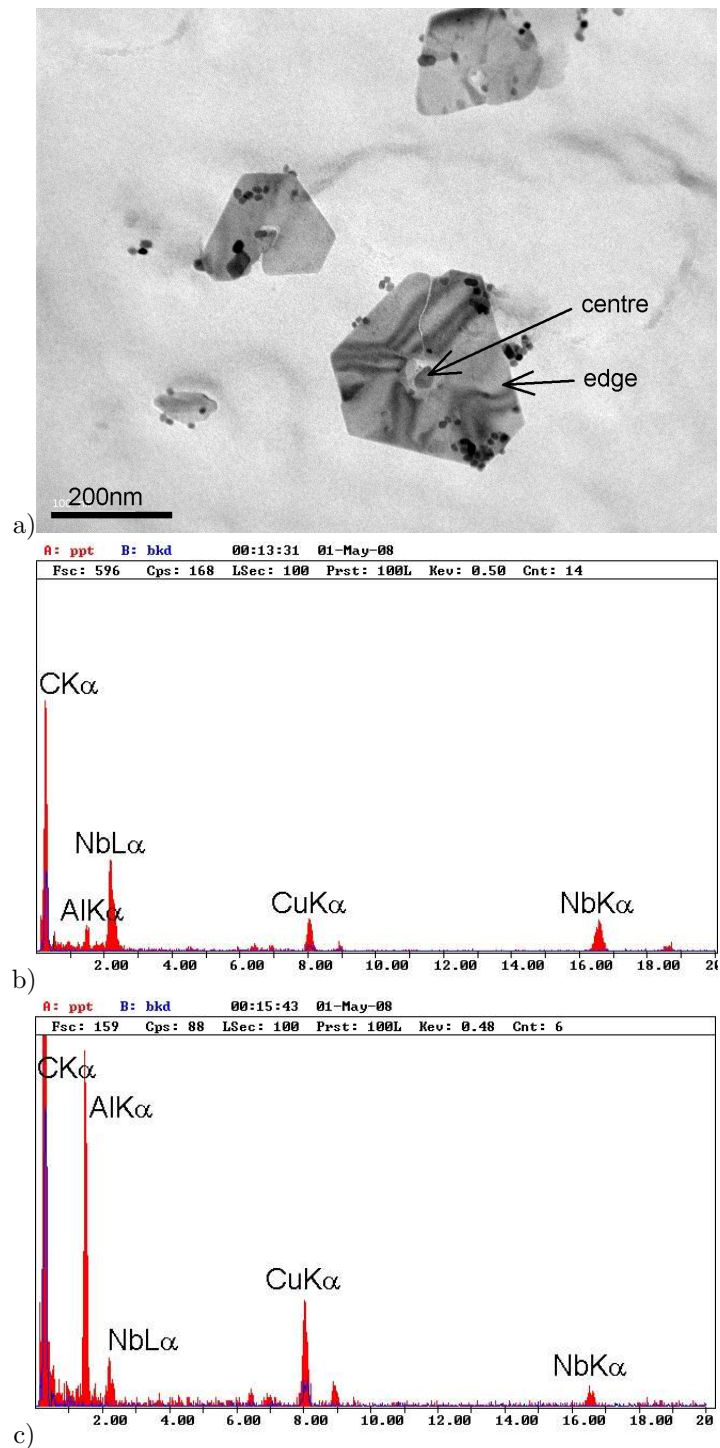


Figure 6.12: 1.05%Al steel, reheated to 1460°C and tested at 900°C (TEM sample 1052-3900-1uD) a) plate AlN with Nb(C,N) at centre, b) EDS analysis for the central region showing high Nb content and c) EDS of plate edge showing high Al content. The CuK $\alpha$  peak originates from the copper support grid.

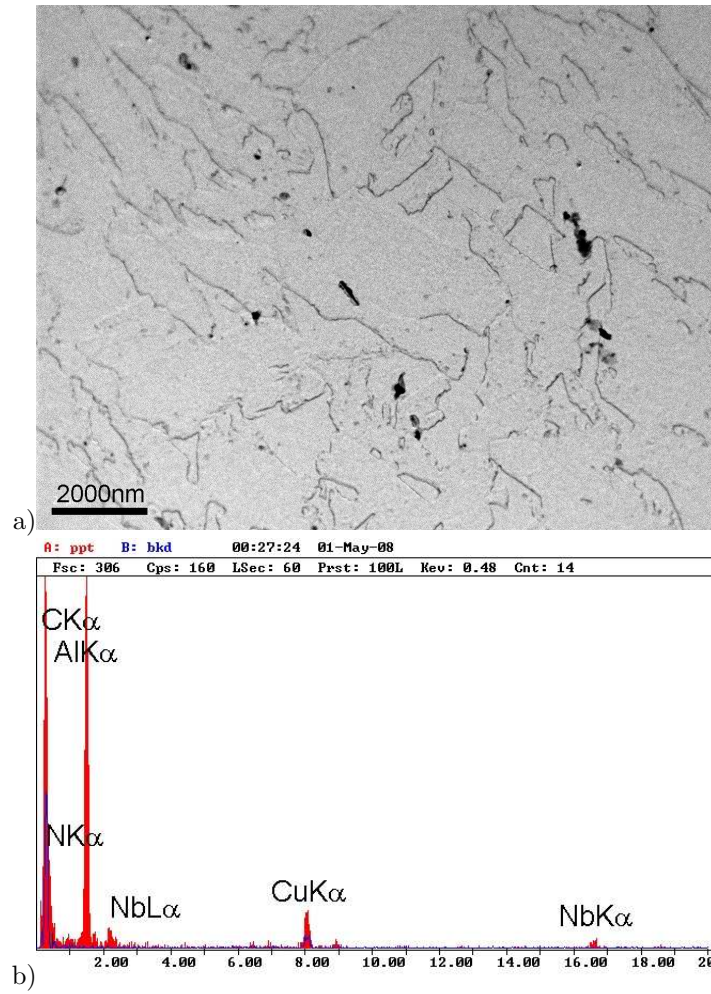


Figure 6.13: 1.05%Al steel, reheated to 1460°C and tested at 900°C (TEM sample 1052-3900-1uD) showing a) needle AlN, b) EDS analysis of the same. The CuK $\alpha$  peak originates from the copper support grid.

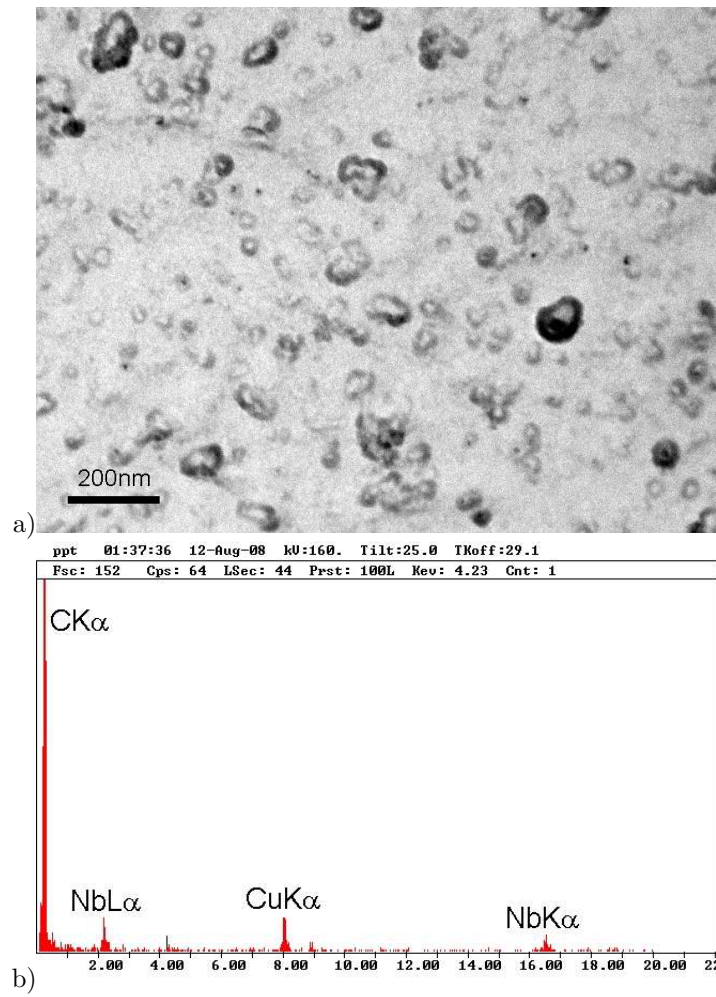


Figure 6.14: 1.05%Al steel, reheated to 1460°C and tested at 1100°C (TEM sample 105 2-1 at 1100uM, 2 replicas, 3 observations): Fine (>7nm) Nb(C,N) precipitation,  $15 \pm 7.6$ nm. The CuK $\alpha$  peak originates from the copper support grid.

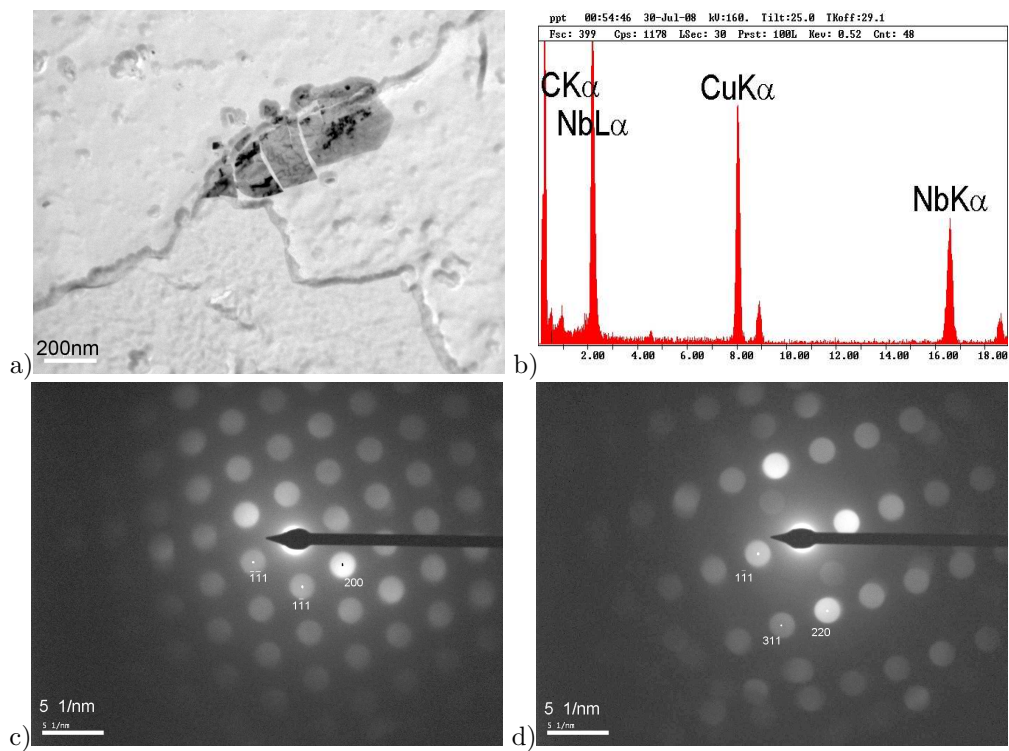


Figure 6.15: 1.05%Al steel, reheated to 1460°C and tested at 1100°C (TEM sample 105 2-1 at 1100uM, 2 replicas, 3 observations) a) and b) Large (577nm) eutectic Nb(C,N)precipitation. c) Zone axis pattern [011] fcc, d) Zone axis pattern  $\bar{1}12$  fcc crystal structure). Lattice spacing is calculated to be 0.456nm. The CuKα peak originates from the copper support grid.

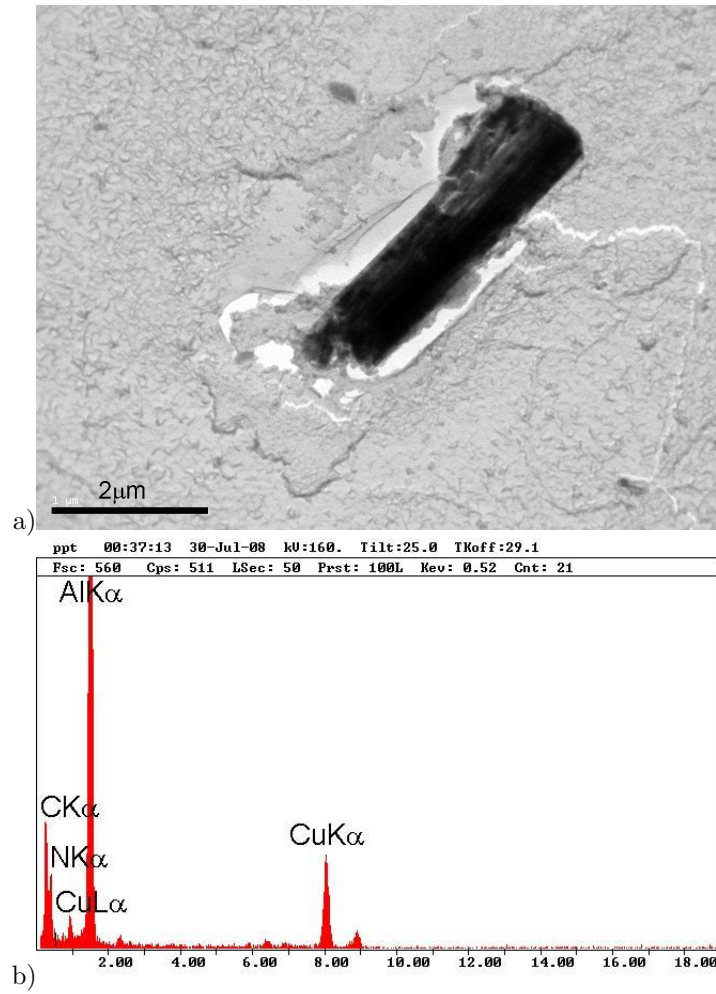
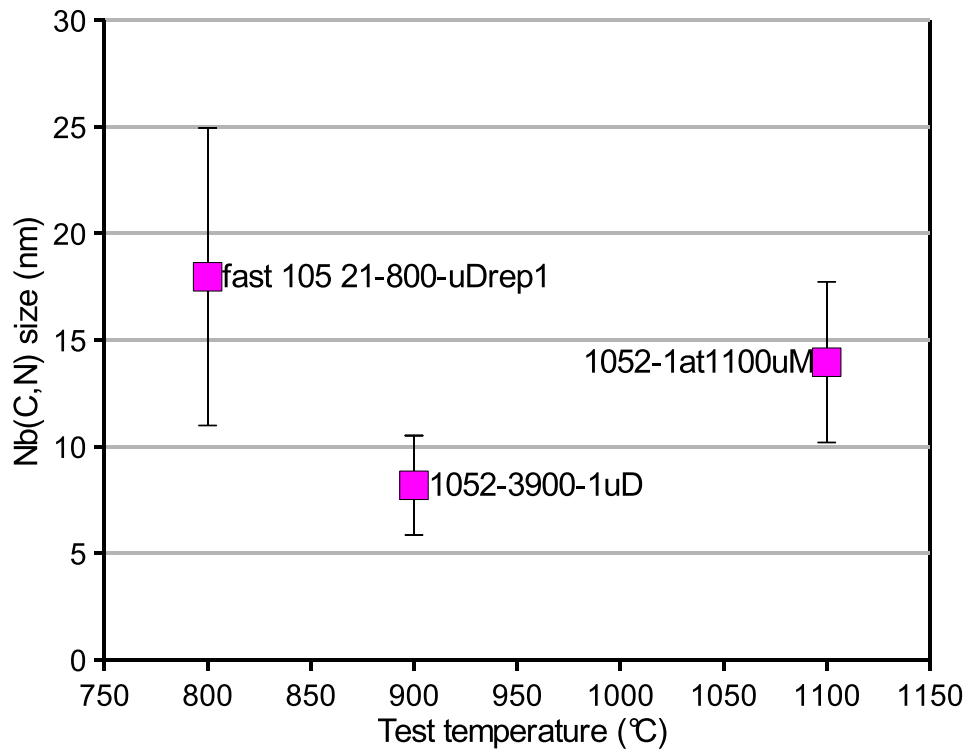
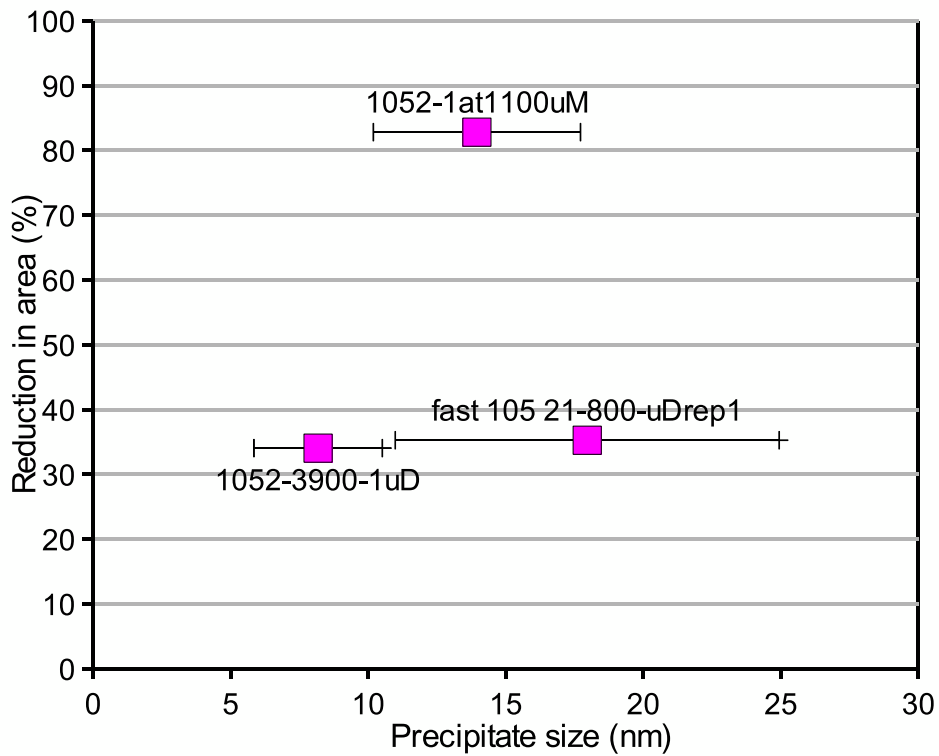


Figure 6.16: 1.05%Al steel, reheated to 1460°C and tested at 1100°C (TEM sample 105 2-1 at 1100uM, 2 replicas, 3 observations) Showing a) AlN needle, b) analysis of particle. The CuK $\alpha$  peak originates from the copper support grid.



a)



b)

Figure 6.17: 1.05%Al steel, a) average Nb(C,N) size as a function of test temperature and b) ductility as a function of average Nb(C,N) size.

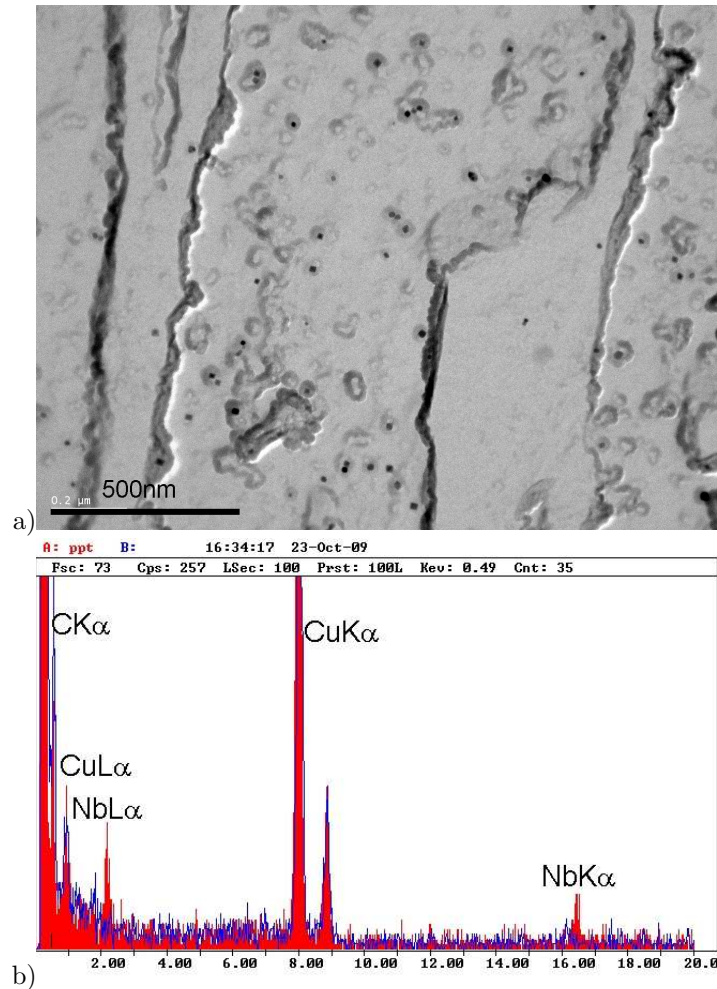
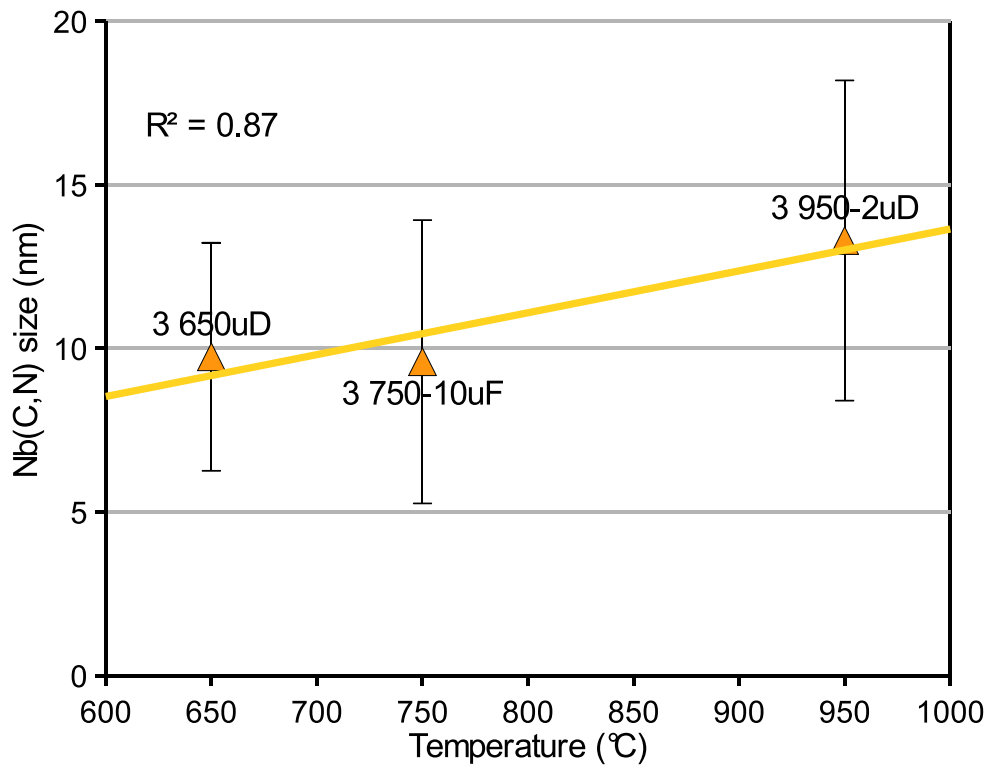


Figure 6.18: 1.53%Al steel, a) Nb(C,N) with b) analysis at 950°C test temperature. The  $Cu_{K\alpha}$  peak originates from the copper support grid.

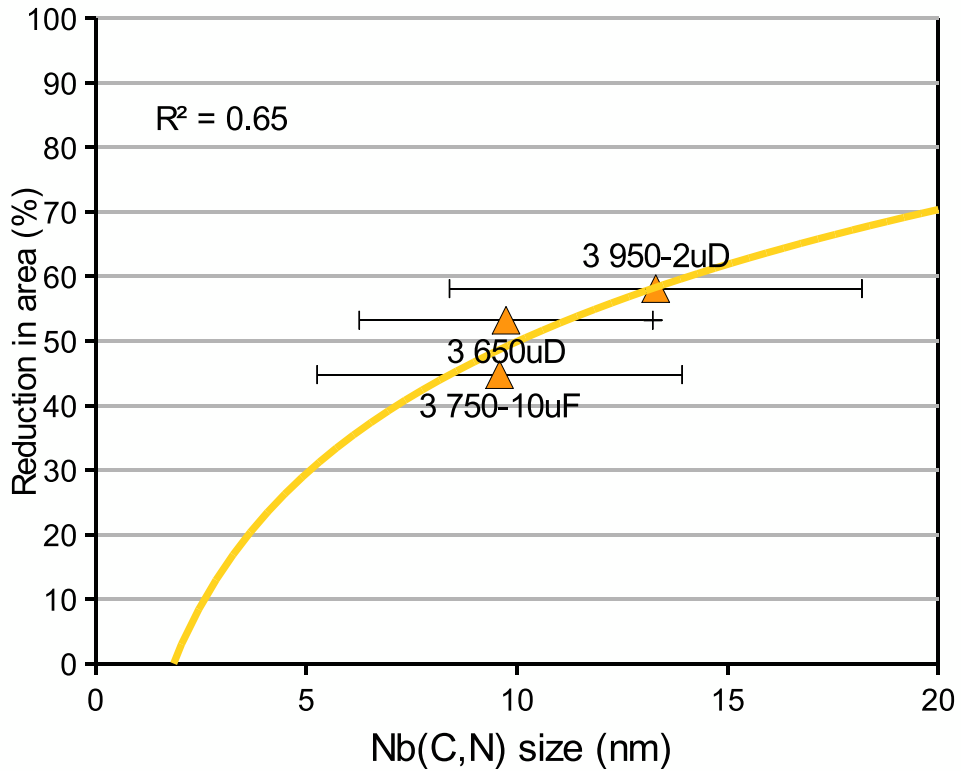
### 6.3.3 1.53% Aluminium steel

The Nb(C,N) precipitation was most easily found in the 1.53%Al steel samples, Figure 6.18. The presence of precipitation of Nb(C,N) in deformation induced ferrite and austenite in the 1.5%Al steel showed no consistent trend between the phases. This suggests that dynamic precipitation could be taking place in either phases. As the test temperature decreased the average precipitate size decreased as expected, Figure 6.19a, however, there was only a fair correlation between ductility and average precipitate size, Figure 6.19b, again showing that precipitate size was not the only variable influencing hot ductility. Needle AlN was observed in the 650°C test sample. In all three samples, Nb(C,N) precipitate populations were normal.

The lattice spacing of the AlN precipitation was estimated from the calibrated diffraction



a)



b)

Figure 6.19: 1.53%Al steel, a) average Nb(C,N) size as a function of test temperature and b) ductility as a function of average Nb(C,N) size. Trend line in b) is of the form  $y = m \log(x) + c$ .

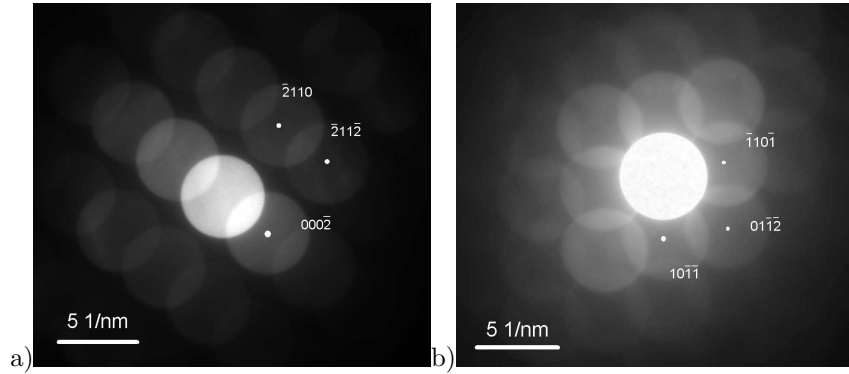


Figure 6.20: Diffraction patterns for AlN precipitate in the 1.5%Al steel, reheated to 1460°C and tested at 1100°C, a) Zone axis pattern  $[01\bar{1}0]$  hcp crystal structure b) Zone axis pattern  $[01\bar{1}1]$  hcp crystal structure). Lattice spacing is calculated to be as  $a=0.323\text{nm}$  and  $c=0.499\text{nm}$ .

patterns in Figure 6.20, using:

$$\frac{1}{d^2} = \frac{4}{3a^2} (h^2 + hk + k^2) + \frac{1}{c^2} l^2, \quad (6.2)$$

where  $c$  is the c-axis lattice spacing,  $d$  is the d-spacing and  $h, k, l$  are the spot indices, as previously given in Equation 6.1. This was confirmed using a diffraction pattern simulation program (JEMS), Figure D.2.

## 6.4 General remarks on the transmission electron microscopy results

A large population of Nb(C,N) precipitates was taken for the 0.05%Al and 1.53%Al steel, to ensure that the precipitate size was statistically relevant. The Nb(C,N) precipitation was generally very fine (10-18nm) even up to high temperatures; 1100°C in the case of the 1%Al steel. This indicates that the precipitation must be dynamic. Such fine precipitation would, from previous work [39], cause a marked deterioration in ductility. The lack of data points makes it very difficult to be clear on the influence of test temperature on precipitation size, which again, from previous work would be expected to coarsen with temperature. There is some indication that a slight coarsening may be occurring with the 0.05 and 1.5%Al steels and this is reflected in the improvement in the hot ductility with temperature. However, the 1%Al steel does not appear to show any evidence of coarsening with temperature. Consequently, there is no relationship between precipitate size and ductility. In the 1%Al containing steel the most striking feature observed was the dendritic AlN precipitation at the grain boundaries.

Table 6.4: Summary of TEM results.

Steel (%Al)	AlN	AlN morphology	eutectic Nb(C,N)ppt	Nb(C,N)ppt related to temp/ductility
0.05	no	-	no	ductility
1.05	fcc	dendritic	yes	neither
1.53	hcp	hexagonal plate, needle	no	temperature

The fact that Nb(C,N) precipitation was most easily found in the 1.53%Al steel samples, is most likely a result of the finer grain size in this steel. The expected decrease in minimum precipitate size with decreasing test temperature was found in this steel.

## 6.5 Conclusions of transmission electron microscopy analysis

1. In the 0.05%Al steel, Nb(C,N) precipitation was only found in the general vicinity of the prior austenite grain boundaries. For this steel there was a good relationship ( $R^2 = 0.99$ ) between precipitate size and ductility. No AlN precipitation or eutectic Nb(C,N) was observed.
2. In the 1%Al steel, the Nb(C,N) precipitate size was not related to ductility or to test temperature. Copious precipitation of dendritic AlN was found and identified as fcc with  $a=0.460\text{nm}$ . The thickness of dendritic precipitation has been estimated at 70-130nm. Fcc eutectic Nb(C,N) was observed with  $a=0.46\text{nm}$ .
3. In the 1.5%Al steel, the Nb(C,N) precipitate size was strongly related to the test temperature ( $R^2 = 0.87$ ). The AlN was hcp with lattice spacing of  $a=0.323\text{nm}$  and  $c=0.499\text{nm}$ .
4. There was a similarity of precipitate size across temperatures so that the R of A recovery at high temperatures cannot be attributed to the lack of sub 20nm Nb(C,N).

## Chapter 7

# Thermodynamic Modelling Simulations

### *Summary of thermodynamic modelling simulations*

Increasing the Al content changes the phase transformation and precipitation response of the steels dramatically. It is therefore necessary to characterise the thermodynamic behaviour so as to better understand these effects. Various simulation packages as well as solubility equations from literature were used. The calculations showed that as the Al level increases, the steel changes from hyper-peritectic to hypo-peritectic. Ranking the steels in relation to the peritectic reaction aids in comparative discussions of the steels. The minimum ductility improved with increasing fraction of AlN precipitating in the delta ferrite, also, there was a strong relationship between the minimum ductility and proximity to the peritectic point. The two thermodynamic model predictions only differed on average by 3°C of each other from the Ae<sub>3</sub> to the melting point. These phase simulations showed that both 0.05 and 1%Al steel had a wide, high single phase austenite region, while this field started at lower temperatures and was narrower in the 1.53%Al steel. The solubility equations for precipitation from literature showed great variation (e.g. AlN ±151°C) and yielded less helpful information than the thermodynamic modelling.

## 7.1 Introduction

Some of the common solution and precipitation models from literature [166, 165]<sup>1</sup> are ineffective for determining the phase diagrams and precipitation reactions in the present steels as they do not include the influence of Al. It was therefore necessary to characterise the thermodynamic behaviour to better understand the variation in ductility behaviour of the

---

<sup>1</sup>Discussed in section 2.4.3, page 89.

steels. The aim of this chapter is to help rank the steels in relation to the constitutional phase diagram, to improve the understanding of the phase transformations, so as to supplement rather than supersede the microstructural analysis. Three modelling systems were used, the first, developed for ArcelorMittal by K. Blazek[140] and the other two based on Gibbs free energy calculations (FactSage(TM) version 6.1 and Thermo-Calc version 4). The details of the peritectic calculator of Blazek may be found in Section 2.4.3, while the databases used for the FactSage and Thermo-Calc packages may be found in Appendix E. Since the current steels will be compared in the discussion to other TRIP steels from literature[10, 11] as well as additional microalloyed steels from Mintz and Mohamed [62] and Mintz and Cowley [55], these will also be included as compositions in the phase simulations (Table 7.1). The comparative discussions will follow in the main discussion Section 8.4, page 206.

## 7.2 Peritectic calculator for aluminium containing steels of varying carbon and manganese levels

Aluminium additions alter the peritectic behaviour by shifting the peritectic reaction to higher carbon levels. To facilitate comparison of the ductility of the steels highlighted in Table 7.1, and Figure 7.1 which have varying Al as well as C and Mn contents, the distance from the effective peritectic carbon point for each steel, was used as the x axis, as follows:

$$x = C_{actual} - C_{peritectic} \quad (7.1)$$

The  $C_{peritectic}$  was calculated from equation 2.9, using equations 2.7 and 2.8 to calculate  $C_A$  and  $C_B$  (page 92). This acted to ‘standardise’ the steels. The minimum ductility vs  $C_{actual} - C_{peritectic}$  for the steels is plotted in Figure 7.1 and was lowest at the peritectic composition range. The approximate limits of the peritectic reaction have been inserted between the steels where the peritectic calculator showed there was a change in behaviour from hyper-peritectic to peritectic and peritectic to hypo-peritectic. These limits are indicated by the vertical lines set either side of 0.00 in Figure 7.1 at the 0.05 and -0.05 positions on the x-axis. When a steel is hypo-peritectic, it lies to the left of the peritectic area and the  $C_{actual} - C_{peritectic}$  values  $\ll 0$ , while a steel is hyper-peritectic it lies to the right of the peritectic area and the  $C_{actual} - C_{peritectic}$  values are  $\gg 0$ . In practice the worst peritectic contraction occurs at slightly lower carbon contents than the exact peritectic carbon level [140].

The low (0.05%) Al steel, Trip 9, falls outside of the peritectic range and was hyper-peritectic. The 1.5%Al steel, Trip 3, was outside of the peritectic region on the low C side, Figure 7.1. However, the 1%Al steel, Trip 2-1, fell within the peritectic region. The effect of being close

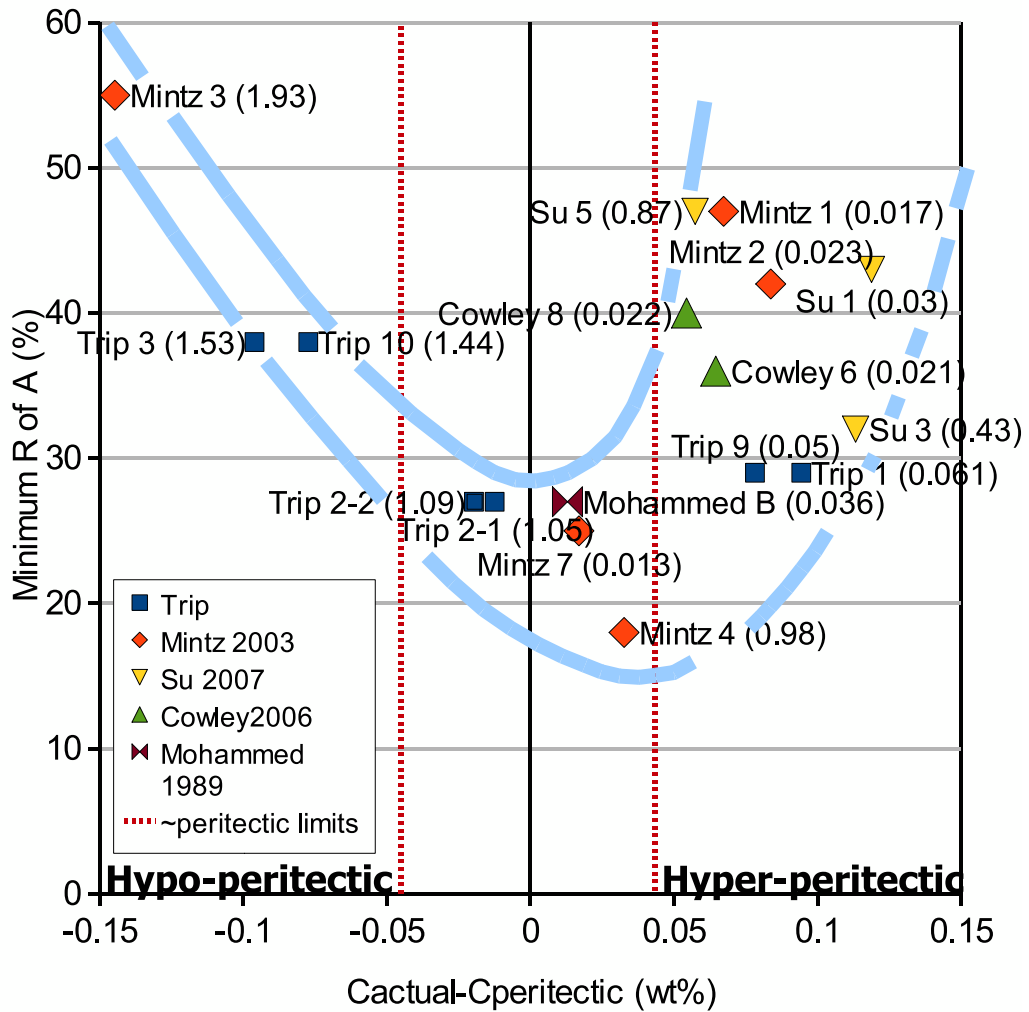


Figure 7.1: Ductility vs  $C_{actual} - C_{peritectic}$ . The ductility in the trough is poorest close to the peritectic point, ie  $C_{actual} - C_{peritectic} = 0$ . %Al contents in brackets.

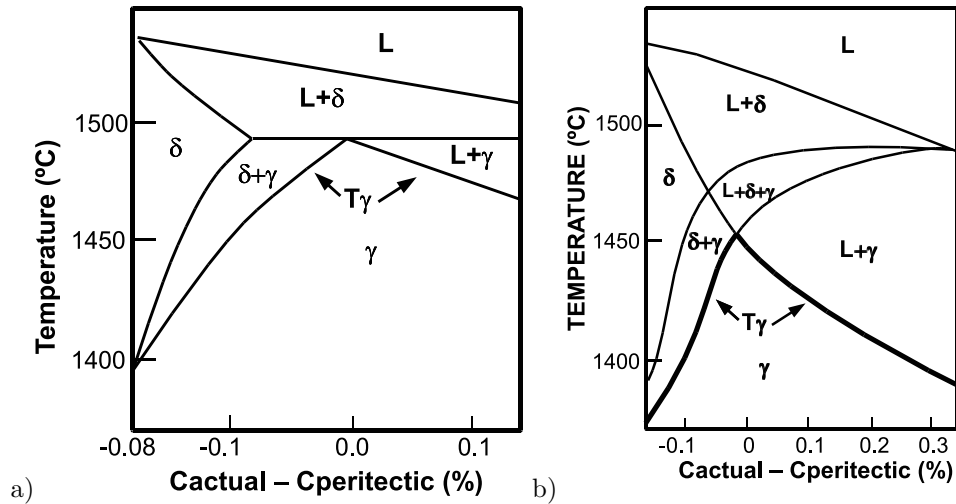


Figure 7.2: Phase transformations at high temperatures in the peritectic region of the a) Fe-C constitutional diagram, b) Fe-C constitutional diagram with additional elements 0.02%P and 0.002%S, adapted from [164] and [166], showing how, at the peritectic point ( $C_{actual} - C_{peritectic}=0$ ), the pure austenite phase forms at the highest temperature. In practice the worst peritectic contraction occurs at slightly lower carbon contents than the peritectic point [140].

to the peritectic point is that the single austenite phase field starts at higher temperatures as indicated schematically in Figure 7.2, so encouraging grain growth.

If the volume fraction of AlN precipitation is sufficiently high (as a result of the high Al additions) and the grain size is coarse enough, the boundaries become pinned and ductility is at its worst. The greater the volume fraction of precipitates at the boundaries and the larger the grain size, the greater is the coverage of grain surface by precipitation, and this effectively pins the boundaries so encouraging intergranular failure. Given the complexity of these steels, it is hard to rank them in relation to the peritectic without simulating the phase stabilities, especially at the hyper-peritectic side (Trip 1,9 0.05%Al). This is the motivation for further modelling.

### 7.3 FactSage and Thermo-Calc programmes for phase diagram and precipitation volume fractions

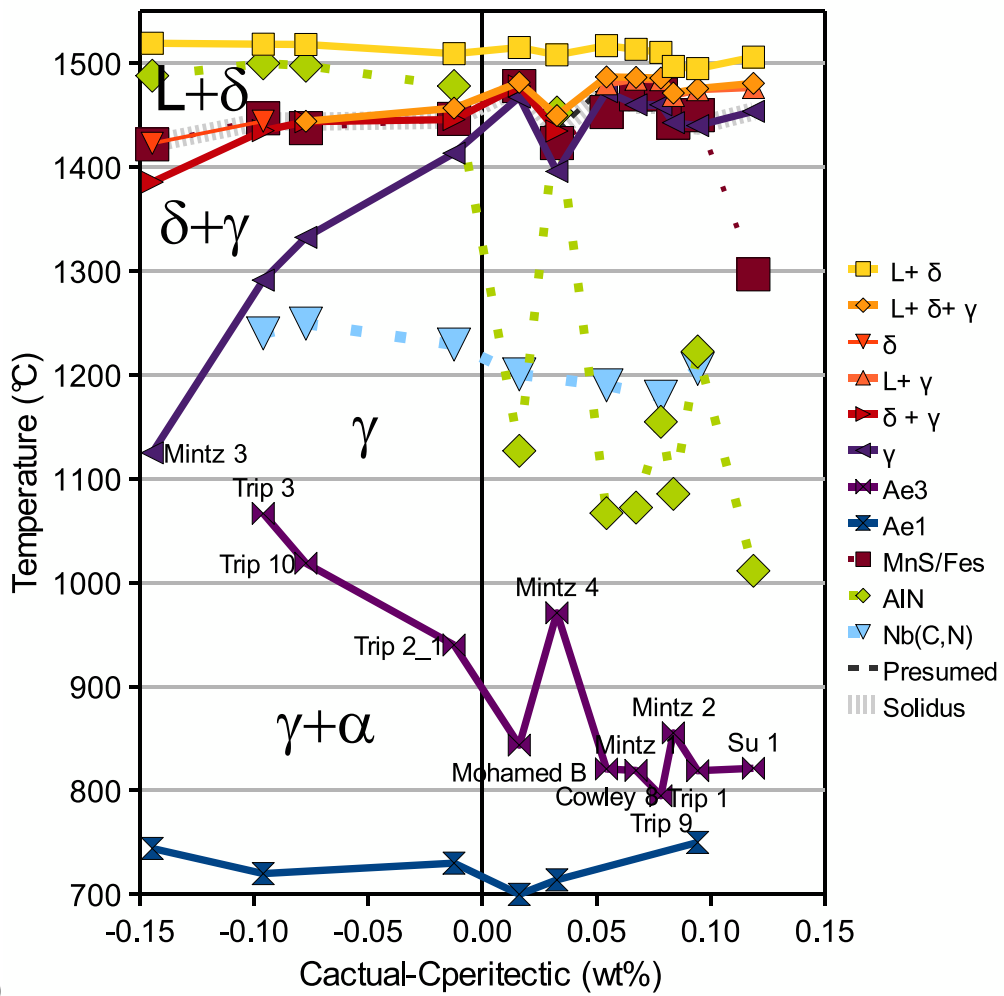
The compositions that were used in the programmes are given in Table 7.1. Some modified compositions are listed in Table 7.2, to enable the effect of Al and Mn on the austenite phase field in the high Al steels (2%Al - Mintz steel 3[10] and 1.5%Al - Trip steel 3) to be investigated. The modelling was performed over the temperature range from from 1600 to 700°C, (typical curves are shown in Figure E.1 in Appendix E, page 255).

In order to develop confidence in the phase simulations, two packages, FactSage(TM) v6.1 and Thermo-Calc v4 were used. Both these models yielded very similar results for phase changes (phase fields). The full details of the differences/similarities may be found in Appendix E.3, Table E.4, page 259 for selected steels. The databases and phases that were used in each software package are listed in Tables E.3 and E.2 in Appendix E.

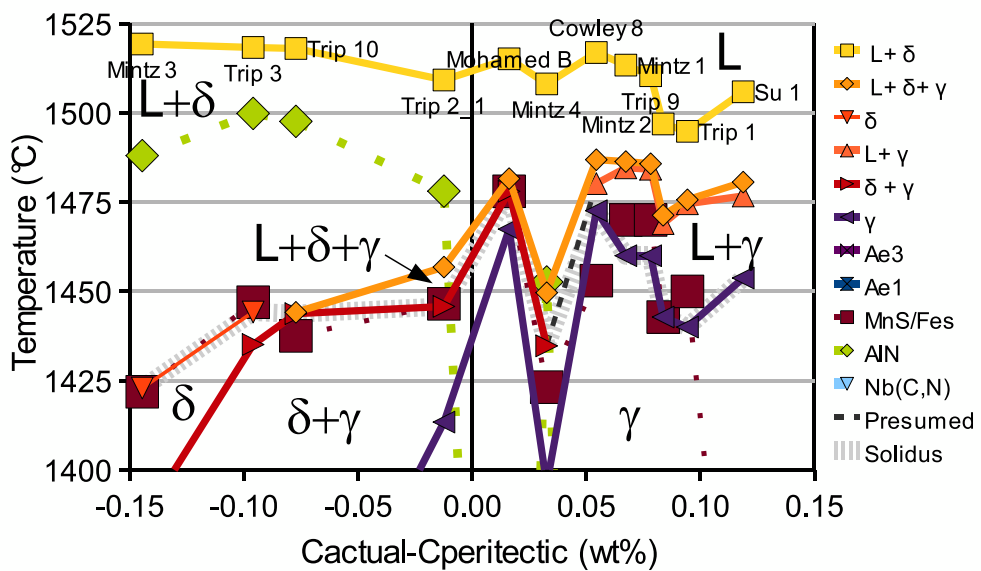
Table 7.1: Compositions (wt%) used in the phase simulations.

Sample	C	Mn	P	S	Si	Nb	Al	N
Trip 1	0.15	2.42	0.011	0.0045	1.050	0.025	0.06	0.0080
Trip 9	0.14	2.41	0.011	0.0050	0.210	0.025	0.05	0.0072
Trip 2-1	0.15	2.47	0.011	0.0048	0.490	0.024	1.05	0.0066
Trip 3	0.15	2.49	0.011	0.0055	0.000	0.025	1.53	0.0057
Trip 10	0.15	2.50	0.011	0.0040	0.002	0.028	1.44	0.0068
Mintz 1	0.15	1.45	0.003	0.0080	0.29	0.0	0.02	0.0060
Mintz 2	0.16	1.41	0.009	0.005	1.22	0.0	0.02	0.0032
Mintz 3	0.22	1.45	0.009	0.0050	0.02	0.0	1.93	0.0034
Mintz 4	0.21	1.41	0.010	0.0040	0.61	0.0	0.98	0.0042
Su 1	0.20	1.50	0.08	0.001	0.39	0.0	0.03	0.0012
Su 3	0.22	1.53	0.08	0.001	0.4	0.0	0.43	0.0024
Su 5	0.22	1.51	0.08	0.001	0.41	0.0	0.87	0.0022
Cowley 8	0.140	1.400	0.026	0.006	0.100	0.031	0.022	0.005

The phase boundaries were taken from the phase fraction and temperature simulation data and plotted against the  $C_{actual} - C_{peritectic}$ , in Figure 7.3 and 7.4 for the FactSage and Thermo-Calc models respectively. Also included in the curves are the precipitate and inclusion volume fractions as a function of  $C_{actual} - C_{peritectic}$  for each of the steels in Table 7.1. The data will be used later in the discussion to investigate precipitation volume fractions in relation to phase boundary temperatures (Figures 8.12, 8.14; pages 218, 221 respectively).

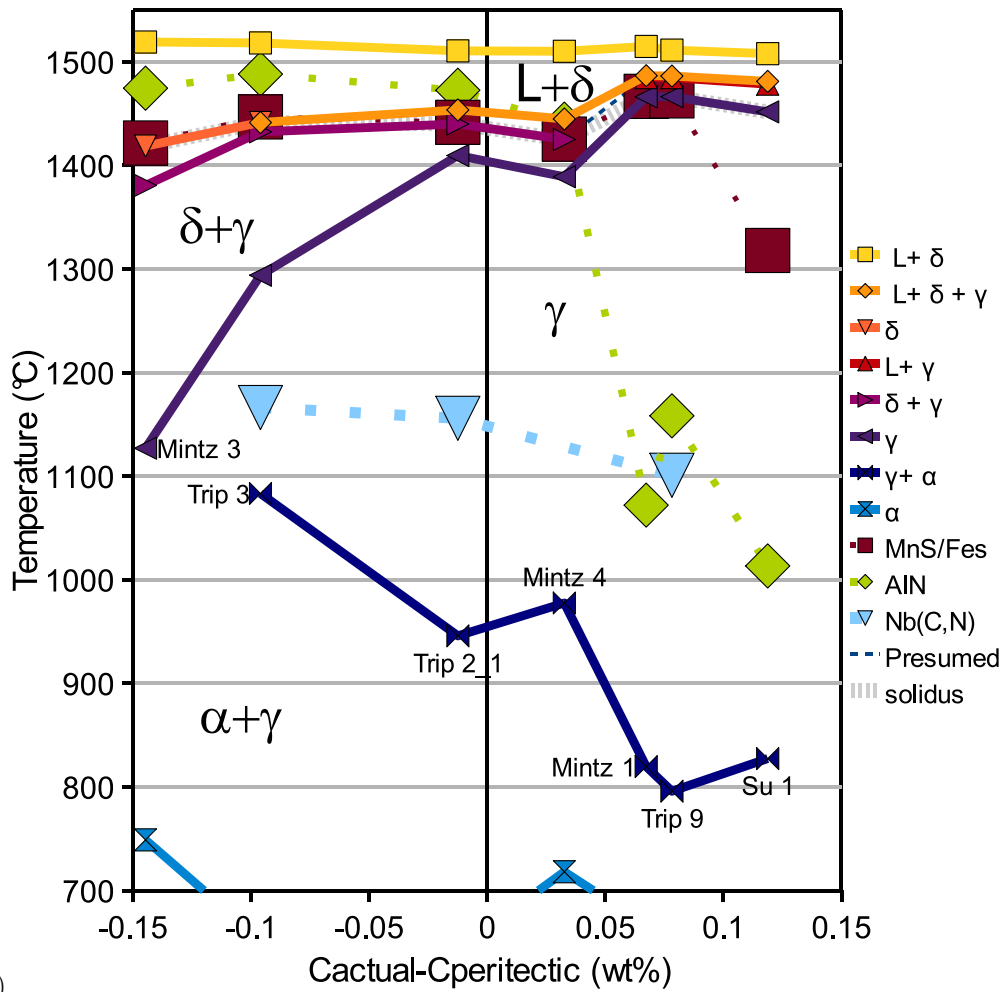


a)

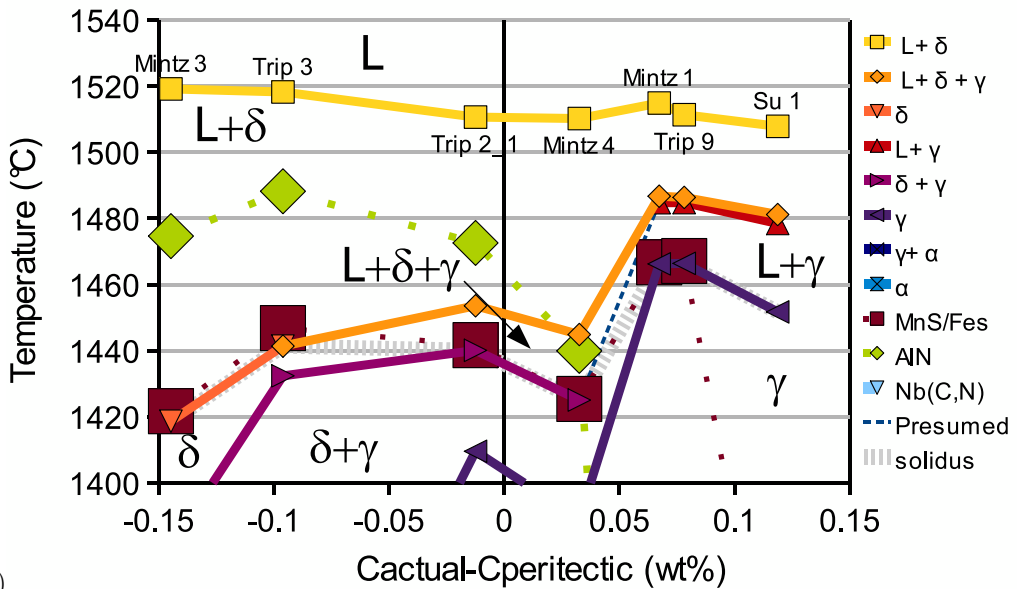


b)

Figure 7.3: FactSage phase and solubility fields a) entire field b) enlargement of higher temperature range. Identification of each steel is given at one data point and applies to all other curves in vertical alignment with that data point.



a)



b)

Figure 7.4: Thermo-Calc phase and solubility fields a) entire field b) enlargement of higher temperature range. Identification of each steel is given at one data point and applies to all other curves in vertical alignment with that data point.

The two simulations compared favourably (Figures 7.3, 7.4 and Table 7.3) with each other for all steels, (full details in Appendix E, Table E.4), as can be seen from the graphical comparison shown in Figures 7.3a, 7.4a and Figures 7.3b, 7.4b. The maximum difference between the two packages in terms of the phase transformations is 26°C, but on average the difference was only 1°C. Neither model consistently predicts phase temperatures above or below the other. However, the precipitate solution (AlN, Nb(C,N) and MnS) temperatures had a much greater variation in temperature range (104°C) with an average value of 9°C. The correlation below 700°C is poor, but the correlation between the  $A_{e3}$  and the temperature of single phase austenite, which is of most interest, was good at a maximum difference of 16°C difference<sup>2</sup>.

Considering the phase transformations of the steels examined in Table 7.1, it can be seen in Figures 7.3, 7.4 that for the hypo-peritectic steels where  $C_{actual} - C_{peritectic} \ll 0$ , transformation is from  $L \rightarrow L+\delta \rightarrow \delta \rightarrow \delta+\gamma \rightarrow \gamma$ . The closer one is to the peritectic, the higher the temperature at which the austenite starts to form, resulting in a coarser grain size. The temperature at which  $\alpha$  ferrite first forms is also observed to decrease indicating a wide austenite field and a narrowed two phase ( $\gamma + \alpha$ ) field. At the peritectic point the transformation is from  $L \rightarrow L+\delta \rightarrow L + \delta + \gamma \rightarrow \gamma$  and on the hyper-peritectic side where  $C_{actual} - C_{peritectic} \gg 0$ , the transformation is from  $L \rightarrow L+\delta \rightarrow L+\gamma \rightarrow \gamma$ . Note that the equations for  $C_{actual} - C_{peritectic}$  (Equations 2.7, 2.8, 2.9) are a simplified estimate of the peritectic point as compared the phase simulations so that there is a slight difference in terms of the exact positioning of the peritectic point.

If the precipitation behaviour of the steels examined in Table 7.1 is considered, there is little difference in the temperature,  $\sim 1200^\circ\text{C}$ , required for complete dissolution of Nb(C,N) precipitation (large triangles in Figures 7.3a, 7.4a), for MnS precipitation again there was little difference in the re-resolution temperature this being around  $\sim 1450^\circ\text{C}$ , except for the

<sup>2</sup> $A_{e4}$  is defined as the temperature of delta ferrite to austenite transformation and thus only exists in pure iron transformations [164].

Table 7.2: Additional compositions (wt%) used in the phase simulations.

Sample	C	Mn	P	S	Si	Nb	Al	N
Mintz 3 1Al	0.22	1.45	0.009	0.0050	0.02	0.0	1	0.0034
Mintz 3 1.2Al	0.22	1.45	0.009	0.0050	0.02	0.0	1.2	0.0034
Trip 3 1.5Mn	0.15	1.50	0.011	0.0055	0.000	0.025	1.53	0.0057
Trip 3 2Mn	0.15	2.00	0.011	0.0055	0.000	0.025	1.53	0.0057
Cowley 6	0.150	1.41	0.007	0.007	0.090	0.0	0.021	0.007
Mintz 7	0.1	1.42	0.011	0.004	0.31	0.033	0.013	0.0071
Mohamed B	0.1	1.39	0.007	0.01	0.42	0.026	0.036	0.0075

very low S steel (0.001%S of Su1). However, for AlN precipitation, the hypo-peritectic steels (>1%Al) were not fully soluble until 1480°C whereas the peritectic and hyper-peritectic steels had a wide variation in the solubility temperature but it was generally less than 1200°C.

### 7.3.1 Use of calculations for predicting ductility behaviour

It can be seen from Figure 7.1 that the worst ductility occurs in the peritectic region  $-0.05 < C_{actual} - C_{peritectic} < 0.05$ . Figures 7.3 and 7.4 give the temperature for complete dissolution of the precipitates of AlN, Nb(C,N) and MnS (Large diamond, triangles and squares respectively with dashed lines) for each of the steels given in Table 7.1. It can be seen that these dissolution temperatures change very little for the MnS and Nb(C,N) precipitation for the steels examined. For AlN precipitation however, it can be seen that the solubility of AlN drops markedly at the peritectic composition and for steels having hyper-peritectic composition ( $C_{actual} - C_{peritectic} \geq 0$ ).

A very important result observed from phase transformation behaviour and the AlN precipitation was that the minimum ductility improves with the volume fraction of AlN precipitating in the delta ferrite range as shown in Figure 7.5. This plots the minimum R of A against the volume fraction of AlN precipitated in the delta ferrite for steels which are expected to precipitate AlN in the delta ferrite. If the AlN precipitates in the delta ferrite, when the steel transforms to austenite, the AlN is unlikely to be situated at the austenite grain boundaries and hence is not able to influence ductility.

In contrast if the AlN precipitates directly in the austenite, it will remain on the grain boundaries which undergo no further grain boundary movement on cooling further through in the austenite range. Presumably, in this manner, AlN is rendered harmless if it is allowed to precipitate in the  $\delta$  ferrite rather than in the austenite. This may not occur in the

Table 7.3: Maximum variation, average variation and standard deviation between the Thermo-Calc and FactSage simulations for all phase field boundaries for all steels in Table 7.1. The maximum variation is Thermo-Calc value minus FactSage value.

	Bulk phases: Liquidus, solidus, Ae <sub>3</sub> , °C	Precipitation: AlN, MnS, Nb(C,N), °C	All phases, °C
Maximum variation	-10 to +17	-78 to +26	-78 to +26
Average	1	-9	-3
Standard deviation	5	28	18

industrial process as the actual cooling rate at these temperatures is much higher, so AlN may not precipitate out to the same degree. More accurate cooling path ductility testing is required to confirm whether this beneficial AlN precipitation in delta ferrite occurs during continuous casting.

Table 7.4: Theoretical AlN precipitation in delta ferrite and austenite.

Sample	Al, wt%	Peritectic behaviour hypo/peri/hyper	$V_f$ in $\delta$ $\times 10^{-4}$	$V_f$ in $\gamma$ $\times 10^{-4}$	$V_f$ in $\alpha$ $\times 10^{-4}$	Minimum R of A (%)
<b>Trip 9</b>	0.05	hyper	0.0	2.9	0.0	29
<b>Trip 2-1</b>	1.05	peri	1.3	1.3	0.0	27
<b>Trip 3</b>	1.53	hypo	2.4	0.3	0.0	38
Trip 10	1.44	hypo	2.2	0.5	0.0	-
Mintz 1	0.17	hyper	0.0	2.3	0.1	47
<b>Mintz 2</b>	0.023	hyper	0.0	1.2	0.0	42
Mintz 3	1.930	hypo	1.4	0.0	0.0	55
<b>Mintz 4</b>	0.980	(peri)	0.6	1.0	0.0	18
Su 1	0.030	(hyper)	0.0	0.5	0.0	43
Su 3	0.430	(hyper)	0.0	1.0	0.0	32
Su 5	0.870	(hyper)	0.0	0.9	0.0	47
Cowley 6	0.021	(peri)	0.0	2.8	0.1	36
Cowley 8	0.022	(peri)	0.0	2.0	0.1	40
Mohamed B	0.036	(peri)	0.0	2.9	0.0	18

From the foregoing, the phase in which the AlN precipitation occurs is important in controlling ductility. If it precipitated solely in the delta ferrite it had little influence on ductility but if it precipitated mainly in the austenite then it was very damaging to the ductility. The volume fraction that precipitated out in the austenite is also obviously important and the equilibrium volume fraction can be calculated as a function of temperature for the austenite phase. When precipitation of AlN occurred in the austenite it more detrimental and it is therefore important to know the  $Ae_3$  temperature. The next section is devoted to establishing these values for TRIP type steels having a range of Al and Mn levels. It should be noted that knowledge of  $Ae_3$  is also important for interpreting the hot ductility behaviour as it marks the highest temperature at which deformation induced ferrite forms and the minimum ductilities are generally associated with the presence of the DIF film. The other important temperature is the  $Ar_3$  below which ferrite can form in large quantities prior to deformation and so improve ductility. As already shown, the  $Ae_3$  temperature for these high Al steels can be calculated from FactSage and Thermo-Calc programmes.

However, there is one problem with very high Al steels for example the 2%Al steel, Mintz steel 3 [10], in that there is no apparent  $Ae_3$ , Figure 7.6. For this steel, the peak austenite temperature of 1120°C (the temperature giving the greatest amount of austenite) was taken as approximating the  $Ae_3$ , Figure 7.6.

For example, in Figure 7.7, increasing the Al level for Mintz steel 3 [10] from 1 to 1.2 to 1.93%Al causes the  $Ae_3$  to increase from 868°C to 984°C to an effective  $Ae_3$  of 1120°C, Figure 7.7a. Decreasing the Mn level for the Trip from 2.5 to 2 to 1.5%Mn shows that the apparent  $Ae_3$  increases from 1067 to 1175 to 1180°C, respectively Figure 7.7b. If the Mn level is lowered in the Trip 3 or the Al content is raised in the Mintz 3 steel, these have the a similar effect on the  $Ae_3$ . This shows the that it is reasonable to use the peak austenite fraction as an estimate of the  $Ae_3$ .

In contrast to the AlN precipitation, the volume fractions of Nb(C,N) precipitated under equilibrium conditions remained approximately constant between steels, Table 7.5. It should also be noted that with deformation, the reaction kinetics of Nb(C,N) can be increased by over an order of magnitude (discussed further in Section 8.5.3), so that in the time taken to carry out the tensile test equilibrium conditions can be achieved.

Table 7.5: Maximum precipitation temperature and volume fraction ( $V_f$ ) Nb(C,N) precipitated (FactSage model).

Sample	Temperature °C	$V_f$ Nb(C,N)
Trip 1	1205.78	0.0001474
Trip 9	1178.98	0.0001473
Trip 2-1	1229.18	0.0001415
Trip 3	1239.94	0.0001474
Trip 10	1249.34	0.0001651

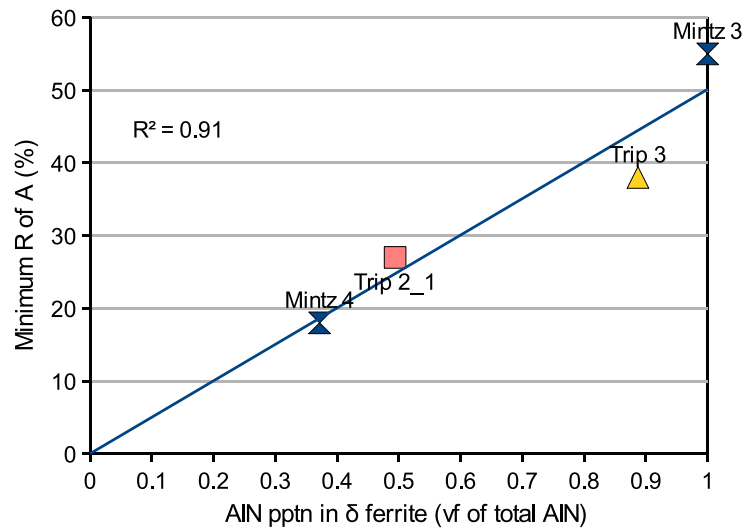


Figure 7.5: Relationship between AlN precipitation in delta ferrite and minimum ductility for the steels which have AlN precipitation in the delta ferrite (Trip2-1 and Trip 3 with 1.05 and 1.53%Al respectively, as well as Mintz 3, 4 with 1.93 and 0.98%Al from [10]). The volume fraction is taken from the Factsage program and the minimum ductility taken from the ductility curves.

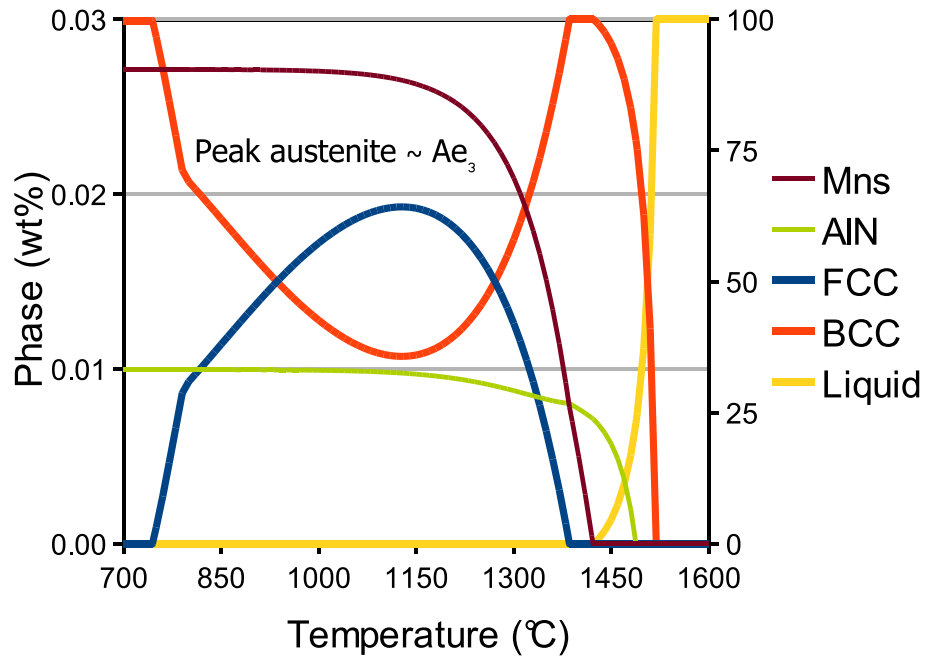
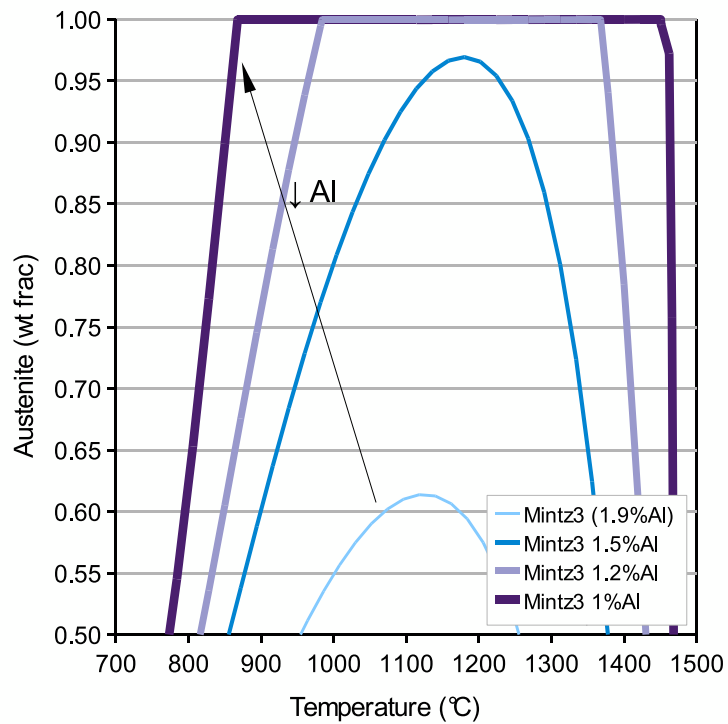
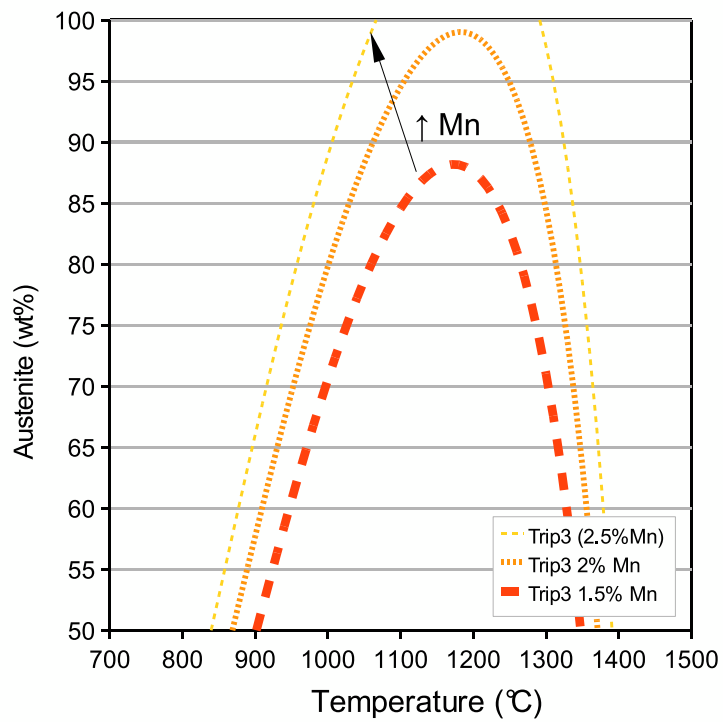


Figure 7.6: Mintz steel 3[10]  $Ae_3$  determination.



a)



b)

Figure 7.7: Plot of phase proportion vs temperature for a) Mintz 3[10] and b) Trip 3 steels with modified Al and Mn contents (original content in brackets). Decreasing the Al in the Mintz 3 steel on the  $A_{e3}$  has the same effect as increasing Mn in the Trip 3 steel. It is reasonable to use the peak austenite level as the  $A_{e3}$ . Increasing Mn leads to a higher carbon equivalent, while increasing Al leads to a lower carbon equivalent.

## 7.4 Constitutive phase diagrams for the current steels

FactSage was also used to construct phase diagrams along the 0.05, 1 and 1.5%Al iso-planes. These may be found in Figures 7.8, 7.9, 7.10 respectively. In the case of the 0.05%Al steel, Figure 7.8, the transformation is  $L \rightarrow L + \delta \rightarrow L + \gamma \rightarrow \gamma$  with the formation of single phase austenite at  $\sim 1500^\circ\text{C}$ . In the case of the 1.05%Al steel, Figure 7.9, the transformation is  $L \rightarrow L + \delta \rightarrow L + \delta + \gamma \rightarrow \delta + \gamma \rightarrow \gamma$  with the formation of single phase austenite at  $\sim 1400^\circ\text{C}$ . In the case of the 1.53%Al steel, Figure 7.10, the transformation is  $L \rightarrow L + \delta \rightarrow \delta \rightarrow \delta + \gamma \rightarrow \gamma$  with the formation of single phase austenite at  $\sim 1300^\circ\text{C}$ . It can be seen that increasing the Al content raises the  $Ae_3$  temperature and increases the alpha and delta ferrite phase fields. This increase also results in a limited, single austenite phase field at higher Al contents. This confirms the trend of Figure 7.7a where as the Al level increases, the single phase austenite field becomes smaller.

## 7.5 Other solubility equations

The equations that have been listed in the literature (Section 2.4.2, Table 2.4, page 88) were used for the steels in Table 7.1. It has been assumed that AlN precipitation does not influence the Nb(C,N) precipitation, which is a fair assumption [54]. It was decided not to explore the other solubility models for Nb(C,N) in depth as they, among themselves, showed greater variation than the free energy simulations. Solubility equations can be more accurate in practice than the thermodynamic model as they are based on practical experimentation where the times are realistic rather than infinitely slow. The free energy simulations were considered adequate, and the solubility equations are merely a rough check.

The MnS solubility equations of Turkdogan [146], are between  $120^\circ\text{C}$  higher and  $23^\circ\text{C}$  lower than the phase simulations, Figure 7.11. The best agreement occurs in the peritectic range  $C_{actual} - C_{peritectic}$  of 0.025 to 0.05%C where the MnS dissolution temperature is at its lowest. The AlN solubility ranges  $495^\circ\text{C}$  above to  $440^\circ\text{C}$  below the values predicted by FactSage, Figure 7.12.

If all the Nb(C,N) precipitation/solubility equations (from Table 2.4) are used to calculate the precipitation temperatures for the various steel and this is plotted against  $C_{actual} - C_{peritectic}$ , the variation in the predicted Nb(C,N) solubility temperatures, Figure 7.13, is  $151^\circ\text{C}$ . The Thermo-Calc falls roughly along the average predicted solubility temperatures, while the FactSage values are higher than most predicted solubility temperatures. This can be expected as some of these are experimentally determined.

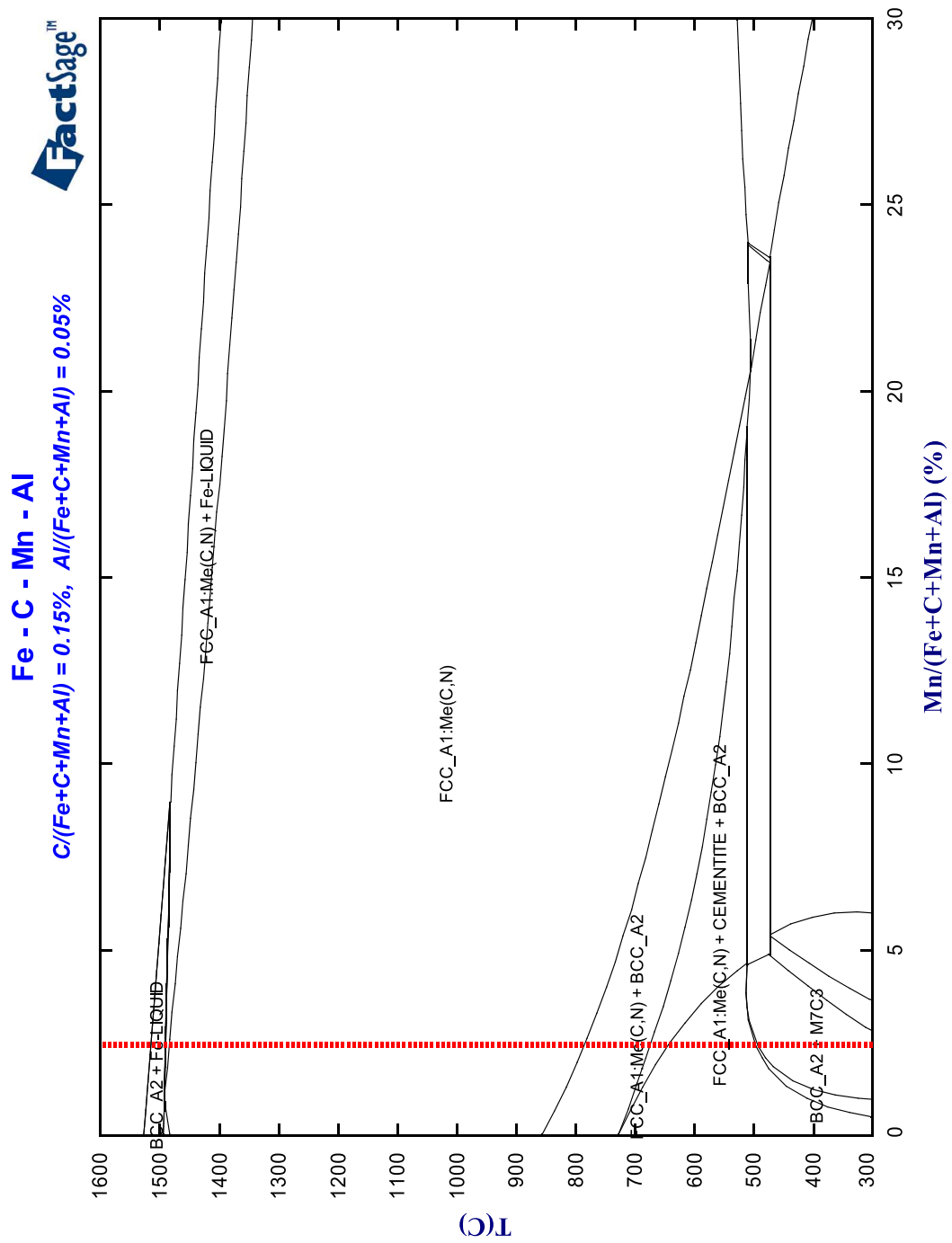


Figure 7.8: Plot of phase diagram along the 0.05%Al iso-plane. Dotted line indicates Mn = 2.4%.



**Fe - C - Mn - Al**  
 $C/(Fe+C+Mn+Al) = 0.15\%$ ,  $Al/(Fe+C+Mn+Al) = 1.0\%$

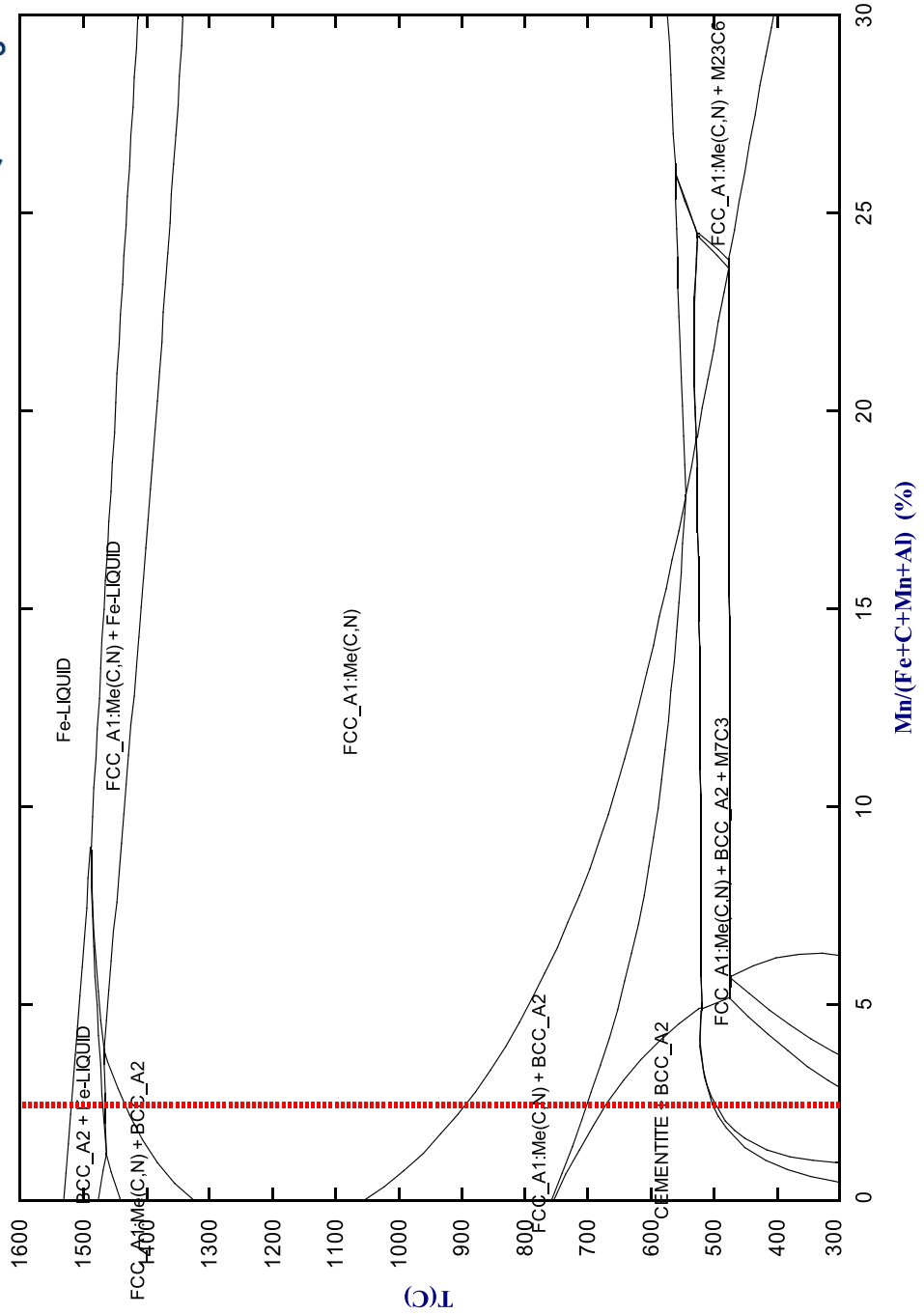


Figure 7.9: Plot of phase diagram along the 1%Al iso-plane. Dotted line indicates Mn = 2.4%.

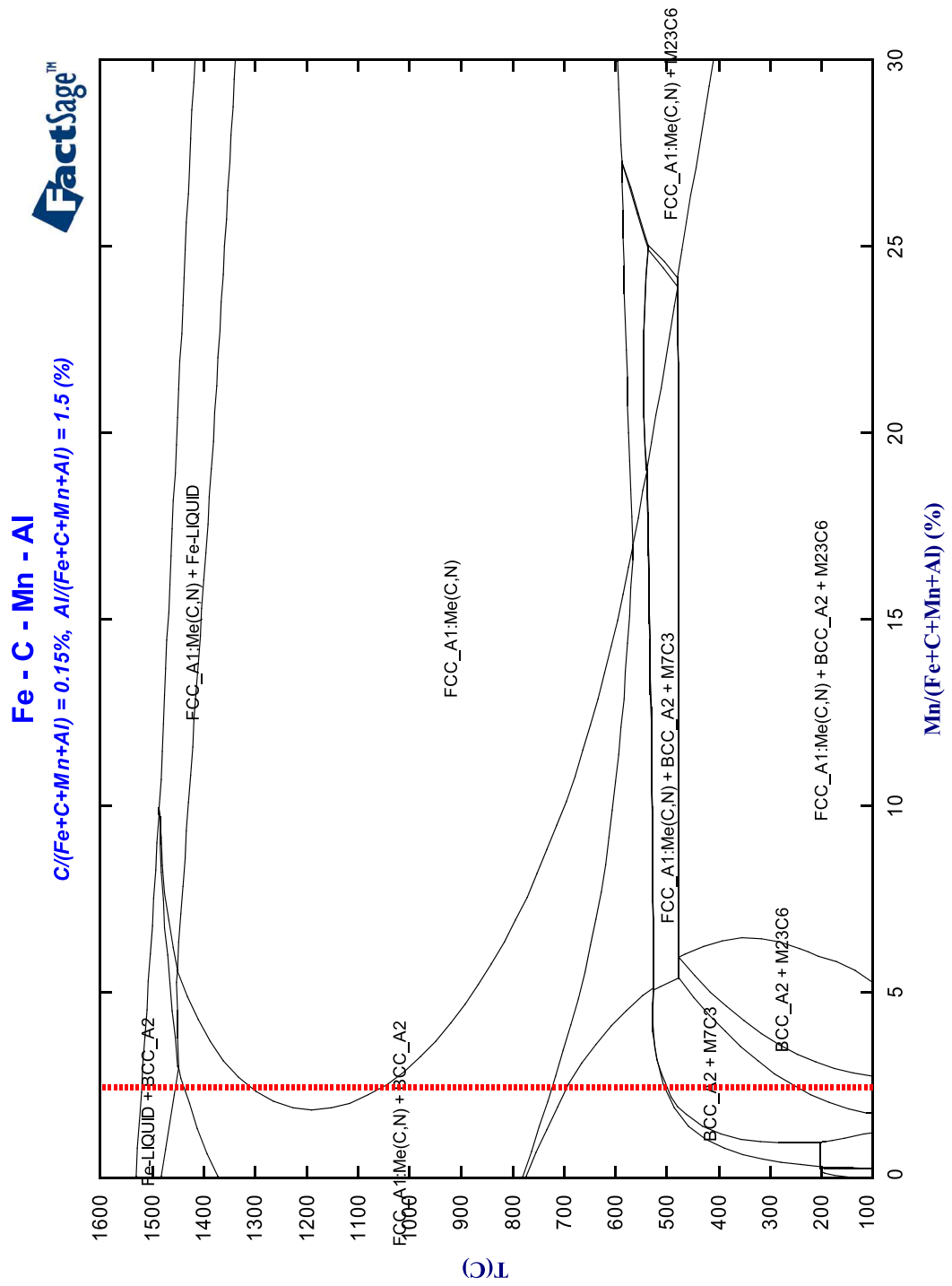


Figure 7.10: Plot of phase diagram along the 1.5%Al iso-plane. Dotted line indicates Mn = 2.4%.

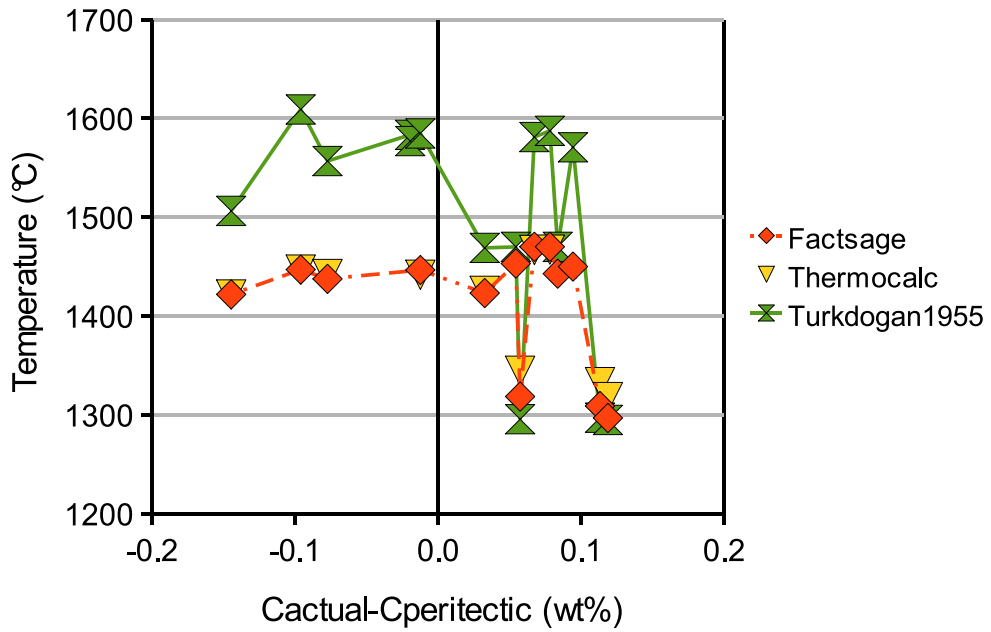


Figure 7.11: MnS solubility temperatures for steels in Table 7.1 and 7.2.

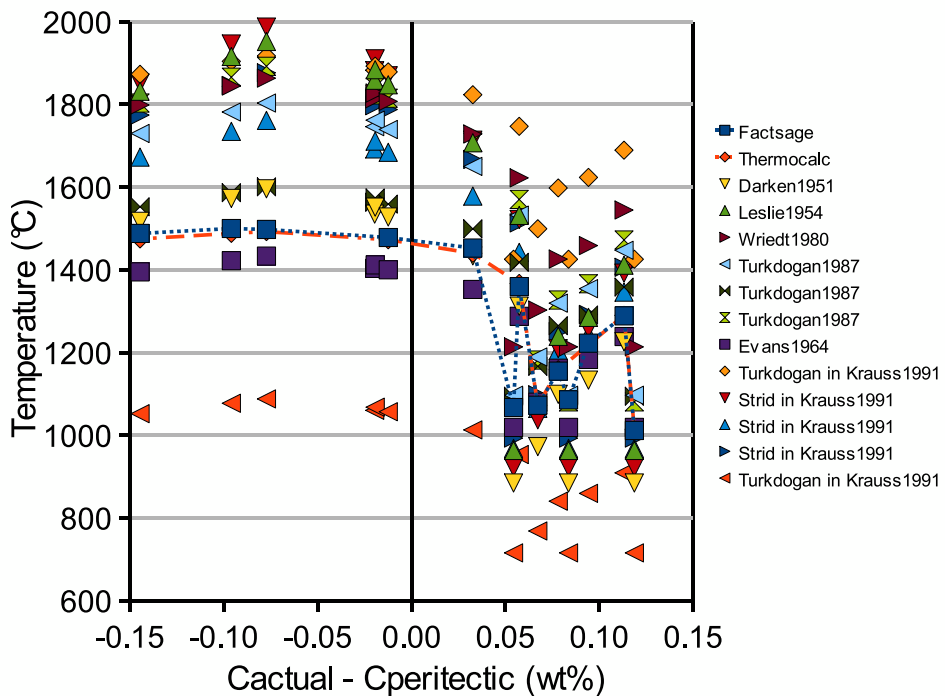


Figure 7.12: AlN solubility temperatures for steels in Table 7.1 and 7.2.

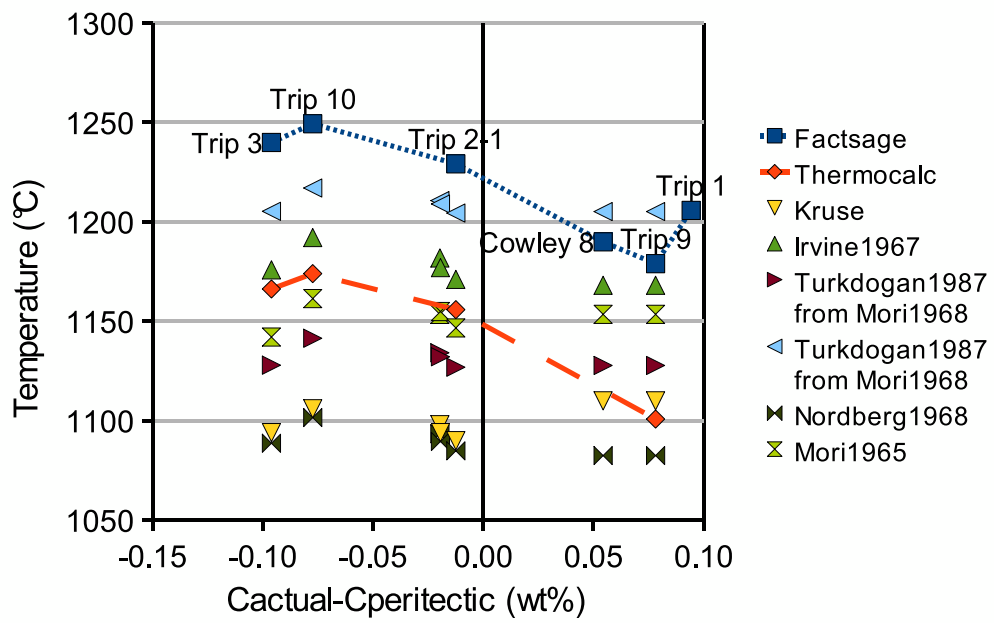


Figure 7.13: Nb(C,N) solubility temperatures for TRIP steels in Table 7.1 and 7.2.

Table 7.6:  $A_{r3}$  temperatures as determined using a theta dilatometer [182].

Steel	%Al	$A_{r3}, 2^{\circ}\text{Cs}^{-1}$	$A_{r3}, 1^{\circ}\text{Cs}^{-1}$	Posco lable
1	0.05	581	-	TR1-1
9	0.05	536	561	TRIP9-1
2	1.04	573	562	TRIP2
3	1.5	584	-	TRIP3-5

## 7.6 $A_{r3}$

The  $A_{r3}$  temperatures were determined at  $1^{\circ}\text{Cs}^{-1}$  and  $2^{\circ}\text{Cs}^{-1}$  using a theta dilatometer [182]. The results are shown in Table 7.6. This is discussed further in section 8.5.5, page 224 and Figures 8.16-8.18<sup>3</sup>.

## 7.7 Conclusions of thermodynamic modelling simulations

1. The effective peritectic point,  $C_{actual} - C_{peritectic}$ , can be used as an effective means of comparing the hot ductility behaviour of steels of varying Al, C and Mn contents.
2. It was shown that the steels range from hyper-peritectic (0.05%Al steel) to hypo-peritectic for the 1.5%Al steel. The 1%Al steel fell within in the peritectic range and had the lowest minimum ductility. Where the single austenite phase field starts at high temperatures and grain growth is encouraged.
3. Phase simulations using two commercial packages (FactSage and Thermo-Calc) yielded similar phase fields. The two simulations compared favorably with each other for all steels from the  $A_{e3}$  to the melting point.
4. The minimum ductility improved as the mass fraction of AlN precipitating in the delta ferrite increased.
5. The MnS solubility equations of Turkdogan [146], predict temperatures that were between 120 higher and 23°C lower than the phase simulations temperatures. The AlN solubility ranged 495°C above to 440°C below the values predicted by FactSage. The Nb(C,N) precipitation temperature from the solubility equations had a 151°C variation.
6. Precipitation solubility equations gave a much wider variability than the thermodynamic phase predictions at high Al levels.

---

<sup>3</sup>Starting on page 224

## Chapter 8

# Discussion

### *Summary of discussion*

In the 0.05%Al and 1.5%Al steel the ductility loss has been shown to be statistically dependant on the Nb(C,N) precipitation size and the grain size. The Nb(C,N) precipitates served to immobilize the grain boundaries and reduced ductility by facilitating cavity/crack link up. The failure mechanism in these two steels was therefore the interaction of precipitation size and density (inter particle distance). The inter particle distance was influenced by both the grain size and the volume fraction precipitation, this was the reason for the 0.05%Al steel having poorer ductility at the same volume fraction and size of the Nb precipitation as the 1.5%Al steel, the difference being the grain size, the finer grain size in the 1.5%Al steel increasing the interparticle distance. In Al-Nb TRIP steels, the Al radically altered the phase stabilities, leading to steels that varied from hypo-peritectic through to hyper-peritectic compositions as the Al level decreased from 1.5 to 0.05%Al. From phase transformation behaviour, it was shown that the minimum ductility improves with the volume fraction of AlN precipitating in the delta ferrite range. In contrast, at 1%Al a significant amount of AlN precipitated in the austenite and the steel was in the peritectic range. If the AlN precipitated in the delta ferrite, then when the steel transformed to austenite the AlN was unlikely to be situated at the austenite grain boundaries and hence was not able to influence ductility. In contrast if the AlN precipitated directly in the austenite, it will remain on the grain boundaries which undergo no further grain boundary movement on cooling further in the austenite range. Therefore, the 1%Al steel the trough was wider than the  $A_{e3} - A_{r3}$ , due to the high density of AlN along the grain boundaries at all temperatures.

## 8.1 Introduction

This chapter integrates the results (Chapters 3-7) and the literature survey chapter (Chapter 2). It also proposes the failure mechanisms for the high Al-Nb containing steels. The main findings of the results chapters are summarised below so that the discussion can proceed from a wider scenario:

**Hot Ductility.** In many of the samples that were melted prior to hot tensile testing porosity was found to be  $>10\%$ . The result was that detailed interpretation of the R of A curves could only be performed for unmelted tests. The 1.53%Al steel has the best hot ductility behaviour. The ductility trough was similar for the low ( $<0.05\%$ Al) and high (1.53%Al) steels. However for the 1.05%Al steel an extended trough was observed, similar to the work performed at CUL [179]. The statistical analysis on four samples at the same temperature ( $1000^{\circ}\text{C}$ ) showed that R of A has a Gaussian distribution with average of 41% and standard deviation of 9.7%.

**Optical Microscopy observations.** In the 0.05 and 1.53%Al steel there was a reasonable correlation between grain size close to the fracture surface and the ductility ( $R^2 = 0.76$  and 0.82 respectively); the finer the grain size the higher the R of A. This indicated that the grain size and R of A are related but that grain size was not the only variable that significantly affects the R of A. In the 1.05%Al steel, grain size did not appear to influence R of A, owing to the presence of dendritic AlN precipitation at the boundaries at all temperatures which dominated the fracture process.

**SEM observations.** The fracture behaviour and porosity of the steels that were observed under the optical microscope was confirmed with SEM. From the presence of hexagonal plate AlN precipitation in the pores in the 1 and 1.5%Al steel, it was deduced that AlN precipitation occurred in the melt. The extended trough for the 1.05%Al was attributed to the copious precipitation of dendritic AlN, resulting in an intergranular rock candy failure mode. In the 1.05%Al steel, needle and plate precipitation were also present at higher R of A values.

**TEM observations.** In the 0.05 and 1.5 %Al steels ductility correlated fairly with precipitate size ( $R^2 = 0.99$  and 0.65 respectively). Test temperature was only strongly related to precipitate size ( $R^2 = 0.87$ ) for the 1.5%Al steel. In the 0.05%Al steel cubic Nb(C,N) precipitation was only found in the vicinity of the grain boundaries. Eutectic Nb(C,N) was also observed. In the 1%Al steel precipitate size was not related to ductility or to test temperature. Ductility loss was attributed to the dendritic and hexagonal plate AlN precipitation along austenite grain boundaries. Thin (100nm) dendritic AlN precipitation was observed in the 1.05%Al steels and was identified as

fcc, with a lattice parameter of 0.460nm. In the 1.5%Al steel, the hexagonal plate AlN was hcp with a lattice spacing of  $a=0.323\text{nm}$  and  $c=0.499\text{nm}$ . The improvement in R of A values at temperatures above 1100°C could not be attributed to the coarsening of sub 20nm Nb(C,N), since the precipitate size was similar above and below this temperature.

**Modelling of phases.** The Al addition changed the phase transformations and precipitation sequence in the steels dramatically. Calculations by Blazek[140] showed that as the Al level increased, the steel changed from hyper-peritectic to hypo-peritectic. There was a convincing relationship with the minimum ductility and proximity to the effective peritectic point. The two thermodynamic models, Thermo-Calc and FactSage, showed that both 0.05 and 1%Al steels had a wide high single phase austenite region. In the case of the 1%Al steel the precipitation of the AlN started in the liquid + delta ferrite phase region. The minimum ductility improved as the mass fraction of AlN precipitating in the delta ferrite increased. The solubility equations for MnS, Nb(C,N) and AlN precipitation from literature demonstrate a wide range of solubility temperatures. The AlN solubility temperatures is from 700 to 1500°C at the 0.05%Al level, a variation of 800°C). Hence these equations yielded less helpful information than the thermodynamic modelling for the high Al steels.

## 8.2 Ductility

This section deals with the ductility behaviour in the light of previously reported results. The slightly higher ductilities reported by Kang *et al.*[178, 179], for these steels is likely to be a result of porosity.

While there is little in the literature which can be used as a comparison to the Al rich TRIP steels, a similar steel at lowest Al levels is that of Mintz and Mohamed [62], which is reproduced in Figure 8.1 with the present results. The S and Si levels are significantly different when compared to the Trip steel <sup>9</sup>1. The 0.05%Al steel is the only steel of which there is sufficient previous work, like Mintz and Mohamed [62, 83] to make a comparison. Their curve for a 1.4%Mn Nb containing steel differs from the 0.05%Al curve only in that the 0.05%Al steel curve is displaced to lower temperatures by 50°C due to the higher Mn content. This is in agreement with the  $Ae_3$  transformation temperatures to be expected from Andrews equation [167] (which are 800 and 853°C for the Trip 9 and Mohamed B steels respectively). These are higher than the non-deformation  $Ar_3$  for the Trip 9 steel which is 536°C, although this will be discussed in Section 8.5.5. The shifting of the temperature of

---

<sup>1</sup>Table 7.1, page 178 and Table 7.2, page 181 for Trip 9 and Mohamed B respectively.

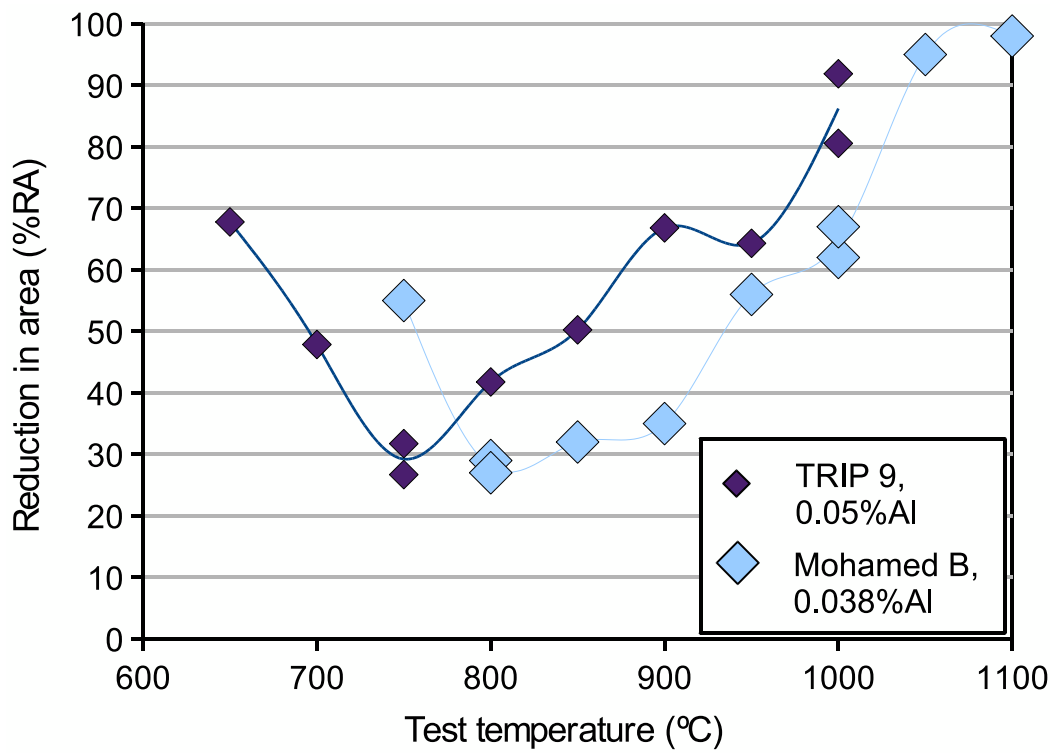


Figure 8.1: Hot ductility curves for present 0.05%Al steel and previous ductility curves from the work of Mintz and Mohamed [62]. Mohamed steel B contains 0.1C; 1.39Mn; 0.007P; 0.01S; 0.42Si; 0.026Nb; 0.038Al; 0.0038N.

the minimum ductility up 50°C to 800°C for the 1.5%Al steel could also be expected as increasing Al has the same effect on the phase stabilities as decreasing the Mn level (see Figure 7.7 page 186), by raising the  $Ae_3$ .

In the case of the work by Mintz *et al.*[10] who also studied Al rich TRIP steels, the carbon levels are slightly higher, 0.15-0.22%C, and the Mn levels are lower, 1.4-1.5%Mn. The steels also contained no niobium additions. These are set below one another in Figure 8.2<sup>2</sup>. The most obvious similarity is that the 1%Al steel has the worst ductility, whereas steels with Al levels above and below 1% perform better. Additionally, in both sets of steels the temperature at which minimum ductility occurs increases as the Al content increases.

While the results of Mintz *et al.*[10] followed a similar trend to the present work, other workers [11] showed less correlation. In Su *et al.*[11] work, reproduced in Figure 2.34d, the 0.87%Al steel also had a wide trough. The minimum ductility (the ‘bottom’ of the trough) is plotted as a function of Al content in Figure 8.3 for all investigations. In Su *et al.*’s work the minimum ductility is probably higher than the present results due to its low N content (0.0025%N) and consequent reduction in AlN volume fraction. Both the TRIP steels in literature [10, 11] contain no Nb, and as a result, the bottom of the troughs are, on the whole, ~25% higher than the present work. The exception is the 1%Al steel of Mintz *et al.*[10] which has the lowest minimum ductility. The lack of Nb makes direct comparison of the ductility values difficult, although the general trend can be expected to be similar.

In low Al steel, Zhang *et al.*[44], found poorer ductility in melted specimens compared to ‘unmelted’ samples, the opposite to what has been observed in the low Al steel in this work. However, in the present work, the fractures tended to be intergranular rather than interdendritic<sup>3</sup>.

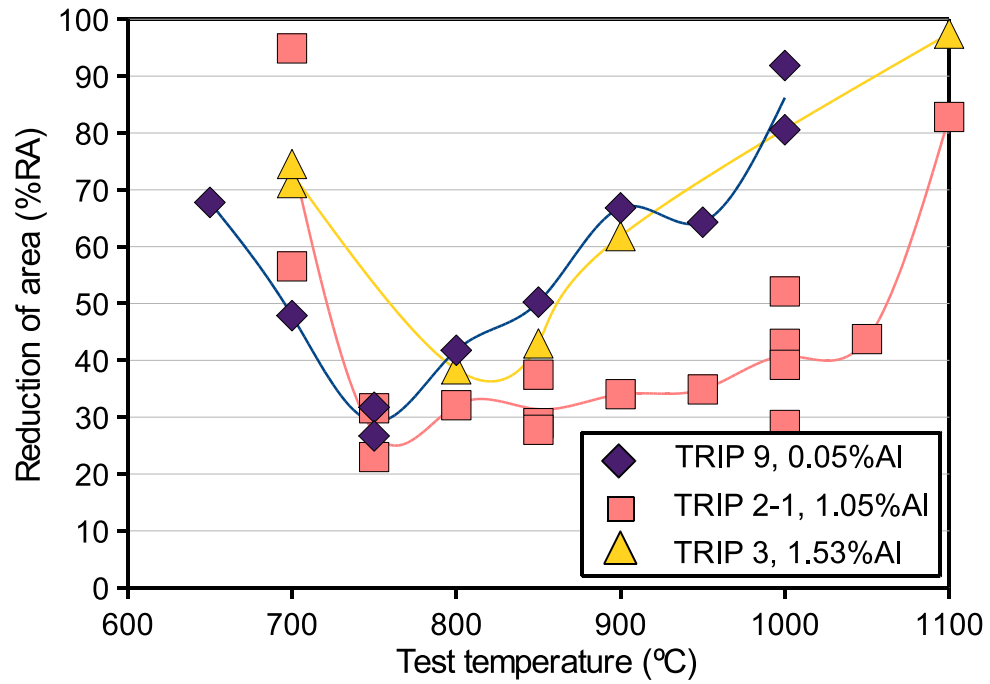
The use of the minimum ductility to compare steels has been chosen as a method of ranking the castability of these steels. The trough depth is known to correlate with the problem of transverse cracking because at the very least the depth of the trough is influenced by the same variables as transverse cracking [17]<sup>4</sup>. The use of the trough width as a means of ranking ductility was much less successful, especially since the  $Ae_3$  temperatures vary markedly with Al content. The differences in hot ductility behaviour for all the steels required a more detailed examination of the influence of Al on the peritectic reaction, the  $Ae_3$  and what volume fractions AlN are precipitating in the various phases in each of the steels. For this reason thermodynamic simulations were required (these will be dealt with in Section 8.5.2). However, before the phase simulation is discussed, it is necessary

---

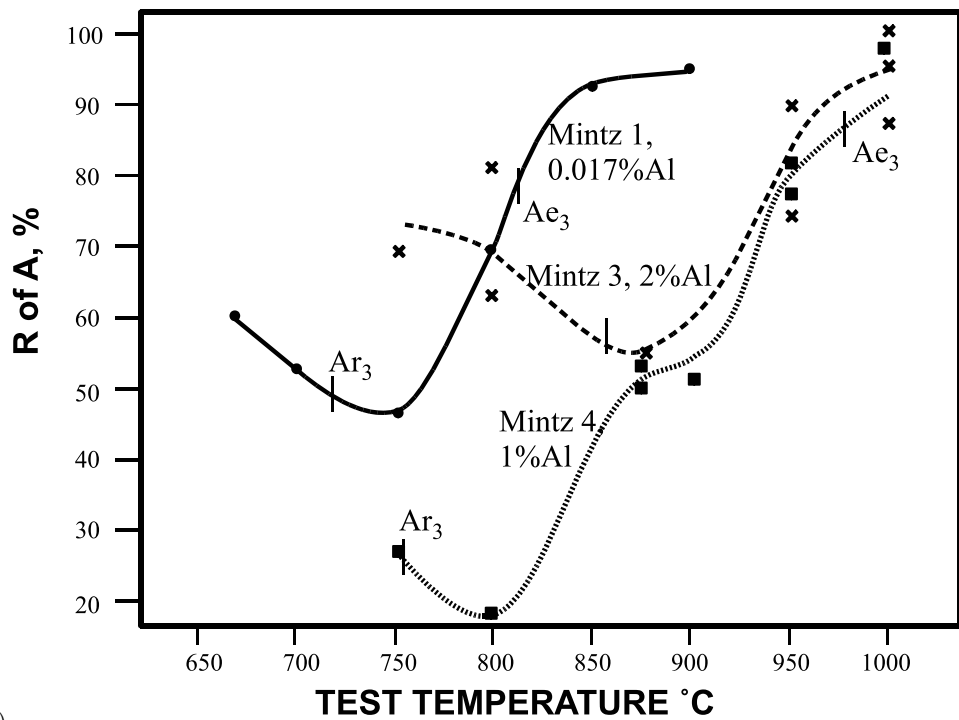
<sup>2</sup>Results are reproduced from Figures 3.7-3.9 page 112-113. Mintz *et al.*[10] taken from Figure 2.33 on page 84-85.

<sup>3</sup>Figure 4.2a, page 120

<sup>4</sup>Discussed on page 53



a)



b)

Figure 8.2: Hot ductility curves for a) present study ductility. Ductility curves from the work of b) Mintz *et al.*[10]. Mintz steel 1 contains 0.017Al, Mintz 3 - 1.93%Al and Mintz 4 - 0.98%Al. The present results (a) showed wider trough behaviour while the previous work (b) showed deeper trough behaviour.

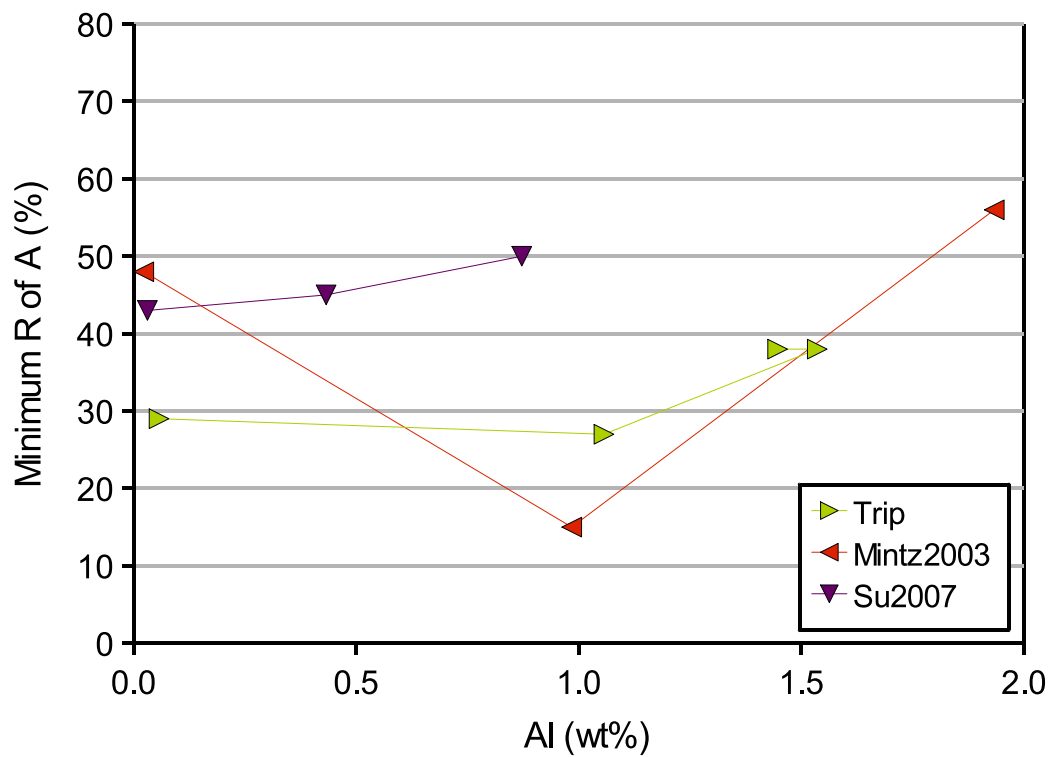


Figure 8.3: Plot of aluminium content versus minimum ductility for the present study (Trip). Also included are the results for Mintz *et al.*[10] (Mintz2003) and Su *et al.*[11] (Su 2007) investigations.

to integrate the ductility behaviour of each of the steels with the different aspects of the microscopy: OM, SEM, TEM.

## 8.3 Microscopy

### 8.3.1 0.05% Aluminium steel

In the 0.05%Al steel no AlN precipitation was seen at any test temperature. Even on the fracture surface where strain had to have occurred, no AlN was seen with FEG-SEM. This is in contrast to the work of Chamont *et al.*[91]<sup>5</sup> where strain induced AlN precipitation is observed in steels containing <0.03%Al. However, considering that Mn is predicted to have a retarding effect on AlN precipitation [108]<sup>6</sup>, the 2.5%Mn in these steels compared with the 1.5%Mn in Chamont *et al.*'s[91] steel, might be expected to prevent AlN precipitation. Nevertheless, while it is not clear from the microscopy whether precipitated AlN may be having an effect in the 0.05%Al steel, the presence of the Nb(C,N) in the microstructure does indicate that it's influence as a fine precipitate will have preceded the AlN, thus can be considered as more pivotal. With regards to the absence of Nb(C,N) in large areas away from the grain boundaries and the fine size distribution of the precipitation, it is likely that dynamic precipitation occurred (this is discussed further in Section 8.5.3, page 220). In this steel the greatest influences on ductility were the grain size and Nb(C,N) precipitation.

### 8.3.2 1.05% Aluminium steel

The most obvious feature of the ductility curve at this Al level, was the width of the trough, which is similar in Su *et al.*'s[11] work. In Mintz *et al.*'s[10] work it is less apparent because of the very low minimum ductility but the width of the trough is still extended (compare Mintz 1 with Mintz 4 in Figure 8.2).

An important microstructural feature was the rock candy fracture, associated with dendritic AlN precipitation. This type of precipitation was observed in the cross section taken from the tensile specimens, fracture surfaces and replica's<sup>7</sup>, and has been reported before [31]<sup>8</sup>, [46]<sup>9</sup>, [14, 91, 136, 137, 138, 139]. Crowther *et al.*[137] observed dendritic AlN precipitation even though they heated directly to test temperature, although Woodfine and Quarrell [46]

---

<sup>5</sup>Discussed on page 78

<sup>6</sup>Discussed on page 82

<sup>7</sup>Figure 4.7, page 127; Figure 5.8, page 147; Figure 5.4c page 140 and Figure 6.9 page 161

<sup>8</sup>Discussed in Figure 2.5, page 42

<sup>9</sup>Discussed in Figure 2.31, page 82

describe it as precipitation formed in the final stages of interdendritic solidification. This will be discussed further when considering the thermodynamic simulations (Section 8.4).

In considering the morphological aspects of AlN precipitation, the width of the dendritic precipitation was overestimated using the SEM, since the measurement of 800nm was not exactly end on (Figure 5.6 page 145), but probably in reality would be closer to the TEM measurements estimate of 100nm (Figure 6.7, page 160). These were electron transparent as observed by Wright and Quarrell [136]<sup>10</sup>, but appeared to be thicker than the precipitates that Wilson and Gladman [14] have reported. The dendritic AlN precipitates in the 1% steel were fcc, not the normal hexagonal close packed type, something that has only been reported before[14] for AlN with smaller cuboid morphologies which precipitate out at lower temperatures in the ferrite (650°C). Although the lattice parameter in the current work (0.460nm) is on the upper limit of the lattice sizing (0.410-0.417nm[14]) it is still within the 10% experimental error that can be expected from electron diffraction[181]. Chamont *et al.*[91], observed needle precipitation (in <0.03%Al steels) after straining. In the present work, the needle type precipitates were seen in the regions of porosity, indicating they were not necessarily strain induced in the 1.05%Al steel.

The AlN co-precipitated with both Nb(C,N) and MnS. The combination of Nb(C,N) and plate AlN clearly decorated grain boundaries (Figure 6.11, page 163). These precipitates, together with the dendritic type of AlN precipitation are expected to immobilize the grain boundary, as can be seen by the fracture along AlN decorated grain boundaries (Figure 5.2c, page 138). Leap and Brown[139] have also observed co-precipitation of Nb(C,N) on AlN, although in their case the AlN morphology was needle like.

The present work shows the overwhelming evidence for the perniciousness of the AlN precipitation which for the 1%Al steel, was considered to override and mask any influence of the Nb(C,N) size or morphology, austenite grain size or test temperature on hot ductility.

### 8.3.3 1.53% Aluminium steel

This steel had a remarkably finer average grain size than the lower Al steels. Additionally, AlN did not appear to have precipitated as densely on grain boundaries as it did in the 1%Al steel, as would be expected for this significantly finer grain size, Figure 8.4. The lower density was therefore a result of the greater grain boundary area. Both the finer grain size and the lower AlN precipitation density would be expected to encourage DRX.

The SEM work demonstrated that AlN precipitation was formed above the solidus (Figure

---

<sup>10</sup>Discussed on page 79

5.9, page 149). However, as the TEM work did not show a clear order of precipitation as the Nb(C,N) precipitates have been seen at both the AlN plate centre and edge (Figure 6.12, page 164), AlN and Nb(C,N) may have co-precipitated. AlN precipitates were hexagonal close packed, with lattice parameter calculated as  $a=0.323\text{nm}$ , and  $c=0.499\text{nm}$ . This was within 10% [181] to that reported ( $a=0.310\text{-}0.312\text{nm}$  and  $c=0.498\text{-}0.499\text{nm}$  [14]) in literature.

The Nb(C,N) was most easily seen in the 1.5%Al steel, possibly because high Al accelerates the precipitation of Nb(C,N) [27, 54], even though the high Mn may be having the opposite effect in slowing the precipitation as Michel and Jonas [108] have observed<sup>11</sup>. Increasing the test temperature caused the Nb(C,N) precipitation size to coarsen and that in turn affected the ductility in the expected manner [41, 79, 94, 95, 96].

### 8.3.4 General discussion on the microscopy

In general the intergranular fracture surfaces were a combination of microvoid coalescence and grain boundary sliding, as described by others [41, 42],[43]<sup>12</sup>. The current results also concurred with Crowther and Mintz [41] that high temperature rupture only occurs at ductility levels in excess of 80%. The dendritic AlN was similar to that reported by Croft *et al.* [31]<sup>13</sup>, and in cross section is similar to the grain boundary precipitation of Wright and Quarrell [136]. This rock candy phenomenon was not exclusive to the 1%Al steels (where it was seen in both melted and ‘unmelted’ samples), but was also observed in one instance in melted 1.5%Al steel. This is difficult to explain with such low sample populations so will be left unexplored. More testing on the 1.5%Al steel should be done to understand under what conditions rock candy fracture may occur.

The observation of the fair to strong correlation of inverse grain size and ductility (Figures 4.3,4.9, page 123 and 130) is prominent in this work. Although there is a the potential for coarsening the grains, this requires time that is not normally available in testing (although could be added to testing as Revaux *et al.* [69] did with a grain coarsening step in their testing). It would be expected that the austenite grain size prior to tensile testing in this work would not be strongly influenced by the test temperature but would be fixed approximately at that formed at the highest fully austenitic temperature.

Figure 8.5 shows the relationship between  $C_{actual} - C_{peritectic}$  and grain size at 750°C, which shows the grain refining effect of the Al addition. It changes solidification behaviour from hyper-peritectic side of the constitutional diagram to the hypo-peritectic side. This points

---

<sup>11</sup>Discussed in Section 2.4.1, page 72.

<sup>12</sup>discussed on page 45

<sup>13</sup>Reproduced in Figure 2.5 page 42

towards the effect of Al on the phase stabilities, which again emphasises the requirement to look closely at the phase stabilities.

Considerable work [17, 41, 92] has been carried out into the influence of un-recrystallised grain size on hot ductility. It is found that refining grain size improves ductility but the effect becomes smaller with coarser grain size due to a square root or exponential relationship. The relationship between ductility and grain size (from Section 4.2.2, page 123 and page 130) strictly only holds for a single temperature [92], so that other factors such as change in intrinsic strength are eliminated. However, using regression analysis as an engineering method, improves confidence in the argument that a increase in grain size has a small but negative influence on ductility.

The curve of precipitate size vs ductility for the 1.5 and 0.05%Al steels (Figure 6.19 page 171 and 6.5 page 158), has a similar logarithmic shape as that reported in literature[17]<sup>14</sup>, so that even if the linear regression correlation is low, there may be some merit in investigating these relationships. To this end, both Nb(C,N) precipitate size and grain size must be included as factors in a regression relationship.

### 8.3.5 Regression equations for grain size and precipitate size on the ductility of 0.05 and 1.53% aluminium steels

The aim of the following section is to try to use the data to show simple trends of how grain size and precipitate size influence ductility. However, this is not to be used as a fundamental study - since there are factors (such as Mn, cooling rate and strain rate) that are being held constant in the current work so that this analysis cannot be applied in a general manner. Other literature models are either inadequate in accounting for grain size [67]<sup>15</sup> or they are only applicable at much lower Al levels [94],[97]<sup>16</sup> and show very poor correlation with current work. Since neither the Nb(C,N) precipitate size (p) or grain size (D) completely explained the ductility properties, a regression of both was performed. It is known [39]<sup>17</sup>, [94] that

$$RA \propto p^{\frac{1}{3}}, \quad (8.1)$$

and for D, although Sellars[121] uses  $D^{\frac{1}{2}}$ , and Mintz *et al.*[17] uses  $D^{-\frac{1}{2}}$ <sup>18</sup>, both Crowther and Mintz[41]<sup>19</sup> and Maehara *et al.*[92]<sup>20</sup> found a reciprocal relationship more suitable and

---

<sup>14</sup>Figure 2.19, reproduced on page 66

<sup>15</sup>Equation 2.13 on page 102

<sup>16</sup>Equations 2.16-2.17 on page 103

<sup>17</sup>Figure 2.20 page 67 and discussed on pages 66 and 103

<sup>18</sup>Discussed on pages 103-104

<sup>19</sup>Figure 2.39 on page 94

<sup>20</sup>Figure 2.40, page 95

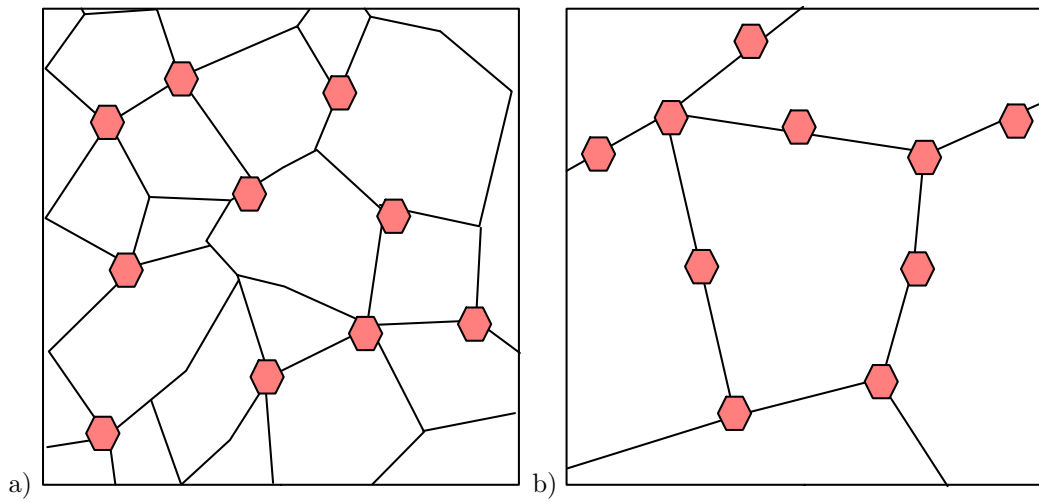


Figure 8.4: Effect of grain size and precipitation density on the grain boundaries. For the same amount of precipitation, the finer grain material (a) has a higher grain boundary area and a lower precipitate density than the coarse grain material (b).

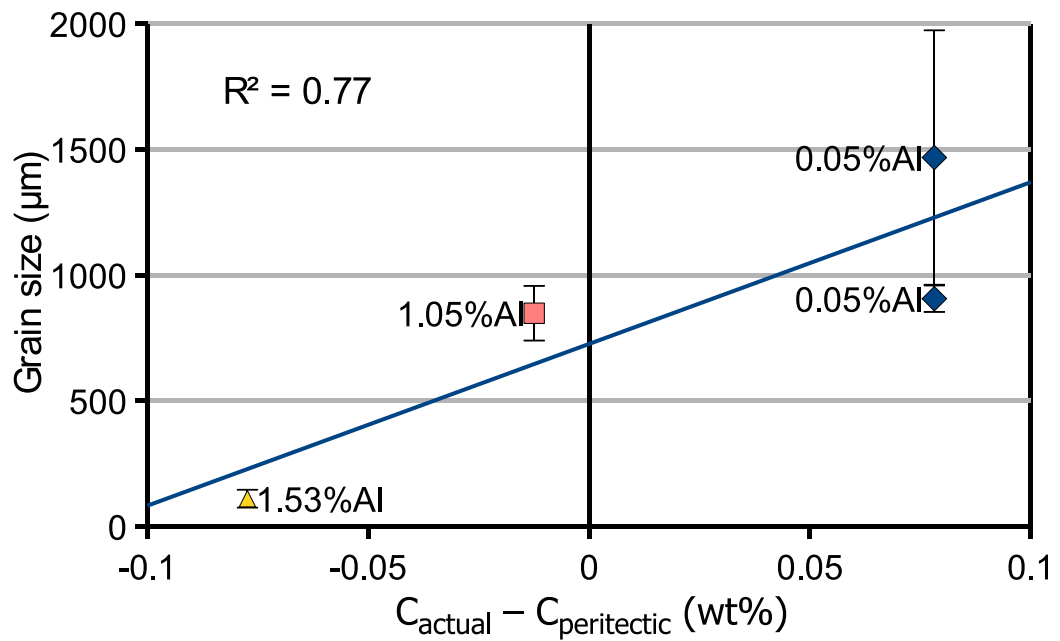


Figure 8.5: Relationship between grain size at 750°C and the effective carbon content,  $C_{actual} - C_{peritectic}$ .

this has been used in the present analysis<sup>21</sup>. So that

$$RA \propto D^{-1}, \quad (8.2)$$

and this regression would then take the form

$$RA = ap^{\frac{1}{3}} + bD^{-1} + c, \quad (8.3)$$

where p is in nm and D is in  $\mu\text{m}$ . The resultant regression was

$$RA = 128.9p^{\frac{1}{3}} + 5563D^{-1} - 274.2 \quad (8.4)$$

with  $R^2=0.88$ , ( $F_{2,7}=15.4$ ,  $p=0.01$ ) and all coefficients,  $a$ ,  $b$ ,  $c$ , had t-stats $>2.5$  and P-values $<0.05$ , indicating a good fit, Table 8.1<sup>22</sup>. Thus the combined relationship between

Table 8.1: Regression statistics and coefficients for the regression of grain size and precipitate size on ductility.

R square	0.88		
Standard error	7.5		
Observations	7		
F value	15.4		
Degrees of freedom	2		
p	0.01		
	Coefficients	t-stat	P-value
a	128.9	5.45	0.01
b	5563	3.88	0.02
c	-274.2	-4.47	0.01

grain size and precipitate size correlates with ductility for the 0.05 and 1.53%Al steel (Figure 8.6). It should be noted that in the case of the 1%Al containing steel, the copious precipitation of dendritic AlN along the grain boundaries so dominated the intergranular fracture that neither Nb(C,N) precipitation or the grain size had any significant influence on the ductility.

## 8.4 Thermodynamic simulations

Intergranular fracture and low ductility are enhanced when the austenite grain size is large and this was encouraged when the transformation  $L + \delta \rightarrow \gamma$  or  $L + \gamma \rightarrow \gamma$  temperature is high, as single phase austenite coarsens rapidly [92]<sup>23</sup>. The phase boundary of single phase

<sup>21</sup>Refer to Figure B.2, page 248 for other relationships

<sup>22</sup>As a variable, test temperature did not have a t-stat $>2.5$  and P-value $<0.05$ .

<sup>23</sup>Figure 2.40, page 95

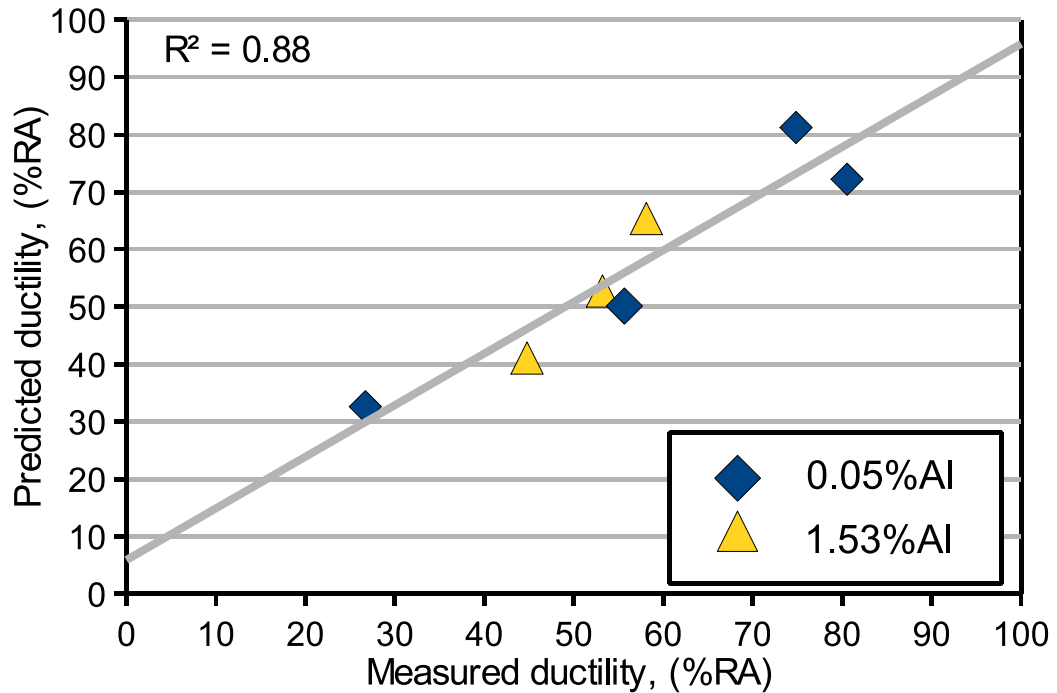


Figure 8.6: Multiple regression for precipitate size and grain size for 0.05 and 1.5%Al steels.  $R^2=0.88$ . Measurements taken over the temperature range 750-1000°C.

austenite is influenced by the C [15], [16]<sup>24</sup>, [63]<sup>25</sup>, [79], Mn [55]<sup>26</sup> and Al [140]<sup>27</sup>, [165, 166] levels which shows the need to compare the results of different authors on a common axis.

Comparing the current Al TRIP steels work with Su *et al.*[11] and Mintz *et al.*[10] high Al, TRIP steels was difficult because the differences in C, Mn and P levels. Thus the relative influence of these elements on the phase boundaries and precipitation presents problems and this was the reason for using simulation methods. For example, although Mintz *et al.*[10] have dealt with similar Al contents to those in the present work, their steels did not contain Nb, which is well known to cause a deterioration in ductility in high strength low alloy steels [17]. The combination of high Al with Nb in the present work is new and important.

#### 8.4.1 Simulation validation

The simulations require validation against data from literature in order to develop a working confidence in them. In both Thermo-Calc and FactSage, equilibrium conditions are predicted which is clearly not the case for the continuous casting operation. In spite of this,

<sup>24</sup>Discussed on page 70

<sup>25</sup>Discussed on page 69

<sup>26</sup>Discussed on page 71

<sup>27</sup>Discussed on page 89

Table 8.2: Reported liquidus and solidus temperatures ( $^{\circ}\text{C}$ ).

Steel	Liquidus Fact- sage	Liquidus Thermo- calc	Liquidus Thomas [162]	Solidus Fact- sage	Solidus Thermo- calc	Solidus Thomas [162]
Trip 9	1510	1511	1510	1460	1466	1485
Trip 2-1	1509	1511	1507	1446	1440	1475
Trip 3	1518	1518	1511	1444	1441	1479
Trip 10	1518	1518	1511	1444	1441	1480
Mintz 1	1513	1515	1514	1460	1466	1489
Mintz 2	1497	no calc	1506	1443	no calc	1476
Mintz 3	1519	1519	1510	1423	1419	1471
Mintz 4	1508	1510	1506	1435	1425	1470
Su 1	1506	1508	1506	1454	1452	1470
Su 3	1506	1508	1504	1442	1438	1463
Su 5	1508	1509	1505	1432	1428	1463
Cowley 8	1517	no calc	1516	1473	no calc	1492
MohamedB	1515	no calc	1517	1478	no calc	1497

deformation can speed up the reaction by significant amounts which can lead to conditions closer to equilibrium. The most widely reported liquidus and solidus temperatures were Thomas's [162] equations, based on experimental work in 1987 (Equations 2.3, 2.4, page 89), which are compared in Table 8.2 and Figure 8.7. The  $\text{Ae}_3$  are compared in Table 8.3 and Figure 8.8. The  $\text{Ar}_3$  and the temperature where DIF occurred were also used since both were expected to always be below the  $\text{Ae}_3$ .

It can be seen that from Table 8.2 and Figure 8.7, for the liquidus temperatures there was generally good agreement between the simulation packages and Thomas's regression, although there were small differences at the highest Al contents (Low  $C_{\text{actual}} - C_{\text{peritectic}}$  values). For the solidus temperature both the Factsage and the Thermo-Calc programmes are in good agreement but Thomas's regression of experimental data is as much as  $40^{\circ}\text{C}$  higher, Table 8.2 and Figure 8.7. As the Al is increased (equivalent to reducing the  $C_{\text{actual}} - C_{\text{peritectic}}$  value), the difference between the Thomas *et al.*'s [162] values and the FactSage/Thermo-Calc values increased.

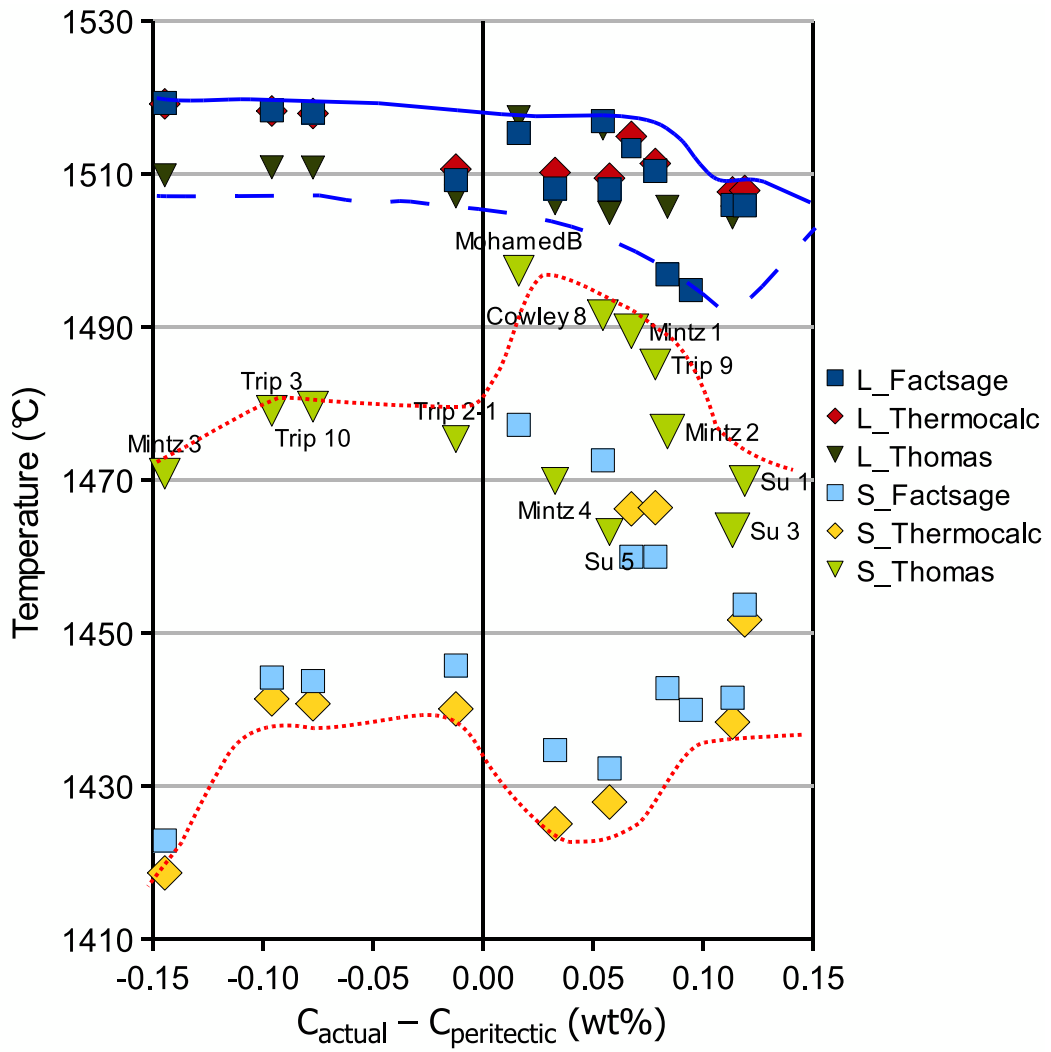


Figure 8.7: Liquidus and solidus vs  $C_{actual} - C_{peritectic}$  for steels in Table 7.1. Data from Table 8.2.

Table 8.3: Reported  $Ae_3$  and  $Ar_3$  temperatures ( $^{\circ}C$ ).

Steel	$Ae_3$ Fact Sage	$Ae_3$ Thermo- calc	$Ae_3$ Andrews [167]	Reported $Ae_3$	Reported $Ar_3$	DIF (ref[179])
Trip 1	819	no calc	844	817 ref[179]	581 ref[182]	800
Trip 9	795	796	800	794 ref[179]	536-579 ref[182]	800 (600)
Trip 2-1	940	946	562	902 ref[179]	573 ref[182]	800 (750)
Trip 3	1067	1083	412	1069 ref[179]	571 ref[182]	950 (1000)
Trip 10	1019	1029	435	-	-	950 (900)
Mintz 1	819	820	828	820 ref[10]	720 ref[10]	-
Mintz 2	855	no calc	884	857 ref[10]	732 ref[10]	-
Mintz 3	1125	1127	316	none ref[10]	855 ref[10]	-
Mintz 4	971	978	594	978 ref[10]	756 ref[10]	-
Su 1	821	827	866	842 ref[11]	825 ref[11]	-
Su 3	860	866	762	990 ref[11]	1025 ref[11]	-
Su 5	937	949	652	1190 ref[11]	750 ref[11]	-
Cowley 6	814	no calc	819	812 ref[55]	700 ref[55]	-
Cowley 8	821	no calc	836	817 ref[55]	670 ref[55]	-
MohamedB	844	no calc	853	860 ref[62]	-	-

For the  $Ae_3$  temperatures (Table 8.3 and Figure 8.8) again, agreement was reasonably close for the Thermo-Calc and FactSage programs but Andrews experimentally determined  $Ae_3$  values are significantly lower. Andrews' [167] work is important for low Al additions when  $C_{actual} - C_{peritectic}$  is  $\sim 0.1$  as there should be little difference between the thermodynamic models and Andrew's experimental equation if the models are to be meaningful. Such agreement was seen to occur with differences of less than  $25^{\circ}C$  except in the case of Su 1 [11]. However, Andrews did not examine high Al containing steels, or steels with higher than 2%Mn and as a result his prediction is very poor at the low  $C_{actual} - C_{peritectic}$  values where the Al level is high. The presence of DIF and the  $Ar_3$ 's as given in Table 8.3, are below the  $Ae_3$ 's as would be expected (discussed further in section 8.5.5).

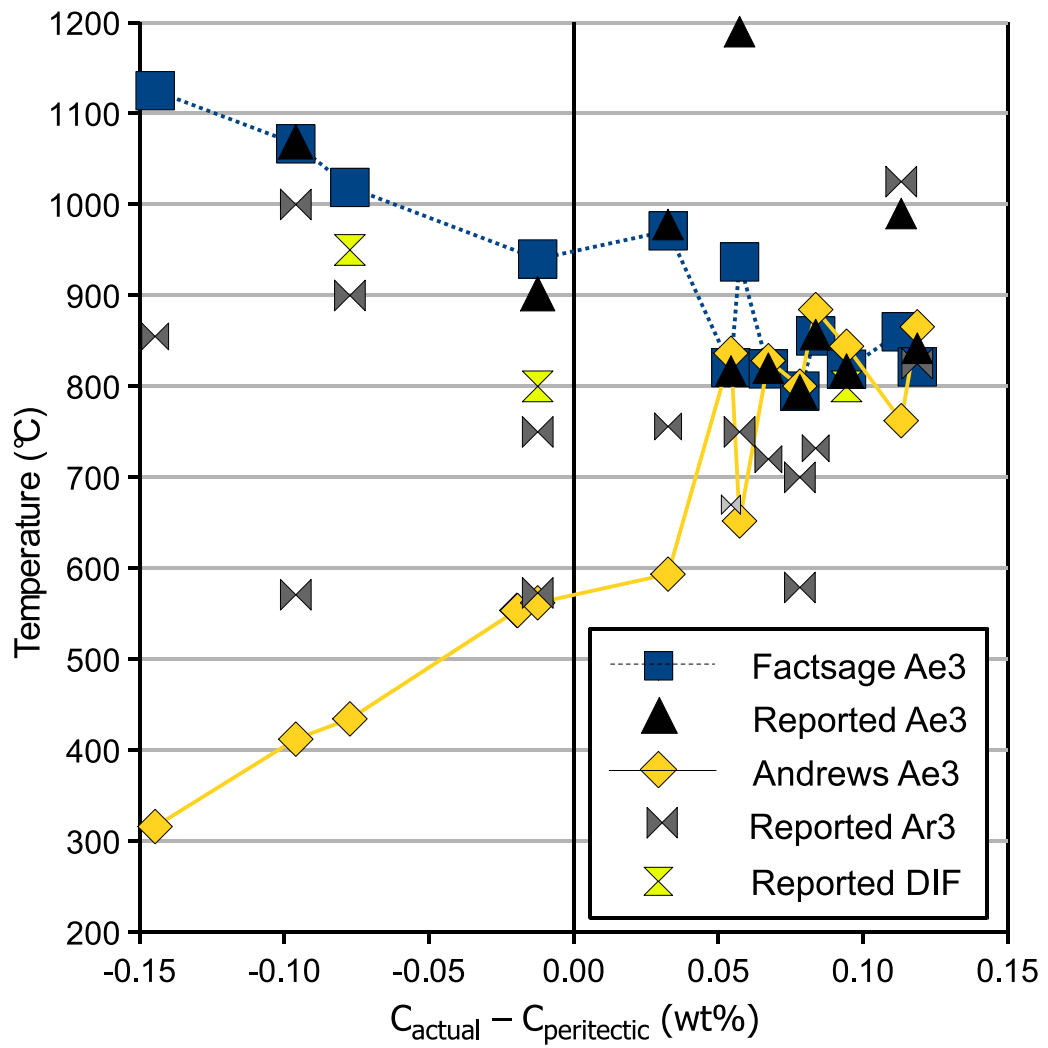


Figure 8.8: Comparison of  $Ae_3$  vs  $C_{actual} - C_{peritectic}$  for steels from Tables 7.1, 7.2. Data may be found in Table 8.3.

## 8.4.2 Anomalies for Su steel 3, Su steel 5

There are anomalies in Su *et al.*'s work, and simplified enlarged version of Figure 8.8 including Su's data, is shown Figure 8.9. The data is also in Table 8.4.

Table 8.4:  $Ae_3$  problems with Su. Temperatures in °C.

Steel	$C_{actual} - C_{peritectic}$	$Ae_3$ FactSage	Reported $Ae_3$	Reported $Ar_3$	DIF
Mintz 4	0.03	971	978 ref[10]	756 ref[10]	-
Cowley 8	0.05	821	817 ref[55]	670 ref[55]	-
Su 5	0.06	937	1190 ref[11]	750 ref[11]	-
Mintz 1	0.07	819	820 ref[10]	720 ref[10]	-
Trip 9	0.078	795	794 ref[179]	536-579 ref[182]	800(600[179])
Mintz 2	0.084	855	857 ref[10]	732 ref[10]	-
Trip 1	0.09	819	817 ref[179]	581 ref[182]	800
Su 3	0.11	860	990 ref[11]	1025 ref[11]	-
Su 1	0.12	821	842 ref[11]	825 ref[11]	-

In Su *et al.* work [11], the onset of DIF as noted from the metallography is higher than predicted for their steel (Su steel 3) but much lower than predicted for their high Al containing steel (Su steel 5, Figure 8.9). It is possible, in the case of Su steel 3, that the cooling after testing was not fast enough to prevent ferrite from forming in the test or segregation has occurred along grain boundaries so that the phases equilibria may be different[11]<sup>28</sup>. Furthermore, the N levels in these steels is much lower than the other TRIP steels and this is not accounted for in the peritectic prediction equations 2.7, 2.8<sup>29</sup>, so that they may be differently placed along the  $C_{actual} - C_{peritectic}$  axis. Additionally, these steels are higher in P than the other TRIP steels<sup>30</sup>, and could affect the  $Ae_3$  by encouraging the formation of polygonal ferrite as Suzuki *et al.* [79],<sup>31</sup> suggests. The influence of P is not being investigated in the present study so both Su steel 3, Su steel 5 will be ignored.

## 8.4.3 $Ae_3$ for Mintz steel 4

A second difficulty was that the high Al steel in the work of Mintz *et al.*[10], did not have a single phase region for austenite, so that there is no  $Ae_3$  reported. However, when the steel was 'modified' by increasing the Mn or decreasing the Al (modified chemistries can be

<sup>28</sup>Discussed on page 87

<sup>29</sup>Discussed on page 92

<sup>30</sup>Compositions may be found in Table 7.1, page 178.

<sup>31</sup>Discussed on page 74

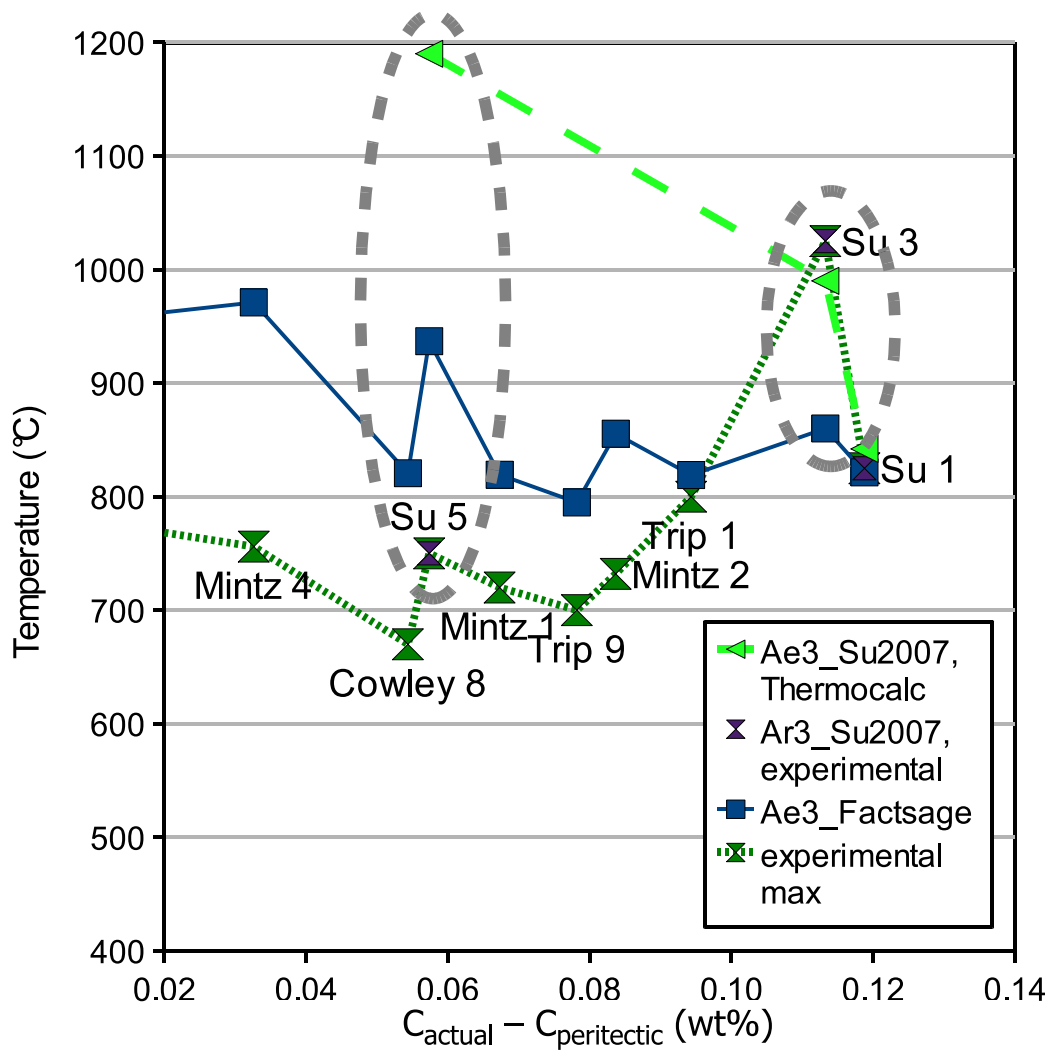


Figure 8.9:  $Ae_3$  anomalies for Su *et al.*'s steels.

found in Table 7.2) an  $Ae_3$  could be obtained, Figure 7.6. It is therefore reasonable to use the peak austenite fraction as an estimate of the  $Ae_3$ .

## 8.5 Integration of results chapters

The aim of this section is to understand the effect of the chemistry (Al and Nb content) on the ductility by studying the influence of these elements on the microstructure and the phase transformations. Therefore the the effect of Al content on the grain size, AlN precipitation behaviour, Nb(C,N) precipitation behaviour,  $Ae_3$ ,  $Ar_3$ , MnS and recrystallisation will be discussed. The industrial implications of the results will be discussed in a separate chapter (Chapter 11, page 233).

### 8.5.1 Grain size and the peritectic reaction

There was a direct correlation for the Al containing steels, between grain size and temperature when the microstructure was fully austenitic, Figure 8.10. This was also the reason for the relationship between  $C_{actual} - C_{peritectic}$  and grain size in Figure 8.5. High Al contents appeared to lower the start temperature of the single phase austenite and raise the  $Ae_3$ , effectively reducing the austenite phase field and, as a result, reduced the grain size, Figure 8.6. As predicted from the literature [166]<sup>32</sup>, the lower the temperature at which single phase austenite started, the less the grains could grow. It was also part of the reason for the shifting of the ductility trough to higher temperatures in the higher Al steels (1.5%Al) as film like deformation induced ferrite could appear at higher temperatures. The cause of the poorest ductility at the peritectic point is the reaction  $L + \delta + \gamma \rightarrow \gamma$ , this being the highest temperature where the microstructure is fully austenitic, Figure 7.1, page 176.

The relative position of the peritectic reaction will also influence the phases in which the AlN and Nb(C,N) can precipitate. For simplicity the AlN precipitation will be dealt with separately from the Nb(C,N) precipitation in Sections 8.5.2 and 8.5.3 respectively.

### 8.5.2 Effective aluminium nitride precipitation in austenite

While grain size correlated with starting temperature of the single phase austenite, the fact that the R of A trough width was greatest and the minimum ductility was lowest in the 1.5%Al steel remains to be explained. It is therefore of merit to explore in which phases the

---

<sup>32</sup>Discussed on page 91

AlN precipitation occurs. This is illustrated in Figure 8.11. If the AlN precipitated in the delta ferrite matrix or the delta ferrite grain boundaries then it was less likely to exist on the austenite phase boundaries at test temperature. AlN precipitation in  $\delta$  ferrite appeared to be beneficial (Figure 7.5, page 185). When precipitation predominates in the austenite it was more likely to remain at the grain boundaries and affect ductility.

However, one of the problems with AlN precipitation is that it is very difficult to detect even when it has an effect on the ductility. It is well known that AlN is sluggish in precipitating out in austenite [14]. Researchers such as Chamont *et al.* [91] show, that at the [Al][N] product level of  $\sim 1.5 - 2.3 \times 10^{-4} \text{wt}\%^2$  results in AlN precipitation at the fracture surface, and this is confirmed industrially by Triolet *et al.* [32] and Bannenberg [74] who give an upper limit of [Al][N] of  $1 \times 10^{-4} \text{wt}\%^2$  to avoid cracking in Al steels. At  $[\text{Al}][\text{N}] > 1.5 \times 10^{-4} \text{wt}\%^2$ , AlN precipitation widens and deepens the ductility trough by dynamically precipitating at the fracture surface without being readily detected in the bulk microstructure below the fracture<sup>33</sup>. This is because AlN precipitation can be a magnitude faster in material deformed to 5% [103]. Thus its absence in the general microstructure is not necessarily a true reflection of the AlN precipitation behaviour at the fracture surface where the strains are likely to be in excess of 5%. In the present work, the kinetics of Al precipitation in the bulk microstructure appeared to be prohibitively slow below 0.05%Al, but this was not the case for AlN precipitation at 1% or 1.5%Al level due to the much higher driving force for precipitation. The limit  $[\text{Al}][\text{N}] > 1.5 \times 10^{-4} \text{wt}\%^2$  was therefore used as the limit of effective strain induced AlN precipitation in the 0.05%Al steel, and the microscopy provided some confirmation of the presence of AlN at the higher Al levels (although it was not always able to reveal the strain induced AlN at the fracture). The equilibrium volume fractions were taken from the phase simulations. The phase simulations were ‘modified’ to accommodate these considerations. It was assumed that when AlN precipitates in delta ferrite the reaction was at equilibrium, while in the gamma and alpha phase the precipitation was only ‘complete’ if the  $[\text{Al}][\text{N}] > 1.5 \times 10^{-4} \text{wt}\%^2$  or if AlN was observed from the TEM analysis. Table 8.5 compares the analytical microscopy evidence, [Al][N] product and the theoretical volume fractions ( $V_f$ ) and gives the expected effective AlN precipitation. For convenience the FactSage model will be used.

These values are ranked by the value of  $C_{\text{actual}} - C_{\text{peritectic}}$ , and compared to the minimum ductility in the trough, Figure 8.12. In Figure 8.12 there are four curves, A,B,C and D. Curve A is for the minimum ductility. Curves B-D are the effective volume fraction of AlN precipitated in the delta ferrite, austenite and ferrite respectively. The curve C is the most important and shows how the volume fraction of AlN precipitation in the austenite varied in relation to the peritectic. It can be seen that the greatest volume of AlN precipitated in the

---

<sup>33</sup>Discussed in Section 2.4.1, page 79

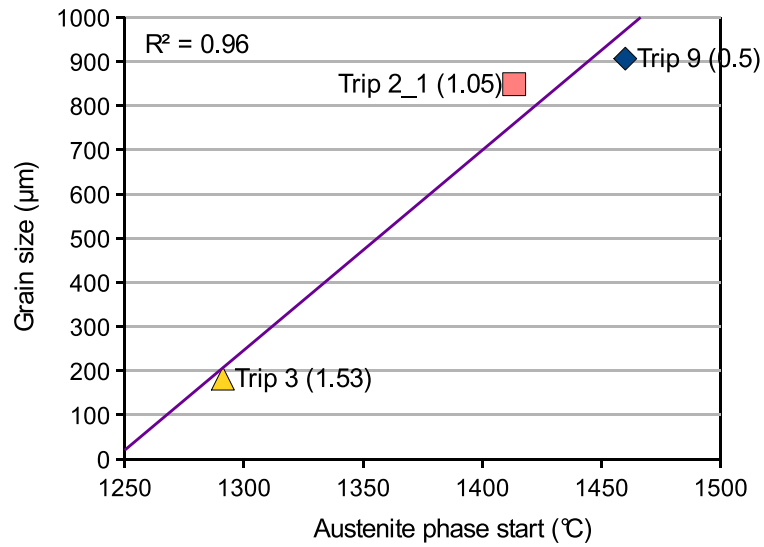


Figure 8.10: Grain size at 750°C vs the temperature at which the TRIP samples are single phase austenite. There is a good correlation between these parameters. Numbers in brackets denote Al content.

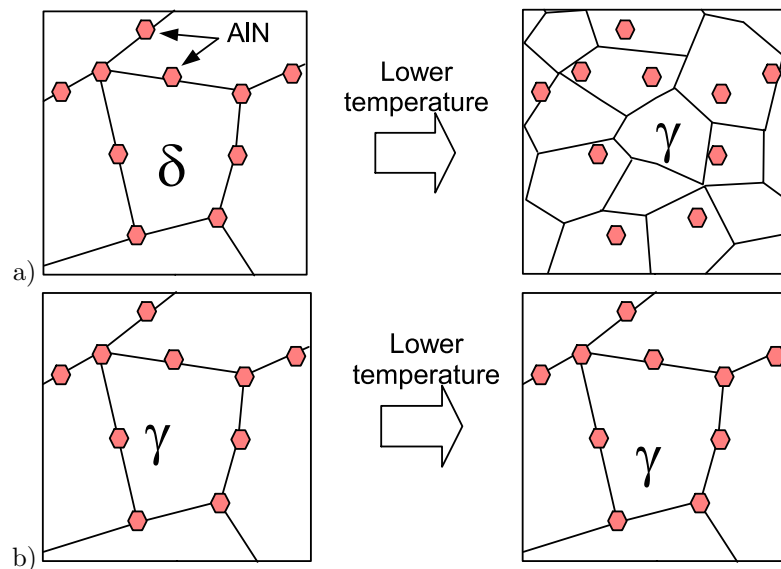


Figure 8.11: Schematic to illustrate the effect of phases transformation on the position of AlN precipitation along grain boundaries. If the AlN precipitates at the delta ferrite grain boundaries a) then it is less likely to exist on the austenite phase boundaries at test temperature, while b) when precipitation predominates in the austenite it is more likely to remain at the grain boundaries and affect ductility.

Table 8.5: Observed, theoretical AlN precipitation and [Al][N] product giving effective AlN precipitation.

Sample	%Al	AlN observed with microscopy	[Al][N] $\times 10^{-4}$ wt% <sup>2</sup>	Theoretical $V_f$ in $\delta$ ferrite $\times 10^{-4}$	Theoretical $V_f$ in $\gamma$ $\times 10^{-4}$	Effective $V_f$ in $\gamma$ $\times 10^{-4}$ , when total [Al][N]>1.5
Trip 9	0.05	no	3.6	0.0	2.9	2.9
Trip 2-1	1.05	yes	69	1.3	1.3	1.3
Trip 3	1.53	yes	87	2.4	0.3	0.3
Trip 10	1.44	yes	98	2.2	0.5	0.5
Mintz 1	0.17	no	1.0	0.0	2.3	-
Mintz 2	0.023	no remark	0.7	0.0	1.2	-
Mintz 3	1.930	no remark	66	1.4	0.0	0.0
Mintz 4	0.980	yes	41	0.6	1.0	1.0
Su 1	0.030	no	0.4	0.0	0.5	-
Su 3	0.430	no	10	0.0	1.0	1.0
Su 5	0.870	yes	19	0.0	0.9	0.9
Cowley 8	0.022	no remark	1.1	0.0	2.0	-
MohamedB	0.036	no remark	2.9	0.0	2.9	1.2

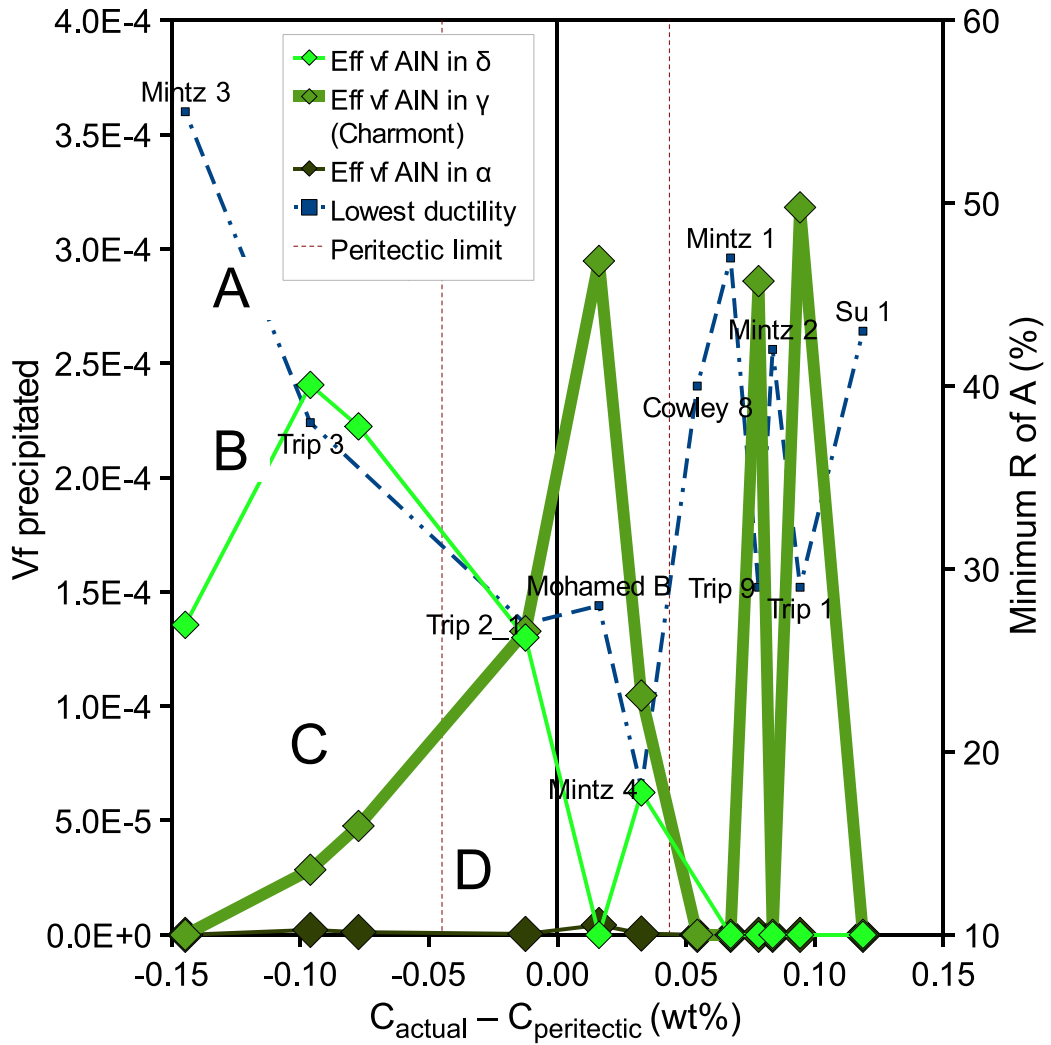


Figure 8.12: Effective precipitation and minimum ductility showing the good correlation between precipitation of AlN in austenite and loss of ductility. A: R of A (on secondary y-axis), B: AlN precipitation in delta ferrite, C: AlN precipitation in austenite, D: AlN precipitation in alpha ferrite.

austenite corresponded to the peritectic and hyper-peritectic steels. The curve of effective volume fraction of AlN precipitated in the delta ferrite phase against  $C_{actual} - C_{peritectic}$  is also plotted (curve B) and indicated that precipitation was a maximum in the hypo-peritectic region after which it steadily reduced and was lowest in the peritectic and hyper-peritectic range. There was also the potential for a small amount of precipitation of AlN in the ferrite (curve D). It is clear that when the volume fraction of AlN precipitation in the austenite reaches a maximum the R of A is lowest. This is where there is both high temperature single phase austenite (grain sizes  $\sim 2\text{mm}$ ) and precipitation of AlN, hence the ductility is poorest. The 1.5%Al steel had a high volume fraction of AlN precipitation in the delta ferrite but the maximum temperature of single phase austenite was relatively low which resulted in a finer grain size ( $\sim 100\mu\text{m}$ ). The result is a higher minimum ductility when compared to the 1%Al steel.

When the [Al][N] product was plotted against minimum ductility in the peritectic and hyper-peritectic range, as shown in Figure 8.13, it confirmed that  $[\text{Al}][\text{N}] > 1.5 \times 10^{-4}\text{wt}\%^2$  gives a reduction in minimum ductility.

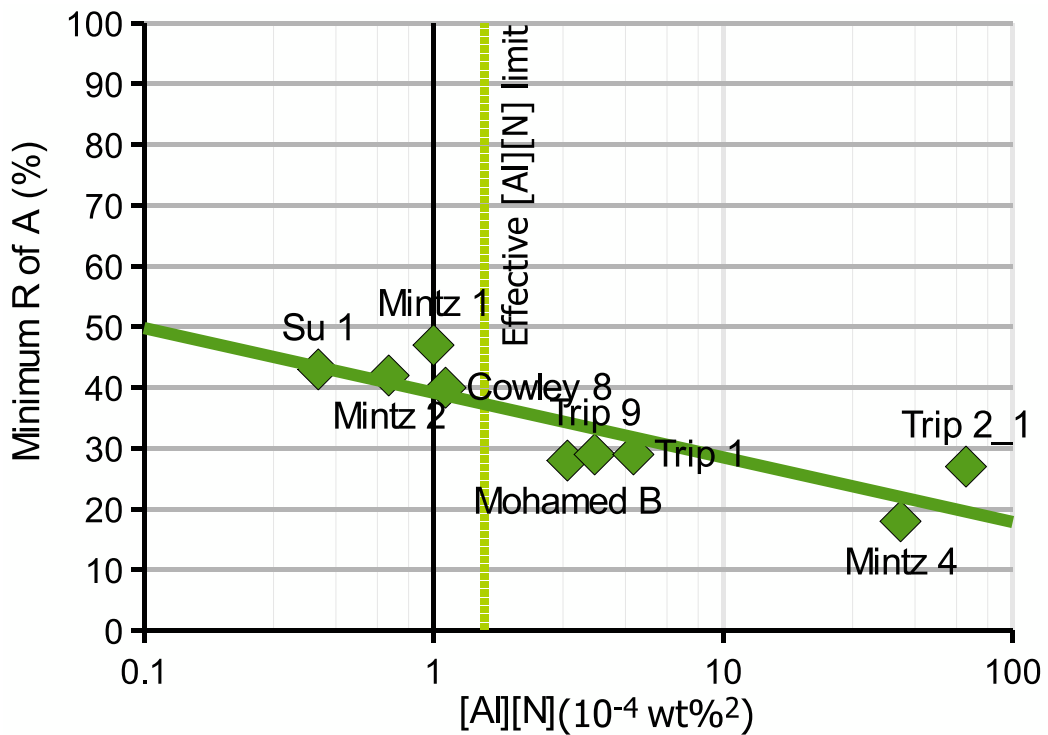


Figure 8.13: [Al][N] product vs minimum ductility for the steels in the hyper-peritectic carbon range. There is a marked drop in ductility when the [Al][N] product exceeds  $1.5 \times 10^{-4}\text{wt}\%^2$ .

If the [Al][N] product is high enough and the grain size large enough to give a shorter than

critical inter-particle AlN distance at the grain boundaries, they are pinned and ductility is poorest. The peritectic and hyper-peritectic steels have largest grain size and high [Al][N] products allow for strain induced precipitation and encourages shorter particle spacing, both criteria are fulfilled, leading to the poorest ductility<sup>34</sup>. In the case of the peritectic steels, with extremely high [Al][N] products (Trip 2-1 and Mintz 4 with  $69 \times 10^{-4}\text{wt}\%^2$  and  $41 \times 10^{-4}\text{wt}\%^2$  respectively), precipitation occurs irrespective of the amount of deformation as in both cases AlN precipitation is observed on the grain boundaries in the material below the fracture surface (Table 8.5) and AlN is predicted to precipitate at all test temperatures, leading to wide trough behaviour.

The fact that the dendritic AlN precipitation was not seen frequently in the 1.5%Al steel may be due to the grain size since a greater amount of nucleation sites may have favoured more conventional hexagonal plate and needle AlN precipitation. Alternatively, when AlN precipitates in delta ferrite, it also precipitates within the matrix as it does in ferrite, as seen in the OM of the 1.53%Al steel (Figures 4.10 and 4.12 on pages 130 and 131 respectively). This will be particularly so with the very coarse grain size present in the delta ferrite temperature range. On transformation to austenite, the AlN precipitates will not be at the grain boundaries, Figure 8.11.

### 8.5.3 Niobium carbo-nitride precipitation

If the foregoing exercise is performed for the Nb(C,N) volume fraction, it is found that in all steels it precipitates in the austenite, Figure 8.14, and the curve of effective Nb(C,N) precipitation, B, remains relatively flat over the hyper, peri and hyper-peritectic composition range. The volume fractions of Nb(C,N) precipitated under equilibrium conditions remains approximately constant between the Nb containing steels and is listed in Table 7.5. If the R of A curve in Figure 8.14 is sorted into Nb containing and Nb free steels vs  $C_{actual} - C_{peritectic}$ , as in Figure 8.15, then it can be seen that the Nb influenced the R of A in the hyper-peritectic carbon region (positive  $C_{actual} - C_{peritectic}$ ) significantly more than at any other carbon level (R of A difference is larger than 15%). Note that the high [Al][N] product is also associated with the high Nb levels, so both phenomena may be contributing to the loss in ductility. Bannenberg *et al.*[74]<sup>35</sup> showed that at high [Al][N] products where the AlN precipitates before Nb(C,N), the Nb has less effect than the AlN. However in the present case, the presence of the Nb(C,N) in the microstructure does indicate that it's influence as a fine precipitate will have preceded the AlN precipitation, thus can be considered as more pivotal. Therefore, the presence of Nb(C,N) is expected to be the primary reason for the

---

<sup>34</sup>Figure 7.3 page 179

<sup>35</sup>Discussed in Section 2.4.1, page 81

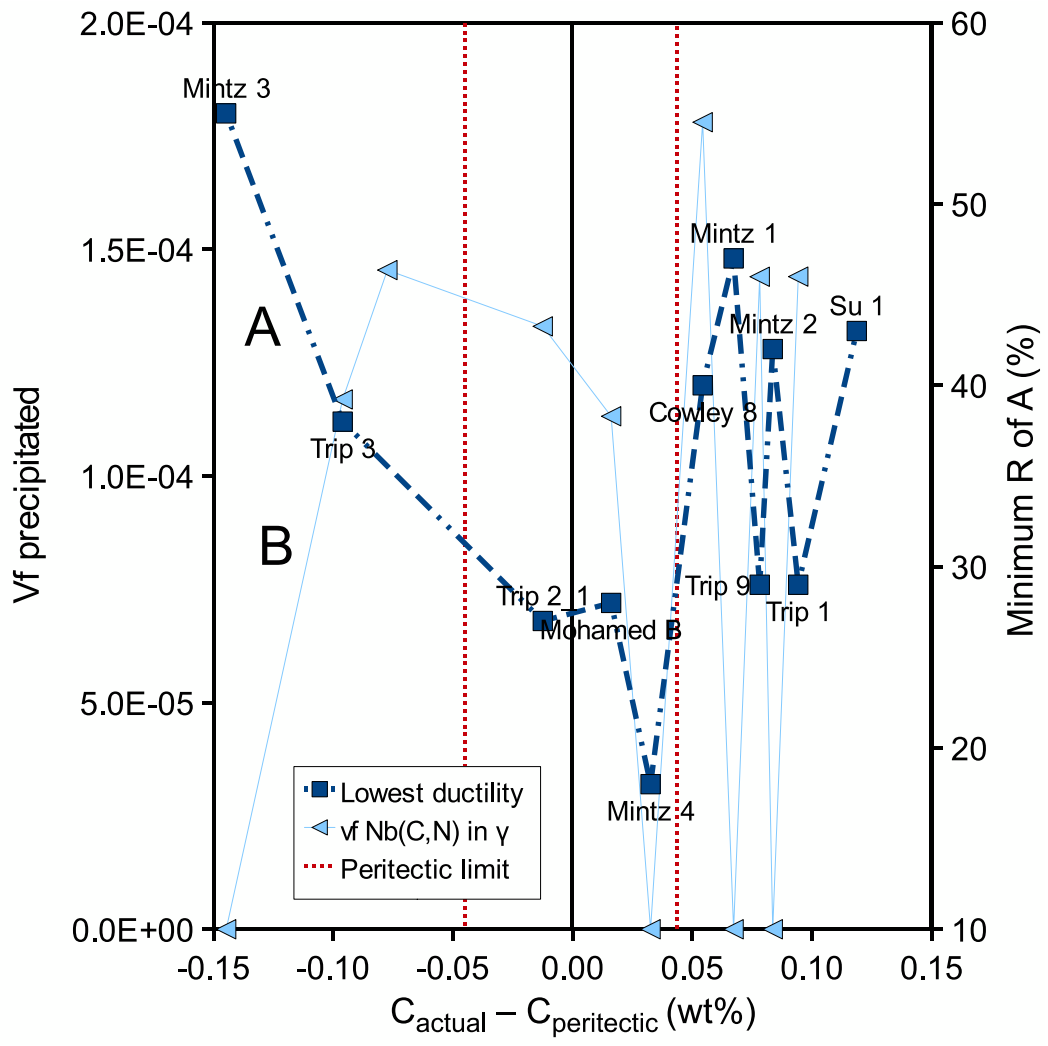


Figure 8.14: Effective precipitation and minimum ductility showing how the Nb decreases ductility in the hyper-peritectic region. A: R of A, B: Nb(C,N) precipitation.

poor ductility of the 0.05%Al steel (Trip 9) when compared to steels with similar Al level steels (0.017%Al for Mintz steel 1[10] and 0.03%Al Su steel 1[11] in Figure 8.14).

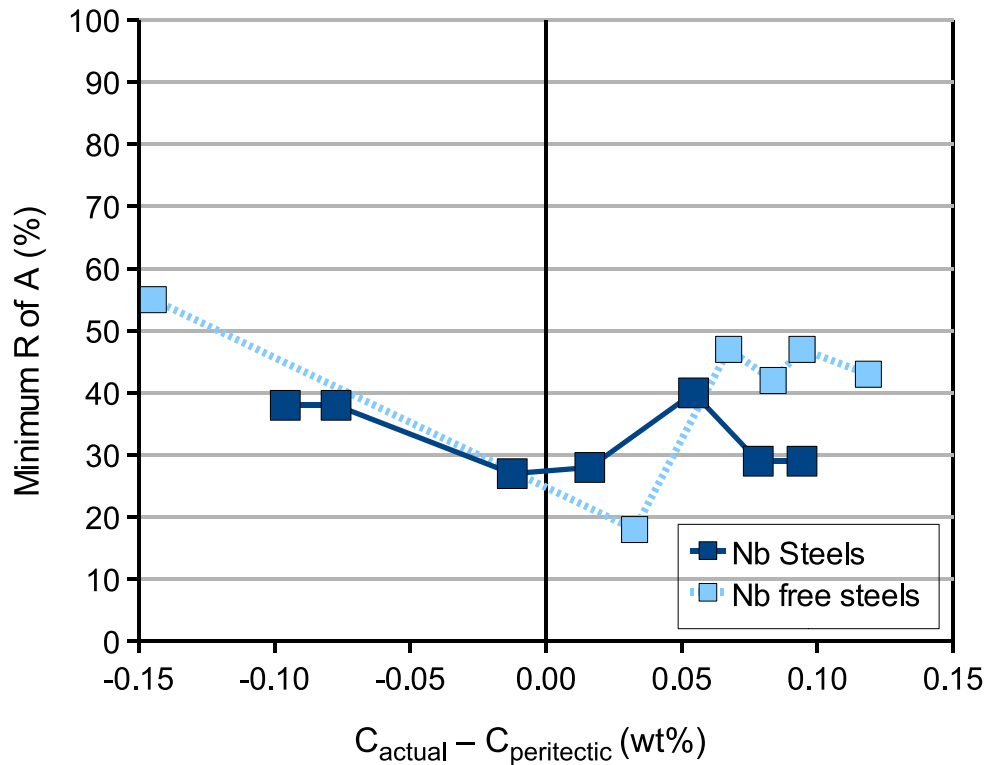


Figure 8.15: Effect of Nb and Nb additions on R of A at different  $C_{actual} - C_{peritectic}$ .

The similarity in Nb(C,N) precipitate size (see Figure 6.2, page 154) at all temperatures showed that precipitation was most likely to be deformation induced, since Nb(C,N) is well known for precipitating in a fine form on deformation [104, 103]. In all the TRIP steels, Nb(C,N) solubility is approximately the same temperature (1150-1200°C, Figure 8.14). The TEM analysis indicated that in all steels precipitate size was not the only critical factor contributing to ductility. It should be noted that although Nb(C,N) precipitation may well be having a detrimental influence on the hot ductility, its effect remained fairly constant throughout the hypo-peritectic and peritectic regions and cannot be responsible for all the changes that are being discussed. However, the hyper-peritectic region is where where the correlation between precipitate size and ductility was the highest,  $R^2 = 0.99$  (Figure 6.5, page 158) showing that it can account for the reduction in R of A. Even though the simulations indicate that there was similar volume fractions of Nb(C,N) in the steels, the interparticle distance of Nb(C,N) precipitation was different for the 1.5%Al steel and the 0.05%Al steel. This is because the grain size was coarser in the 0.05%Al steel, leading to a higher density of precipitation on a lower grain boundary area, Figure 8.4. In the 1%Al steel the effect of AlN precipitation and the peritectic point completely overshadowed the Nb(C,N) effect.

This has been observed before[92]<sup>36</sup> but in that instance C was the dominant contributor to the peritectic reaction. Nb(C,N) precipitation was most readily found in the 1.53%Al steel samples, due to a finer grain size in this steel. The precipitation around grain boundaries could be deformation induced or due to segregation. It is most likely to be strain induced.

Eutectic Nb(C,N) may be partially a result of segregation during testing as observed [62, 61], but it is expected that some eutectic Nb(C,N) always precipitates at these relatively high carbon levels [124]<sup>37</sup>.

The precipitate vs ductility curve in both the 0.05 and 1.5%Al steel, (Figures 6.5 and 6.19 on pages 158 and 171 respectively) showed a ‘plateau’ at around 15-20nm as previously observed[94], Figure 2.20 page 67. However the plateau is at higher ductilities than previously reported, possibly due to the lack of matrix precipitation.

In summary: At high Al contents the grain size has the greatest effect on R of A. At intermediate Al contents, dendritic AlN precipitates on austenite grain boundaries and has the greatest effect on R of A. At low Al levels the Nb(C,N) precipitation reduces the R of A.

#### 8.5.4 Recrystallisation

While Kang *et al.* [179] attributed the recovery of the ductility at 1100°C to the evidence that recrystallisation has started at 1050°C[179], this sample was unavailable to the current research. However, the improvement in ductility at the high temperatures in 0.05 and 1.5%Al steel may well be as a result of recrystallisation, as reported by Kang and Mintz[179]. Even in the 1%Al steel where the dendritic AlN was expected to have already precipitated prior to reaching the deformation temperature of 1100°C, the grain boundaries would be mobile and escape the precipitation (4.7, page 127) as has been described elsewhere [66]<sup>38</sup>.

According to Crowther and Mintz [41]<sup>39</sup>, it is expected that fine AlN<sup>40</sup> precipitation may act to delay DRX, and coarser AlN may permit it. This was not the case for the 1%Al steel, where the interparticle spacing along the grain boundaries was very small in spite of the large precipitates (consider Figure 5.2c on page 137). In the 1 and 1.5%Al steels DRX only occurred at test temperatures >1000°C, and any ductility recovery before then probably took place by grain boundary migration for the most part, especially since the ferrite appeared at relatively high temperatures in these steels and ferrite is known to prevent DRX directly [66]. Mn is not expected to influence DRX [102], although it does encourage the formation of

---

<sup>36</sup>Discussed on page 70

<sup>37</sup>Discussed on page 48

<sup>38</sup>Discussed on page 68

<sup>39</sup>Discussed on page 67

<sup>40</sup>No doubt that Nb(C,N) precipitation may act in the same manner

deformation induced ferrite [67] and/or slows down the AlN precipitation. High Mn can be expected to keep the DIF thin and retard AlN precipitation, causing finer lower temperature precipitation. This in turn may lead to reduced DRX.

### 8.5.5 The effect of $Ae_3$ , $Ar_3$ and deformation induced ferrite on ductility.

In the 0.05%Al steel the ductility trough was reported [179] to extend from the  $Ar_3$  to the  $Ae_3$ . The  $Ar_3$  (at a cooling rate of  $1^\circ\text{C/s}^{-1}$ ) as determined by dilatometry[182] is well below these temperatures. When the fracture surface was studied using SEM, deformation induced ferrite was apparent at higher temperatures, around  $800^\circ\text{C}$  (from Figure 5.5 page 141). These points are illustrated on the ductility curve in Figure 8.16. This suggests that ductility recovery at the low temperature end of the ductility trough may occur without large amounts of ferrite being present before straining. It is likely that at these low  $Ar_3$  temperatures ductility of the austenite may be improving because grain boundary sliding is no longer taking place. The film like deformation induced ferrite may be contributing to the reduction in ductility as suggested by Mintz and Cowley [55]<sup>41</sup>, and some of the wide trough behaviour could be attributed to deformation induced ferrite forming just below the  $Ae_3$  and remaining fine until the ductility recovered at around  $700^\circ\text{C}$ .

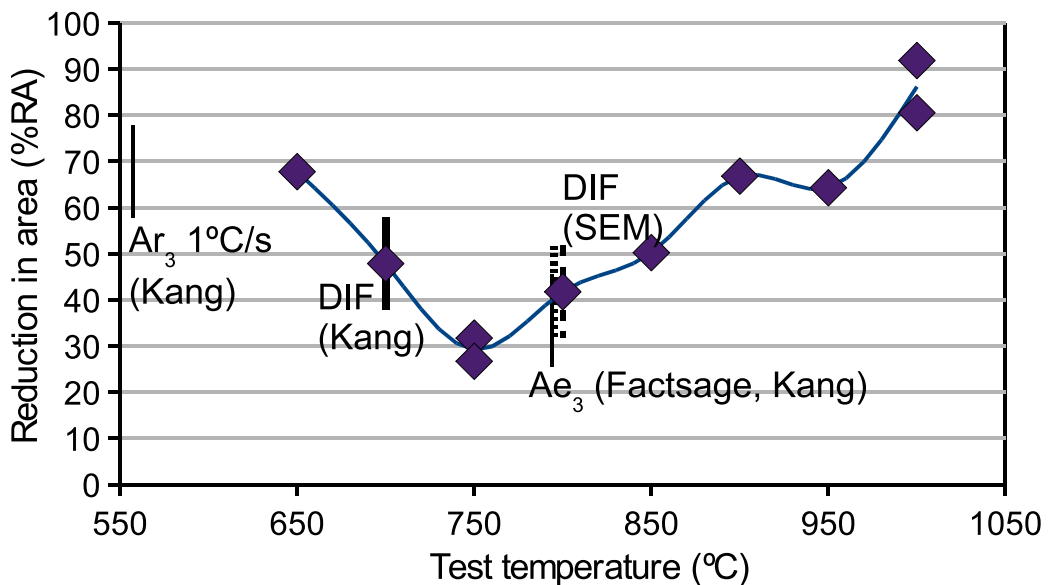


Figure 8.16:  $Ae_3$  and  $Ar_3$  values for the 0.05%Al steels superimposed on the ductility curve for 0.05%Al steel steel.

<sup>41</sup>Discussed on page 62

In the 1.0%Al steel the poor ductility behaviour persisted beyond the  $Ae_3$ , Figure 8.17. The  $Ar_3$  (at a cooling rate of  $1^\circ\text{C/s}^{-1}$ ) as determined by dilatometry[182] was well below the test temperatures.

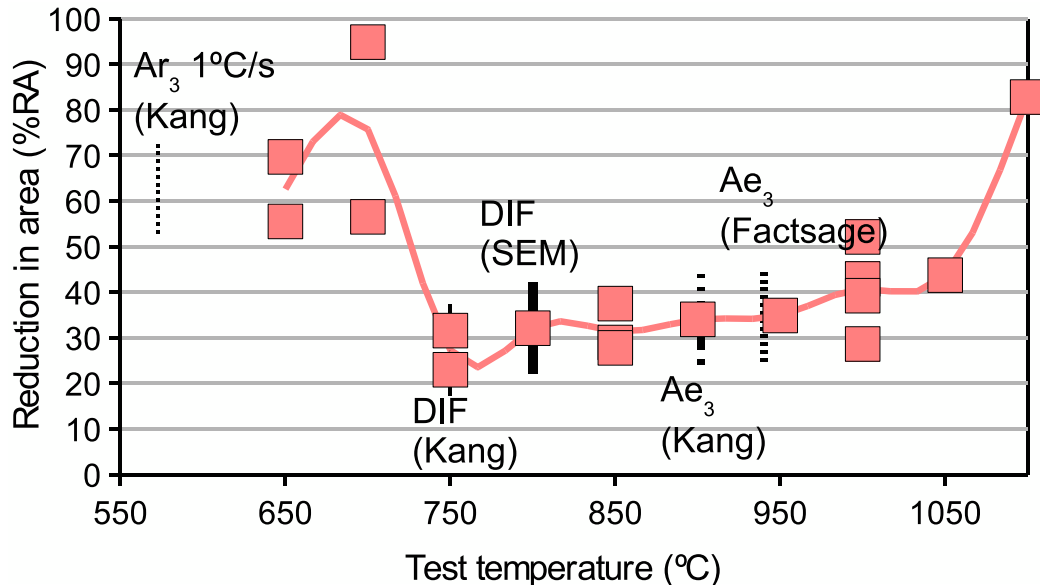


Figure 8.17:  $Ae_3$  and  $Ar_3$  values for the 1.0%Al steel superimposed on the ductility curve for the same steel.

In the 1.5%Al steel the trough was below all stated  $Ae_3$  and  $Ar_3$ , Figure 8.18. The  $Ar_3$  (at a cooling rate of  $1^\circ\text{C/s}^{-1}$ ) as determined by dilatometry[182] was well below the test temperatures. The implication of the SEM observations (Figure 5.5 page 141) is that at the actual fracture surface, deformation induced ferrite forms very close to the  $Ae_3$ , due to the high strain at the fracture tip.

## 8.6 Experimental issues

While the literature [20, 25, 35, 49, 50, 51, 52, 53] shows that modifications to the standard hot ductility test can reveal more information, the disadvantage is that the R of A cannot be compared to other conventional tests that are already published in literature. So much of the past work used the conventional test, as in this work, that alternative testing procedure would make comparisons difficult. The present study could not have relied so heavily on Mintz *et al.*'s [10] work as a very effective comparison, if the test conditions were different. In any case the standard test for Nb containing steels seems to satisfactorily approximate the industrial conditions[17].

### 8.6.1 Porosity

There is some concern that a high proportion of the samples experienced porosity. Nevertheless, enough ‘unmelted’ samples existed to obtain a curve. The high degree of experimental porosity could be attributed to the increased shrinkage associated with peritectic steels. However, a sufficiently high temperature to redissolve the AlN in the high Al steels is necessary, and since AlN was seen on the dendrites (Figure 5.7, page 146), complete melting is required to dissolve all AlN. That being said, resource constraints do not allow more experimental work.

### 8.6.2 Melting/reheat

From Figure 8.19, it can be seen that the FactSage and Thermo-Calc solidii were below the reheat temperature, indicating that at least partial melting in the mushy zone occurred during reheat tests. While there is some valid concern that in the ‘unmelted’ samples the AlN did not all go into solution, Guillels *et al.*'s[68]<sup>42</sup> work seems to indicate that, at least in the peritectic range soak temperatures approaching the liquidus are acceptably representative of industrial castability.

## 8.7 Failure mechanisms

The worst ductility occurred when there was significant amounts of AlN precipitation in the austenite and peritectic steel behaviour was predicted. It can be seen from Table 8.5 and Figure 8.12, that the steels giving the worst ductility will be those having around 1%Al. A very important result observed from phase transformation behaviour and the AlN precipitation is that the minimum ductility improved with the volume fraction of AlN precipitating in the delta ferrite range as shown in Figure 7.5. If the AlN precipitated in the delta ferrite, then when the steel transforms to austenite the AlN was unlikely to be situated at the austenite grain boundaries and hence was not able to influence ductility. In contrast, if the AlN precipitated directly in the austenite, it remained on the grain boundaries which undergo no further grain boundary movement on cooling further in the austenite range.

Presumably, in this manner, AlN is rendered harmless if it is allowed to precipitate in the  $\delta$  ferrite rather than in the austenite. When AlN precipitates in delta ferrite, it probably precipitates within the matrix as it does in alpha ferrite. This will be particularly so with the very coarse grain size present in the delta ferrite temperature range. On transformation to

---

<sup>42</sup>Discussed on page 54

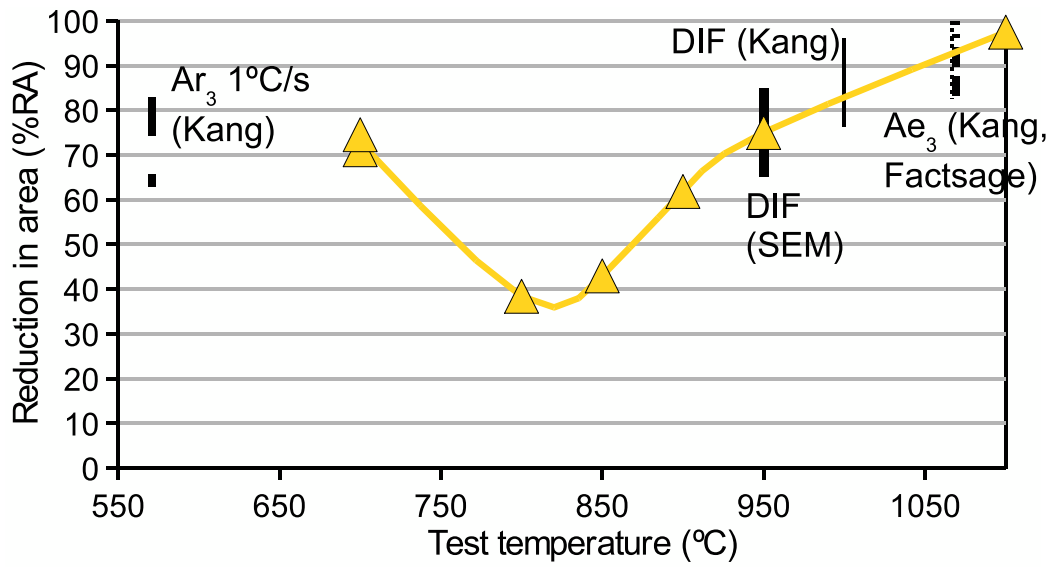


Figure 8.18: Ae<sub>3</sub> and Ar<sub>3</sub> values for the 1.5%Al steel superimposed on the ductility curve for the same steel.

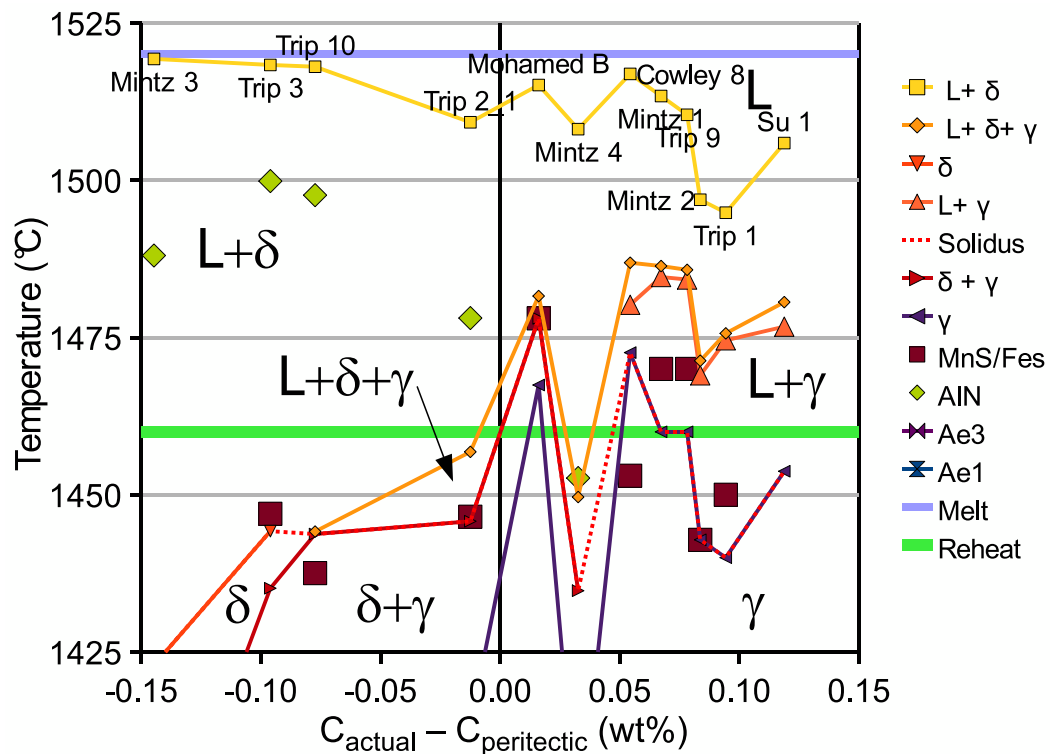


Figure 8.19: Predicted solidii and liquidii temperatures compared with the melting and reheating temperatures in for this study, FactSage model.

austenite, the AlN precipitates will not be at the grain boundaries. Furthermore, even if the AlN precipitated at the delta ferrite grain boundaries it is unlikely that on transformation and growth of the austenite they would remain at the boundaries and the austenite grain boundaries would not be pinned by the AlN precipitates. Industrially this may not happen as the actual cooling rate at these temperatures is so much higher that AlN may not precipitate out to the same degree. Hence, more accurate cooling path ductility testing is required to confirm whether this beneficial activity occurs during continuous casting.

The 0.05%Al and 1.5%Al steel behaved in a similar manner and the ductility loss was shown to be statistically dependant on the Nb(C,N) precipitation size and the austenite grain size. The 0.05%Al steel had a poorer ductility than the 1.5%Al steel, at the same volume fraction and size of Nb precipitation, since it had a larger grain size resulting in a lower inter-particle distance. Subsequently AlN may also have precipitated at higher strains at the fracture surface as the [Al][N] product is sufficiently high. In the 0.05%Al steel the trough extended marginally higher than the  $Ae_3$  due to the presence of Nb(C,N) precipitation along the grain boundaries. These precipitates serve to immobilize the grain boundaries and reduce ductility by facilitating cavity/crack link up, as Mintz and Mohamed [62] have observed and as many other researchers have found [59, 62, 63, 65, 79, 83, 93, 112, 118, 119, 120]<sup>43</sup>. The failure mechanism is always the interaction of precipitation size and density (inter particle distance). The inter particle distance is influenced by both the grain size and the volume fraction precipitation. This is the reason for the 0.05%Al steel having poorer ductility at the same volume fraction and size of Nb precipitation as the 1.5%Al steel, the difference being the grain size.

---

<sup>43</sup>Discussed on page 75

## Chapter 9

# Conclusions

**R of A.** It was found that the ductility trough in 0.15C-2.5Mn-0.025Nb TRIP steels was similar for the low (<0.05) Al and high (1.53) Al steels, but that in the 1.05%Al steel there was an extended trough. The statistical analysis on four samples of the 1.05%Al steel at the same temperature (1000°C) showed that R of A has a Gaussian distribution with an average of 41% and standard deviation of 9.7%.

**Microscopy.** In the 0.05%Al and 1.5%Al steel the ductility loss was shown to be statistically dependant on the Nb(C,N) precipitation size (p, in nm) and the austenite grain size (D, in  $\mu\text{m}$ ), so that a regression equation of the form

$$\text{RA} = 128.9p^{\frac{1}{3}} + 5563D^{-1} - 274.2, \quad (9.1)$$

with  $R^2=0.88$ , showed a good fit. In general the intergranular fracture surfaces were a combination of microvoid coalescence and grain boundary sliding. In contrast, at the 1%Al level a significant amount of dendritic AlN precipitated on the austenite grain boundaries. This precipitation has been observed before, but in the current analysis it was an fcc rather than hcp structure. This type of precipitation resulted in a rock candy phenomenon on the fracture surface.

**Simulation.** In Al-Nb TRIP steels the Al radically altered the phase stabilities, leading to steels that vary from hypo-peritectic through to hyper-peritectic compositions. From phase transformation behaviour, it was shown that the minimum ductility improved with the volume fraction of AlN precipitating in the delta ferrite range.

**General.** In the 0.05%Al and 1.5%Al steel the Nb(C,N) precipitates served to immobilize the grain boundaries and reduced ductility by facilitating cavity/crack link up. The failure mechanism in these two steels was therefore the interaction of precipitation size and density (inter particle distance). In the case of the 0.05%Al steel there may be the subsequent strain induced precipitation of AlN at the fracture surface. The inter particle distance is influenced by both the grain size and the volume fraction

precipitation. This was the reason for the 0.05%Al steel having poorer ductility at the same volume fraction and size of Nb precipitation as the 1.5%Al steel, the grain size being finer in the 1.5%Al containing steel. Since in Al-Nb TRIP steels the Al radically altered the phase stabilities, at the 1%Al level, a significant amount of AlN precipitated in the austenite and the steel was in the peritectic range so that the austenite grain size was large. When this occurs, the AlN precipitates remain on the grain boundaries which undergo no further grain boundary movement on cooling further in the austenite range. This results in rock candy fracture along the AlN dendrites at the immobile grain boundaries. Therefore, the 1%Al steel the trough was wider than the  $Ae_3 - Ar_3$ , due to the high density of AlN along the grain boundaries at all temperatures. It is therefore advisable to use 1.5%Al levels over the 1%Al levels in TRIP steels containing 0.15C-2.5Mn-0.025Nb.

The recommendations have been divided into the industrial implications and the suggestions for further experimental work, and may be found in Chapters 11 and 12 respectively.

## Chapter 10

# Contributions to Original Knowledge

In order to clarify the originality of this thesis in the metallurgical field of hot ductility, this chapter aims to summarise the unique contributions of the present work. To date, there have been no studies regarding the effect of Nb additions on the hot ductility of TRIP steels [9], and while the implications of this work for industrial processing and further experimental work will be discussed in the chapters to follow, the novel aspects of the work are listed below.

**Peritectic analysis.** The use of the peritectic formulas, combined with the calculation of the volume fraction of AlN precipitating in the austenite, is an extremely effective approach in understanding the effect of Al on the ductility behaviour. This is because Al level affects both the phase stabilities (from hypo to hyper-peritectic behaviour is manifested at Al contents up to 1.5%Al) and the temperature at which AlN starts precipitating, thereby influencing the phase in which the AlN precipitates. The Al levels were most detrimental when there was high temperature austenite (at the peritectic point) and copious precipitation of AlN in the austenite, effectively pinning the grain boundaries and causing fracture along these immobile boundaries. The current work has shown that even the non-linear effect of Al on ductility can be understood using this basis. As such, this contribution has implications for TRIP steel alloy design as well as the processing parameters, as discussed in the following chapter, Chapter 11.

**The effect of Nb at high Al.** In this 0.15C-2.5Mn base steel, Nb(C,N) had the greatest influence on hot ductility at low Al (0.05%) contents than at high (1.5%) and intermediate(1%Al). This was because the Nb(C,N) interparticle spacing is lowest at the largest austenite grains sizes that occur in the hyper-peritectic composition (0.15C-2.5Mn-0.05Al-0.025Nb). At intermediate Al contents the effect of the AlN precipitation was overwhelming. This indicates that the high Al steel has the most promising behaviour during processing, however, this will be discussed in Chapter 11.

**AlN precipitation.** While dendritic AlN precipitation has been reported before, it was shown that the precipitates in the present study were of the fcc rather than hcp structure. The difference in structure is of more academic rather than industrial importance, since it is the morphology rather than the crystal structure that affects ductility.

## Chapter 11

# Recommendations for the Industrial Applications

### *Summary of industrial applications*

In the 1.05%Al steel, there is a high risk of cracking at almost all unbending temperatures. The 1.53%Al TRIP steel shows the greatest promise, although unbending at around 800°C should be avoided. Further testing including complete remelting during the ductility test is recommended. Positive segregation in the 1.5%Al steel at the oscillation mark is expected to deepen oscillation marks and increase local stresses. The likelihood of acceptable properties in the 1.5%Al steels appears to be high as there are other 1.5%Al TRIP steels that have been successfully cast commercially. Al has the effect of raising the Nb(C,N) solubility temperature, so that reheat temperatures may need to be higher than normal. The Mn/S ratios of all the experimental steels are high enough to avoid cracking problems.

## 11.1 Introduction

This work aimed to characterise the behaviour of high Al, Nb-containing TRIP steels during continuous casting, based on their behaviour as simulated by hot ductility testing. While the hot ductility test is a simplified test (to ensure repeatability and control of experimental variables) a number of direct industrial implications can be drawn. The ductility in all the steels is lower than the recommended 40% above which cracking is not a problem [17][39]<sup>1</sup>, for some part of the ductility curve. The projected industrial behaviour for each steel can be summarised as follows:

**0.05%Al steel** Unbending between 700-800°C should be avoided due to the low ductility

---

<sup>1</sup>Discussed in Section 2.2.5, page 56

at these temperatures

**1.05%Al steel** Unbending between 750 and 1000°C carries a high risk of transverse cracking. The 1%Al addition results in combination of maximum dendritic precipitation and high temperature coarse grained austenite. The reheated grain size in ductility testing, closely approximates to the the melted grain size [25]<sup>2</sup> and thus ought to have a strong correlation to industrial behaviour.

**1.53%Al steel** Unbending at around 800°C should be avoided. While the 1.5%Al steel is the most promising steel for casting it does need further testing including complete remelting during the ductility test. The finer grain size is more amenable to casting, and may show great promise to be reduced further, such as in thin slab casting.

Considering the observation that the melted samples (presumably a more accurate simulation) tend to have higher ductility; in the low and high Al steels there may be potential cooling paths that avoid cracking. Unbending above  $\sim 750^\circ\text{C}$  [24]<sup>3</sup> would seem to be a feasible option for 0.05%Al steels and 1.5%Al steels, but simulations with a more accurate thermal path (including complete melting) are recommended to manage this risk more effectively.

Segregation in the hook marks of the oscillation marks [16]<sup>4</sup>, [18, 26], which tends to be a result of positive segregation (ie enriched in Mn) would need careful monitoring as this segregation effect would push the local composition in the case of the 1.5 and 1%Al steel towards the peritectic point (refer to Figure 7.7, page 186). This would lead to deeper oscillation marks and greater stress raisers because the steel would be closer to the peritectic point in the area of positive segregation.

## 11.2 Alloy design considerations

Other development work on TRIP properties at Al levels less than 1% [5], show that the best properties are achieved at the highest Al content, so that Al appears to be an effective alloying agent. Gomez [183] predicts that Al-alloyed TRIP steels ought to have higher strength due to a higher ferrite transformation temperature and subsequent higher C content in the ferrite. In fact “Aluminium alloyed TRIP 600” containing 0.2%C, 1.5%Mn and 2%Al are being commercially offered [184], although lower Mn contents are used. Thus the consequence of having 1.5%Al rather than 1% in terms of properties appears to be acceptable.

---

<sup>2</sup>Discussed on page 52

<sup>3</sup>Discussed on page 43

<sup>4</sup>Discussed on page 39

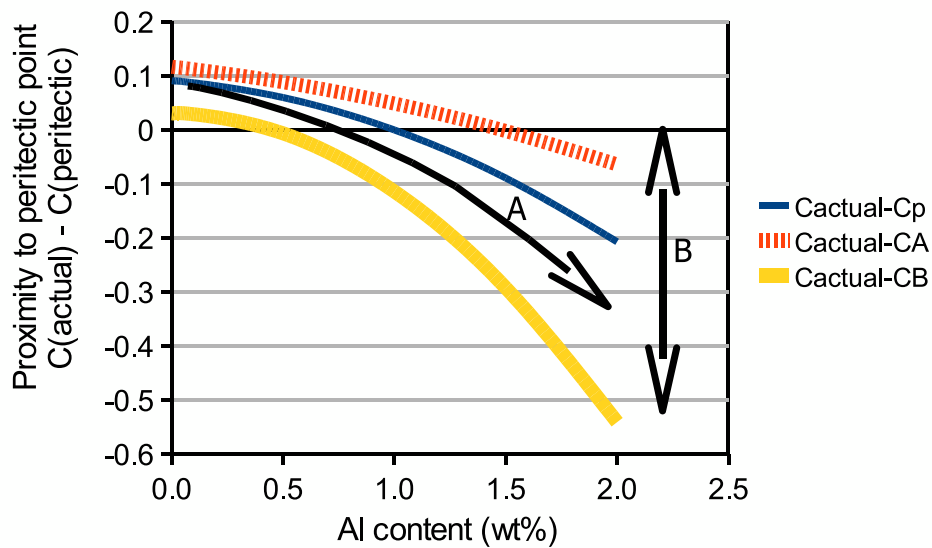


Figure 11.1: Effect of Al content on the peritectic point and peritectic region. As the Al content increases, the peritectic point is moved to lower carbon levels (indicated by arrow A) and the peritectic region becomes wider (indicated by arrow B).

Nevertheless, in the following section, the effect of Al and Mn on the peritectic point will be explored. A plot of the effect of Al on the peritectic point in a 0.15C-2.5Mn-0.011P-0.025Nb-0.0060N steel may be found in Figure 11.1. As the Al content increases, the peritectic point is moved to lower carbon levels (indicated by arrow A) and the peritectic region becomes wider (indicated by arrow B). Similarly, a plot of the effect of Mn level on the peritectic point in a 0.15C-0.011P-0.025Nb-1.5Al-0.0060N steel may be found in Figure 11.2. As the Mn content increases, the peritectic point moves to slightly higher carbon levels (indicated by arrow C). It may be therefore be possible to compensate for the effect of Al by increasing the Mn, however the Mn has less influence on the peritectic point than the Al. Other elements such as P have no effect on the peritectic point and Si has the same effect as Al [140]<sup>5</sup>.

While the replacement of Si with Al for TRIP steels is acceptable in terms of the properties (UTS, elongation, formability) [3], it, like Si, may require longer soaking times in the inter-critical annealing treatment to ensure sufficient retained austenite in the final product. However, Al levels up to 1.5% have been successfully galvanised [9], so Al may still be preferred to Si for TRIP steels. Additionally, Al has the effect of raising the Nb(C,N) solubility temperature, so that reheat temperatures may need to be higher<sup>6</sup>. The presence of eutectic NbC (large, high temperature precipitation of NbC) is expected at these carbon

<sup>5</sup>Using equations 2.7 and 2.8 discussed on page 2.7

<sup>6</sup>As seen in Table 7.5, page 184

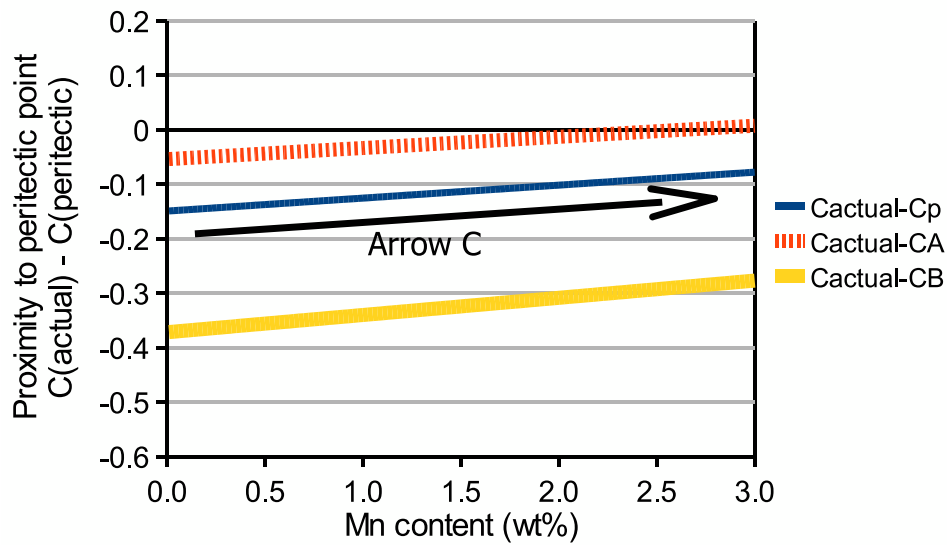


Figure 11.2: Effect of Mn content on the peritectic point and peritectic region. As the Mn content increases, the peritectic point moves to slightly higher carbon levels (indicated by arrow C).

levels [124]<sup>7</sup>. The implications for casting are that if macro segregation is less than optimal casting conditions exists (eg poor roll alignment and high superheat) then severe centreline segregation, including NbC eutectic precipitation, will occur. These NbC precipitates are not easily dissolved during reheating, leading to ineffective use of Nb additions.

Alloying must be done to avoid conditions that encourage dendritic AlN, i.e. avoid high temperature austenite and thus peritectic compositions. One route of reducing the risk of AlN formation would be to remove the N by alloying with Ti as Triolet *et al.*[32] have done, however this would make the Nb(C,N) less effective as a precipitate strengthener.

In evaluating the effect of MnS precipitation on AlN precipitation, MnS appeared to precipitate on an AlN plate<sup>8</sup>. It is thus less harmful than the AlN, and the Mn/S ratios of all the experimental steels are between 450-625, which is well above required critical limit needed to avoid cracking as suggested by De Toledo *et al.*[111]<sup>9</sup>.

<sup>7</sup>Discussed on page 48

<sup>8</sup>Shown in Figure 6.9 of 1%Al tested at 800°C

<sup>9</sup>Discussed on page 72

## Chapter 12

# Recommendations for Further Experimental Work

While the industrial applications and recommendations have already been discussed, there also scope for additional experimental work; time and samples permitting. Therefore, a list of potential further ductility tests is suggested. These include repeat/improved testing of the current steel compositions as well as investigations requiring alternative chemical compositions.

**Complete melting of the current steels.** In the 1.5%Al steel, the liquidus was 1518°C.

This was very close to the melting temperature of 1520°C in the tests (Figure 8.19, page 227). There may have been only partial melting of the samples. It is recommended that the melting temperature be at least 5-10°C above the liquidus. In the current ductility curves the tests temperatures that could benefit from more tests, are specifically:

1. The 1.53%Al unmelted tests at 950-1050°C and
2. all steels would benefit from repeated melt tests at all temperatures.

**The Nb(C,N) distribution in the current 1.53%Al steel.** It may be of merit to investigate the distribution of the Nb(C,N) precipitation in this steel in more depth. If the distribution is uniform or whether it is statistically significant that precipitation occurs close to the grain boundaries rather than within the grains will confirm whether the precipitation is deformation induced or occurs independently of deformation.

**AlN precipitation in the current 1.53%Al steel.** On one occasion, the dendritic AlN precipitation was seen in the 1.5%Al steel (unmelted 1.53%Al steel, tested at 850°C, Figure 4.12), therefore more rigorous testing to characterise when the 1.53%Al steel is susceptible to this type of precipitation should be carried out.

**Alternative compositions with low Mn additions.** Investigate the effect of Al level (0.05, 1, 1.5%Al) at lower Mn levels, such as a lower Mn series of steels with the base composition 0.15C-1.4Mn-Al-0.025Nb steels. If the peritectic point is moved to lower carbon levels by Mn, the widest ductility trough would be expected at higher Al levels.

**Alternative compositions with low P and N additions.** The work of Su *et al.*[11], does not fit well into the current analysis, it is recommended that the effect of low N and P be investigated since they appear to strongly alter the phase stabilities at Al levels between 0.05 and 2%.

**Alternative compositions with vanadium additions.** An alternative microalloy would be V, and may be beneficial for ductility at the low Al levels (0.05%Al) where Nb is detrimental to ductility.

## Appendix A

### Ductility Appendix

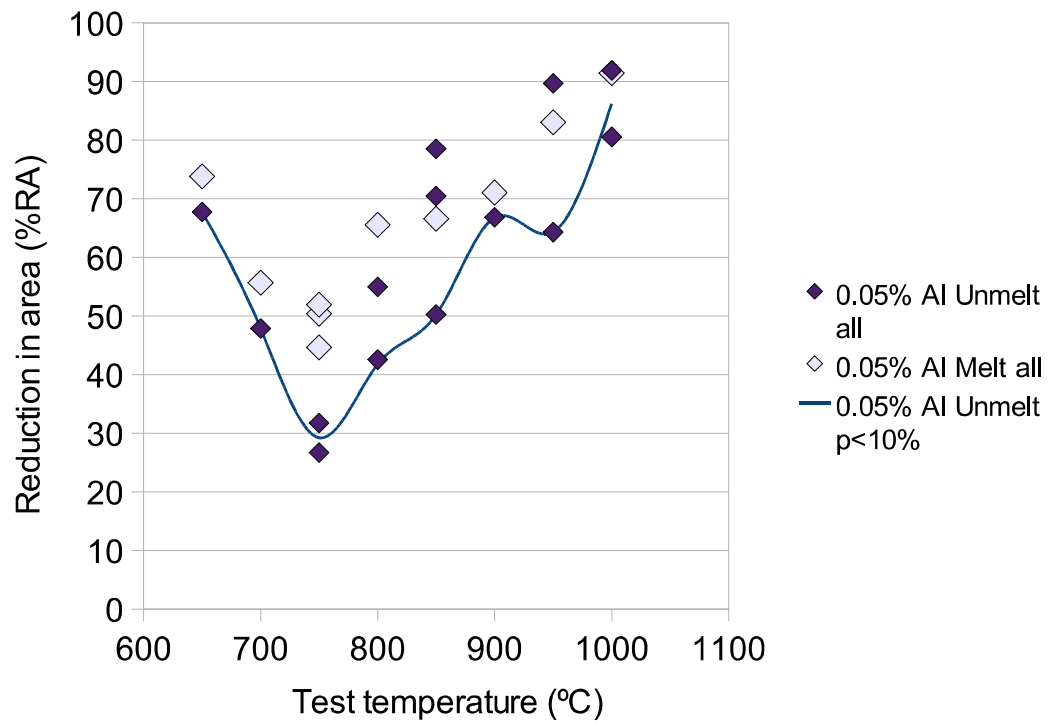


Figure A.1: Hot ductility curves for 0.05%Al TRIP steels.

Table A.1: R of A data for 0.05%Al steel.

Steel	Temp(°C)	melt/unmelt	R of A,%	Porosity,%	Sample label
9	650	melted	75	49	TRIP 9 m 1510 650-1
9	700	melted	56	39	9at700
9	750	melted	50	32	TRIP 9 750-1
9	750	melted	52	-	TRIP 9 750-2 longer
9	750	melted	45	-	TRIP 9 750-2 shorter
9	800	melted	64	44	TRIP 9 800-1
9	850	melted	67	38	TRIP 9 m 850-1
9	900	melted	63	18	TRIP 9 m 1510 900-1
9	950	melted	60	66	TRIP 9 950-1
9.2	1000	melted	91	-	9-2at1000
9	650	un-melted	68	-	9at650
9	700	un-melted	48	-	TRIP 9 700-1
9	750	un-melted	32	-	TRIP 9 750-1 shorter
9	750	un-melted	27	-	TRIP 9 750-1 longer
1	800	un-melted	42	0.4	TRIP 1 800-2
9	800	un-melted	50	16	TRIP 9 800-1
1	850	un-melted	42	67	TRIP 1 850-2
1	850	un-melted	54	63	TRIP 1 850-3
9	850	un-melted	50	-	9at850
9	900	un-melted	67	-	TRIP 9 900-1
1	950	un-melted	78	60	TRIP 1 950-1
9	950	un-melted	64	-	TRIP 9 950-1
9	1000	un-melted	92	-	9at1000 group-1
9	1000	un-melted	81	0	TRIP 9 rht 1000-1

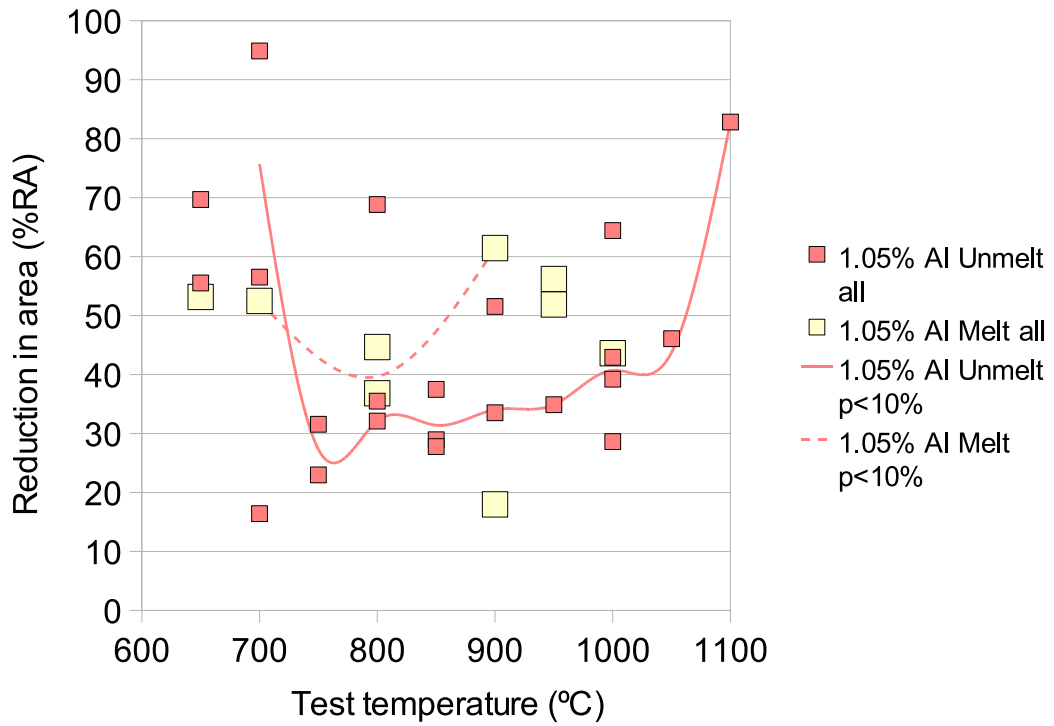


Figure A.2: Hot ductility curves for 1.05%Al TRIP steels.

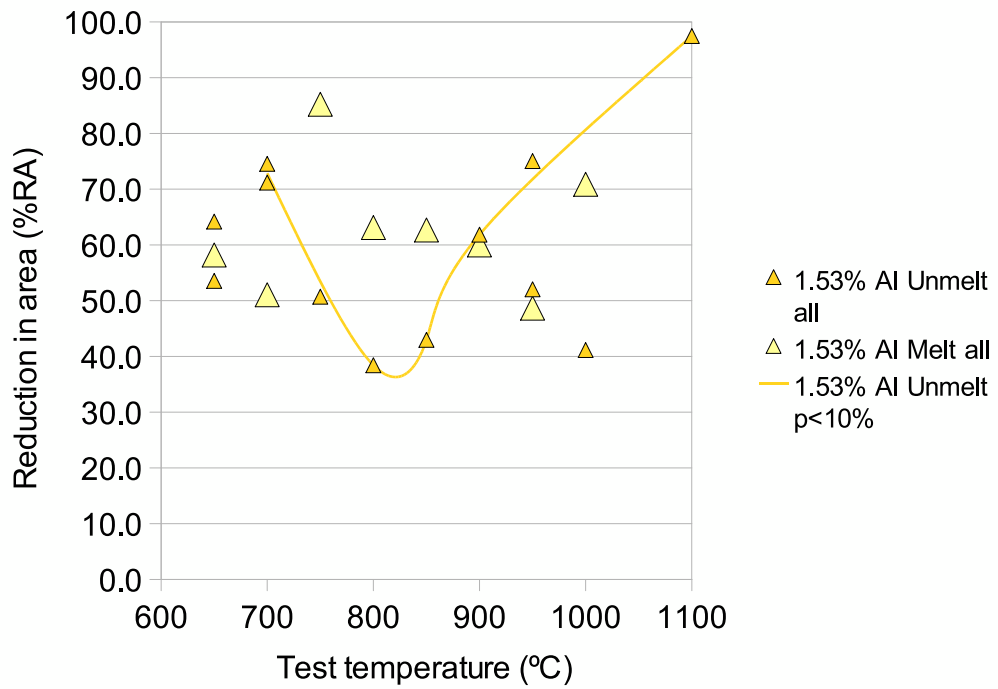


Figure A.3: Hot ductility curves for 1.53%Al TRIP steels.

Table A.2: R of A data for 1.05%Al steel.

Steel	Temp(°C)	melt/unmelt	R of A,%	Porosity,%	Sample label
2	650	melted	53	0	TRIP 2-3 m 1510 650-1
2	700	melted	52	0	TRIP 2-2 m 1510 700-1
2	800	melted	45	0	2-2at800
2	800	melted	35	10	TRIP 2-3 800-1
2	900	melted	17	24	TRIP 2-2 900-1
2	900	melted	61	0	TRIP 2-3 900-3
2	950	melted	47	27	TRIP 2-3 m 1510 950-1
2	950	melted	52	35	TRIP 2-3 950-1
2	1000	melted	37	22	2-2at1000-02
2	650	un-melted	56	0	TRIP 2-2 650-1
2	650	un-melted	70	0	TRIP 2-3 650-1
2	700	un-melted	95	0	TRIP 2-1 700
2	700	un-melted	12	28	TRIP 2-2 700-1
2	700	un-melted	57	0	TRIP 2-3 700-1
2	750	un-melted	23	0	TRIP 2-2 750-1
2	750	un-melted	32	0	TRIP 2-3 750-1
2	800	un-melted	35	38	TRIP 2-1 800-1
2	800	un-melted	34	74	TRIP 2-2 800-1
2	800	un-melted	32	0	TRIP 2-3 800-1
2	850	un-melted	29	0	2-1at850
2	850	un-melted	28	0	TRIP 2-2 850-1
2	850	un-melted	37	0	TRIP 2-3 850
2	900	un-melted	47	37	TRIP 2-1 900
2	900	un-melted	34	2	TRIP 2-3 900-1
2	950	un-melted	35	0	TRIP 2-3 950-3
2	1000	un-melted	43	0	2-1at1000
2	1000	un-melted	52	7	TRIP 2-1 1000-3
2	1000	un-melted	29	0	TRIP 2-2 1000-1
2	1000	un-melted	39	0	TRIP 2-3 1000-1
2	1050	un-melted	44	5	TRIP 2-1 1050
2	1100	un-melted	83	0	2-1at1100

Table A.3: R of A data for 1.53%Al steel.

Steel	Temp(°C)	melt/unmelt	R of A,%	Porosity,%	Sample label
10	650	melted	55	26	TRIP 10 650-1
10	700	melted	42	28	TRIP 10 m 1520 700-1
10	750	melted	74	0	TRIP 10 750-2
10	800	melted	59	12	TRIP 10 m 1520 800-1
10	850	melted	44	44	TRIP 10 850-1
10	900	melted	42	43	TRIP 10 m 1520 900-1
10	950	melted	47	17	TRIP 10 950-3
10	1000	melted	63	26	TRIP 10 m 1520 1000-1
3	650	un-melted	53	37	TRIP 3 650
3	650	un-melted	42	36	TRIP 3 rht 650
3	700	un-melted	71	0	TRIP 3 700
3	700	un-melted	75	0	3at700
3	750	un-melted	45	21	TRIP 3 rht 750 10
3	800	un-melted	38	0	TRIP 3 800
3	850	un-melted	43	0	3at850
3	900	un-melted	62	0	TRIP 3 900-1
3	950	un-melted	58	52	TRIP 3 950-2
3	950	un-melted	75	unknown	TRIP 3 rht 950 unmelt
3	1000	un-melted	53	38	3at1000
3	1100	un-melted	97	0	TRIP 3 1100-1

## Appendix B

# Optical Microscopy Appendix

### B.1 Macro optical microscopy

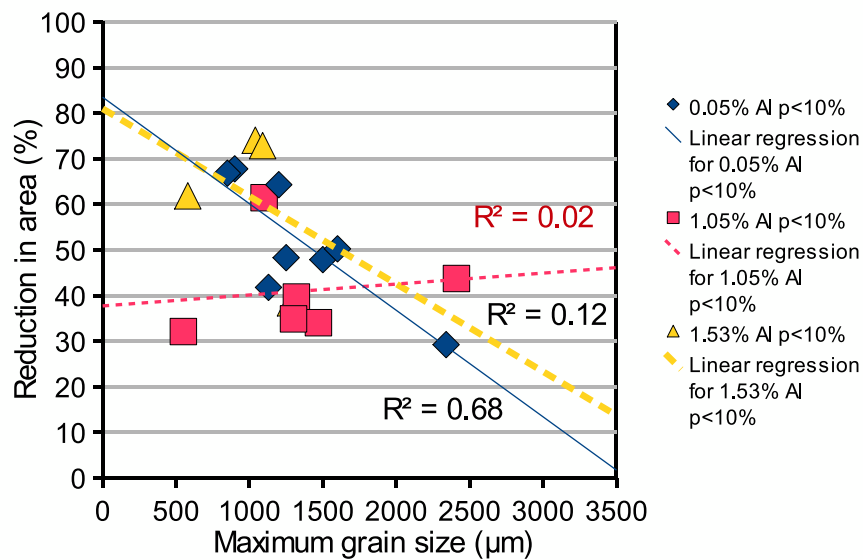


Figure B.1: Relationship between inverse maximum grain size (from the macro OM fracture surface) and hot ductility.

### B.2 Cross sectional microscopy

Various relationships are suggested to relate grain size to ductility:  $d$ ,  $d^{-1}$ ,  $d^{0.5}$ ,  $d^{-0.5}$ ,  $\log(d)$ . Figure B.2 shows the various possible correlations<sup>1</sup>.

<sup>1</sup>Since the question is bound to be asked.

Table B.1: Hot ductility (%) for 0.05%Al steels, indicating the type of failure from macro OM. Intergranular failure predominates at low Al content. “P” indicates that the sample has greater than 10% porosity.

Temp (°C)	ig	ig/tg	tg	HTDR	Sample
650 (melt)	75P	-	-	-	005-9-650-mF
700 (melt)	56P	-	-	-	005-9-700-mJ
750 (melt)	50P	-	-	-	005-9-750-1mD
750 (melt)	52	-	-	-	005-9-750-2lmN
750 (melt)	45	-	-	-	005-9-750-2smN
800 (melt)	-	64P	-	-	005-9-800-1mD porosity
850 (melt)	67P	-	-	-	005-9-850-1mF
900 (melt)	63P	-	-	-	005-9-900-1mF
950 (melt)	60P	-	-	-	005-9-950-1mD porosity
1000 (melt)	-	-	-	91	005-9-1000-mJ
650	68	-	-	-	005-9-650-uM
700	48	-	-	-	005-9-700-uD
750	32	-	-	-	005-9-750-1suN
750	27	-	-	-	005-9-750-1luN
800	42	-	-	-	005-1-800-2uD
800	50P	-	-	-	005-9-800-1uD
850	42P	-	-	-	005-1-850-2uD
850	54P	-	-	-	005-1-850-3uD
850	50	-	-	-	005-9-850-uM
900	67	-	-	-	005-9-900-1uD
950	64	-	-	-	005-9-950-1-uD
950	78P	-	-	-	005-1-950-1uD porosity
1000	-	-	-	92	005-9-1000-uM
1000	-	-	81	-	005-9-1000-1uF

Table B.2: Hot ductility (%) for 1.05%Al steels, indicating the type of failure from macro OM. A combination of intergranular and transgranular failure occurs at intermediate Al contents. “P” indicates that the sample has greater than 10% porosity.

Temp (°C)	ig	ig/tg	tg	HTDR	Sample
650 (melt)	53	-	-	-	105-2-3-650-1mF
700 (melt)	52	-	-	-	105-2-2-700-1mF
800 (melt)	-	45	-	-	105-2-2-800-mJ
800 (melt)	35	-	-	-	105-2-3-800-1-mD
900 (melt)	-	17P	-	-	105-2-2-900-1-mD
900 (melt)	-	61	-	-	105-2-3-900-3-mD
950 (melt)	47P	-	-	-	105-2-3-950-1mF
950 (melt)	-	52P	-	-	105-2-3-950-1-mD
1000 (melt)	-	37P	-	-	105-2-2-1000-02-mJ
650	-	-	-	70	105-2-3-650-1uD
700	-	-	-	95	105-2-1-700-uD
700	-	12P	-	-	105-2-2-700-1-uD
700	-	-	-	57	105-2-3-700-1uD
750	-	-	23	-	105-2-2-750-1-uD
750	-	32	-	-	105-2-3-750-1uD
800	35P	-	-	-	105-2-1-800-1-uD
800	34P	-	-	-	105-2-2-800-1-uD
800	32	-	-	-	105-2-3-800-1uD
850	-	-	29	-	105-2-1-850-uM
850	28	-	-	-	105-2-2-850-1uD
850	37	-	-	-	105-2-3-850-uD
900	47P	-	-	-	105-2-1-900-uD
900	-	34	-	-	105-2-3-900-1uD
950	-	35	-	-	105-2-3-950-3uD
1000	-	-	43	-	105-2-1-1000-uM
1000	-	52	-	-	105-2-1-1000-3-uD
1000	-	29	-	-	105-2-2-1000-1-uD
1000	-	39	-	-	105-2-3-1000-1uD
1050	-	44	-	-	105-2-1-1050-uD
1100	-	-	-	83	105-2-1-1100-uM

Table B.3: Hot ductility (%) for 1.53%Al steels, indicating the type of failure from macro OM. A combination of intergranular and transgranular failure occurs at high Al contents. “P” indicates that the sample has greater than 10% porosity.

Temp (°C)	ig	ig/tg	tg	HTDR	Sample
650 (melt)	-	55P	-	-	153-10-650-1-mD
700 (melt)	-	-	42P	-	153-10-700-1mF
750 (melt)	-	74	-	74	153-10-750-2-mD mixed
800 (melt)	-	59P	59P	-	153-10-800-1mF
850 (melt)	-	44P	-	-	153-10-850-1-mD
900 (melt)	-	-	42P	-	153-10-900-1mF
950 (melt)	-	47P	-	-	153-10-950-3-mD
1000 (melt)	-	-	63P	-	153-10-1000-1mF
650	-	53P	-	-	153-3-650-uD
650	42P	-	-	-	153-3-650-uF
700	71	-	-	71	153-3-700-uD mixed
700	-	-	-	75	153-3-700-uM
750	45P	-	-	-	153-3-750-10uF
800	-	38	-	-	153-3-800-uD
850	-	-	43	-	153-3-850-uM
900	-	62	-	-	153-3-900-1-uD
950	-	58P	-	-	153-3-950-2-uD
950	-	-	-	-	153-3-950-uF no fracture
1000	-	53P	-	-	153-3-1000-uM
1100	-	-	-	97	153-3-1100-2-uD

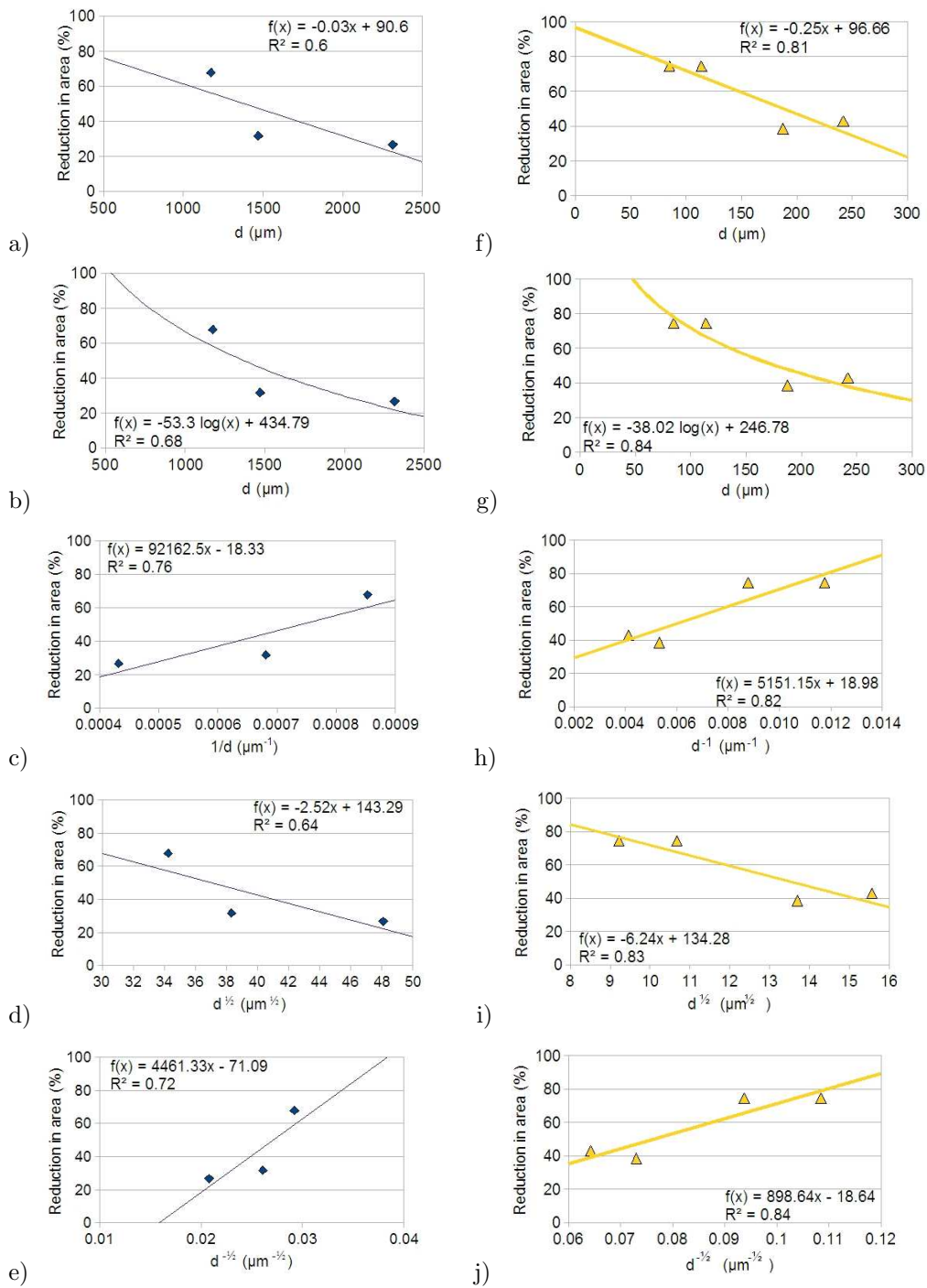


Figure B.2: Relationship between ductility and grain size a)-e) 0.05%Al steel for  $d$ ,  $\log(d)$ ,  $d^{-1}$ ,  $d^{0.5}$ ,  $d^{-0.5}$  respectively; f)-g) 1.53%Al steels for  $d$ ,  $\log(d)$ ,  $d^{-1}$ ,  $d^{0.5}$ ,  $d^{-0.5}$  respectively. The population excludes samples with >10% porosity and DRX.

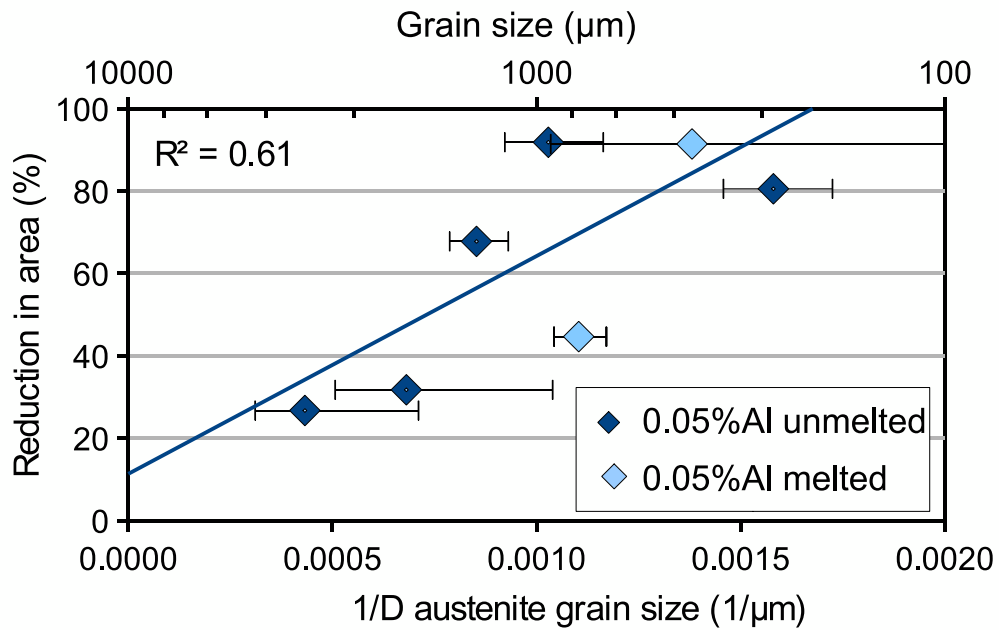


Figure B.3: Relationship between inverse grain size and reduction in area in all 0.05%Al steel. The addition of the DRX samples and the melted samples reduces the correlation slightly.

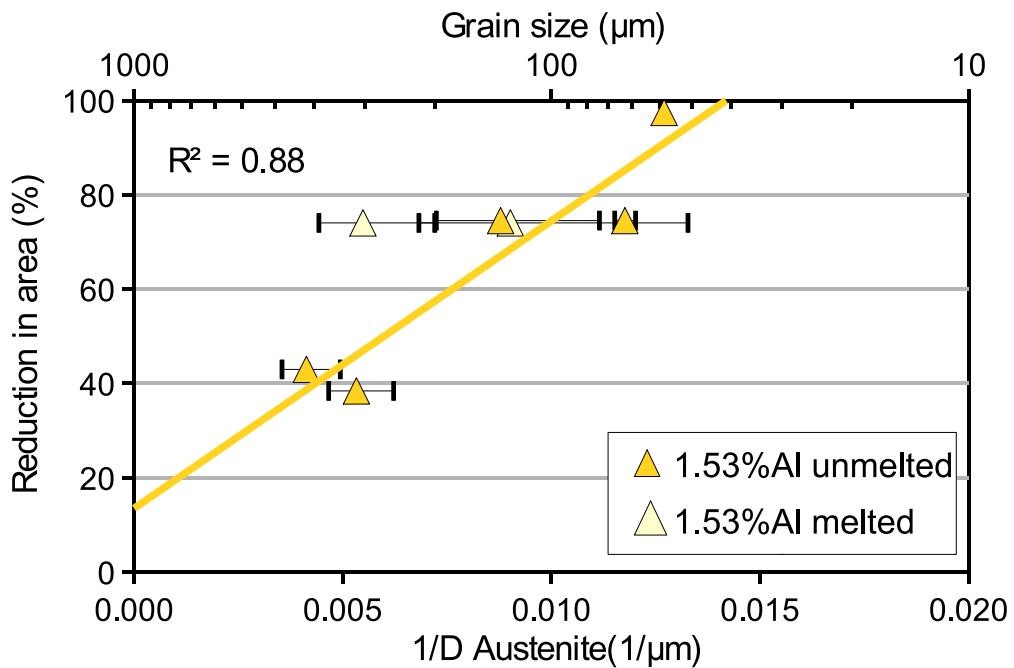


Figure B.4: Relationship between grain size and R of A in the 1.53%Al steel (regression only for unmelted tests). A very good relationship between R of A and austenite grain size.

## Appendix C

# Scanning Electron Microscopy Appendix

Table C.1: SEM grain size for 0.05%Al steel.

Sample	Test temp(°C)	un/melt	%R of A	Grain size, $\mu\text{m}$
0059650uM	650	unmelt	69	1419 $\pm$ 277
00597501sM	750	unmelt	39	2863 $\pm$ 855
00518002uD	800	unmelt	73	933 $\pm$ 90
0059850uM	850	unmelt	53	916 $\pm$ 143
00599501uD	950	unmelt	66	1459 $\pm$ 169
00597502smD	750	melt	41	1036 $\pm$ 286

Table C.2: SEM grain size for unmelted 1.05%Al steel.

Sample	Test temp(°C)	%R of A	Grain size, $\mu\text{m}$
105218001uD	800	39	1030 $\pm$ 59
10521900uD	900	49	898 $\pm$ 76
105211050uD	1050	41	2818 $\pm$ 1459
1052110003uD	1100	48	1075 $\pm$ 325

Table C.3: SEM grain size for unmelted 1.53%Al steel.

Sample	Test temp(°C)	%R of A	Grain size, $\mu\text{m}$
15331000uM	1000	45	4414 $\pm$ 1595
1533800uD	800	41	416 $\pm$ 104
1539502uD	950	48	690 $\pm$ 160

## Appendix D

# Transmission Electron Microscopy

## Appendix

### D.1 Diffraction analysis using an electron diffraction simulation program

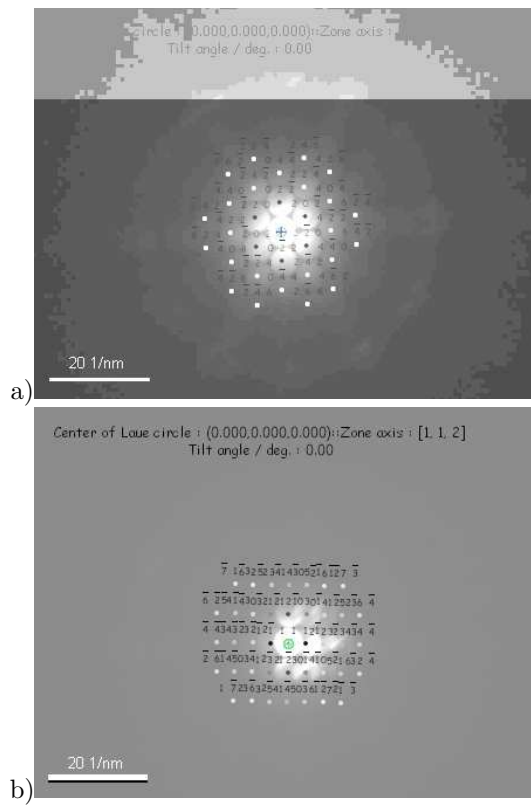


Figure D.1: Selected area diffraction patterns of dendritic AlN precipitate in 1.05%Al steel, (the same SAD's from Figure 6.8) identified with JEMS electron diffraction simulation program as a) fcc [111] zone axis pattern and b) [112] zone axis pattern. Used [185] from the International Crystal Structure Database [186].

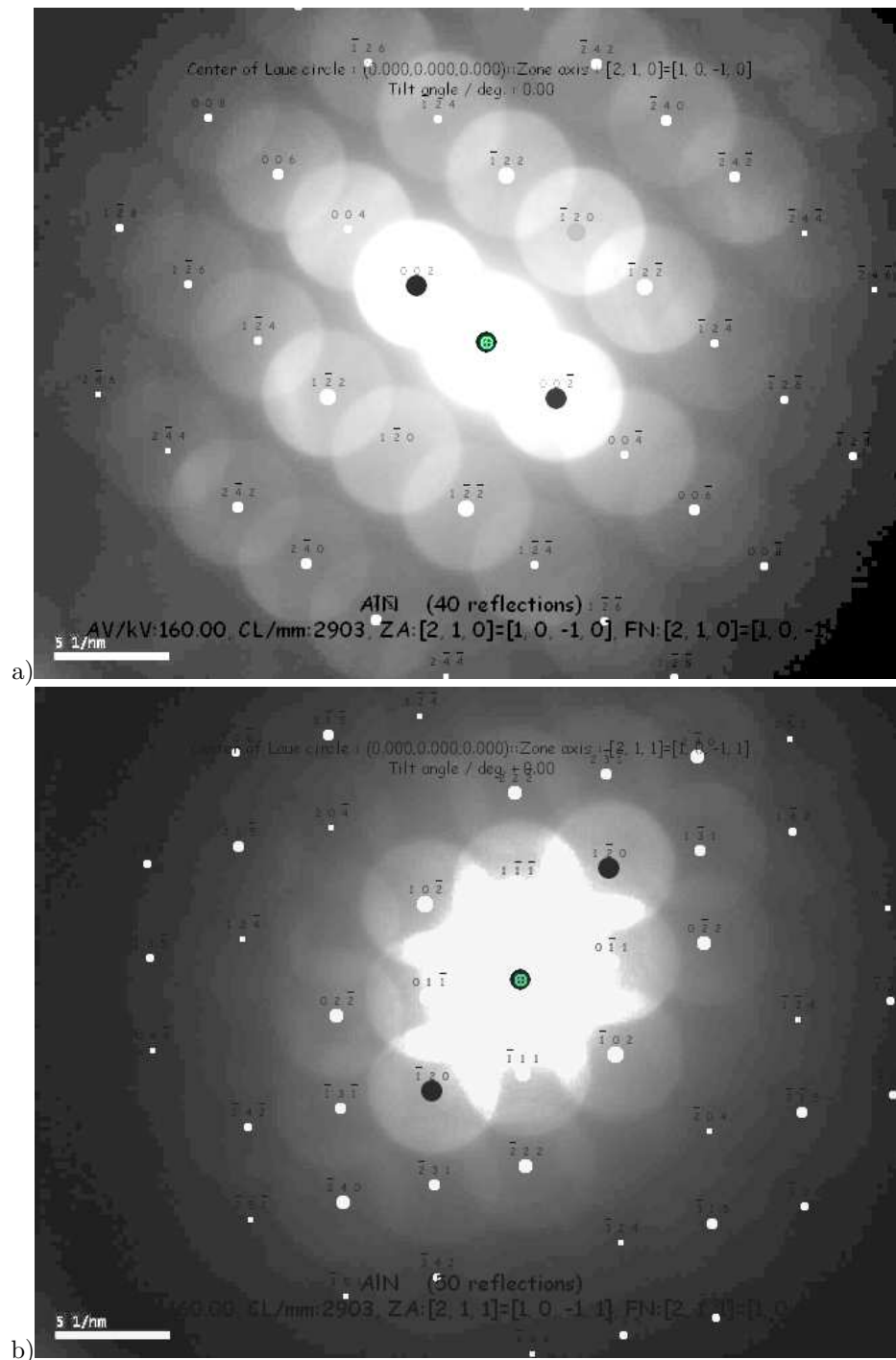


Figure D.2: Diffraction patterns for AlN precipitate in the 1.5%Al steel, reheated to 1460°C and tested at 1100°C, (the same SAD's from Figure 6.20) a) Zone axis pattern  $[210]$  or  $[10\bar{1}0]$  hcp crystal structure b) Zone axis pattern  $[211]$  or  $[10\bar{1}1]$  hcp crystal structure. Used [187] from the International Crystal Structure Database [186].

## D.2 Slow cool rate transmission electron microscopy appendix

Table D.1: Precipitation summary for samples cooled at the slower cooling rate.

Test temp °C	Sample	Nb(C,N) size (nm)	AlN	other comments
650	00592650uM	no ppt	no ppt	no $\alpha$ . oxides.
750	00597501suO	no ppt	no ppt	no $\alpha$ . MnS, CuS. Oxides (Fe, Ag, Se).
750	0059750-2smN	no ppt	no ppt	no $\alpha$ . Sulphides. Oxides, large Al <sub>2</sub> O <sub>3</sub> .
950	0059950-1uD	13±8.9	no ppt	thin $\alpha$ . Nb(C,N) also with Mn, Fe, and Ti. Larger Nb(C,N) ppt on prior $\gamma$ gb.
1000	00591000g1uM	24±11	no ppt	no $\alpha$ . Ti in Nb(C,N) larger ppt. CuS. Oxides.
650	1052-3650-1mF	8±8	Needle	no $\alpha$ .
700	1052-1700	37±16	Plate needle	no $\alpha$ Nb(C,N) ppt after AlN plate and needle. Mn,CuS.
900	1052-3900-3mD	32±11	>500nm needle	Nb(C,N) ~ in $\alpha$ . Mn,CuS. No Nb(C,N) ppt on needle.
1050	1052-11050uD	62±27	Dendritic AlN	Nb(C,N) ppt on dendritic AlN
750	153750-2nmD	9.4±4.1	no ppt	Nb(C,N) ppt not always in $\alpha$ .
800	1533800uD	47±14, 9±4.2, 18±3.0	no ppt	Nb(C,N) ppt not always in $\alpha$ . Variable Nb(C,N) size.
1100	15331100-1uD	25±15	900nm needle, plate	Nb(C,N) in $\alpha$ . Nb(C,N) ppt on AlN needle.

## Appendix E

# Thermodynamic Modelling Appendix

### E.1 The effective peritectic point and relative carbon level from peritectic point for all steels

Table E.1:  $C_{actual} - C_{peritectic}$  values for all steels.

Grade	$C_A$	$C_B$	$C_{peritectic}$	$C_{actual} - C_{peritectic}$
Trip 1	0.03	0.12	0.06	0.09
Trip 9	0.04	0.12	0.06	0.08
Trip 2-1	0.1	0.3	0.16	-0.01
Trip 2-2	0.11	0.32	0.17	-0.02
Trip 2-3	0.11	0.32	0.17	-0.02
Trip 3	0.16	0.46	0.25	-0.1
Trip 10	0.15	0.42	0.23	-0.08
Mintz steel 1 [10]	0.05	0.15	0.08	0.07
Mintz steel 4 [10]	0.12	0.32	0.18	0.03
Mintz steel 3 [10]	0.23	0.69	0.36	-0.14
Mintz steel 7 [10]	0.05	0.15	0.08	0.02
Su steel 1 [11]	0.05	0.15	0.08	0.12
Su steel 3 [11]	0.07	0.18	0.11	0.11
Su steel 5 [11]	0.11	0.27	0.16	0.06
Cowley steel6 [55]	0.06	0.15	0.09	0.06
Cowley steel8 [55]	0.05	0.15	0.09	0.05
Cowley steel2 [55]	0.08	0.14	0.08	0.08
Mohammed B [62]	0.05	0.15	0.08	0.016

## E.2 Data base details for FactSage and Thermo-Calc

Table E.2: Thermo-Calc4 for windows data base.

Gas	(VPV)	GAS
Liquid	(VPV)	LIQUID
Predominant solids	(VPV)	ALN, BCC_A2#1, BCC_A2#2, FCC_A1#1, FCC_A1#2, GRAPHITE, M5C2, MNS
Other Solids	(VPV)	AL4C3, CU3P1, DIAMOND_FCC_A4, FC_ORTHORHOMBIC, FE2SI, FE4N_LP1, FE8SI2C, FECN_CHI, FEP, FES, HCP_A3, KSL-CARBIDE, LAVES_PHASE_C14, M23C6, M2P, M3P, M3SI, M5SI3, M6C, M7C3, MSI, MU_PHASE, NBNI3, RED_P, SIC, SIGMA, WHITE_P

Table E.3: Data base (FACT53, Fsstel) for FactSage: Duplicates were suppressed, Pure liquid and solid species considered.

Liquid	Fe(liq) liquid
Predominant solids	MnS(s) mns; Fe(s) bcc_a2; Fe(s2) fcc_a1; MnS(s) alabandite; AlN(s) solid; NbC(s) solid; Nb8C7(s) solid; NbN(s) solid-a
Other Solids	C(s) graphite; C(s2) diamond; Al(s); Al4C3(s); Si(s) diamond_a4; SiC(s)_alpha; SiC(s2) _beta; Si3N4(s)_alpha; P(s)_white; P(s2)_red_v; P(s3)_red_iv; P(s4)_black; P3N5(s); AlP(s); SiP(s); S(s) orthorhombic; S(s2) monoclinic; AlS(s); Al2S3(s); SiS(s); SiS2(s); P2S3(s); P4S3(s); P2S5(s); P4S5(s); P4S6(s); P4S7(s); Mn(s)_alpha; Mn(s2)_beta; Mn(s3)_gamma; Mn(s4)_delta; Mn3C(s)-a (cementite); Mn3C(s2)-b; Mn7C3(s); Mn4N(s); Mn5N2(s); MnSi(s); Mn3Si(s); Mn5Si3(s); Mn10Si17(s); MnP(s); MnP3(s); MnS2(s) hauerite; Mn5C2(s); Mn20Mn3C6(s); Mn6N4(s); Mn6N5(s); Al4Mn(s); Al6Mn(s); Al12Mn(s); Al11Mn4(s); Mn11Si19(s); Mn17Si3(s); Mn33Si7(s); Fe(s) bcc; Fe(s2) fcc; Fe3C(s)-a; Fe3C(s2) ksi_carbide; Fe2N(s); Fe4N(s)-a; Fe4N(s2)-b; FeAl3(s); FeSi(s); FeSi2(s); Fe3Si(s); Fe3Si7(s); FeP(s); FeP2(s); Fe2P(s); Fe3P(s); Fe3P(s2); Fe5Si3(s); Fe8Si2C(s); FeS(s); FeS(s2); FeS(s3); FeS2(s) pyrite; FeS2(s2) marcasite; Fe7S8'(s); Fe10S11'(s); Fe11S12'(s); C2Fe5(s); Al5Fe2(s); Al61Fe31(s); Al2FeSi(s); Al3FeSi(s); Al2Fe2Si(s); Al14Fe3Si3(s); Al11Fe3Si6(s); Al96Fe10Mn14Si18'(s)_alpha; Nb(s) bcc_a2; Nb2C(s) hcp_a3; Nb4C3(s); NbN(s2)-b; Nb2N(s); NbSi2(s); Nb5Si3(s); NbS(s); NbS2(s); NbFe2(s); CNb(s) fcc_a1

### E.3 Typical FactSage and Thermo-Calc results

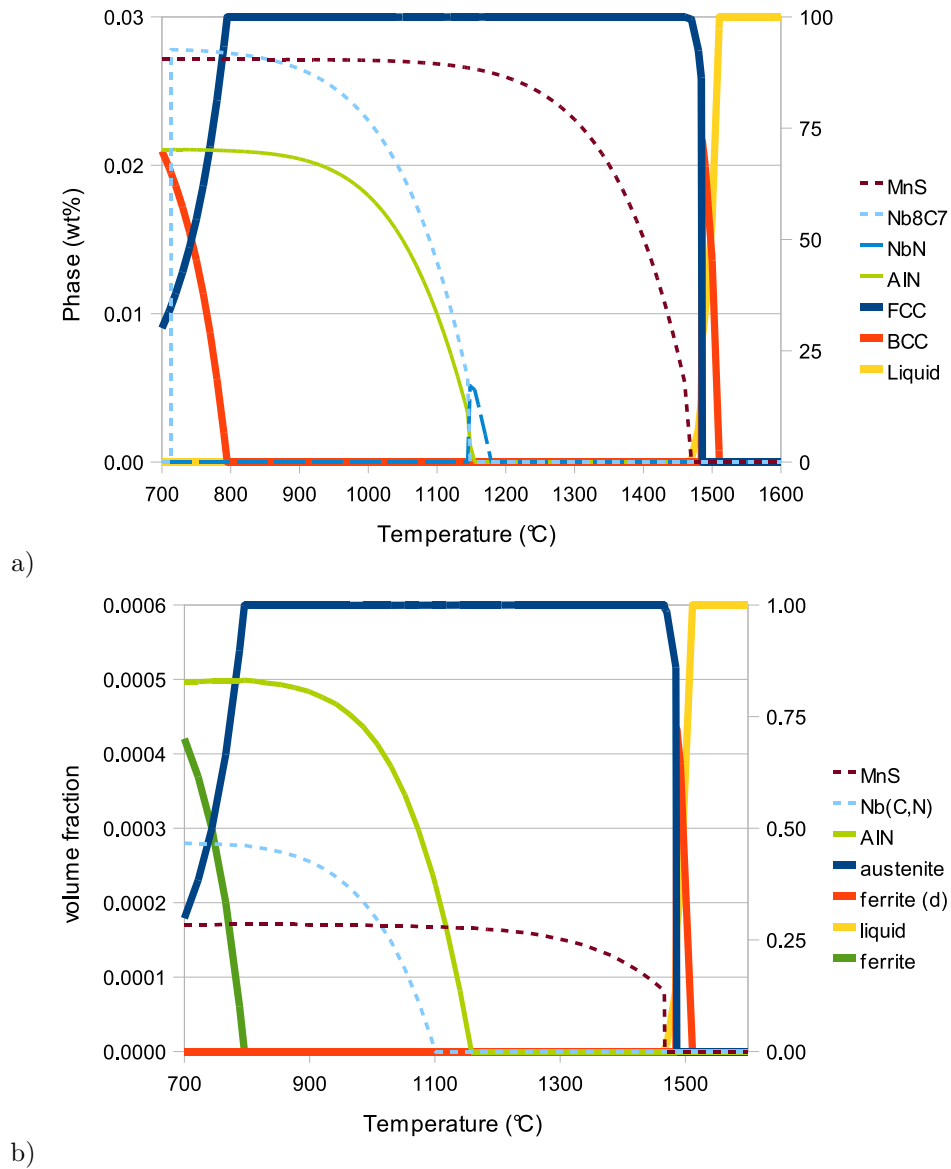


Figure E.1: Typical a) FactSage (wt% vs temperature) and b) Thermo-Calc (volume fraction vs temperature) curves, (Trip 9, 0.05%Al). The Fe phases are plotted on the second Y axis.

“There and Back Again, a Hobbit’s Holiday”

The Hobbit, JRR Tolkien

Table E.4: Comparison of the FactSage (FS) and Thermo-Calc (TC) simulations for all phase field boundaries for all Trip steels in Table 7.1. All temperatures in °C. Relative difference (%) is with respect to the Thermo-Calc value.

	TC Trip 9	FS Trip 9	Difference	% difference to TC
L+ $\delta$	1511	1510	0.97	0.06
L+ $\delta$ + $\gamma$	1486	1486	0.62	0.04
L+ $\gamma$	1485	1484	0.58	0.04
$\gamma$	1466	1460	6.41	0.44
$\gamma$ + $\alpha$	796	795	1.01	0.13
MnS/Fes	1467	1470	-2.86	-0.20
AlN	1158	1155	3.46	0.30
Nb(C,N)	1101	1179	-78.12	-7.10
	TC Trip 2-1	FS Trip 2-1	Difference	% difference to TC
L+ $\delta$	1511	1509	1.44	0.10
L+ $\delta$ + $\gamma$	1454	1457	-3.21	-0.22
$\delta$ + $\gamma$	1440	1446	-5.67	-0.39
$\gamma$	1410	1413	-3.8	-0.27
$\gamma$ + $\alpha$	946	940	5.87	0.62
MnS/Fes	1442	1447	-4.82	-0.33
AlN	1473	1478	-5.48	-0.37
Nb(C,N)	1156	1229	-73.29	-6.34
	TC Trip 3	FS Trip 3	Difference	% difference to TC
L+ $\delta$	1518	1518	-0.09	-0.01
$\delta$	1441	1444	-2.8	-0.19
$\delta$ + $\gamma$	1432	1435	-2.73	-0.19
$\gamma$	1294	1291	2.78	0.21
$\gamma$ + $\alpha$	1083	1067	16.66	1.54
MnS/Fes	1447	1447	-0.12	-0.01
AlN	1488	1500	-11.63	-0.78
Nb(C,N)	1166	1240	-73.69	-6.32
	TC Trip 10	FS Trip 10	Difference	% difference to TC
L+ $\delta$	1518	1518	-0.13	-0.01
L+ $\delta$ + $\gamma$	1441	1444	-2.88	-0.20
$\delta$ + $\gamma$	1441	1444	-2.96	-0.21
$\gamma$	1327	1332	-5.47	-0.41
$\gamma$ + $\alpha$	1029	1019	9.81	0.95
MnS/Fes	1443	1438	5	0.35
AlN	1492	1498	-5.22	-0.35
Nb(C,N)	1174	1249	-75.36	-6.42

## References

1. M. De Meyer, B.C. De Cooman, and D. Vanderschueren. Influence of Al on the properties of cold rolled C-Mn-Si TRIP steels. *I&SM*, pages 55–63, February 2000.
2. M. Bouet, J. Root, E. Es-sadiqui, and S. Yue. The effect of Mo in Si-Mn Nb bearing TRIP steels. In *40th MWSP Conf. Proc.*, pages 675–684. ISS, 1988.
3. M. De Meyer, D. Vanderschueren, and B.C. De Cooman. The influence of the substitution of Si by Al on the properties of cold rolled C-Mn-Si TRIP steels. *ISIJ International*, 39(8):813–822, 1999.
4. G. Frommeyer, U. Brück, and P. Neumann. Supra-ductile and high-strength manganese-TRIP/TWIP steels for high energy absorption purposes. *ISIJ International*, 43(3):438–446, 2003.
5. J. E. Garcia-Gonzalez, C.I. Garcia, M. Hua, and A.J. DeArdo. Fundamental study of the austenite formation and decomposition in high strength low-Si, Al added Nb-Mo TRIP steels. In *MS&T'05*, volume 2, Pittsburgh, September 2005.
6. O. Grässel, L. Krüger, G. Frommeyer, and L.W. Meyer. High strength Fe-Mn-(Al,Si) TRIP/TWIP steels development - properties - applications. *International Journal of Plasticity*, 16:1391–1409, 2000.
7. Dual phase and TRIP steels. Niobium Products Company GmbH, Steinstrasse 28, D-40210 Düsseldorf, Germany, 1997. Niobium Information No. 15/97.
8. Z. Li and D. Wu. Study of the high strength and low yield ratio cold forging steel. *Materials Science and Engineering A*, 452-453:142–148, 2007.
9. B. Mintz. Hot dip galvanising of transformation induced plasticity and other intercritically annealed steels. *International Materials Reviews*, 46(4):169–197, 2001.
10. B.M. Mintz, A. Tuling, and A. Delgado. Influence of silicon, aluminium, phosphorus and boron on hot ductility of TRansformation Induced Plasticity assisted steels. *MS&T*, 19:1721–1726, December 2003.

11. H. Su, W. D. Gunawadarna, A. Tuling, and B. Mintz. Influence of Al and P additions on hot ductility of steels. *MS&T*, 23(11):1357–1366, 2007.
12. K Sugimoto, T. Muramatsu, S. Hashimoto, and Y. Mukai. Formability of Nb bearing ultra-high-strength TRIP-aided sheet steels. *Journal of Materials Processing*, 177:390–395, 2006.
13. I. B. Timokhina, E. V. Perloma, and P.D. Hodgson. Microstructure and mechanical properties of C-Si-Mn(-Nb) TRIP steels after simulated thermomechanical processing. *MS&T*, 17:135–140, February 2001.
14. F.G. Wilson and T. Gladman. Aluminium nitride in steel. *International Materials Reviews*, 33(5):221–286, 1988.
15. H. Mori. Defects in continuous casting of steel, causes and prevention, part 1. *Tetsu-to-Hagané*, 60(7):784–793, 1974. Translated by H.Brutcher.
16. W.R. Irving. *Continuous casting of steel*. The Institute of Metals, 1993.
17. B. Mintz, S. Yue, and J.J. Jonas. Hot ductility of steels and its relationship to the problem of transverse cracking during continuous casting. *International Materials Reviews*, 36(5):187–217, 1991.
18. S. Harada, S. Tanaka, H. Misumi, S. Mizoguchi, and H. Horiguchi. A formation of transverse cracks on CC slab surface. *ISIJ Int.*, 30(4):310–316, 1990.
19. S.G. Hibbins and J.K. Brimacombe. Characterisation of heat transfer in the secondary cooling system of a continuous slab caster. *ISS Transactions*, 3:77–89, 1983.
20. A.M. El-wazri, F. Hassani, S. Yue, and E. Es-sadiqi. Influence of physical simulation on the hot ductility behaviour of a microalloyed steel in the continuous casting process. *I&SM*, pages 37–41, January 1998.
21. B. Mintz. Private communication, 2010.
22. K. Wünnenberg and K. Schwerdtfeger. Principles in thin slab casting. *I&SM*, pages 25–31, April 1995.
23. T. Nozaki, J. Matsuno, K. Murata, H. Ooi, and M. Kodama. A secondary cooling pattern for preventing surface cracks of continuous casting slab. *Transactions of the ISIJ*, 18:330–338, 1978.
24. J.K. Brimacombe, P.K. Agarwal, S. Hibbins, B. Pradhbaker, and L.A. Baptista. Spray cooling in the continuous casting of steel. In *Continuous Casting of Billets, Blooms and Slabs.*, pages 541–555, Vancouver, B.C. Canada, March 1987. University of British Columbia.

25. R. Dippenaar, S-C. Moon, and E.S. Szekeres. Strand surface cracks - the role of abnormally large prior austenite grains. In *AISTech 2006 Proceedings*, volume 1, pages 833–843, 2006.
26. C. Cucutti, J. Petroni, G. Di Gresis, M. Dziuba, and E. Lagos. Transverse corner crack formation in continuously cast slab. In *1997 Steelmaking Conference Proceedings*, pages 365–371, 1997.
27. W.R. Irving, A. Perkins, and R. Gray. Effect of steel chemistry and operating parameters on surface defects in continuously cast slabs. *Ironmaking and Steelmaking*, 11(3):146–151, 1984.
28. K. Yamanaka, F. Terasaki, H. Ohtani, M. Oda, and M. Yoshihara. Relation between hot ductility and grain boundary embrittlement of low-carbon killed steels. *Transactions ISIJ*, 20:810–816, 1980.
29. S.V. Subramanian, S. Shima, G. Ocampo, T. Castillo, J.D. Embury, and G.R. Purdy. The effect of nitrogen content on the evolution of precipitates and on the processing of Ti-Nb bearing HSLA steel slabs. In J.M. Gray *et al.*, editor, *HSLA Steels Metallurgy and Applications*, pages 151–161. ASM-International, 1986.
30. N. H. Croft. Solubility model to predict the effects of aluminium and nitrogen contents on the susceptibility of steel castings to intergranular embrittlement. *Metals Technology*, 10:285–290, August 1983.
31. N.H. Croft, A.R. Entwisle, and G.J. Davies. Origins of dendritic AlN precipitates in aluminium-killed-steel castings. *Metals Technology*, 10:125–129, April 1983.
32. N. Triolet, K. Poelmans, P. Maybelly, and Y.L. Papillon. Prevention of corner cracks in slab continuous casting. *Revue de Metallurgie*, (11):508–517, November 2009.
33. I.V. Samasekera, R. Bommaraju, and J.K. Brimacombe. Factors influencing the formation of oscillation marks in the continuous casting of steel billets. In *24th Annual Conference of Metallurgists/15th Annual Hydrometallurgical Meeting 1985*, Vancouver, B.C., Canada, August 1985. CIM.
34. E.T. Turkdogan. Causes and effects of nitride and carbonitride precipitation in HSLA steels in relation to continuous casting. In *AIME Steelmaking Conf. Proc.*, volume 70, pages 399–416, Warrendale, PA, 1987.
35. M. Suzuki, H. Hayashi, H. Shibata, T. Emi, and I-J. Lee. Simulation of transverse crack formation on continuously cast peritectic medium carbon steel slabs. *steel research*, 70(10):412–419, 1999.

36. T.E. Shelenberger, A.A. Ekis, T. Kondo, and M. Suzuki. Prevention of transverse cracking in continuously cast slabs. In *Proceedings of the Sixth International Iron and Steel Congress*, pages 377–384, Nagoya, 1990. ISIJ.
37. T. Kato, A. Yamanaka, and T. Watanabe. Prevention of transverse cracking in microalloyed continuously cast slabs by microstructure control. In *1997 Steelmaking Conference Proceedings*, pages 345–349, 1997.
38. T. Kato, Y. Ito, M Kawamoto, A. Yamanaka, and T. Watanabe. Prevention of slab surface transverse cracking by microstructure control. *ISIJ Int*, 43(11):1742–1750, 2003.
39. B. Mintz. The influence of composition on the hot ductility of steels and to the problem of transverse cracking. *ISIJ International*, 39(9):833–855, 1999.
40. J.R. Wilcox and R.W.K. Honeycombe. Influence of proir precipitation on hot ductility of C-Mn-Nb-Al steels. In *Proceedings of Conference on Hot working and forming processes*, pages 108–112. Sheffield Eng, July 1979.
41. D.N. Crowther and B. Mintz. Influence of grain size and precipitation on hot ductility of microalloyed steels. *MS&T*, 2:1099–1105, November 1986.
42. H.G. Suzuki, S. Nishimura, and S. Yamaguchi. Characteristics of hot ductility in steels subjected to the melting and solidification. *Transactions of the Iron and Steel Institute of Japan*, 22:48–56, 1982.
43. B. Mintz, J.R. Wilcox, and D.N. Crowther. Hot ductility of directly cast C-Mn-Nb-Al steel. *MS&T*, 2:589–594, June 1986.
44. H. Zhang, H. Guo, and B. Wu. Effect of Nb on hot ductility of continuously cast low carbon manganese steels. *ISIJ*, pages 170–177, 1988.
45. T. Prucha. *Metals Handbook*, volume 15, chapter 6, Foundary equipment and processing, pages 544–560. ASM International, Metals Park, Ohio, ninth edition, 1988.
46. B.C. Woodfine and A.G. Quarrell. Effect of Al and N on the occurence of intergranular fracture in steel castings. *JISI*, pages 409–414, August 1960.
47. B.L. Bramfitt. *Metals Handbook*, volume 15, chapter 3, Solidification structures of steel, pages 623–628. ASM International, Metals Park, Ohio, ninth edition, 1988.
48. M.F. Ashby and R. Ebeling. On the determination of the number, size, spacing and volume fraction of spherical second-phase particles from extraction replicas. *Transactions of the Metallurgical Society of the AIME*, 236:1396–1404, October 1966.

49. C. Ouchi and K. Matsumoto. Hot ductility in Nb-bearing High-Strength Low-alloy steel. *Trans. ISIJ*, 22:181–189, 1982.
50. B. Mintz, A. Cowley, and R. Abushosha. Importance of columnar grain in dictating hot ductility of steels. *MS&T*, 16:1–5, January 2000.
51. J. Hertel, H. Litterscheidt, U. Lotter, and H. Pircher. Laboratory simulation of strand shell stresses and strains during continuous casting. In *Continuous Casting*, volume 8, pages 211–222, 1997.
52. H. Heibler and C. Bernhard. Mechanical properties and crack susceptibility of steel during solidification. *steel research*, 70(8+9):349–355, 1999.
53. A.M. El-wazri, F. Hassani, S. Yue, E. Es-sadiqi, L.E. Collins, and K. Iqbal. The effect of thermal history on the hot ductility of microalloyed steels. *ISIJ Int.*, 39(3):253–262, 1999.
54. B. Mintz and J.M. Arrowsmith. Hot-ductility behaviour of C-Mn-Nb-Al steels and its relationship to crack propagation during the straightening of continuously cast strand. *Metals Technology*, pages 24–32, January 1979.
55. B. Mintz and A. Cowley. Deformation induced ferrite and its influence on the elevated temperature tensile flow stress/elongation curves of plain C-Mn and Nb containing steels. *MS&T*, 22(3):279, 2006.
56. A. Cowley and B. Mintz. Relative importance of transformation temperatures and sulphur content on hot ductility of steels. *MS&T*, 20:1431–1439, November 2004.
57. D.N. Crowther and B. Mintz. Influence of grain size on hot ductility of plain C-Mn steels. *MS&T*, 2:951–955, September 1986.
58. B. Mintz. Private communication, 2009.
59. B. Mintz and R. Abushosha. Effectiveness of hot tensile testing in simulating straightening in continuous casting. *MS&T*, 8:171–177, February 1992.
60. K. Yasumoto, Y. Maehara, S. Ura, and Y. Ohmori. Effects of sulphur on hot ductility of low-carbon steel austenite. *MS&T*, 1:111–116, February 1985.
61. B. Mintz and R. Abushosha. The hot ductility of V, Nb/V and Nb containing steels. *Materials Science Forum*, 284-286:461–468, 1998.
62. B. Mintz and Z. Mohamed. Hot ductility of directly cast micro-alloyed steels. In K. Salama *et al.*, editor, *Proc. 7th Int. Conf. on Fracture*, volume 4, pages 2524–2544, 1989. Pergamon, Oxford.

63. N.E. Hannerz. Critical hot plasticity and transverse cracking in continuous slab casting with particular reference to composition. *Transactions of the Iron and Steel Institute of Japan*, 25:149–158, 1985.
64. R. Abushosha, R. Vipond, and B. Mintz. Influence of titanium on hot ductility of as cast steels. *MS&T*, 7:613–621, July 1991.
65. B. Mintz and J.M. Arrowsmith. Influence of microalloying additions on hot ductility of steels. In C.M. Sellars and G.T. Davies, editors, *Sheffield Int. Conf. on Hot Working and Forming Processes*, pages 99–103. Metals Society, London, 1979.
66. B. Mintz, R. Abushosha, and J.J. Jonas. Influence of dynamic recrystallisation on the tensile ductility of steels in the temperature range 700 to 1150°C. *ISIJ*, 32(2):241–249, 1992.
67. B. Mintz, R. Abushosha, and A. Cowley. Preliminary analysis of hot ductility curve in simple C-Mn steels. *MS&T*, 14(5):222–226, March 1998.
68. A. Guillet, S. Yue, and G. Akben. Influence of heat treatment and carbon content on hot ductility of Nb-Ti microalloyed steels. *ISIJ Int*, 33(3):413–419, 1993.
69. T. Revaux, J.P. Bricout, and J. Oudin. A new tensile testing procedure for predicting transverse cracking susceptibility of continuous casting slabs. *Journal of Materials Engineering Performance*, 5(2):260–268, April 1996.
70. H.G. Suzuki, S. Nishimura, and Y. Nakamura. Improvement of hot ductility of continuous cast carbon steels. *Trans ISIJ*, 24:54–59, 1984.
71. H.G. Suzuki, S. Nishimura, and S. Yamaguchi. Physical simulation of the continuous casting of steel. In *International Symposium on Physical Simulation of Welding, Hot Forming and Continuous Casting*, pages II–1–14, Ottawa, Canada, 1988.
72. A. Cowley, R. Abushosha, and B. Mintz. Influence of  $A_{r3}$  and  $A_{e3}$  temperatures on hot ductility of steels. *MS&T*, 14:1145–1153, November 1998.
73. B. Mintz. Importance of  $A_{e3}$  temperature in controlling ductility and width of hot ductility trough in steels, and its relationship to transverse cracking. *MS&T*, 12:132–138, February 1996.
74. N. Bannenber, B. Bergman, H.-A. Jungblut, N. Müller, and K. Reich. Procedures for successful continuous casting of steel microalloyed with Nb, V, Ti and V. In *Microalloying '95 Conference Proceedings*, pages 83–94.
75. K. Yasumoto, Y. Maehara, and Y. Ohmori. Surface cracking mechanisms of low carbon low alloy steel slabs. In *McMaster Symposium on Iron and Steelmaking*, volume 13, pages 74–107, 1985.

76. B. Mintz, J.J. Jonas, and S. Yue. The influence of dynamic recrystallisation on the hot ductility of steels at low strain rates. In T. Chandra, editor, *Recrystallization '90*, pages 553–558. The Minerals, Metals & Materials Society, 1990.
77. P.D. Nicolaou and S.L. Semiatin. A theoretical investigation of the effect of material properties and cavity architecture/shape on ductile failure during the hot torsion test. *Metallurgical and Materials Transactions A*, 29A:2621–2630, October 1998.
78. P. Heritier, A. Fourdeux, and A. Kobylanski. The influence of aluminium nitride on the hot ductility of ultra high purity steels. *Scripta Metallurgica*, 15:753–755, 1981.
79. H.G.Suzuki, S.Nishimura, J.Imamura, and Y.Nakamura. Embrittlement of steels occurring in the temperature ranges from 1000 to 600°C. *Transactions of the Iron and Steel Institute of Japan*, 24:169–177, 1984.
80. Y. Maehara, K. Yasumoto, H. Tomono, T. Nagamichi, and Y. Ohmori. Surface cracking mechanism of continuously cast low carbon low alloy steel slabs. *MS&T*, 6:793–805, September 1990.
81. K.J. Irvine and F.B. Pickering. Ferrite networks. *Iron and Steel*, pages 219–223, 1957.
82. D.N. Crowther, M.J.W. Green, and P.S. Mitchell. The influence of composition on the hot cracking susceptibility during casting of microalloy steels processed to simulate thin slab casting conditions. *Materials Science Forum*, 284-286:469–476, 1998.
83. B. Mintz and Z. Mohamed. Intergranular failure in micro-alloyed steels and its relationship to carbon content. In K. Salama *et al.*, editor, *Proc. 7th Int. Conf. on Fracture*, volume 4, pages 2545–2553, 1989. Pergamon, Oxford.
84. B. Mintz and J.J. Jonas. Influence of strain rate on production of deformation induced ferrite and hot ductility of steels. *MS&T*, 10:721–727, August 1994.
85. B. Mintz, M. Shaker, and D.N. Crowther. Hot ductility of an austenitic and a ferritic stainless steel. *MS&T*, 13:243–249, March 1997.
86. B. Mintz, R. Abu-Shosha, and M. Shaker. Influence of deformation induced ferrite, grain boundary sliding and dynamic recrystallisation on the hot ductility of 0.1-0.75 %C steels. *MS&T*, 9:907–914, October 1993.
87. R. Abushosha, S. Ayyad, and B. Mintz. Influence of cooling rate and MnS inclusions on hot ductility of steels. *MS&T*, 14:227–235, March 1998.
88. J.Y. Fu, C.I. Garcia, and A.J. DeArdo. On the hot ductility of continuously cast microalloyed steels. In *8th PTD Conference Proceedings*, pages 43–49, 1988.

89. J. Lewis, J.J. Jonas, and B. Mintz. The formation of deformation induced ferrite during mechanical testing. *ISIJ Int*, 38(3):300–309, 1998.
90. B. Mintz. Understanding the low temperature end of the hot ductility trough in steels. *MS&T*, 24(1):112–120, 2008.
91. B. Chamont, P. Chemelle, and H. Biauxser. Nitrures d’aluminium et ductilité à chaud des aciers coulés en continu. In J Bowker, editor, *Physical simulation techniques for welding, hot-forming and continuous casting*, volume 2, pages 48–52, Ottawa, Canada, 1992. Canmet.
92. Y. Maehara, K. Yasumoto, Y. Sugitani, and K. Gunji. Effect of carbon on hot ductility of as-cast low alloy steels. *Trans ISIJ*, 25:1045–1052, 1985.
93. I. Weiss and J.J. Jonas. Dynamic precipitation and coarsening of niobium carbonitrides during the hot compression of HSLA steels. *Met Trans A*, 11A:403–410, March 1980.
94. R. Abushosha, O. Comineli, and B. Mintz. Influence of Ti on hot ductility of C-Mn-Al steels. *MS&T*, 15:278–286, March 1999.
95. H. Zhang, Z. Lu, and B. Wu. Study of hot ductility of microalloyed steels under continuous casting conditions. In T. Chandra and T. Sakai, editors, *Thermec '97, International Conference on Thermomechanical Processing of Steels and Other Materials*, pages 571–578. The Minerals, Metals & Materials Society, 1997.
96. B. Mintz and R. Abushosha. Influence of vanadium on hot ductility of steel. *Ironmaking and Steelmaking*, 20(6):445–452, 1993.
97. O. Comineli, R. Abushosha, and B. Mintz. Influence of titanium and nitrogen on hot ductility of C–Mn–Nb–Al steels. *MS&T*, 15:1058–1068, September 1999.
98. K.Suzuki, S.Miyagawa, Y.Saito, and K.Shiotani. Effect of microalloyed nitride forming elements on precipitation of carbonitride and high temperature ductility of continuously cast low carbon Nb containing steel slab. *ISIJ International*, 35(1):34–41, 1995.
99. B. Garbarz, J. Marcisz, and J. Wojtas. TEM analysis of fine sulphides dissolution and precipitation in steel. *Materials Chemistry and Physics*, 81:486–489, 2003.
100. O. Comineli, H. Luo, H-M. Liimatainen, and L.P. Karjalainen. Influence of Ni alloying on hot ductility of Ti-Nb microalloyed steels. In *59th Annual Conference of Associação Brasileira de Metalurgia e Materias*, São Paulo, 19-22 July 2004. ABM. Ref 3639.
101. J.R. Wilcox and R.W.K. Honeycombe. Effect of precipitation on hot ductility of niobium and aluminium microalloyed steels. *MS&T*, 3:849–854, October 1987.

102. S.F. Medina and A. Guispe. Influence of strain on induced precipitation kinetics in microalloyed steels. *ISIJ International*, 36(10):1295–1300, 1996.
103. J.J. Jonas and I. Weiss. Effect of precipitation on recrystallization in microalloyed steels. *Metals Science*, pages 238–245, March-April 1979.
104. I. Weiss and J.J. Jonas. Interaction between recrystallization and precipitation during the high temperature deformation of HSLA steels. *Met Trans A*, 10A:831–839, July 1979.
105. D.N. Crowther and B. Mintz. Influence of carbon on hot ductility of steels. *MS&T*, 2:671–676, July 1986.
106. M. Wolf and W. Kurz. The effect of carbon content on solidification of steel in the continuous casting mold. *Metallurgical Transactions B*, 12B:85–93, March 1981.
107. M. Militzer, R. Pandi, and E.B. Hawbolt. Ferrite nucleation and growth during continuous casting. *Metallurgical and Materials Transactions A*, 27A:1547–1556, June 1996.
108. J.P. Michel and J.J. Jonas. Precipitation kinetics and solute strengthening in high temperature austenites containing Al and N. *Acta Metallurgica*, 29:513–526, 1981.
109. L.A. Erasmus. Effect of small additions of vanadium on the austenitic grain size, forgeability, and impact properties of steel. *JISI*, pages 128–134, February 1964.
110. W.T. Lankford. Some considerations of strength and ductility in the continuous casting process. *Met Trans*, 3:1331–1357, June 1972.
111. G.A. de Toledo, O. Campo, and E. Lainez. Influence of sulphur and Mn/S ratio on the hot ductility of steels during continuous casting. *steel research*, (6):292–299, 1993.
112. Y. Maehara and T. Nagamichi. Effects of sulphur on hot ductility of niobium containing low carbon steels during low strain rate deformation. *MS&T*, 7:915–921, October 1991.
113. G.A. Osinkolu, M. Tacikowski, and A. Kobylanski. Combined effect of AlN and sulphur on hot ductility of high purity iron-based alloys. *MS&T*, 1:520–525, July 1985.
114. Z.L. Zhang, Q.Y. Lin, and Z.S. Yu. Non-equilibrium intergranular segregation in ultra low carbon steel. *MS&T*, 16:305–308, April 2000.
115. H. Kobayashi. Hot-ductility recovery by manganese sulphide precipitation in low manganese mild steel. *ISIJ Int*, 31(3):268–277, 1991.

116. H. C. Chen, H. Era, and M. Shimizu. Effect of phosphorus on the formation of retained austenite and mechanical properties in Si-containing low-carbon steel sheet. *Met Trans A*, 20A:437–445, March 1989.
117. B. Mintz, A. Cowley, C. Talian, D.N. Crowther, and R. Abushosha. Influence of P on hot ductility of high C, Al, and Nb containing steels. *MS&T*, 19:184–188, February 2003.
118. B. Mintz. Influence of nitrogen on hot ductility of steels and its relationship to problems of transverse cracking. *Ironmaking and Steelmaking*, 27(5):343–347, 2000.
119. D.N. Crowther, Z. Mohamed, and B. Mintz. The relative influence of dynamic and static precipitation on the hot ductility of microalloyed steels. *Metallurgical Transactions A*, 18A:1929–1939, November 1987.
120. M.G. Akben, B. Bacroix, and J.J. Jonas. Effect of vanadium and molybdenum addition on high temperature recovery, recrystallization and precipitation behaviour of niobium-based microalloyed steels. *Acta metall.*, 31:161–174, 1983.
121. C.M. Sellars. The physical metallurgy of hot working. In *Proc. Int Conf. on hotworking and forming processes*, pages 3–15. Sheffield University, July 1979.
122. Z. Luo, H. Zhang, and B. Wu. Effect of niobium on hot ductility of low C-Mn-steel under continuous casting simulation conditions. *Steel Research*, 61(12):620–623, 1990.
123. A. J. DeArdo. Fundamental metallurgy of niobium in steel. In *Niobium Science and Technology*, pages 427–500. TMS, Niobium 2001 Ltd, December 2001.
124. V. K. Heikkinen and R.H. Packwood. On the occurrence of Fe-NbC eutectic in niobium-bearing mild steel. *Scan. J. Metallurgy*, 6:170–175, 1977.
125. T.H. Coleman and J.R. Wilcox. Transverse cracking in continuously cast HSLA slabs - influence of composition. *MS&T*, 1:80–83, 1985.
126. B. Mintz and DN. Crowther. The influence of small additions of Ti on the hot ductility of steels. In T.N. Baker, editor, *Titanium technology in microalloyed steels*, pages 98–115. The Institute of Metals, December 1994.
127. F. Vodopivec. On the influence of hot deformation of low-carbon steel by rolling on the precipitation of aluminium nitride. *JISI*, pages 664–665, September 1973. Technical note.
128. E. Furubayashi, H. Endo, and H. Yoshida. Effects of prior plastic deformation on the distribution and morphology of AlN precipitates in  $\alpha$ -iron. *Materials Science and Engineering*, 14:123–130, 1974.

129. H. Yin and G. Skoczylas. In-situ observations and thermodynamics of the chemical reaction between AlN particles and molten slag. In *AISTech 2006 Proceedings*, page 753, 2006.
130. D. Hall and G.H.J. Bennett. Inhibition of austenite grain growth by aluminium nitride. *JISI*, pages 309–314, March 1967.
131. M. Zhang, L. Li, R.Y. Fu, D. Krizan, and B.C. De Cooman. Continuous cooling transformation diagrams and properties of micro-alloyed trip steels. *MS&T*, 438:296–299, 2006.
132. Y-L. Kang, H. Yu, J. Fu, K. Wang, and Z. Wang. Morphology and precipitation kinetics of AlN in hot strip of low carbon steel produced by compact strip production. *Materials Science and Engineering A*, A351:265–271, 2003.
133. H.S. Choi, C.M. Lee, and J. Choi. Precipitation and coarsening behavior of aluminium nitride in the Fe-Al-N alloy. *Journal of the Korean Institute of Metals*, 16(6):485–494, 1978.
134. A. Güth, L. Kaun and A. Köthe, D.Müller, and J. Richter. Investigation of the influence of reheating temperature on size and composition of precipitates in microalloyed HSLA steels by analytical electron microscopy. *Scripta Metallurgica*, 21(2):163–168, 1987.
135. S. Hasebe. Effects of aluminium nitride on the high-temperature ductility and on the welding crack of low-carbon steel. *Tetsu-to-Hagane*, 48(12):1575–1581, 1962.
136. J.A. Wright and A.G. Quarrell. Effect of chemical composition on the occurrence of intergranular fracture in plain carbon steel castings containing aluminium and nitrogen. *JISI*, 200:299–307, April 1962.
137. D.N. Crowther, Z. Mohamed, and B. Mintz. Influence of micro-alloying additions on the hot ductility of steels heated directly to test temperature. *Trans. ISIJ*, 27:366–375, 1987.
138. M. Leger and B. Guillaume. Microfractographic diagnosis of the embrittlement of steel castings by aluminum. *International Cast Metals*, pages 40–46, September 1980.
139. M.J. Leap and E.L. Brown. Crystallography of duplex AlN-Nb(C,N) precipitates in 0.2 %C steel. *Scripta Materialia*, 47:793–797, 2002.
140. K.E. Blazek, O. Lanzi III, P.L. Gano, and D. L. Kellogg. Calculation of the peritectic range for steel alloys. *Iron and Steelmaking*, (5):80, July 2008. First Published in AISTech 2007, Proc. AIST, Indianapolis 2007, Vol 12 pp81-87.

141. R.C. Sharma, V.K. Lakshmanan, and J.S. Kirkaldy. Solubility of niobium carbide and niobium carbonitride in alloyed austenite and ferrite. *Met. Trans. A*, 15A:545–553, March 1984.
142. Z. Lui, Y. Kobayashi, and K. Nagai. Crystallography and precipitation kinetics of copper sulphide in strip casting low carbon steel. *ISIJ Int*, 44(9):1560–1567, 2004.
143. B. Mintz, R. Abushosha, and D.N. Crowther. Influence of small additions of copper and nickel on hot ductility of steels. *MS&T*, 11:474–481, May 1995.
144. W.C. Leslie, R.L. Ricket, C.L. Dotson, and C.S. Walton. Solution and precipitation of aluminium nitride in relation to the structure of low carbon steels. *Trans. ASM*, 46:1470–1499, 1954.
145. G. Krauss, D. O. Wilshynsky, and D.K. Matlock. Processing and properties of interstitial-free steels. In L.E. Collins and D. L. Baragar, editors, *Proceeding International Symposium on Interstitial Free sheet: Processing, fabrication and properties*, pages 1–14, Ottawa, Ontario, August 1991. Canadian Institute of Mining, Metallurgy and Petroleum.
146. E.T. Turkdogan, S. Ignatowicz, and J. Pearson. The solubility of sulphur in iron and iron-manganese alloys. *JISI*, 180:349–354, 1955.
147. W. J. Lui, J.J. Jonas, and E.B. Hawbolt. Thermodynamic prediction of carbonitride and sulphide precipitation in multicomponent austenite. In S. Yue, editor, *Canmet*, pages 457–466, Hamilton, Ontario, Canada, 1990. Canadian Institute of Mining and Metallurgy.
148. L.S. Darken, R.P. Smith, and E.W. Filer. Solubility of gaseous nitrogen in gamma iron and the effect of alloying constituents - aluminium nitride precipitation. *Trans. AIMME*, 191:174, 1951. in reference [144].
149. K.J. Irvine, F.B. Pickering, and T. Gladman. Grain refined C-Mn steels. *JISI*, pages 161–182, February 1967.
150. H.A. Wriedt. *Met. Trans. A*, 11A:1731–1736, 1980. in reference [34].
151. D.B. Evans and R.D. Pehlke. *Trans. AIME*, pages 1651–1656, 1964. in reference [34].
152. E. T. Turkdogan. Causes and effects of nitride and carbonitride precipitation during continuous casting. *Iron and Steelmaker*, 16(5):61–75, 1989. in reference [145].
153. J. Strid and E.K. Easterling. On the chemistry and stability of complex metal carbides and nitrides in microalloyed steels. *Acta Metall.*, 33(11):2057–2074, 1989. in reference [145].

154. T. Gladman and F.B. Pickering. Grain-coarsening of austenite. *JISI*, pages 653–664, June 1967.
155. T. Mori, M. Tokizane, K. Yamaguchi, E. Sunami, and Y. Nokazima. Thermodynamic properties of niobium carbides and nitrides in steels. *Tetsu-to-Hagané*, 7:763–776, 1968. used by [34].
156. H. Nordberg and B. Aronsson. Solubility of niobium carbide in austenite. *JISI*, pages 1263–1266, December 1968.
157. T. Mori, M. Tokizane, Y. Nakazima, and T. Saheki. Thermodynamic behaviours of niobium carbide-nitride and sulphide in steel. *Tetsu-to-Hagané*, 51(11):2031–2033, 1965.
158. L. Santella. *Grain growth and high-temperature hot rolling behavior of low-alloy steel austenite*. Ph.D. thesis, University of Pittsburgh, 1981. in reference [123].
159. J. M. Cabrera, A.A. Omar, and J.M. Prado. Effect of second phase particles on the grain size of a multi-microalloyed medium carbon steel. *Z. Metallkd*, 89(1):47–58, 1998.
160. T. Gladman. Aluminium for grain size control. *Heat Treatment of Metals*, 1:11–14, 1994.
161. L.H. Cheng, E.B. Hawbolt, and T.R Meadowcroft. Modelling of AlN precipitation in low carbon steels. *Scripta Materialia*, 41(6):673–678, 1999.
162. B. G. Thomas, I. V. Samarasekera, and J.K. Brimacombe. Mathematical model of thermal processing of steel ingots: Part 1. Heat flow model. *Met Trans*, 18B:119–130, 1987.
163. A. Jablonka, K. Harste, and K. Schwerdtfeger. Thermomechanical properties of iron and iron-carbon alloys: density and thermal contraction. In M. Wolf, editor, *Continuous Casting*, volume 9, pages 155–163. Iron & Steel Society, 1997. Originally published in *Steel Research*, vol 62, 1991, pp24-33.
164. N. F. Kennon. *Optical Microscopy of Carbon Steels*, chapter “Phase transformations”, pages 41–44. American Society for Metals, Metals Park, Ohio, 1980.
165. M. Wolf. Initial soludification and strand surface quality of peritectic steels, Addendum 1. In M. Wolf, editor, *Continuous Casting*, volume 9, pages 59–68. Iron & Steel Society, 1997.
166. K. Yasumoto, T. Nagamichi, Y. Maehara, and K. Gunji. Effects of alloying elements and cooling rate on austenite grain growth in soludification and the subsequent cooling process of low alloy steels. *Tetsu-to-Hagané*, 73(14):1738–1745, 1987.

167. K.W. Andrews. Empirical formulae for the calculation of some transformation temperatures. *JISI*, pages 721–727, July 1965.
168. D. Kruse. Spreadsheets for standard thermodynamic predictions in steel. Excel Spreadsheets, Arcelor-Mittal, 2008.
169. D.P. Rizio, R.B. Oldland, and D. W. Borland. The effect of austenite grain refinement on the hot ductility of steel. In *Physical metallurgy of thermomechanical processing in steel and other metals, Thermec '88*, pages 178–185, Tokyo, Japan, 1988. The Iron and Steel Institute of Japan.
170. V. Kutumba Roa, D.M.R. Taplin, and P. Rama Rao. The grain size dependence of flow and fracture in a Cr-Mn-N austenitic steel from 300 to 1300K. *Met Trans A*, 6A:77–86, January 1975.
171. T. Maki, T. Nagamichi, N. Abe, and I. Tamura. Formation behavior of proeutectoid ferrite and hot ductility in  $(\alpha + \gamma)$  two phase region in low carbon steels. *Tetsu-to-Hagane*, 71(10):1367–1374, 1985.
172. Y. Maehara, K. Yasumoto, H. Tomono, and Y. Ohmori. Morphology of carbonitrides and hot ductility of low carbon low alloy steels. *Transactions of the ISIJ*, 27:222–228, 1987.
173. W.P. Sun, M. Militzer, and J.J. Jonas. Strain-induced nucleation of MnS in electrical steels. *Met. Trans. A*, 23A:821–830, March 1992.
174. K. Yasumoto, Y. Maehara, T. Nagamichi, and H. Tomono. Effect of thermo-mechanical history on surface cracking of as-cast low carbon low alloy steel slabs. *Trans ISIJ*, 29(11):933–939, 1989.
175. K. Yasumoto, Y. Maehara, T. Nagamichi, and H. Tomono. Effect of thermo-mechanical history on surface cracking of as-cast low carbon low alloy steel slabs. *Tetsu-to-Hagane*, 73(10):1381–1388, 1987.
176. R. Abushosha, S. Ayyad, and B. Mintz. Influence of cooling rate on hot ductility of C-Mn-Al and C-Mn-Nb-Al steels. *MS&T*, 14:346–351, April 1998.
177. S.E. Kang, A. Tuling, and B. Mintz. The hot ductility of Nb containing TRIP steels. In *3rd International Conference on Thermomechanical Processing of Steels*, Padua, 10-12 September 2008.
178. S.E. Kang and B. Mintz. The hot ductility of TWIP steels and Nb containing TRIP steels melted in situ. Final report, POSCO, August 2007.
179. S.E. Kang and B. Mintz. The hot ductility of TWIP steels and Nb containing TRIP steels. Interim report, POSCO, March 2007.

180. D.C. Montgomery. *Design and analysis of experiments*. John Wiley & Sons, 4th edition, 1997.
181. D.B. Williams and C.B. Carter. *Transmission electron microscopy: a textbook for materials science*, volume 1. Plenum, 1996.
182. Peter Kang. Private communication, 2010.
183. M. Gomez, C.I.Garcia, D.M. Haezebrouck, and A.J. DeArdo. Design of composition in (Al/Si)-alloyed TRIP steels. *ISIJ International*, 49(2):302–311, 2009.
184. Advanced low carbon cold rolled steel strip. Internet, 2010. <http://www.steeluniversity.org/content/html/eng/3200-0100.htm>.
185. A. F. Wright and J. S. Nelson. Consistent structural properties of AlN, GaN and InN.
186. International crystal structure database. Database, 2009.
187. H. Schultz and K.H. Thiemann. Crystal structure refinement of AlN and GaN. *Solid State Communications A*, 23:815–819, 1977.